Developing a novel, non-invasive detection technique in hot and cold atomic systems based on spin noise spectroscopy (SNS)

Department of Light and Matter Physics (LAMP)
Raman Research Institute
Bangalore - 560 080, India

Thesis submitted for the degree of

Doctor of Philosophy
to
Jawaharlal Nehru University
New Delhi - 110067, India

by
Maheswar Swar

Supervisor: **Dr. Saptarishi Chaudhuri**
Co-Supervisor: **Dr. Dibyendu Roy**

March, 2022

Declaration of Original and Sole Authorship

I, **Maheswar Swar**, declare that this thesis entitled "**Developing a novel, non-invasive detection technique in hot and cold atomic systems based on spin noise spectroscopy (SNS)**" and the data presented in it are original and my own work under the supervision of **Dr. Saptarishi Chaudhuri** and **Dr. Dibyendu Roy**. I confirm that the work presented here has not been submitted for the award of any other degree, diploma, membership, associateship, fellowship, etc. of any other university or Institute. I further confirm that References to the work of others have been clearly acknowledged. Quotations from the work of others have been clearly indicated, and attributed to them and in cases where others have contributed to part of this work, such contribution has been clearly acknowledged and distinguished from my own work. I have also run the thesis through the Turnitin software.

Maheswar Swar

(Signature of the student)
Maheswar Swar
Date: March 7, 2022

Dibyendu Roy

(Signature of the co-supervisor)
Dr. Dibyendu Roy
Date: March 7, 2022

Saptarishi

(Signature of the supervisor)
Dr. Saptarishi Chaudhuri
Date: March 7, 2022

Certificate

This is to certify that the work contained in the thesis titled **"Developing a novel, non-invasive detection technique in hot and cold atomic systems based on spin noise spectroscopy (SNS)"**, submitted by **Maheswar Swar** (Enrollment No. - RRI/2015/007) to **Jawaharlal Nehru University** for the award of the degree of **Doctor of Philosophy** in Physical Sciences, is the bonafide record of original research work carried out by the candidate from August 2015 - February 2022, under my guidance and supervision at the **Raman Research Institute**, Bengaluru, India. The results embodied in the thesis have not been submitted to any other University or Institute for the award of any degree or diploma.

(Signature of the director)
Prof. Tarun Souradeep Ghosh
Date: March 7, 2022

(Signature of the co-supervisor)
Dr. Dibyendu Roy
Date: March 7, 2022

(Signature of the Supervisor)
Dr. Saptarishi Chaudhuri
Date: March 7, 2022

Abstract

In this thesis, we report for the first time, the measurement of intrinsic spin-coherences from an ensemble of a cold rubidium atoms using non-invasive Faraday rotation fluctuation measurements. We employ off-resonant Raman coupling between the Zeeman states of a ground hyperfine level of rubidium atoms in a magneto-optical trap (MOT) to enhance the spin-coherences, and thereby detect it non-destructively using a far off-resonant probe laser field. We have developed a comprehensive theoretical model based on optical Bloch equations (OBE) to study the characteristics of the Raman driven spin-coherences, and find a way to measure the quantity - intrinsic spin-relaxation rate (γ') of the system under investigation. First, we have implemented the Raman driven technique to characterize the measurement methods in thermal rubidium atoms. We have compared the extracted value of γ' using Raman driven technique, with a separate measurement done using intrinsic spin noise spectroscopy (SNS) [1–5] technique. We have demonstrated a good qualitative and quantitative agreement in measuring γ' between these two techniques in thermal rubidium atoms. After this characterization, we have moved to the cold atom measurements, and implemented this technique to extract the value of intrinsic spin-relaxation rate, γ'.

Spin is a unique characteristic of the subatomic particles, such as electrons and nucleus (protons and neutrons) of an atom. Measurements of electronic spin properties of a system, in particular its lifetime in an energy state and de-coherence rate, is the backbone of understanding its interactions with various potentials, and applications to metrology purposes. Our novel detection technique non-invasively probe the intrinsic spin dynamics of a system with much longer duration than its characteristic time and provides valuable information about the physical properties of the system. This detection method have significant potential applications for precision magnetometry [6, 7], high-resolution imaging [8–12], non-invasive probing of quantum phase transitions [13–16] in cold atoms and other similar systems, e.g., cold ions, cold molecules. In this thesis, we indicate all these possibilities using cold atom spin-coherence measurements by our theoretically developed and experimentally demonstrated non-perturbative detection technique.

This thesis work had been started, mainly focusing on detecting the intrinsic spin-coherence in the cold and ultra-cold atomic systems to develop a non-perturbative spin based imaging technique for similar systems. However, prior to this thesis work, the measurements of intrinsic spin-coherence using the SNS technique had not been performed in the cold atoms. Nevertheless, our technique of Raman driven SNS, mentioned earlier, predicts several orders of magnitude enhancement in the atomic spin-coherence between the adjacent Zeeman states in comparison to their intrinsic signal. Such a huge enhancement in the signal strength made it possible to detect the Raman driven signal from cold atoms. With the help of our theory and from the measured Raman driven spectrum, we have extracted the value of γ' of the cold atomic sample.

In the cold atom experiments, we have trapped more than 10^7 ^{85}Rb atoms at 150 μK temperature from a vapor loaded MOT inside a glass chamber maintaining background pressure of 10^{-11} mbar. The cooling beams were generated from an external cavity diode laser (ECDL) and frequency stabilized to the 12 MHz red detuned with respect to $5S_{1/2}, F = 3 \rightarrow 5P_{3/2}, F' = 4$ (D_2) transition. The 'repumping' laser beams were derived from another ECDL and frequency stabilized to the $5S_{1/2}, F = 2 \rightarrow 5P_{1/2}, F' = 3$ (D_1) transition. A pair of magnetic coils in anti-Helmholtz configuration produces the required spatial magnetic field gradient. We coincided the optical and magnetic field centers with an accuracy of ~ 30 μm. Thereafter, we coherently drive the trapped cold atoms in $F = 3$ hyperfine level using a pair of phase coherent Raman radiation fields with laser frequency detuned by 2γ (γ is the natural line-width of the excited hyperfine level) in blue side from the $5S_{1/2}, F = 3 \rightarrow 5P_{3/2}, F' = 4$ (D_2) transition of ^{85}Rb (see Fig. 1(b)). The driving fields create coherence between the consecutive Zeeman states in $F = 3$ hyperfine level, and dispersively detect the spin coherence at the two photon detuning ($\delta_{12}(\equiv (\omega_{s1} - \omega_{s2})/2\pi)$, where $\omega_{s1}(\omega_{s2})$ is the frequency of the Raman field 1 (2), respectively) of the Raman fields on the polarization states of the linearly polarized probe laser field, see Fig. 1(a) (inset). The probe laser field is kept at the 20γ blue detuned away from the same transition to minimize the scattering rate. We subsequently vary the δ_{12} while keeping one of the Raman field frequency fixed. We have explored the response of the spin-coherence in a wide range of frequency span. The response at each δ_{12} is a delta peak (whose width is limited by the relative frequency stability of the Raman fields during the measurement duration) with strength determined by the second order correlation of the density matrix formed by these Zeeman state coherences. The composite spectrum over a wide frequency span represents the Raman driven spin-coherence signal from cold atomic cloud.

We have repeated the experiment for many runs, recorded the peak strength at each δ_{12}, and plotted the average value of peak strength in terms of frequency δ_{12}. We

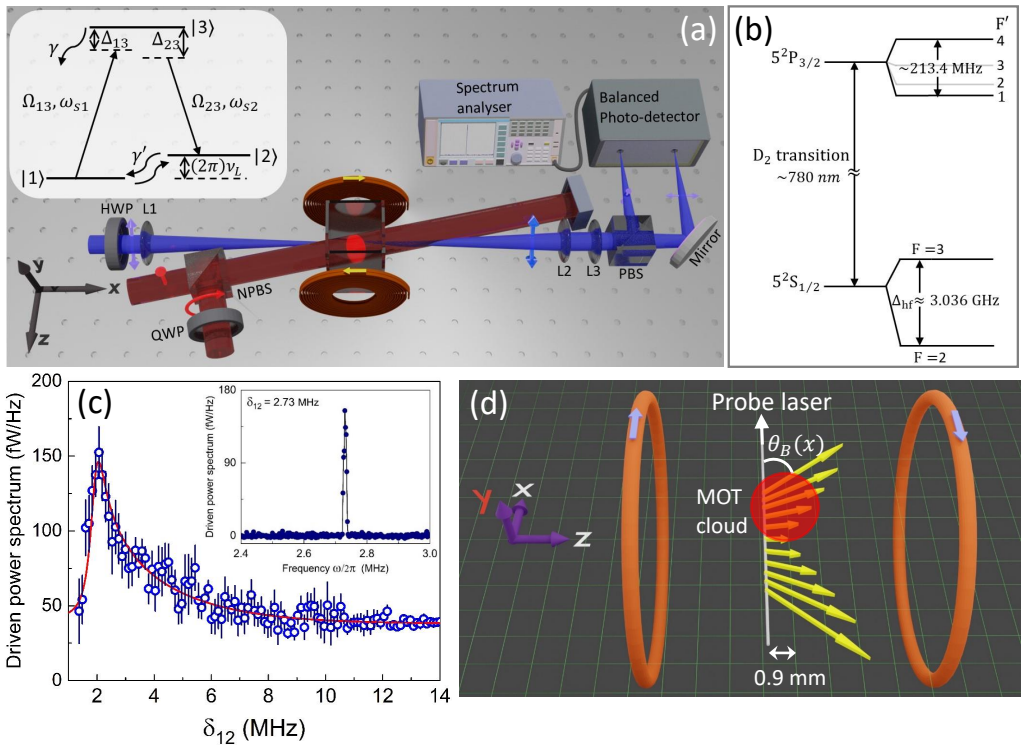

Figure 1: Cold atom spin-relaxation rate (γ') measurement using Faraday rotation fluctuation measurements. (a) Schematic diagram of the experimental set-up for the measurements, (a-inset) Raman coupling scheme used in these experiments. (b) energy level diagram for ^{85}Rb atom, (c) recorded representative envelope spectrum for the arrangement of the probe laser position depicted in (d). (c-inset) representative spin-correlation signal of cold atoms at $\delta_{12} = 2.73$ MHz.

have done the experiment for various positions of the probe laser field to come across different magnetic field distribution within the cold atomic cloud. A representative spectrum is shown in Fig. 1(c) for z =900 μm, and the experiemtal arrangement is shown in Fig. 1(a,d). We fit those individual composite spectra with our theory including corrections due to magnetic field variations, atom density distributions, and multilevel contributions. From these fits, we have extracted the average value of the measured spin-relaxation rate (γ') to be $\sim 2\pi\times0.5$ kHz [17]. In this thesis, we have indicated the implementation of this novel detection technique in other cold and ultracold atomic, molecular, and ionic systems where the measurements of intrinsic γ' is possible, and also addressed the realizability of non-perturbative optical imaging technique in such systems. We also study with characterising the spectrum strength at a particular δ_{12} with the various relative polarization states of Raman fields, and indicate the unique nature of the light-matter coupling with varying (local) quantization axis.

Since our measurements rely on spin transport in cold atoms, we have also sepa-

rately performed a study on mass transport in the cold atomic systems. In particular, we have studied the response function of the cold atomic cloud in response to an external perturbations [18].

Measurements with thermal atoms: We have characterized the Raman driven SNS technique with thermal ^{87}Rb atoms in a glass cell filled with neon buffer gas. The extracted value of the γ' using Raman driven envelope spectrum fitted with our theory coincides within 25% error bars with a totally independent measurement of the intrinsic SNS. We have confirmed the fact that the huge enhancement of the Raman driven signal strength, as predicted by our theory, around the vicinity of the separation between the consecutive Zeeman states ($\delta_{12} \to \nu_L$) in comparison to the intrinsic spin noise (SN) signal.

The experimental arrangement for Raman driven SNS in vapor cell is similar as shown in Fig. 1(a). In these measurements, the circular coil pairs produced a homogeneous magnetic field (in Helmholtz configuration) and instead of the cold atomic cloud we use a vapor cell filled with rubidium atoms and neon buffer gas at $\sim$ 370K temperature. The arrangements of the probe laser (blue beam), Raman lasers (red beams), and the detection set-up is similar to Fig. 1(a). We coherently drive the ^{87}Rb atoms with weak Raman fields ($\Omega/\gamma \sim 10^{-2}$, where Ω is the resonant Rabi frequency of the individual Raman field, and γ is the pressure broadened linewidth of the excited hyperfine level) between the adjacent Zeeman states in $F = 2$ level. We observed an enhancement of about 10^5 in the signal strength compared to its intrinsic SN spectrum [4, 5]. The signal strength is maximum at the Raman resonance condition i.e. $\delta_{12} = \nu_L$, and the Lorentzian envelope spectrum made by the series of peaks at δ_{12} is centered around ν_L. A representative Raman driven spectrum is shown in Fig. 2(a), whereas in comparison, the intrinsic ($\Omega = 0$) SN spectrum is shown in Fig. 2(b). This observation justifies our theoretical model, especially the enhancement of the signal strength, and the appearance of the delta peak (broadened by experimental noise) at δ_{12} [17]. Since the individual peak in the driven spectrum is extremely narrow ($\sim$ kHz) in comparison to the intrinsic SN spectrum width ($\sim$ 100 kHz), the Raman driven SNS technique can measure the unknown magnetic field with higher precision than the traditional techniques use for this purpose.

We have experimentally verified the consistency of the measured value of γ' in different temperatures of the vapor cell with two methods - Raman driven SNS and intrinsic SNS technique. Our theory on Raman driven SNS, in one hand provides the profile of the envelope spectrum for a fixed Ω, and in other hand gives the dependency of the on-resonance (at $\delta_{12} = \nu_L$) signal strength with Ω. We performed those two sets

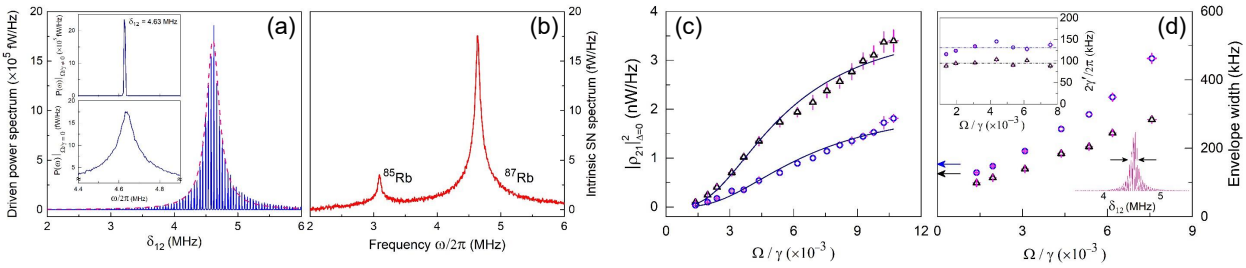

Figure 2: The Raman driven (a) and intrinsic ($\Omega = 0$) spin noise (SN) (b) spectrum of thermal ^{87}Rb atoms. The individual peak at δ_{12} and enhancement in signal strength is shown in (a - inset). The value of γ' is extracted using (c) and (d) for different temperatures.

of experiments for different temperatures, and fitted with our theory to estimate the value of γ'. The measurement results are shown in Fig. 2(c - d). We have observed a consistency, within 25% error bars, in the extracted value of γ' using this method with the measurements done using separate intrinsic SNS technique. The reason for this minor discrepancy can be understood by comparing two competing physical processes , (a) the perturbation induced by the Raman driving, and (b) the suppression of spin projection noise due to coherent coupling. This observation affirms that the SNS technique along with the Raman coupling can be implemented to extract the value of γ' of a system where the intrinsic measurement is not feasible due to the extremely low signal strength, e.g. in cold atoms.

We have also studied the transfer of coherence from one atomic species ^{85}Rb ($|g_F| = 1/3$) to another ^{87}Rb ($|g_F| = 1/2$) via the spin-exchange collision (SEC). In general, the efficiency of the coherence transfer between different atomic species via SEC are maximum when they are resonantly coupled i.e. when their Lande$^{'}$ g-factors are similar. The coherence transfer between atoms with same Lande$^{'}$ g-factors are observed in [19]. The Raman field induced transfer of coherence from one atomic species (^{85}Rb, abundance $\sim 10\%$) to another (^{87}Rb, abundance $\sim 90\%$) is observed via spin-exchange collisions. This coherence transfer to ^{87}Rb atoms narrowed down the intrinsic SN spectrum width by one order of magnitude, while the Raman fields coherently drive the other atomic species. The enhancement of the spin-lifetime of ^{87}Rb atoms can be controlled by the Raman field parameters, and find applications in atomic physics experiments. This observation is shown in Fig. 4(iv).

We have also investigated the fidelity of the induced Zeeman coherences in $F-$level by the Raman fields polarization state. We have recorded the overall envelope spectrum with various combinations of the polarization state of the Raman fields while keeping their intensity fixed. This observation validates the angular momentum conservations

in coherent coupling schemes. However, with strong intensity of the Raman fields, higher order harmonics at δ_{12} (till fourth orders) is observed in the spectrum when the Raman resonance condition is satisfied (both the frequency and polarization). This observation indicates the possibility of measuring the magnetic fields more accurately in comparison to the low Ω measurements described earlier.

We start our investigation by measuring the intrinsic spin-relaxation rate of thermal atoms using SNS technique. Note that, using this technique, we detect the spin dynamics of the valance electron bounded in an (alkali) atom. Thermal fluctuations causes the atomic spins to randomly flip over its Zeeman state spaces, resulting random magnetization orientation along any axis at finite temperature. The other sources, including collisions with other atoms, container walls, magnetic field inhomogeneity depolarises the atomic magnetization at room temperatures. The effect of such collisional and thermal fluctuations on atomic magnetization reduces at low temperature, and vanishes at absolute zero, where quantum fluctuation dominates. SNS can detect the spin dynamics in all temperature range which in turn provides the details of the nature of the spin interactions in classical, quantum and their transition regime, expecting to give the clear insight about the magnetism, and its origin. The traditional SNS technique [4, 5, 20, 21] dispersively detects the spontaneous magnetization ($M(t)$) of a system on the polarization angle ($\theta(t)$) of a far-off resonant probe laser field ($\hat{k} \parallel \hat{x}$, refer to Fig. 1(a)). A homogeneous magnetic field (along $\hat{z}$) orthogonal to the probe laser propagation direction (Voigt geometry) is applied on the system to detect the intrinsic SN spectrum at the Larmor frequency (ν_L). The component of the spontaneous magnetization along the probe laser propagation direction ($M_x(t)$) is imprinted on the polarization angle, causes the paramagnetic Faraday rotations ($\theta_F(t)$) of the probe laser polarization. In SNS technique, it turns out that the $\theta_F(t)$ of the probe laser polarization is a measure of the evolution of the magnetization of the system along the x-axis (i.e., $M_x(t) \propto \theta_F(t)$). In the experiment, the probe laser after passing through the glass cell is separated into s- and p-polarized components using a polarization sensitive set-up comprising of a half-wave plate and polarising beam splitter. The two components of light are then fed into the two ports of a balanced photo detector. The output of the balanced detector is connected to a spectrum analyzer to record the SN spectrum. The spectrum for the spontaneous magnetization fluctuations of the system has a Lorentzian line-shape centered around ν_L (see Fig. 2(b)), and the full-width at half-maxima (FWHM) gives a measure of the transverse spin-relaxation rate ($\propto 1/T_2$). The strength of the detected intrinsic SN spectrum can be written as, $\langle\theta_F(t)\theta_F(0)\rangle^{1/2} \propto \frac{I_p}{|\delta_L|}\sqrt{\frac{nl}{A}}$, where, I_p, δ_L, and A are the probe laser intensity, detuning, and diameter, respectively. n and l are the atom density and the length of the glass

cell containing rubidium atoms.

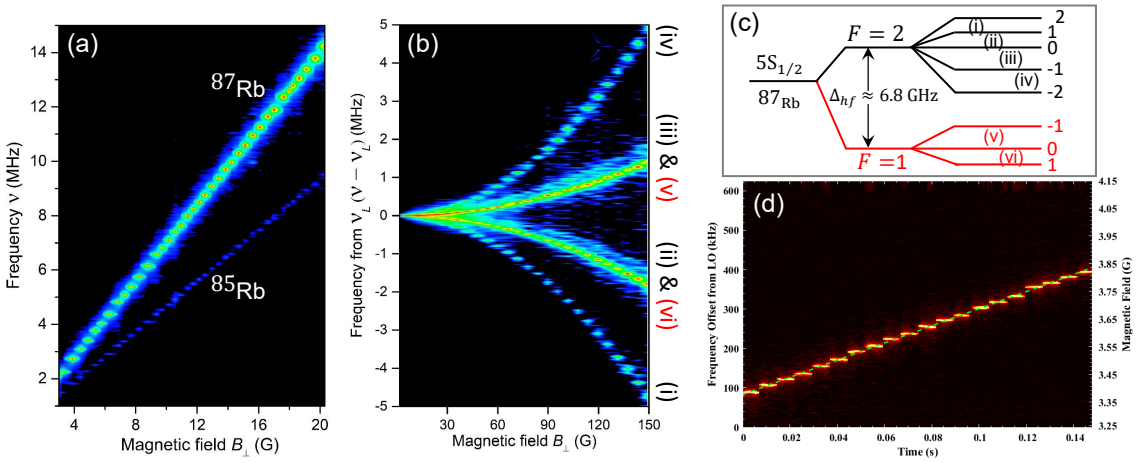

Figure 3: The traces of the intrinsic spin noise (SN) spectrum peak positions in linear (a) and quadratic (b) Zeeman regime of the external magnetic field strength. (c) Schematic of the Zeeman splittings of the ground hyperfine levels ($F = 1$ and $F = 2$) of ^{87}Rb. (d) The trace for real time measurements of the magnetic field strength with Raman coupling, and digital receiver systems (DRS).

After characterizing the intrinsic SNS with various parameters, we moved to extract the different atomic, nuclear and magnetic parameters using this technique. For this purposes, we have measured the intrinsic SN spectrum in presence of various strength of the external magnetic field. A series of such spectrum in linear (a) and quadratic (b) Zeeman regime of the magnetic field strength is shown in Fig. 3 in 2D false color map. Fig. 3 (a) gives the precise measure of the $g-$factors of the ground hyperfine levels (g_F) of the rubidium isotopes, and their abundance ratios in the cell. The energy separation between the successive Zeeman levels in each ground hyperfine levels are not same in the quadratic Zeeman regime, rather the splitting follows Breit-Rabi formula as schematically shown in Fig. 3 (c). We have identified each and individual Zeeman coherences signal from ^{87}Rb atoms in the SN spectrum in a wide range of the external magnetic field strength as shown at the right side in Fig. 3 (b). We have demonstrated that using this spectrum one can detect the strength of an unknown static magnetic field within an accuracy of 500 μG. This method can be applied in any range of magnetic field strength where the four Zeeman coherence peaks are resolved. This accuracy is superior compared to the commercially available magnetometers based on the Hall effect measurements, and need no calibration. Additionally, by measuring the adjacent peak separation in the spectrum, we have measured the ^{87}Rb clock transition (Δ_{hf}) within an accuracy better than 0.5%. For higher strengths of the external magnetic field, the nuclear contribution (g_I) in the electronic SN spectrum is appreciable and

all six Zeeman coherences signal corresponds to $F = 1$ and $F = 2$ are resolved. From the consecutive peak separation of $F = 1$ and $F = 2$ SN spectrum (either, between (ii) and (vi), or between (iii) and (v) in Fig. 3 (b)), a precise measurements of g_I is possible.

We have also developed a software-defined digital receiver system (DRS) for high resolution measurement of the unknown time-varying external magnetic fields. Initially, we have started this work mainly focusing on the detection of a short lived and narrow bandwidth signal with a high speed, higher spectral resolution and good signal-to-noise ratio (SNR) than the traditional swept-frequency spectrum analysers (SFSA). Our developed DRS is built on the STEMLab $125-14$ FPGA platform, and it has two different modes of operation: FFT spectrometer and real-time raw voltage recording mode. The FFT spectrometer mode of the DRS quickly detects the position of the SN signal peak with lower resolution, and the real-time data recorder (RTDR) mode measures the spectrum with higher temporal and spectral resolutions. We have shown that the SNR in detecting the intrinsic SN spectrum is improved by more than one order of magnitude with the FFTS compared with that of the commercial SFSA. We have demonstrated that our DRS system in RTDR mode has an precision of 800 μG in measuring the external magnetic field strength which is varying in time as frequent as 100 ms intervals [20]. One such representative measurement is shown in Fig. 3 (d).

We have extended the SNS technique in an out-of-equilibrium atomic systems where an additional optical field (control laser) is employed along the probe laser propagation direction to manipulate the relative population between the ground hyperfine levels. The optical pumping (OP) of atoms using the control laser field polarises the atomic population in a particular hyperfine level and reduces the hyperfine-exchange collisions. Moreover, we can precisely control and manipulate the atomic spin polarization using OP scheme by tuning the control laser field frequency and intensity, and detect them non-perturbatively using SNS technique.

The intrinsic SN spectrum for ^{87}Rb atoms at high magnetic field where all the six Zeeman coherence peaks are resolved is shown in Fig. 4 (i - b). Fig. 4 (ii) shows the different OP schemes (red and blue) to control the atomic populations in various ground hyperfine levels ($F = 1$ and $F = 2$). The OP scheme, shown in the red color in Fig. 4 (ii), is to transfer atoms from $F = 1$ level to $F = 2$ level. The SN spectrum in this optically pumped situation is shown in Fig. 4 (i - a) with different control laser field intensities. These spectra show the efficiency of the OP of atoms to $F = 2$ level with the intensity (I_c) of the control laser field, as the contribution of SN peaks from $F = 1$ level disappears at higher I_c. The OP scheme for spin polarising the atoms in $F = 1$ level is schematically shown in blue in Fig. 4 (ii), and the corresponding SN spectrum is

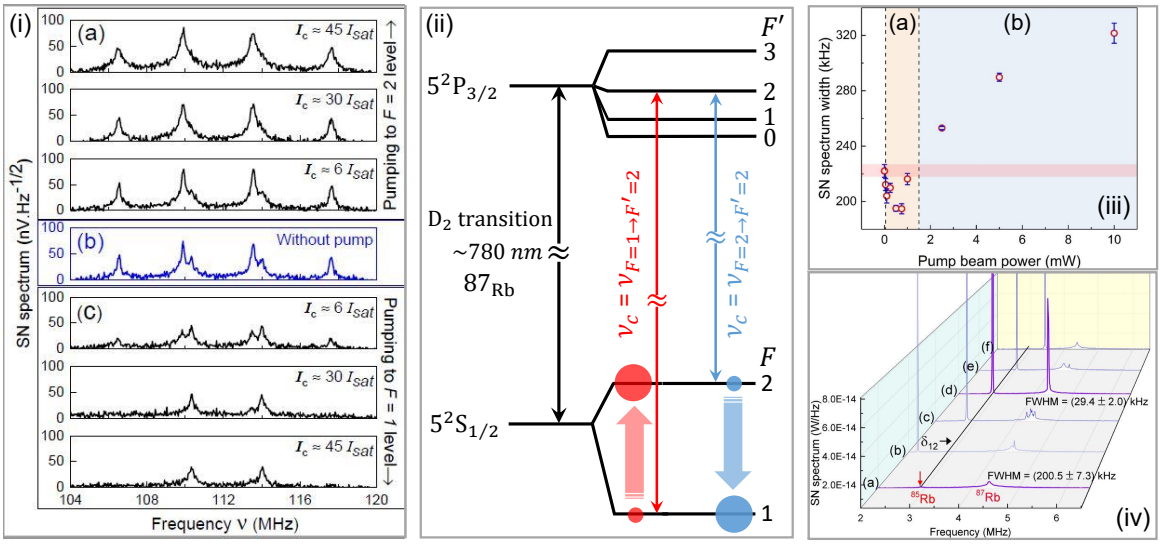

Figure 4: (*i*) The controlled optical pumping between the hyperfine levels and non-invasive detection using intrinsic SNS technique. (a) shows the driven spin noise (SN) spectrum when the atoms are pumped to $F = 2$ level and (c) shows the same for pumping the atoms in $F = 1$ level, while (b) shows the intrinsic SN spectrum. (*ii*) The optical pumping scheme used in the experiments. (*iii*) The variation of SN spectrum width with pump laser power while the atoms are being pumped to $F = 2$ level. (*iv*) Spin-exchange collision and reduction of the intrinsic SN spectrum width of ^{87}Rb atoms while the ^{85}Rb atoms are subjected to the Raman coupling.

shown in Fig. 4 (i - c). We have also demonstrated that the SNS technique with OP has the ability to precisely detect the narrow electronic transitions of a system in presence of various spectral broadening mechanisms such as homogeneous and inhomogeneous broadening. The precision of finding the electronic lines using this method is about three times better than intrinsic SN measurement or using absorption spectroscopy. This optical pumping scheme is the precursor to two photon Raman driving scheme discussed earlier.

We have also systematically studied the spin-relaxation rate (γ') of the optically pumped atoms with control laser field intensity. The measurement is performed in the non-SERF (spin-exchange relaxation free) regime, where the Larmor precession rate ($\sim$ 5 MHz) for the ground $F-$levels of ^{87}Rb atoms are much faster than the spin-relaxation rate ($\sim$ 0.2 MHz) of the atoms at 373K. Fig. 4 (iii) shows the variations of the measured Lorentzian FWHM of the SN spectrum with control laser field power while the atoms are being optically pumped to $F = 2$ level. We have observed a significant reduction as much as 15% in the FWHM of the SN spectrum at the saturation intensity of the control laser field as shown in the shaded vertical region (a) in Fig. 4 (iii). The FWHM of the spectrum progressively increase with respect to the intrinsic SN spectrum width

for higher power of the control laser field as shown in the shaded region (b). In region (a), the FWHM of the spectrum is reduced due to the reduction of the spin-exchange collisions between the levels $F = 1$ and $F = 2$. However, in region (b), the off-resonant excitation of the $F = 2$ level atoms by the control laser field dominates over the spin-exchange rate. Therefore, the width in region (b) is increased with control laser power.

Summary and Outlook: We have measured the intrinsic spin-relaxation rate of cold atoms using Faraday rotation fluctuation measurement for the first time. This experiment opens up new possibilities to probe intrinsic spin properties and their interactions with various potentials in similar cold and ultra-cold atomic, molecular and ionic systems. Traditional non-invasive spin noise spectroscopy (SNS) technique have been used, along with Raman driving to the atoms, to probe the spin-correlation of the cold atomic system. We have also developed a theory of Raman driven SNS based on optical Bloch equations (OBEs). First we characterize this technique with thermal atoms, and later implement to cold atoms to extract the intrinsic spin-relaxation rate. We have shown a consistent measurement of spin-relaxation rate of thermal atoms using intrinsic and Raman driven SNS technique. A coherence transfer from one atomic species to another via spin-exchange collision has also been observed when the one of the atomic species is subjected to Raman coupling. We have developed and characterized the SNS technique with thermal rubidium atoms and extract atomic, magnetic, nuclear and chemical properties of atomic systems. We make use of the SNS technique to precisely measure the real-time external magnetic field strength with our developed digital receiver system (DRS). We have also implemented the optical pumping (OP) method to precisely control the spin population between the ground hyperfine levels of rubidium atoms and detect them non-invasively using SNS technique.

This novel detection technique along with Raman coupling scheme can be applied to diverse quantum materials, such as semiconductor heterostructures, quantum dots, photonic crystals, atomic vapors, and Bosonic and Fermionic ultra cold gases to probe the spin correlations. The techniques developed during this thesis work promises to advance our knowledge about the origin of quantum magnetism. On the application front, these techniques can be utilize to develop high precision, real-time, and miniaturised magnetometers for quantum sensing. Reliable measurements of spin fluctuations as described in this thesis, can be a promising tool for quantum information processing and computation.

Abbreviations

ADC	analog-to-digital converter
AMO	atomic, molecular, and optical
AOM	acousto-optic modulator
BEC	Bose-Einstein condensation
BPD	balanced photo-detector
DIO	digital input-output
DOF	degrees of freedom
DRS	digital-receiver system
ECDL	external cavity diode laser
EMI	electro-magnetic interference
FDT	fluctuation-dissipation theorem
FFT	fast Fourier transform
FFTs	fast Fourier transform spectrometers
FM	frequency modulation
FPGA	field-programmable gate array
FR	Faraday rotation
FWHM	full-width at half-maxima
HWP	half-wave plate
IF	intermediate frequency
LO	local oscillator
LRT	linear response theory
LZR	linear Zeeman regime
MB	Maxwell-Boltzmann
MCD	magnetic circular dichroism
MOT	magneto-optical trap
NPBS	non-polarising beam splitter
NZR	non-linear Zeeman regime
OBEs	optical Bloch equations
OM	optical molasses

OP	optical pumping
PBS	polarizing beam splitter
PID	proportional–integral–derivative
PL	programmable logic
PRF	position response function
PS	processing system
PSD	power spectral density
PSN	photon shot noise
QDs	quantum dots
QWP	quarter-wave plate
RBW	resolution bandwidth
RF	radio-frequency
RTDR	real time data recorder
RWA	rotating-wave approximation
SAS	saturation absorption spectroscopy
SEC	spin-exchange collisions
SERF	spin-exchange relaxation free
SFSA	swept-frequency spectrum analyzer
SN	spin noise
SNS	spin noise spectroscopy
SOC	System on Chip
3LS	three-levels system
TOF	time-of-flight
UHV	ultra-high vacuum
VCO	voltage control oscillator
VIs	virtual instruments

Acknowledgements

Ph.D. is a training process that advances a person's knowledge, skill, passion, patience, personality that helps a researcher to become an independent explorer of nature's mystery. During the Ph.D. tenure, many people's contribution makes the journey memorable. First, I would like to thank my supervisor, Dr. Saptarishi Chaudhuri, who believed in me and gave me complete freedom to work in the laboratory. The friendly discussions with him on any topic resulted in a solution every time. His presence in and out of the laboratory spreads positive energy that encourages and motivates me to work hard. His expertise, passion, and dedication to experimental physics make me believe that he understands exactly how a machine behaves! He took all the unnecessary burdens on his shoulder to make us feel free and concentrate only on science. I have learned a significant lesson from him that improves my view on science and lifestyle as well. In the same line, I would also like to thank my co-supervisor Dr. Dibyendu Roy for his immense support throughout my Ph.D. journey. In his busy schedule, he always managed time for discussions. His passion and patience to understand any topic from the core, in many ways, help my research journey to function smoothly.

I thank my collaborators Dr. Sanjukta Roy and Prof. Hema Ramachandran for their support and valuable discussions. I also thank Mrs. Meena Suresh and Dr. Mugundhan Vijayaraghavan for their help in developing and characterizing various electronic components and equipment. I also thank Prof. Supurna Sinha for giving fruitful suggestions during the annual assessment. I would also like to thank Prof. Fabien Bretenaker and Prof. Andal Narayanan for their time in discussions with me.

I would like to show my sincere gratitude to the members of the RRI workshop, library, administration, accounts, store, and carpentry for their support throughout my stay at RRI. I sincerely thanks Ibrahim, Manjunath and Savitha for their help. I thank the members of SAAC for their help and support. I would also like to thank the RRI canteen staff for providing food, gardeners for making the campus beautiful and alive, cleaning staff for making the campus and hostel clean, security staff, shuttle drivers, electricians, and clinic staff for their respective work. I sincerely acknowledge the effort paid by Mangalaji and her team at Vyalikaval hostel for serving us hygienic

meals as per our demand and taking care of each individual.

I sincerely thank Dhanalakshmi D for her help and support in the laboratory and many other issues during the early stage of my research career. I profoundly thank my colleagues Subhajit Bhar, Sagar Sutradhar, Rohit Prasad Bhatt, Lakshmi Priyanka, Shrestha Biswas, and Snehal Baburao Dalvi, with whom I have actively worked in the laboratory, discuss scientific and non-scientific things, and learned a lot of things from them. I also thank our past and present group members − Shovan Kanti Barik, Bidyut Bikash Boruah, Shreya Bagchi, Silpa B.S., Anindya Sundar Pal, Sukanya Mahapatra, Sutapa Ghosh, Sayari Majumdar, Neema Prakash, Swarnava Barui, Dixith Manchaiah, Gourab Pal, Anirban Misra, and Vikram Bakaraju for their help and frankness while having discussions with me. I would also like to thank Nishant Joshi, Adwaith K.V., Kaushik Joarder, Pradosh Kumar Nayak, Arup Bhowmick, Surya Narayan Sahoo, Sreyas P. Dinesh, and Mohammed Arsalan Ashraf for the productive scientific and technical discussions related to my work.

Next, I would like to thank my friends, juniors, and seniors at RRI − who are the most integral part of my life in the Ph.D. journey. I sincerely acknowledge each and everyone's support, love, and trust in me. Moreover, I will never forget the exciting life I spent together with them. I wholeheartedly thank Avik, Sagar Da, Kaushik, Agnibha, Bapan, Rishab, Tanuman, Anindya Da, Shovan, Subhajit, Dipak, Abhishek, Sourav Da, Arup Da, Souradeep Da, Rajkumar Da, Naren Da, Shreya, Marichandran, Shreyas, Sayan, and Reetam. I truly acknowledge my friends at RRI and outside RRI − Nishant, Sanyukta, Purbasha Di, Antara, Sourav pal, Arif, Sourav Kundu, Maity, Debargya, Shoubhik, Debabrata, Saawan, Rajendra, Adwaith, Sai chand, Sebanti, Swarnak, Irla, Nancy, Vishnu, Sanchari, Animesh da, Ankita Di, Abhinandan, Sudip, Sudip Roy, Pradosh, Sushil, Subhadip, Arun, Sandeep, Ion, Swarnadeep, Saikat, Sukanya, Subodh, Vardhan, Abhishek, Saumya, Abir Da, Kartick Da, Sangeet, and Rajkumar. I would like to thank all the members of the RRI football committee. I would also like to thank my juniors at RRI − Srijit, Jasim, Soumen, Sovan and Sayantan. I thank from the core of my heart to those local shopkeepers who provided us the basic ingredients during the first and second lockdown. I sincerely apologize if I miss someone whom I should have acknowledged.

I would like to express my cordial gratitude to all my teachers who taught me − especially, Pintu sir, Kedar sir and Arif Da: I will never forget their contributions to my life. I would also like to thank the "anonymous" referees who helped me, in many ways, understand our work more clearly.

Last, but not the least, I would like to thank my family. It is difficult for me to express their contributions in my life. Therefore, I am not trying to do this. All I want

to say to them, something that I had never said before, “I love you all”. I dedicate this thesis to my family.

উৎসর্গ
পরিবারকে

List of publications

1. "Measurements of spin properties of atomic systems in and out of equilibrium via noise spectroscopy", **M. Swar**, D. Roy, D. Dhanalakshmi, S. Chaudhuri, S. Roy, and H. Ramachandran, Opt. Express **26**, 32168 (2018).

2. "Measurements of Temporal Fluctuations of Magnetization in Alkali Vapor and Applications", **M. Swar**, D. Roy, D. Dhanalakshmi, S. Chaudhuri, S. Roy, and H. Ramachandran, Emerging Trends in Advanced Spectroscopy, ISBN: 9788770220828, 2019).

3. "A Real-Time Digital Receiver for Correlation Measurements in Atomic Systems", V. Mugundhan, **M. Swar**, S. Bhar, S. Chaudhuri, IEEE Transactions on Instrumentation and Measurement **70**, 1 (2021).

4. "Detection of spin coherence in cold atoms via Faraday rotation fluctuations", **M. Swar**, D. Roy, S. Bhar, S. Roy, and S. Chaudhuri, Phys. Rev. Research **3**, 043171 (2021).

5. "Measurements and analysis of response function of cold atoms in optical molasses", S. Bhar, **M. Swar**, U. Satpathi, S. Sinha, Rafael D. Sorkin, S. Chaudhuri, and S. Roy, Opt. Continuum **1**, 171-188 (2022).

6. "Raman induced coherence transfer between thermal atoms with different g-factors",

   M. Swar *et. al* (Manuscript in preparation).

Media and DST coverage

1. **Reliable and real-time measurements of magnetic fields**, April 5 (2021), Research Matters.

2. **Scientists develop magnetometer for low cost, reliable & real-time measurements of magnetic fields**, May 19 (2021), DST, India.

3. **Long lived correlations between waves in atomic systems at ultralow temperatures can be exploited for efficient quantum computing**, December 28 (2021), DST, India.

4. **Indian scientists devise technique for more efficient quantum computing**, December 30 (2021), GADGETS NOW (TOI).

Contents

List of Figures

List of Tables

Chapter 1

Prerequisite for the thesis

In this thesis, we report an experimental study on spin dynamics of neutral atoms over a wide range of temperatures ranging from μK to 400 K. Coherent and incoherent atom-light interactions have been employed as a tool for these studies.

Atoms and light are the basic ingredients for atomic, molecular, and optical (AMO) physics experiments. Atom can interact with electromagnetic (EM) field via dipole coupling. The electronic excited levels of an atom possess finite electric dipole moment which can be coupled to the ground level (which does not have electric dipole moment) using the electric field of EM radiation. This light-matter coupling makes it possible to study atomic structure using light. A light field in a particular mode affects the external and internal degrees of freedom of an atom and shows various physical phenomenon that has been observed in atomic physics experiments. In this thesis, we use light to manipulate the population in accessible energy levels and detect various optical phenomena using *dipole coupling*.

1.1 Alkali atoms

An atom is the smallest part of a substance that is composed of subatomic particles such as the nucleus (protons and neutrons) and electrons. The nucleus is heavy (contains $>$ 99.9 % mass of the atom) but tiny (diameter $\sim 10^{-15}$ m) object situated at the centre of an atom with electric charge $+Ze$ (where, Z is the atomic number and $e \approx 1.602 \times 10^{-19}$ coulombs). The electrons (electric charge $-e$) are the light particle and revolve around the nucleus in various electronic orbitals of the atoms due to the Coulomb potential generated by the ionic core of the nucleus.

The electrons of an atom are arranged in different orbitals according to Hund's rules and the Pauli exclusion principle. Electrons have both orbital ($\vec{l}$, due to its motion

around the nucleus) and spin ($\vec{s}$, due to the motion around itself) angular momentum which couples during its motion, known as spin-orbit coupling and provides total orbital angular momentum $\vec{j}$ ($= \vec{l} + \vec{s}$). For a multi-electron atom, the total number of electrons in a shell n (n is the principle quantum number, integer and $n \geq 1$) is $2n^2$. The electronic configuration of an atom can precisely be known using the four quantum numbers known as: principle quantum number (n), azimuthal or orbital quantum number ($l = 0, 1, .., (n-1)$), magnetic quantum number ($m_l = -l, -l+1, .., l-1, l$) and spin quantum number ($m_s = -s, -s+1, .., s-1, s$). Among all the atoms in the periodic table, only the inert gas (He, Ne, Ar, Kr,..) atomic shell is completely filled and the other atomic species has extra electrons which arrange in various orbitals in the next shell. The electronic configuration of an atom can be symbolically written as $n^{2s+1}l_j$.

Alkali metal atoms (Li, Na, K, Rb, Cs, and Fr) have an unpaired electron in the outermost S-orbital (in ground level) and the inner orbital electrons are filled up to the last shell as the inert atomic species. The ground state electronic configuration of the valance electron for alkali metal atoms can be written as $n^2\mathrm{S}_{1/2}$, where S stands for "**S**harp" ($l = 0$). Since the inner shell electrons screen the nucleus heavily, the valance electron of the alkali metal atoms is loosely bound to the nucleus by the electromagnetic force. Therefore, the valance electron ($l = 0$, S-orbital) can easily be excited to the other level ($l = 1$, P-orbital−P stands for "**P**rinciple") by the electromagnetic field via dipole coupling.

1.1.1 Energy levels of alkali metal atoms

The ground state electronic configuration for alkali metal atoms, as discussed in section 1.1 is $n\mathrm{S}^1$. This unpaired electron in the S-orbital has orbital angular momentum $l = 0$ and spin angular momentum $s = 1/2$. Electron, neutron and proton are Fermions with spin angular momentum $s = 1/2$. Therefore, the total angular momentum of the valance electron for alkali metal atoms after the spin-orbit coupling ($\propto \vec{l} \cdot \vec{s}$) is $j = |l - s|$ to $|l + s|$, i.e. $j = 1/2$. The first excited state for the atom is $n\mathrm{P}^1$, which have one unit of orbital angular momentum i.e. $l = 1$. Therefore, for P-state the possible values of j are $j = 1/2$, $3/2$.

The nucleus of the alkali metal atoms also possess spin angular momentum (nuclear spin $\vec{I}$) after arranging the neutrons and protons according to the nuclear shell model. The interactions between the nuclear spin angular momentum $\vec{I}$ and the total angular momentum of the valance electron $\vec{j}$ give rise to the hyperfine coupling ($\propto \vec{I} \cdot \vec{j}$). Therefore the energy levels of the atomic states are designated by the hyperfine levels

as $\vec{F} = \vec{I} + \vec{j}$. For a particular value of I, the hyperfine level index ranging between $F = |I - j|$ to $|I + j|$ with integer step.

Therefore, the ground states for alkali atoms have two hyperfine levels such as $F = I \pm 1/2$. Similarly, the first excited states can also be written as $F' = I \pm 1/2$ and $F' = I \pm 3/2$ with integer steps.

1.1.2 Rubidium atoms

In this thesis, we have used the rubidium (Rb) atoms to investigate the spin properties in its ground hyperfine levels in equilibrium and out-of-equilibrium conditions. Rb is the alkali metal atom with atomic number $Z = 37$. Its place in the periodic table is in the group: 1, and period: 5. Natural Rb has two isotopes: stable ^{85}Rb with the abundance of 72% and slightly radio-active ^{87}Rb with the abundance of 28% (the superscript represents the atomic mass number of these two isotopes). The half-life of the ^{87}Rb isotope is as long as 49 billion years. At standard temperature and pressure, the rubidium atom appears in the solid phase and has a melting point of 312.45 K.

The ground state electronic configuration of the Rb atom is [Kr] $5S^1$, where [Kr] represents the closed shell electronic configuration of the inert gas Krypton (Kr). ^{87}Rb has nuclear spin $I = 3/2$. Therefore, the ground hyperfine levels for ^{87}Rb atoms are F $= 3/2 \pm 1/2 = 1$ and 2. Likewise, the ground hyperfine levels for ^{85}Rb atoms with $I = 5/2$ are F $= 5/2 \pm 1/2 = 2$ and 3.

The first excited state electronic configuration of the Rb atom is [Kr] $5P^1$ with $l = 1$. Therefore the total orbital angular momentum of this state is $j = 1/2$, $3/2$. The (optical) transition connecting $j = 1/2$(S)$\leftrightarrow$ $j = 1/2$(P) is called D_1 line. The hyperfine levels for $j = 1/2$ (P) excited states of ^{87}Rb atoms are $F' = 1$ and 2. Similarly the D_2 line for ^{87}Rb atom represents the (optical) transition $j = 1/2$(S)$\leftrightarrow$ $j = 3/2$(P). The hyperfine levels for $j = 3/2$ (P) excited states of ^{87}Rb atoms are $F' = 0, 1, 2$ and 3. The excited state energy levels of ^{85}Rb atom can also be calculated using the same manner. The ground and first excited state energy level diagram for both the isotopes of Rb atoms are shown in Fig. 1.1.

Natural linewidth of the ground and excited levels. The inverse of the line width of an atomic energy level is a measure of the lifetime of an electron in this particular energy level. The ground levels ($l = 0$) of the alkali metal atoms do not possess any permanent electric dipole moment. In an ideal situation, the line width of these levels is extremely narrow and the lifetime of the electron (atom) is infinite. However, The line width of these levels is modified (or broadened) due to the various

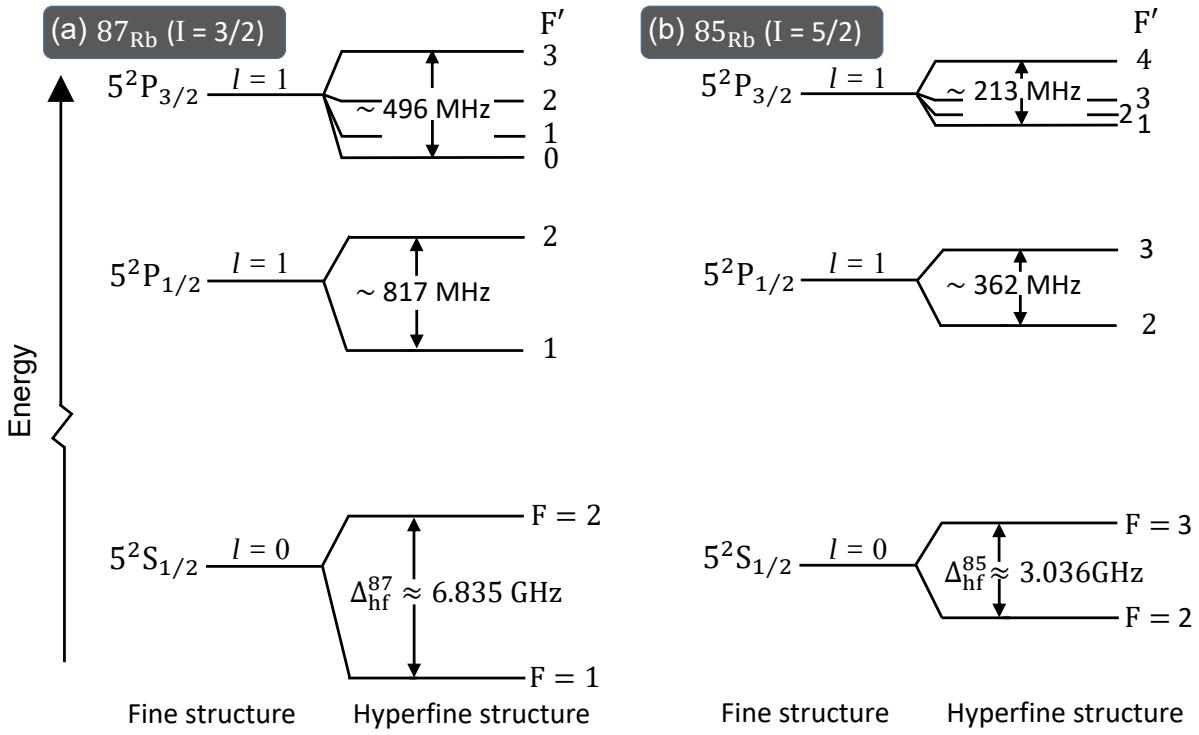

Figure 1.1: The ground (valance electron in S-orbital, $l = 0$) and the first excited state (valance electron in P-orbital, $l = 1$) electronic energy level diagram of stable rubidium (Rb) isotopes: (a) ^{87}Rb, and (b) ^{85}Rb. The transition connecting $S_{1/2} \leftrightarrow P_{1/2}$ is the D_1 line ($\sim$ 795 nm line) and the transition connecting $S_{1/2} \leftrightarrow P_{3/2}$ is the D_2 line ($\sim$ 780 nm line). $\Delta_{hf}^{87/85}$ is the clock transition for corresponding Rb isotopes. Care should be taken in reading the energy separations shown in this figure is multiplied by 2π. F (F′) represents the ground (excited) state hyperfine levels. The energy shown here is not in scale.

spectral broadening mechanisms present in the environment around the atoms, and this mechanism will be discussed later in this chapter. The broadening in the ground level limits the lifetime of an atom in a particular level and insists to move randomly within the ground level manifolds and their sub-levels (magnetic states).

The excited states ($l = 1$) of an alkali metal atom constitute a permanent electric dipole moment that can interact with the various modes of the vacuum electromagnetic field present in the universe. Nevertheless, the temporal fluctuation present in the electric field of the vacuum EM-fields makes the excited states of the alkali metal atoms unstable and broadens the energy uncertainty of these levels. This broadening limits the lifetime of an atom in the excited states and returns the atom in the ground states by spontaneously emitting a photon in random mode. The natural linewidth of the excited states are Lorentzian in shape, and its value at the full-width at half-maxima (FWHM) for Rb isotopes are $\gamma \sim 2\pi\times 6$ MHz.

The experimentally measured linewidth (γ) of the excited states can further get broadened due to the finite velocity of the atoms (Doppler broadening) and the presence of foreign gases, such as buffer and quenching gases (pressure broadening). All these spectral broadening mechanisms of the electronic energy levels of an atom affects significantly in the measurements of the electronic spin noise (SN) of an atom and are discussed in detail as the time comes.

1.1.3 Rubidium atoms in a magnetic field

Larmor precession. The combined magnetic dipole moment of the ground levels (F) of Rb atoms due to the electron and nuclear spin can be written as, $\vec{\mu}_F = \upsilon\vec{F}$, where the constant υ is the gyromagnetic ratio and $\vec{F}$ is the total angular momentum. In presence of an uniform magnetic field ($\vec{B}$), $\vec{\mu}_F$ experiences a torque $\vec{\tau} = \vec{\mu}_F \times \vec{B}$, and precess about the magnetic field with Larmor precession frequency (ν_L). For low magnetic field strength, the value of ν_L is proportional to the strength of the B and can be written as $\nu_L = \upsilon B$. Let us consider a case where the uniform magnetic field is applied along the z-axis, i.e. $\vec{B} = \mathrm{B}_0\ \hat{z}$ and the magnetic moment $\vec{\mu}_F$ makes an angle θ_z with respect to the z-axis. In this scenario, the projection of $\vec{\mu}_F$ on the $x-y$ plane will precess at the frequency ν_L while maintaining a constant angle θ_z along the z-axis as shown in Fig. 1.2. Therefore the transverse spin component (F_{x-y}) carries the information about the Larmor frequency (ν_L) and the longitudinal component (F_z) provides the information about the projection of the magnetic states along the z-axis, i.e. Zeeman splitting.

Zeeman splitting. Magnetic field shifts the energy of an atomic energy level and breaks the degeneracy into various magnetic states. This phenomenon is known as the Zeeman effect. The interaction Hamiltonian for the Zeeman effect of an atomic spin in a uniform magnetic field along z-axis can be written as,

$$\mathcal{H}_{\mathcal{Z}}^{'} = -\vec{\mu}_F \cdot \vec{B}, \tag{1.1}$$

where, $\vec{\mu}_F$ is the total magnetic dipole moment due to the electron ($\vec{\mu_j}$) and nucleus ($\vec{\mu}_I$) spin, i.e. $\vec{\mu}_F = \vec{\mu_j} + \vec{\mu}_I$, and $\vec{B} = \mathrm{B}_0\ \hat{z}$. Let's first discuss the interaction of electronic spin with the magnetic field and later include the nuclear spin. The interaction of the electronic spin ($\vec{j}$) with magnetic field can be written according to the Eqn. 1.1 as,

$$\mathcal{H}_{\mathcal{Z}}^{'} = \frac{e}{2m}(\vec{l} + 2\vec{s}) \cdot \vec{B}, \tag{1.2}$$

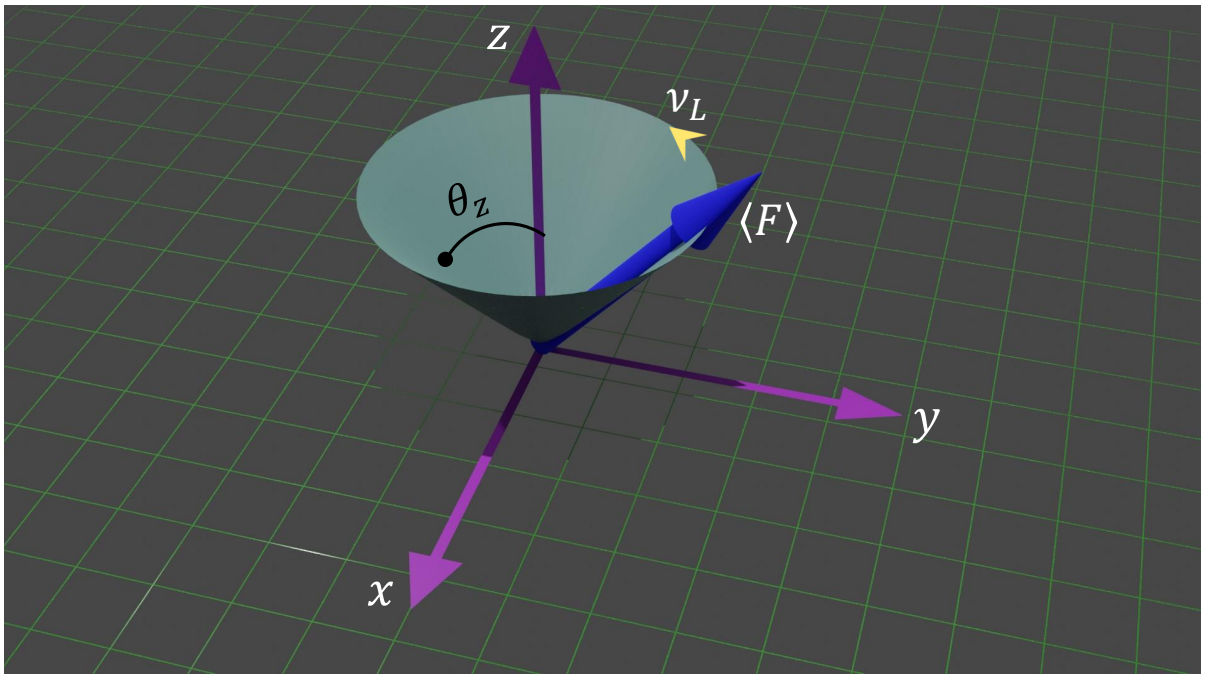

Figure 1.2: Schematic shows the Larmor precession of an atomic spin about a uniform magnetic field applied along the z-axis. ν_L is the Larmor frequency of the atomic spin $\langle F \rangle$. θ_z is the angle between the electronic spin with respect to the applied magnetic field ($\hat{z}$). The expectation value of the spin components along three Cartesian axes can be written as, $\langle F_x \rangle = \frac{\hbar}{2} \sin(\theta_z) \cos(2\pi\nu_L t)$, $\langle F_y \rangle = -\frac{\hbar}{2} \sin(\theta_z) \sin(2\pi\nu_L t)$ and $\langle F_z \rangle = \frac{\hbar}{2} \cos(\theta_z)$, where $\hbar$ is the reduced Planck constant.

where m is the mass of the electron. However, when the strength of the external magnetic field B_0 is much weaker than the internal magnetic field (B_{int}) of the atom produced by the proton, the Hamiltonian $\mathcal{H}'_Z$ can be treated as a perturbation compared to the fine structure ($\vec{l} \cdot \vec{s}$) Hamiltonian. Since the Zeeman Hamiltonian is treated as a perturbation, the individual angular momentum l and s is not conserved during the motion rather the total angular momentum j and its projection along $\vec{B}$, m_j is a conserved quantity. Therefore in this regime of external magnetic field strength, j precesses about the $\vec{B}$, and the good quantum numbers are $\{l, s, j, m_j\}$. The effect of the Zeeman Hamiltonian on the fine structure line can be solvable using time-independent perturbation theory. $\mathcal{H}'_Z$ lift the degeneracy of the fine structure line j, and split into $(2j+1)$ lines from $-m_j$ to m_j projected along the direction of the external magnetic field as discussed in Sec. 1.1.3. The shift in the energy levels of each Zeeman states (m_j) within j-level can be written as, $\mu_B g_j B_0 m_j$, where $\mu_B = \frac{e\hbar}{2m}$ is the Bohr magneton, and g_j is the Lande$^{'}$ g-factor for the level j. However, due to the hyperfine coupling ($\hat{j} \cdot \hat{I}$), the atomic energy levels are designated by the quantum number F (via $\vec{F} = \vec{j} + \vec{I}$). Therefore, for low magnetic fields, the good quantum numbers of atoms are

$\{s, I, F, m_F\}$ (since $l = 0$). Nevertheless, the nuclear magneton, $\mu_N = \frac{e\hbar}{2m_p}$, where m_p is the mass of the proton, is three orders of magnitude lower than the μ_B. Therefore for weak B_0, the anomalous Zeeman splitting mostly depends on the electron's spin quantum number s. Therefore, principally, we study the spin physics of Rb valance electrons in this regime of external magnetic field strength.

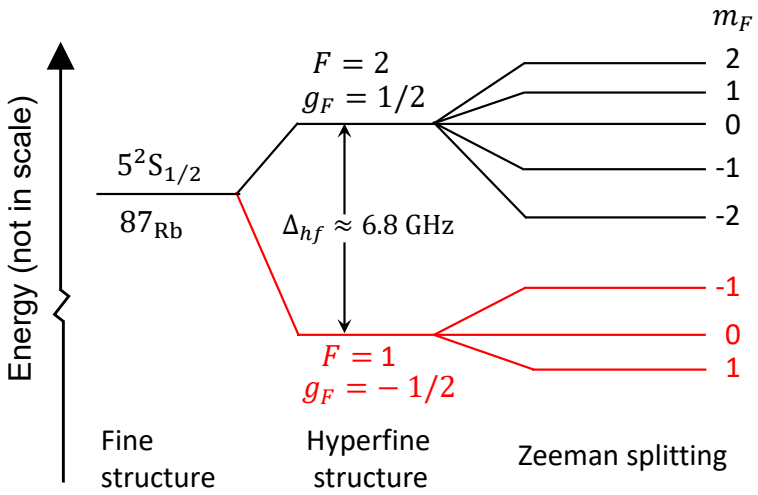

Figure 1.3: The general structure of the Zeeman splitting of the ground hyperfine (F) levels of ^{87}Rb atom at any arbitrary magnetic field strength. Care should be taken on noting the g-factors of the two hyperfine levels, and their corresponding Zeeman states orientation.

When the external magnetic field is much stronger than the internal magnetic field ($B_0 \gg B_{int}$), the individual $\vec{s}$ and $\vec{I}$ precess about the $\vec{B}$ for the ground state of Rb atom. In this case, the fine structure Hamiltonian can be treated as a perturbation, and the good quantum numbers are $\{s, I, m_s, m_I\}$. Here we do not discuss this scenario in detail, since except in a few places in the thesis this situation will not arise. Nevertheless when the strength of these two magnetic fields are comparable (i.e. $B_0 \approx B_{int}$), the analysis for the energy level splitting is a bit complicated. However, the energy level structure at any strength of the external magnetic field for the ground hyperfine levels of alkali atoms can exactly be solvable using Breit-Rabi formula, and that will be discussed later in the thesis.

g-factors of the ground levels. The Lande$^{'}$ g-factor or the magnetic splitting factor of an atomic energy level is a dimensionless quantity which characterizes the Zeeman splitting in an external magnetic field. The sign of the g-factor indicates the sense of rotation of the angular momentum vector about the external magnetic field. In the weak magnetic field (anomalous Zeeman) regime, The g-factor for the hyperfine levels

(g_F) can be written as,

$$\begin{aligned} g_F &= g_j \frac{F(F+1) - I(I+1) + j(j+1)}{2F(F+1)} + g_I \frac{F(F+1) + I(I+1) - j(j+1)}{2F(F+1)}, \\ &\simeq g_j \frac{F(F+1) - I(I+1) + j(j+1)}{2F(F+1)}. \end{aligned} \tag{1.3}$$

The value of g_j for the ground ($l = 0$) fine structure level ($5^2S_{1/2}$) of Rb atom is $g_j \simeq 2$. The value quoted here for g_j ignored the effects of the inner shell electronic structure of Rb atoms and quantum electrodynamics (QED) effects. The nuclear $g-$factor (g_I) is ignore here since its value is more than three orders of magnitude lower than g_j. For the hyperfine level $F = 2$ of ^{87}Rb atom, the value of g_F using Eqn. 1.3 turns out to be 1/2. For $F = 1$ of ^{87}Rb atom, $g_F = -1/2$. Notice that the value of g_F for both the ground hyperfine levels of ^{87}Rb atom are same in magnitude but are opposite in sign. This signifies that the sense of rotation of the atomic spin about a magnetic field are opposite for $F = 1$ and $F = 2$ hyperfine levels as shown in Fig. 1.4. However, using Eqn. 1.3, one can calculate the hyperfine $g-$factors for excited levels also. The $g-$factors for the ground hyperfine levels $F = 2$ and $F = 3$ of ^{85}Rb atom are $g_{F=2} = -1/3$ and $g_{F=3} = 1/3$, respectively.

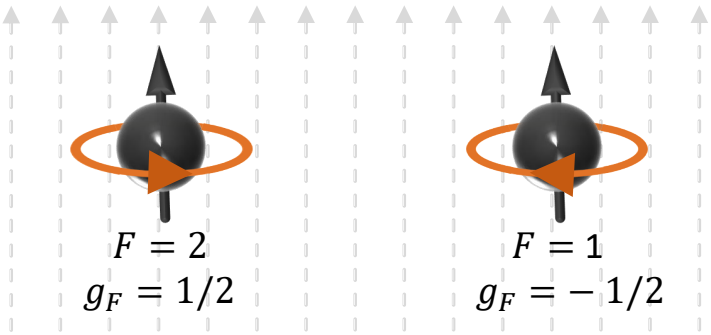

Figure 1.4: The sense of rotation of the electronic spin in the ground hyperfine levels of ^{87}Rb atom in a homogeneous magnetic field. The faint broken arrows show the homogeneous magnetic field lines.

When the Zeeman splitting is much lower than the hyperfine splitting, the energy separations between any two consecutive Zeeman states ($E_{F,m_F} - E_{F,m_F-1}$) of a particular hyperfine level are same and linearly proportional to the strength of the external magnetic field. However, one can show that this energy separation is equal to the Larmor precession frequency (i.e. $E_{F,m_F} - E_{F,m_F-1} = 2\pi\nu_L$).

1.1.4 Bloch equations for spin dynamics

So far we have discussed the Larmor precession of an atomic spin which is free from any kind of relaxation process. However, during the precession of the atomic spin about magnetic fields, the spins undergo various collisions that result in the relaxation of the spin state. Such collisions include spin-exchange and spin destruction collisions with the homo and hetero-nuclear atoms, collision to the container walls, collisions with the buffer and quenching gases (if present in the cell), and so on. Here, the term homo-(hetero-) nuclear atoms signifies the atoms with similar (different) atomic masses. The scattering cross-section for spin-exchange and spin destruction collisions for similar or different atomic species are different and they contribute differently to the relaxation rate. We have discussed the spin-exchange and spin destruction collision towards the end of this chapter. However, all these collisional mechanisms cause spins to flip to other energy states. Along with such collisional mechanisms, the magnetic field inhomogeneity over the extension of the atomic container can also cause spin to flip. All these mechanisms limit the coherence time of an atom in a spin state. Two different kinds of relaxation times are defined in the literature depending on the relaxation of the spin with respect to the quantization axis (the direction of the homogeneous magnetic field, as we defined along $z-$axis). The relaxation of the atomic spins along the $z-$axis is known as the longitudinal relaxation time (T_1) and is related to the energy relaxation of a particular state of the spin. The transverse spin relaxation time (T_2) is related to the dephasing of the atomic spins orthogonal to magnetic field direction (i.e. on the $x-y$ plane). In general, spin relaxation time is defined as the average lifetime of an atomic spin in a particular energy state.

In 1946, Felix Bloch came up with a set of macroscopic phenomenological equations for nuclear magnetization ($\vec{M}(t)$) in presence of an arbitrary magnetic field ($\vec{B}(t) \equiv (B_x(t), B_y(t), B_z(t))$) when the relaxation is present in the system. These equations can also be applied to the atomic spin ($\vec{F}(t) \equiv (F_x(t), F_y(t), F_z(t))$) to track its dynamics in an external magnetic field when T_1 and T_2 are present.

The Bloch equations for the electronic spin dynamics can be written as,

$$\frac{dF_x(t)}{dt} = \upsilon(\vec{F}(t) \times \vec{B}(t))_x - \frac{F_x(t)}{T_2}, \tag{1.4}$$

$$\frac{dF_y(t)}{dt} = \upsilon(\vec{F}(t) \times \vec{B}(t))_y - \frac{F_y(t)}{T_2}, \tag{1.5}$$

$$\frac{dF_z(t)}{dt} = \upsilon(\vec{F}(t) \times \vec{B}(t))_z - \frac{F_z(t) - F_0}{T_1}. \tag{1.6}$$

In the above equations, the first term represents the Larmor precession of the atomic spin about the magnetic field and $z-$axis is the quantization axis. F_0 is the steady-state atomic spin in the $z-$axis. In this thesis, we will talk about the detection of the transverse spin dynamics of Rb atoms in the ground hyperfine levels in equilibrium and out-of-equilibrium situations.

1.2 Electromagnetic radiation field: Light

According to the classical electrodynamics and Maxwell's equations, the light is a transverse electromagnetic oscillatory field with velocity c $(= 1/\sqrt{\mu_0 \varepsilon_0})$ in the free space. Here, μ_0 is the vacuum permeability and ε_0 is the vacuum permittivity. However, the velocity of light in a medium with refractive index n will get modified to c/n. The oscillating electric and magnetic field of light field propagating along $\hat{k}$ direction can be written as,

$$\vec{E}(\vec{r},t) = \widetilde{\mathcal{E}}_0\, e^{i(\vec{k}\cdot\vec{r}-\omega t)}\, \hat{m}, \tag{1.7}$$

$$\vec{B}(\vec{r},t) = \frac{1}{c}\,\hat{k} \times \vec{E}(\vec{r},t). \tag{1.8}$$

Where $\widetilde{\mathcal{E}}_0$ is the amplitude of the electric field and in general is complex valued. $\hat{m}$ is the polarization (electric field oscillation) vector of the light field and orthogonal to its propagation direction, i.e. $\hat{m}\cdot\hat{k} = 0$. The magnitude of the propagation vector $(\vec{k})$, is called the wave number k and $k = 2\pi/\lambda = \omega/c$. λ and ω are the wavelength and angular frequency of the light (radiation) field, respectively.

The electromagnetic field has a wide range of spectral distribution from radio waves ($\lambda \sim 10^{8}$ m) to gamma rays ($\lambda < 10^{-12}$ m). However, the optical transition wavelength for the D_1 and D_2 transition of the rubidium atoms are ~ 795 nm and ~ 780 nm, respectively, and fall in the infra-red (IR) region. Therefore, we have used a couple of grating stabilized diode lasers operating at that wavelength to manipulate, control, and detect the atomic spins of rubidium atoms by optical means. The frequency stabilization and its linewidth, the polarization selection of the laser beams are discussed later in this thesis.

In this thesis, we mostly treat the laser beam as classically and consider that it is a source of coherent electromagnetic fields as described by Eqn. 1.7 and Eqn. 1.8. The light can also be treated as quantum mechanically, i.e. it is a stream of photons with specific linear $(\hbar\vec{k})$ and angular momentum $(\sigma^{\pm} \Rightarrow \pm 1, \pi \Rightarrow 0)$, and energy $(\hbar\omega)$.

1.3 Light-matter interaction

In this section, we discuss briefly the light-matter interactions in the semi-classical approach. We indicate the interaction Hamiltonian responsible for the absorption and stimulated emission process. The atom is treated quantum mechanically i.e. an array of discrete and separate energy levels with defined angular momentum whereas the radiation field is treated as classically, i.e. a transverse electromagnetic (EM) wave with a specific mode.

Global Hamiltonian. The complete Hamiltonian describing the atoms in the presence of radiation fields and an external magnetic field together can be written as [24],

$$\mathcal{H} = \frac{1}{2m}[\,\vec{p} - q\vec{A}_{\perp}(\vec{r})\,]^{\,2} - \vec{\mu}_F \cdot \vec{B}(\vec{r}) + V_{Coul} + \mathcal{H}_{\mathcal{R}}\,. \tag{1.9}$$

Here, the first term describes the kinetic energy of the particle in the Coulomb gauge. m and q are the mass of the particle and the charge of the electron, respectively. $\vec{A}_{\perp}(\vec{r})$ is the transverse component of the vector potential of the radiation field at the position $\vec{r}$.

The second term is related to the interaction of the atomic spins with the external magnetic field ($\vec{B}(\vec{r})$) at the position $\vec{r}$.

The third term (V_{Coul}) is associated with the longitudinal field of the radiation, the Coulomb energy,

$$V_{Coul} = \frac{\varepsilon_0}{2}\int d^3r\, E^2_{\parallel}(\vec{r}). \tag{1.10}$$

The fourth term ($\mathcal{H}_{\mathcal{R}}$) represents the energy associated with the transverse field of the radiation,

$$\mathcal{H}_{\mathcal{R}} = \frac{\varepsilon_0}{2}\int d^3r\, [E^2_{\perp}(\vec{r}) + c^2B^2(\vec{r})]. \tag{1.11}$$

Particle and radiation field Hamiltonian. The global Hamiltonian ($\mathcal{H}$) described in Eqn. 1.9 can be split into three parts, i.e.

$$\mathcal{H} = \mathcal{H}_{\mathcal{P}} + \mathcal{H}_{\mathcal{R}} + \mathcal{H}_{\mathcal{I}}. \tag{1.12}$$

Here $\mathcal{H}_{\mathcal{P}}$ represents the unperturbed Hamiltonian of the particle, and depends only on $\vec{r}$ and $\vec{p}$. It contains the kinetic energy of the free particle and the Coulomb energy, i.e.

$$\mathcal{H}_{\mathcal{P}} = \frac{\vec{p}^{\,2}}{2m} + V_{Coul}. \tag{1.13}$$

Whereas the radiation Hamiltonian ($\mathcal{H}_{\mathcal{R}}$) depends on the transverse component of the EM radiation field and is described in Eqn. 1.11.

Interaction Hamiltonian. The interaction Hamiltonian ($\mathcal{H}_{\mathcal{I}}$) depends on both the atomic variables ($\vec{r}$ and $\vec{p}$) and the radiation field variable ($\vec{A}_{\perp}(\vec{r})$). $\mathcal{H}_{\mathcal{I}}$ can also be split in three parts depending on the appearance of their order of the field,

$$\mathcal{H}_{\mathcal{I}} = \mathcal{H}_{I1} + \mathcal{H}^{s}_{I1} + \mathcal{H}_{I2}. \tag{1.14}$$

The first order dependence in the $\mathcal{H}_{\mathcal{I}}$ of the field are,

$$\mathcal{H}_{I1} = -\frac{q}{m}\vec{p}\cdot\vec{A}_{\perp}(\vec{r}), \tag{1.15}$$

and

$$\mathcal{H}^{s}_{I1} = -\vec{\mu}_{F}\cdot\vec{B}(\vec{r}). \tag{1.16}$$

Finally, the second order dependence can be written as,

$$\mathcal{H}_{I2} = \frac{q^2}{2m}\vec{A}^{2}_{\perp}(\vec{r}). \tag{1.17}$$

Here Eqn. 1.15 is the dipole interaction Hamiltonian between the atoms and light, and is responsible for the absorption and stimulated emission of the light by the interacting atoms. Eqn. 1.16 represents the interaction of the atomic spins with the external magnetic field and is responsible for the Zeeman splitting. However, the third term in Eqn. 1.17 is quadratic of the electric field parameter and ignored in the light-matter coupling term for low radiation field intensities.

1.4 Spectroscopy in atomic systems

The primary objective of spectroscopy in atomic systems is to find out the relevant energy structures and associated relaxation mechanisms present in the system. In atomic physics, the energy level structures of valance electron(s) bound in the ionic core of the nuclear potential generate the fine and hyperfine levels which are the characteristic fingerprints for the associated atoms. However, for alkali-metal atoms, the frequency difference between the fine structure levels fall in the optical to the infra-red range (10^{14}– 10^{15} Hz). Therefore, to detect such fine structure lines and the related hyperfine lines therein, an electromagnetic radiation field with frequency in this range needs to be coupled with the atoms (see Eqn. 1.15). The selection rules for the light-

matter coupling within dipole-approximation can be find out in [24–27]. Absorption, Faraday rotation, Hanle spectroscopy technique can be implemented to find out the corresponding energy structure and the lifetime of the excited levels. For the measurements of precise magnetic fields, spin density, spin coherences, etc, Faraday rotation, Hanle spectroscopy technique can be performed.

The degeneracy of the energy level structures breaks in presence of the external electric and magnetic fields. These are known as the Stark and Zeeman effects, respectively. For a reasonable strength of these fields, the energy splitting falls into the range of the radio-frequency (RF) ($10^6 - 10^9$ Hz) regime. Such an energy structure can be found experimentally by optical means using Faraday rotation, Kerr effect, Hanle spectroscopy, etc, or by employing RF spectroscopy technique i.e. electron spin resonance (ESR) or nuclear magnetic resonance (NMR) spectroscopy for nuclear systems. The Zeeman or stark energy structure as well as the spin lifetime (T_1), coherence time (T_2), etc can be extracted from such measurements. In the following, we briefly discuss some of the important atomic spectroscopy techniques which are related to the work presented in this thesis.

1.4.1 Absorption spectroscopy

As we have discussed earlier that the excited atomic levels ($l > 0$) have finite (natural) lifetime (τ_{nat}) due to its interaction with the vacuum field [24]. Therefore according to the uncertainty principle, these levels have finite natural line-width ($\gamma \equiv \gamma_{\text{nat}}$) which is related to τ_{nat} via, $\gamma_{\text{nat}} = 1/2\pi\tau_{\text{nat}}$. The natural line-width of first excited level ($l = 1$) of alkali atoms varies between 4-10 MHz (with a factor of 2π). This information can be obtained experimentally by performing an absorption spectroscopy to alkali atoms at rest ($v = 0$). A weak probe laser beam with frequency being scanned around the vicinity of the resonance line, after interacting with the atomic system can be detected on a photo-detector. The absorption signal has a Lorentzian line-shape centered at the resonance frequency ($\nu_0 = (E_e - E_g)/h$, where $E_g(E_e)$ is the ground (excited level) energy) and the FWHM gives the natural line-width of the atoms.

However, the measured line-width of the excited level of the atoms can broaden due to various spectral broadening factors. The most dominating factor includes Doppler broadening due to the thermal motion of the atoms and pressure broadening due to the presence of the buffer gas. Since the atomic velocity distribution follows Maxwell-Boltzmann distributions: individual atoms have their distinct velocity distribution ranging from $-\infty$ to ∞ inside the cell. Therefore the broadening in the spectral line due to the atomic velocity is in-homogeneous, and the line shape is Gaussian.

Typically the Doppler broadening can spread the spectral line up to the GHz range. The presence of the buffer gas inside the cell interacts with the excited level due to the electromagnetic interactions and is the same for all the atoms. Such an interaction relaxes the excited atomic level much faster which significantly broadens the spectral lines. This broadening is known as homogeneous pressure broadening and can have a value ranging between (1-100) GHz depending on the density of the buffer gas. The spectral line shape due to the pressure broadening is Lorentzian in nature.

When both the Doppler and pressure broadening are present in the system, the resulting absorption line-shape can be represented as a Voigt profile [28]. The complex form of the Voigt profile is [29],

$$\mathcal{V}(\nu-\nu_0) = \frac{2\sqrt{\ln 2/\pi}}{\gamma_{\mathrm{G}}}\mathcal{W}\left(\frac{2\sqrt{\ln 2}\big[(\nu-\nu_0)+i\gamma_{\mathrm{P}}/2\big]}{\gamma_{\mathrm{G}}}\right), \tag{1.18}$$

where $\gamma_{\mathrm{P}} = \gamma_{\mathrm{nat}} + \gamma_{\mathrm{pr}}$ is line-width of the absorption signal due to the natural life-time of the atoms and the pressure broadening by the buffer gas (γ_{pr}) together. γ_{G} is the FWHM of the absorption signal due to the Doppler effect. In this case ν is the spectral frequency in the optical range. The expression for $\mathcal{W}(x)$ is given by,

$$\mathcal{W}(x) = e^{-x^2}\big(1-\mathrm{erf}(-ix)\big), \tag{1.19}$$

Where 'erf' is the error function, and defined as $\mathrm{erf}(x) = 2/\sqrt{\pi}\int_0^x e^{-t^2}\,dt$. Therefore the broadening due to natural, Doppler, and pressure contribute to the measured width of the absorption signal. However, in general, the line shape of the absorption signal has a Voigt profile given in Eqn. 1.18. When the pressure broadening dominates over the Doppler broadening (i.e. $\gamma_{\mathrm{pr}} \gg \gamma_{\mathrm{G}}$), the Voigt line shape in the absorption signal switches to the Lorentzian-like profile. In the opposite limit, i.e. for $\gamma_{\mathrm{G}} \gg \gamma_{\mathrm{pr}}$, the Voigt profile switches to the Gaussian-like profile.

1.4.2 Faraday rotation spectroscopy

The polarization plane of a linearly polarized light can rotates after traveling through an optical medium (such as atomic) in presence of a magnetic field parallel to the light propagation direction. The rotation of the light field's polarization is a magneto-optical effect that is known as Faraday rotation. The detailed derivation for the Faraday rotation can be found elsewhere [29, 30]. Here we provide a brief description of this method.

When a linearly polarized light (polarization plane along $\hat{z}$) propagates along $x-$direction,

its polarization can be decomposed as a superposition of a left− and right− hand circular components in the following manner,

$$\hat{z} \equiv \frac{1}{\sqrt{2}}\left(\frac{\hat{z}+i\hat{y}}{\sqrt{2}}\right) + \frac{1}{\sqrt{2}}\left(\frac{\hat{z}-i\hat{y}}{\sqrt{2}}\right). \tag{1.20}$$

This light travels through an optical (atomic) medium of length l which is placed in a region of a homogeneous magnetic field along $\hat{x}$. The magnetic field breaks the degeneracy of the ground and excited atomic levels into Zeeman states and the transition frequencies for left− and right− hand circular polarized light becomes shifted in opposite direction from the bare atomic resonance frequency ν_0. This modifies the frequency-dependent index of refraction for those two circular components of light. Therefore, for a particular frequency of light, these two components travel through the medium with different velocities. When the light comes out from the medium, the polarization state of these two circular components acquires different phases. Therefore, the combined polarization state of the light after the medium is again linear, however, its plane now rotates with respect to $\hat{z}$ on the $y-z$ plane. The rotation angle of the polarization plane depends on various factors, such as frequency of the light, magnetic field strength, atom (or spin) density of the medium, the chemical composition of the medium, etc. The Faraday rotation (black trace) and absorption (red trace) signal from an ensemble of cold ^{87}Rb atoms in presence of homogeneous co-linear magnetic field is presented in Fig. 1.5.

1.4.3 Electron spin resonance spectroscopy

Electron spin resonance (ESR) or electron paramagnetic resonance (EPR) spectroscopy is a technique to study the material properties with an unpaired electron. The basic concepts of ESR are similar to the nuclear magnetic resonance (NMR), however, in the ESR technique, the electronic spin is excited by the RF or microwave fields instead of nuclear spin. The fundamentals, experiment and instrumentations, and the applications of EPR techniques are captured in [31, 32].

In the ESR technique, an RF or microwave field with a specific polarization is applied to the electronic system across the homogeneous magnetic field to detect the resonance spectrum. Since the electronic spin system is driven by the external oscillating fields during the measurements, the system can be considered in an out-of-equilibrium or non-equilibrium state.

In this thesis, we discuss the recently developed spin-based spectroscopy technique, known as spin noise spectroscopy (SNS) performed in hot and cold atomic spin ensem-

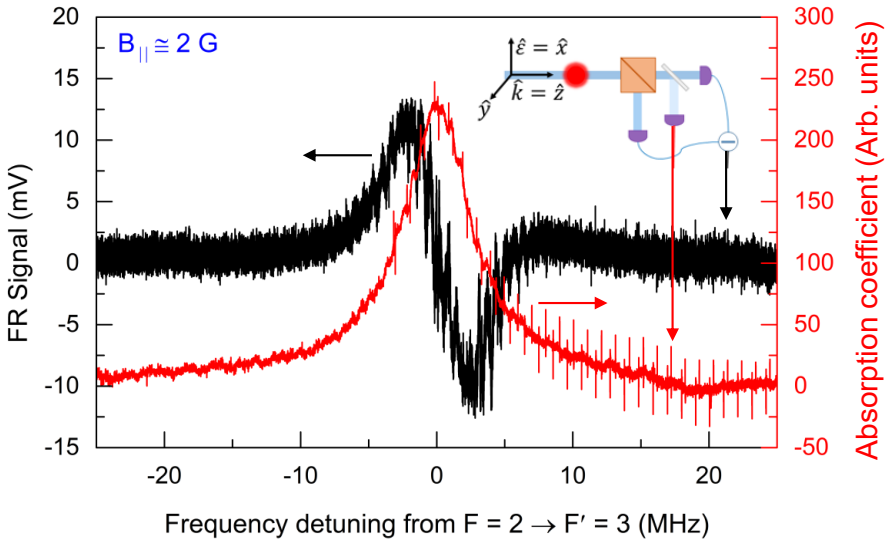

Figure 1.5: The Faraday rotation (black trace) and absorption (red trace) signal from an ensemble of cold ^{87}Rb atoms (red blob) in presence of homogeneous co-linear magnetic field $B_{\|}\hat{x}$ ($\cong$ 2 G). In cold atomic system, the absorption signal is free from Doppler and pressure broadening. Thereby the Lorentzian FWHM of the absorption signal is measured to be $\sim$ 6 MHz, which is limited by the excited level line-width.

bles. We have developed an all-optical setup for the detection of spin properties of the alkali atom's valance electron. In the intrinsic SNS technique, the atoms are not perturbed by any additional external fields which keep the system in equilibrium with the thermal bath and do not perturb the system. Moreover, we have also applied optical fields to drive the system away from thermal equilibrium and detect finer information about the spin system.

1.5 Spin relaxation and spectral line broadening

We have mentioned various spectroscopy techniques to measure the line-width of the ground and excited atomic levels in section 1.4. The measured line-width of a particular level infer the presence of various relaxation processes associated with the detected atomic variables. The origin of the excited level ($l > 0$) line-width is purely quantum mechanical (the presence of vacuum fluctuation of radiation fields in the universe) as discussed earlier and the measured line-width can get broadened due to the inhomogeneous Doppler and homogeneous power and pressure broadening.

In absence of any external driving, at thermal equilibrium, the atoms populate in the ground hyperfine levels. The ground level of alkali metal atoms consists of two hyperfine levels due to the hyperfine coupling as discussed in section 1.1.1. At thermal

equilibrium, the atomic population distributes among these ground hyperfine levels with a population ratio that depends on the number of the magnetic (Zeeman) states involve therein. The atoms are distributed equally among the Zeeman states within the ground hyperfine levels at zero magnetic fields at room or higher temperatures. The atoms in the ground hyperfine levels undergo various collisions due to the thermal motion which significantly affects the lifetime of atomic spins and thereby affects the spin coherence as well. Such relaxation processes broaden the line-width of the magnetic resonance spectrum detected from the atoms in the ground levels at thermal equilibrium. In this section, we briefly present the spin relaxation mechanisms of alkali metal atoms in their ground hyperfine levels which are contained in a quartz cell filled with inert gas at thermal equilibrium. We also indicate some practical techniques that can control the spin relaxation processes and narrow down the magnetic resonance spectrum detected with thermal atomic vapors.

Spin relaxation. The spin relaxation of an atom can be categorized into two parts: spin lifetime (T_1) and spin-coherence time (T_2). The various spin relaxation mechanisms due to the collisions with similar or other alkali atomic species, or buffer gases depend on the collision rate (R),

$$R = n\sigma\bar{v} \tag{1.21}$$

where n is the density of the other atoms, σ is the effective scattering cross-section, and $\bar{v}$ is the average velocity of the atoms in the center of mass frame of the colliding pairs.

In most of the spin relaxation processes, only the electronic spins get depolarized while keeping the nuclear spins unaffected. Therefore, in an ensemble of many atoms, the effective spin of the system preserves the coherence for some finite time after the depolarization of the electronic spin. However, the degree of atomic spin coherence depends on the nuclear spin (I) and the atomic polarization (P) of the system via the nuclear slowing down factor q [29, 33].

The relaxation in the spin-lifetime (T_1) [29, 34] depends on various factors such as spin-destruction rate (R_{SD}), the collision with the container wall (R_{Wall}), interaction with the probe fields etc. The relaxation due to spin-destruction collision can happen due to the collision with the same or other alkali atoms as well as collisions with buffer gas atoms present in the cell.

The spin-exchange collision rate (R_{SE}) and the magnetic field in-homogeneity (R_{MI}) through the cell causes dephasing in the free precession of the transverse spin component of atoms which relaxes the effective transverse magnetization of the system. Such relaxation processes do not affect the longitudinal spin components. However, the relax-

ation processes related to T_1 will also contribute in T_2 since those processes completely randomize the atomic spin after the collision. Therefore the transverse spin-relaxation time or spin coherence time (T_2) can be written as [29],

$$\frac{1}{T_2} = \frac{1}{T_1} + \frac{1}{q_{\rm SE}} R_{\rm SE} + R_{\rm MI}, \tag{1.22}$$

where $q_{\rm SE}$ is the spin-exchange broadening factor.

1.5.1 Spin-exchange collisions

In the spin-exchange collision (SEC) between two alkali atoms, the electronic spin of the individual atoms can be reversed while keeping the combined atomic spins ($\vec{F}_1 + \vec{F}_2$) of the colliding pairs a conserved quantity in the collision [34, 35]. Such a collision can symbolically be written in terms of electronic spin orientation of the individual atoms with respect to the combined atomic spins as [29],

$$A(\uparrow) + B(\downarrow) \Rightarrow A(\downarrow) + B(\uparrow), \tag{1.23}$$

where $A(\uparrow)\,(B(\downarrow))$ represents the colliding alkali atoms $A\,(B)$ with electronic spin oriented along up (down). Since the combined atomic spins are conserved in the SEC, the atoms can change their hyperfine levels after the collision. As a result, the SEC randomly put atoms in different ground hyperfine levels (F) and the magnetic states (m_F) redistribute after the collision leading to a modifications in the spin coherence.

When a constant magnetic field is applied to detect the magnetic resonance spectrum at Larmor frequency (ν_L), the SEC leads to broadening in the spectrum if the spin-exchange collision rate $R_{\rm SE}$ is slower than the ν_L. However, when the rapid SEC collision rate exceeds ν_L, a line narrowing is observed in the spectrum [36–39]. This is similar to the Dicke and motional line narrowing mechanisms known in atomic spectroscopy. This regime ($R_{\rm SE} > \nu_L$) is called the spin-exchange relaxation free (SERF) regime where the atomic spins synchronously precess about the magnetic fields with longer coherence time. In the SERF regime, the atoms which are randomly distributed in the various Zeeman states due to the rapid SEC, spend more time in that hyperfine level which has more statistical weight, i.e. $F = I + 1/2$. Therefore in the SERF regime, the rapid SEC helps to preserve the atomic spin coherence.

However, in the other regime, we call a non-SERF regime, the SEC is the most dominating factor to the loss of the atomic spin coherence [40]. In this thesis, we have performed our measurements in the non-SERF regime i.e. $\nu_L > R_{\rm SE}$.

1.5.2 Spin-destruction collisions

Spin-destruction collision is another important spin relaxation mechanism where the total spin of the colliding atomic pairs is not conserved. Such a collision can take place between alkali-alkali atoms or between alkali-noble gas atoms. During the spin-destruction collision between alkali atoms, the spin angular momentum is transferred to the rotational angular momentum of the colliding dimer [29]. This collision can be symbolically written as,

$$A(\uparrow) + B(\downarrow) \Rightarrow A(\uparrow) + B(\uparrow). \tag{1.24}$$

However, the scattering cross-section for spin-destruction collisions between alkali-alkali atoms is extremely small − two to four orders of magnitude smaller than the SEC. Therefore, the spin-destruction collision between alkali metal atoms does not play a significant role in the relaxation of atomic spin unless the SEC is suppressed.

Further, the spin-destruction collisional cross-section between alkali and noble gas atoms is orders of magnitude smaller than the alkali-alkali spin-destruction collision ([29] and references therein). Additionally, due to the closed shell structure of the noble gas atoms, the alkali metal atoms do not get depolarize even after several collisions. The buffer (noble) gas is generally used in the vapor cell to slow down the motion of the alkali atoms to reduce the rate of collisions with the cell wall. In such an application, the pressure of the buffer gas is chosen such that the spin relaxation due to the collision with buffer gas is less than the most dominating factor of relaxation mechanisms present in the system. However, the spin polarization of the excited level ($l > 0$) valance electron of the alkali metal atoms gets heavily depolarized due to the collision with buffer gas and causes huge pressure broadening in the system. This happens due to the rapid collisional mixing between the excited level Zeeman states of the alkali atoms [29].

1.5.3 Wall collisions

Another source of relaxation for the electronic spin of an atom is the bare inner side glass surface of the container wall. A strong and rapidly fluctuating electric and magnetic field exists on the inner surface of the cell due to the ions and molecules of the glass material [29, 34]. However, when an alkali atom strikes on the surface, it does not bounce back instantaneously. Rather the atoms get adsorbed on the glass surface for some finite length of time (μs to ns range) [41]. During this time, the atom is eventually stuck on the surface and move from one molecular site to another due to the

thermal excitation and experiencing the fluctuating forces. Such rapidly fluctuating and random forces on the glass surface completely depolarise the electronic spin of the alkali atom and the details of the theory are given in the celebrated review article [34]. It is certain that for every collision of the atoms with the bare glass surface, the electronic spin gets completely randomized.

Wall collision is the most dominating factor for the spin relaxation of atomic electrons unless this effect is minimized. For a glass cell of length 2 cm and atomic velocity of 400 m/s, the atom interacts with the glass cell in every $\sim$ 50 μs interval when the vapor pressure of the atom is less inside the cell and no buffer gas is present. To prevent such collisions of the atoms with the walls, two techniques can be implemented. The inner surface of the glass cell can be coated with the long chains of hydrocarbons, such as paraffin so that the atoms can elastically bounce back from the coating surface and do not get adsorbed by the glass surface. This technique can preserve the polarization of the atoms for several thousand or millions of collisions with the glass surface. Another technique is to fill the glass cell with closed-shell inert (buffer) gas to make the slow diffusion of atoms inside the cell and take a long time to reach the cell wall. In most of the high precision vapor cell applications, both techniques are implemented to reduce the effect due to the wall collision. However, in our experiment, we put high-density neon buffer gas inside the cell to reduce the wall collision while keeping the inner surface of the cell coating free.

1.5.4 Magnetic field in-homogeneity

Another source of spectral line broadening mechanism is the magnetic field in-homogeneity across the vapor cell. The magnetic field produced by the current-carrying wires in Helmholtz configuration, in general, does not generate absolute homogeneous magnetic fields throughout the atomic sample. However, across the cell, a slow magnetic field gradient and a small but finite local magnetic field in-homogeneity result from a practical Helmholtz coil. Therefore the atoms at different positions inside the cell precess at a slightly different frequency with respect to the average ν_L, which makes broadening in the magnetic resonance spectrum. If the magnetic field variations across the cell is ∇B, then the broadening in the spectrum can be expressed at $R_{\mathrm{MI}} \sim \upsilon(\nabla B)$.

However, when the vapor cell is free from other foreign gases and molecules and the wall collision is reduced, the atom moves much faster inside the cell due to its thermal motion. The atom spends a much shorter time in a particular position inside the cell and does not significantly experience the local magnetic field variations. In this case, the atoms precess with an average magnetic field which is free from the broadening

due to the magnetic field in-homogeneity. Such a mechanism is called the motional line narrowing in magnetic resonance spectroscopy.

Nevertheless, when the glass cell is filled with buffer gas aiming to make the alkali atom's motion diffusive, the atom spends significantly longer time in a particular position inside the cell and precess about the local magnetic field. In this scenario, the broadening due to the magnetic field in-homogeneity is reflected in the spectrum [42–45].

1.5.5 Transit time broadening

Transit time of the thermal atoms across the probing region is another source of broadening mechanism in the spectral line. The transit time limits the measurement duration of an atomic variable.

In case of cold atoms, the transit time through the probe beam naturally reduces. Thereby, the transit time broadening effects are minimized. In this thesis, we have demonstrated spin noise signal from an ensemble of cold atoms at 150 μK, where transit time broadening effects are negligibly small.

Chapter 2

Fundamentals of spin noise spectroscopy (SNS)

2.1 Introduction

Spectroscopy technique is the fundamental investigatory tool for the determination and characterization of the electronic, nuclear, and magnetic structure as well as chemical compositions of a system with dimensions over a wide range from nano to astronomical scale. The spectroscopic techniques are the backbone for modern scientific advancement and rely on measuring the response of a system in terms of the frequency of the probe radiation field.

The phrase−"*spectroscopy*"−had been grown up by investigating the interaction of the electromagnetic field with the material systems. When a light beam passes through a material, a part of it gets reflected and transmitted through the medium, while the rest gets absorbed. Following the absorption of the light field by the material, an additional light field with another frequency or wavelength can be emitted from the system. The spectroscopy technique provides the knowledge of the frequency of the incident light field will be absorbed and re-scattered. The spectrometers record this information in terms of the incident electromagnetic field frequency−known as "*spectra*"−gives the detailed information about the atomic and molecular structure of the system under investigation. Each system has their characteristic spectra−like a "*fingerprints*"−that uniquely identifies them and distinguish them from other elements and compounds.

In a nutshell, the spectroscopy technique helps us to reveal the chemical and physical structure of a substance, provide a precise structure of magnetic, electronic, nuclear, and molecular levels. It also has important applications in bio-medical imaging. An

enormous number of different spectroscopic techniques has been developed over the past two centuries. Along with these developments, various form of radiative energy, e.g. electromagnetic field, matter-wave, and acoustic wave has been used to analyze the spectra.

In this thesis, we will discuss atomic spectroscopy, more precisely the spectroscopy of the atomic spin. We have used a far off-resonant laser light to probe the instantaneous population dynamics of the atomic spin in ground hyperfine levels of rubidium isotopes. The detected magnetic resonance spectrum in the radio frequency (RF) domain provides useful information in the context of quantum technologies in general, quantum sensing in particular. In a broader sense, our study develops a novel spectroscopy technique within the field of−*spintronics*. We optically detect the *"pattern within randomness"* of the atomic spin projection along the probe radiation field and investigate the associated *"fingerprints"* for the rubidium atoms. This spectroscopy technique, known as "*spin noise spectroscopy* (SNS)" has been developed in the early 1980s in atomic systems and further successfully extend to other physical, chemical, and biological systems. We take forward this technique and develop it further in atomic systems by implementing optical pumping and two-photon Raman coupling to the systems. Our developments of "*all-optical*" spin noise spectroscopy open up the realization of detecting spin correlation in equilibrium (within linear response) and non-equilibrium (beyond linear response) conditions and find useful applications and implications in other atomic, molecular, condensed matter, and photonics systems as well as various metrological purposes. We have employed optical pumping and coherent Raman coupling schemes separately to the rubidium ground hyperfine levels and Zeeman states, respectively to make a steady non-equilibrium system, and thereby detect the temporal transverse spin coherence of such system using a transparent probe laser field. Most importantly we demonstrate experimentally, for the first time, a detection of the intrinsic spin coherence in a ensemble of cold atoms via the technique developed during this thesis work.

The fundamental constituents of an atom, such as electrons and nucleons possess both charge and spin which can interact with any kind of electric and magnetic fields. Over the past few decades, modern scientific research and technologies is shifting its focus in the direction of spin-based rather than charged-based devices. The atomic spin degrees of freedom can be manipulated using external magnetic and electric fields, and measured non-invasively by optical fields. This accessibility of the atomic spins to interact with various realizable fields made the subject rich in recent years. The scientific research area "spintronics", [46, 47] deals with the spin of a system as a carrier of information, and turns out to be a promising tool in quantum information science,

metrology, fundamental test of physics, and various other theoretical and experimental investigations. These possibilities motivate researchers to study the dynamical properties of a spin system in equilibrium and various controllable non-equilibrium situations. The spectroscopy technique based on measurements of temporal fluctuations of spin of a system was developed using thermal sodium (Na) atomic vapor in the early 1980s by Zapasskii *et. al* [48]. This modern spectroscopy technique, termed as – "spin-noise spectroscopy (SNS)" – measures the spontaneous magnetization of a spin system on the Faraday rotation angle of a linearly polarized and far detuned probe laser beam passing through the system.

The spin noise spectroscopy technique is primarily developed as an experimental tool to measure the temporal fluctuations of the magnetization of a spin ensemble in thermal equilibrium. In the early SNS experiments [48–50], the magnetic resonance spectrum between the Zeeman states was experimentally observed in the spin noise (SN) spectrum to verify and show the feasibility and applicability of the technique. In those experiments, a homogeneous magnetic field is applied on the spin ensemble across the propagation direction of a far-off resonant and linearly polarized probe light which passes through the system and detects the temporal fluctuations associated with the Zeeman coherence between the spin components. In an ensemble of thermal atomic or nuclear spins, the magnetization components across the light field direction fluctuate over an average value of zero. However, the magnitude of this temporal fluctuation of the transverse magnetization is extremely small and depends linearly as $\sqrt{n}$ for an uncorrelated paramagnetic spin system, where n is the total number of spins of the system [49, 51]. Moreover, in presence of a homogeneous magnetic field, this instantaneous magnetization precesses at the Larmor frequency. If the system does not possess any spin fluctuations, the average transverse magnetization is always zero at all times. The spontaneous spin fluctuations break the symmetry of the transverse magnetization and appear as noise contained in the magnetization. According to the fluctuation-dissipation theorem (FDT), [52, 53] the spontaneous microscopic fluctuations of the spin ensemble results in a dissipation of the macroscopic magnetization of the system at a particular rate – transverse spin-relaxation rate ($1/T_2$). Therefore, a noise peak in the spectrum at the Larmor frequency is expected from the system in presence of the magnetic field according to the FDT [54] which is known as spin noise. The applicability of this technique was first realized by the researchers about one decade later after this technique have been discovered, while working in different aspects of research such as the non-demolition measurements of the spin squeezing of an atomic ensemble with squeezed light [55], and the quantum noise measurement of a spin-polarized atomic system [56].

The random fluctuations over space and time are prevalent in a wide variety of physical systems, and they can be a valuable resource for probing the characteristic nature and internal structure of the systems. Therefore the measured noise in an experiment is always not avoidable, and in certain circumstances, it provides valuable information about the system from where it is generated. A few important examples of such noises are the Johnson-Nyquist noise [57, 58], and the Brownian motion [18, 59, 60] of a particle immersed in a bath. Using the FDT, the authors in [57, 58], showed the variance of the voltage fluctuations per Hz resolution bandwidth can be written as [52, 61],

$$\langle V^2 \rangle = 4\, k_B T R \tag{2.1}$$

where k_B is the Boltzmann constant and T is the equilibrium temperature in Kelvin. Therefore, at thermodynamic equilibrium, the voltage fluctuations across the leads determine the resistance of the circuit. This particular example shows the two-point temporal correlation of the voltage fluctuations provides detailed information about the quantity resistance in thermodynamic equilibrium.

In the Brownian motion, the random fluctuating force imparted on the heavy object by the thermally agitated molecules in the bath changes the dynamics of the system. This problem can be solved using a simple Langevin equation and using FDT, a relation between the diffusion constant and friction coefficient of the system can be established. The detailed analysis of this problem within the purview of the Langevin equations, FDT, and Fokker-Plank equations in a classical and quantum domain provides a complete dynamical characteristic of the system. Additionally, a few more examples where the noise is a source of information are the intensity fluctuations in the emission of random lasers [62, 63].

The above examples confirm that in some systems the presence of random, intrinsic noise has a significant contribution to the dynamical behavior of the system. The noise in the system helps us to understand the underlying physics and investigate the dynamical structure factor of the system not only in the experimental perspective but also in investigating fruitful theoretical developments [64–68]. In general, a spin system also contains a detectable noise as a form of fluctuations in its magnetization component and provides a valuable information about the system.

Spin noise spectroscopy. The SNS technique relies on measuring the intrinsic fluctuations in the macroscopic magnetization of a spin system projected along the probe beam propagation direction. The noise or fluctuations of a physical observable is defined as the deviation of its instantaneous value from the mean. This noise can have

classical and(/or) quantum origin, however, this is the fundamental quantity associated with any observable. In an atomic spin ensemble, the fundamental noise in magnetization can exist in the form of random population fluctuations between the various magnetic states [56, 69]. Measurement of such magnetization noise of the magnetic material gives the complete picture of the dynamical susceptibility of the system which in turn provides all the details about the magnetic properties of the system [70]. SNS [1, 3, 71–74] is a non-invasive experimental tool that detects the temporal fluctuation of the magnetization of a magnetic system using an off-resonant optical probe laser field through Faraday rotation fluctuation measurements.

As early as 1845, British scientist Michael Faraday discovered the magneto-optical effect, which is known as the Faraday effect or Faraday rotation. Briefly, the Faraday rotation is the rotation of the polarization angle of a linearly polarized light passing through a magnetic material in presence of a magnetic field along the light propagation direction. The Faraday rotation angle is proportional to the strength of the magnetic field and the length of the sample. The origin of the Faraday rotation is the difference in the index of refraction for the left- and right-hand circularly polarized light in the medium − property of the medium known as circular birefringence. A century later, in 1946, Felix Bloch derived the dynamics of the magnetic moment in presence of an external magnetic field in his celebrated paper “Nuclear Induction" [51]. Later, this topic gets more clear in further investigations on the dynamics of magnetic moments in presence of various external effects such as diffusion of magnetic moments, inhomogeneity in magnetic fields, presence of relaxation mechanisms, etc [75]. SNS detects the fluctuations of magnetization of a spin system at Larmor frequency in presence of an external magnetic field. However, in the SNS technique, the linearly polarized probe laser beam detects the fluctuation of magnetization of a spin system as a fluctuation in its' polarization angle, an effect known as paramagnetic Faraday rotation. In the following section 2.2, we describe briefly the basics of the SNS technique.

After the first successful attempts in thermal atomic vapor in 2004 [4] and in solid-state systems in 2005 [76], this technique manifests a highly potential experimental tool to extract valuable information about the system under investigation. After these measurements, in the last two decades, this technique has been established as an interdisciplinary experimental method and applied to numerous spin systems to investigate them. The exploration of new physics and implementation to unexplored systems within this technique has been continuing till date and in the future also. As an example, we have developed a method to detect the intrinsic spin fluctuations from an ensemble of magneto-optically trapped cold rubidium atoms at a temperature of 150 μK [17]. In this paper, we have also indicated the potential of this technique in cold

ionic systems, and ultra-cold (in the nK temperature range) Bose and Fermi gases trapped in optical lattices or magnetic fields, opening up a wide range of exciting physics studies.

Applications in condensed matter and photonic systems. The applications of this technique in semiconductor heterostructures provide useful information about the conduction electronic spins. However the coherence times of the conduction electrons are extremely small (in the range of ns to ps), and the first detected SN signal from n−doped GaAs sample [76] was extremely weak. In this paper, they have measured the spin-relaxation time and Landé $g-$factor of conduction electron. A significant effort has been made [77–79] in developing sophisticated hardware and software to extract the SN signal from such a system with good SNR. The temperature dependence of these two parameters in thermal equilibrium is investigated in [78]. The SN power with different doping concentrations is performed in [80, 81]. The probe laser intensity and wavelength-dependent SN spectrum of bulk semiconductor is explored in [82]. The ultra-fast pulsed measurement of SN in highly $n-$doped GaAs semiconductors show magnetic field dependent large $g-$factor fluctuations and reported in [83]. The inverse Faraday effect [84] using SNS was observed and demonstrated in [85]. The interaction between the spin of conduction electrons and polarized nucleus is observed and reported in [86]. The SNS experiments performed in the condensed matter and photonic systems not only verified the existing theories, however, this technique also revealed some unpredicted physics of the systems. There has been remarkable progress to extend the applicability of SNS in theoretical investigations and experimental realizations in semiconductor heterostructures, quantum dots (QDs), exciton-polaritons and similar systems in recent years [87–142]. These works demonstrate that SNS is an efficient technique to resolve unsolved questions and explore new phenomenon in material science.

Applications in atomic systems. The atomic systems can be classified into two categories depending on their temperatures: (a) Thermal atoms that follow Boltzmann distribution function and are treated as classically, and (b) Cold atoms below the critical temperature for bosons and Fermi temperature for fermions follow Bose and Fermi statistics, respectively and treated as quantum mechanically. The average occupancy for thermal atoms in a state is much less than one, whereas the atoms tend to gather in the lowest energy state for bosons and arrange themselves till Fermi energy for fermions. The origin of spin noise in thermal and cold atoms has emerged from completely different interaction mechanisms and probably has different characteristic

features. So far researchers have extensively studied the SNS with thermal atomic vapor, explored a lot of new physics, discovered practical applications, and proposed new possibilities which can be carried out in the future. On the other hand, the research activities on implementing this technique in cold atoms have just started which surely opens up a new experimental research field full of interesting unexplored questions.

Recently, easily accessible atomic vapors seek significant attention in many practical and low-cost applications, such as precise electric [143] and magnetic field [35] sensing and their imaging, quantum memory, and quantum information processing [144, 145], time and frequency standards, inertial force sensing, optical switches, isotope separation methods [146], spectroscopic reference [147] for cold atom experiments, etc in addition to the fundamental research interests [148–150]. For most of the applications, the measurement is based on the detection of atomic spin polarization in a preferred direction. However, the fluctuations in spin polarization limit the precision achieved to these applications, and the further development of these applications depends on the understanding of the origin of SN and to control them systematically. There have been considerable efforts paid to suppress the undesirable spin fluctuation using feedback control in cold atoms [151, 152] at the temperature of 100's of μK range, which can also be performed in the specially miniaturized thermal atomic sources. The execution of this technique in various systems to explore new physics and for low-cost practical applications have a bright future.

After the successful implementation of SN measurement based on Faraday rotation fluctuations in thermal Rb and potassium (K) atoms by Crooker *et. al* [4], the detailed theoretical derivation for SN spectrum in longitudinal and transverse magnetic field, as well as the inter-hyperfine spin fluctuations of thermal ^{41}K atoms are studied in [153]. The theoretical investigations and measurements of transverse spin-relaxation time (T_2) at low magnetic fields of Rb atoms are investigated in [154]. The SN measurements in presence of a static and oscillating magnetic fields simultaneously was performed in [87]. A quantum random number generator based on atomic SN limited by T_2 is proposed in [155]. After the successful implementations in thermal atomic vapor, a numerous amount of experiments, theoretical studies, proposal and practical applications within the SNS technique has been explored in atomic spin systems [2, 5, 15, 17, 20, 21, 73, 91, 92, 126, 156–179]. In the following section, we will briefly discuss the basics of the formation and detection of SN in atomic systems.

2.2 Theoretical background

Let us first assume a simple magnetic system in which the magnetic coherence is being detected using the Faraday rotation (FR) fluctuation-based SNS technique.

2.2.1 The spin system considered in this thesis

Let us consider an ensemble of non-interacting spins in thermal equilibrium at some temperature T. Here, the spin can be a free or bound electron, hole, or nuclear spin which possess a finite magnetic moment. The equilibrium of the ensemble is achieved through interactions between these spins and the thermal bath surrounding them. In the classical regime, the presence of the thermal bath, as well as collisions, induces fluctuations in spin polarization of the system. In the quantum regime, the spin fluctuation happens due to the various contact interactions of the spin with other spins surrounding them. Irrespective of their origin, the random spin fluctuations are ubiquitous in every physical system, and probing them provides a valuable resource of the characteristic nature and internal structure of the systems.

In this thesis, we have considered the magnetic states (m_F states) within the ground hyperfine levels ($F-$levels) of rubidium atoms as the spin system. We have investigated the various spin properties of such spin ensemble in a wide range of temperatures ranging from 400 K down to 100's of μK. However, in this regime of temperature, the spin fluctuation is governed by the thermal effects, and the atomic spin ensemble can be considered a paramagnetic system. The de Broglie wavelength associated with the atoms is much smaller than the inter-atomic separation. Therefore, the spin fluctuations over space, which infer the quantum many-body effects via spatial overlap of the matter-waves, are not having significant contribution to the observed spin noise signal. Nevertheless, the time-averaged value of the spin polarization or magnetization, $\langle M(t)\rangle_{\mathcal{T}\to\infty}$ ($\mathcal{T}$ is the total averaging time) along any arbitrary quantization axis is zero for this system. However, the variance of the magnetization ($\langle M(t)M(0)\rangle$) is non-zero.

Within the optical SNS technique, a linearly polarized laser light on passing through such a paramagnetic sample can passively detect these magnetization fluctuations along the light propagation in its time-resolved Faraday rotation noise [1, 4]. Such detection is feasible as the magnetization fluctuations in a paramagnetic sample alter its optical properties which lead to Faraday rotation noise. The probe beam is kept far-detuned (with a detuning δ_p) from any allowed optical transition of the medium to ensure negligible scattering by the medium making SNS a relatively non-invasive technique.

2.2.2 Optical detection methods

When light passes through a transparent optical medium, various properties of the optical field, such as polarization, phase, intensity, etc may change depending on the frequency of the light. The light beam after passing through such an optical medium carries information about the static and dynamical properties of the medium in its optical field. The spectral investigations of the transmitted or scattered light from the medium, reveal the linear and non-linear characteristics of the medium. The FR fluctuation-based spin noise detection of a spin ensemble can be distinguished into two independent areas of research fields: the light intensity noise (LIN) spectroscopy and optical field correlation (OFC) spectroscopy.

LIN spectroscopy. The LIN spectroscopy relies on measuring the two-point temporal correlation of the transmitted light beam intensity ($I(t)$) from the medium. The power spectrum of the intensity of transmitted light in the LIN spectroscopy [1]

$$I_{\omega}^{2} = \int \langle I(t)I(t+\tau)\rangle e^{i\omega\tau} d\tau, \tag{2.2}$$

does not carry information at the optical frequency, rather provides dynamical information of the system that modifies the intensity of the light beam in the time domain. In LIN spectroscopy, the range of interest of the frequency depends on the 3 dB detection bandwidth of the photodetector.

In the pre-laser era in 1955, the pioneering work by Forrester *et al.* [180] demonstrate experimentally the Zeeman splittings between two emission lines of mercury (Hg) vapor at the wavelength of 546.1 nm based on the LIN spectroscopy. The main results obtained in this paper are that during the photoelectric conversion of the optical field, the emission probability for electrons is proportional to the square of the total electric field amplitude arising due to interference between its Fourier components. A year later, Hanbury-Brown and Twiss [181] experimentally showed that by measuring the spatial correlation of the light intensity noise coming from a far distanced remote source, it is possible to measure the angular dimension of the source. These two are the earliest and most famous experiments in optical physics which indicate that the noise contained in the optical field can be informative. The experiments reported in [180] and [181] mostly aimed to investigate the properties (spectral) of the emitted light, rather than the dynamical or bulk properties of the medium from where it is generated. In these cases, the light emitted from the source is incoherent in nature, and the power spectral density at the beat note frequency is extremely weak and hard to detect. However, with the advent of laser technology, the development of LIN spectroscopy has

been changed drastically. The laser light has an extremely high luminosity, a coherent source of photon stream and can interact with a medium. These properties of laser make the LIN spectroscopy more realizable and practical in two senses: in one hand, the power spectral density at the beat frequency of the laser intensity modulation exceeds the photon shot noise level, and on the other hand, the transmitted laser light through a medium provides not only the spectral properties of the light but also the dynamical and bulk properties of the medium.

SNS is a type of LIN spectroscopy where the polarization of the transmitted laser light is used and analyzed. The temporal variation of the intensity of transmitted light proportionally varies with the polarization angle if the light is passing through a polarization-sensitive instrument. Therefore, in SNS, the noise contained in the polarization angle of the transmitted light is first converted into noise in the intensity using the polarimetric technique.

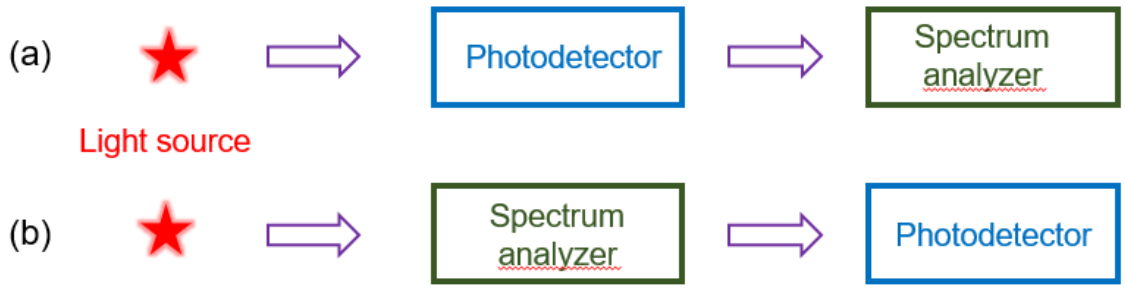

Figure 2.1: The arrangements of the photodetector and spectrum analyzer for LIN (a) and OFC (b) spectroscopy technique [1] discussed in the main text.

OFC spectroscopy. The OFC spectroscopy technique deals with the spectral distribution of the optical field ($E(t)$) at the optical frequencies ($\sim 10^{15}$ Hz), rather than the intensity. In experiments, the OFC spectroscopy is performed by measuring the intensity ($|E(t)|^2$) of the light or by measuring the photo-current generated in the photo-detector electronic channel since one cannot measure $E(t)$, which is, in general, a complex quantity.

The detected intensity at each optical frequency contain information about the correlation properties of the optical field. According to the Wiener–Khinchin theorem [1]

$$I_\omega = \int \langle E(t)E^*(t+\tau)\rangle e^{i\omega\tau} d\tau. \tag{2.3}$$

Therefore, the optical spectroscopy can provide information about the field corre-

lation with a temporal resolution of around 10^{-15} s.

The basic difference between the LIN and OFC spectroscopy is the arrangements of the photo-detector and the spectrum analyzer. In OFC spectroscopy, the spectral decomposition of the light field is analyzed before getting detected by the photo-detector. Whereas, in the LIN spectroscopy, first the photo-current is generated in the photo-detector, and thereafter the spectral decomposition is analyzed in the spectrum analyzer [1] as shown in Fig. 2.1.

2.2.3 Optical detection of spin noise

The principle behind the detection of the noise of a spin ensemble is that the susceptibility of the medium is proportional to the magnetization of the system. Therefore, the dynamics of the spin system magnetization can be read out by investigating the temporal modifications in various optical parameters (intensity, polarization, frequency, etc.) of the transmitted or scattered light through the medium. The "paramagnetic" FR [182] of the transmitted laser light is directly proportional to the instantaneous magnetization of the system. The paramagnetic FR on the polarization of the probe laser happens due to the population fluctuations of the spin system in its available magnetic states.

The difference in population between the ground level Zeeman (m_F) states of a paramagnetic spin system creates the corresponding difference in the absorption coefficient (A) for the left- and right-hand circularly polarized light propagating along the external magnetic field direction as shown in Fig. 2.2. This property of the medium is called magnetic circular dichroism (MCD). The MCD can eventually be observed in the optical absorption spectrum with different strengths for these two circular components of light. For a linearly polarized incident light, the MCD modifies the polarization of the transmitted light to be elliptical. The similar optical anisotropy of the medium, according to the Kramers–Kronig relations, can also be observed in the index of refraction (n) for left- and right- circular polarization, a property of the medium called magnetic circular birefringence. This property of the medium rotates the plane of the polarization angle of an incident linearly polarized laser light passing through the medium is known as Faraday rotation (FR).

It is worth noting that both the procedure, FR and MCD can be used to probe the dynamics of the spin system magnetization. However, since the MCD-based measurements rely on measuring the absorption for two circular components of light near the vicinity of the optical transition frequencies, this method is necessarily perturbative. On the other hand, the FR-based measurements can be performed in the transparency

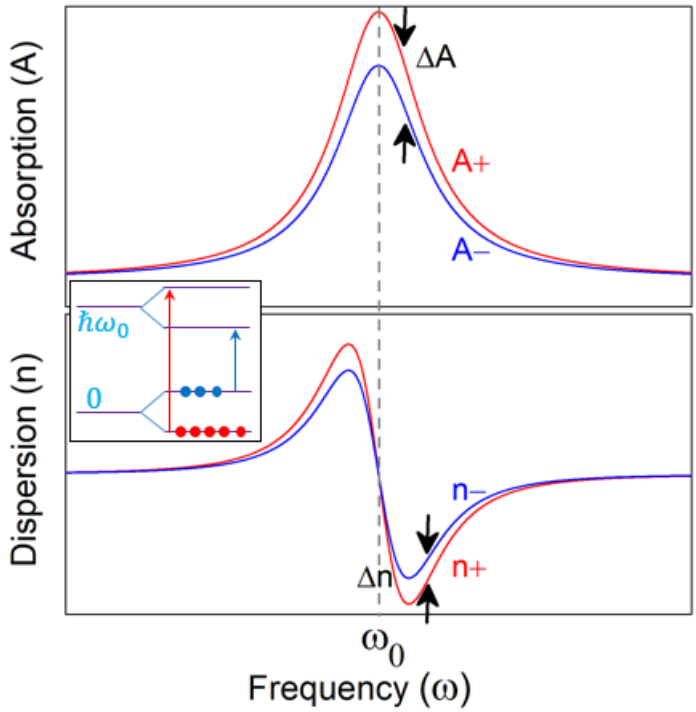

Figure 2.2: The formation of paramagnetic spin noise (SN) within the ground magnetic (Zeeman) states in atomic systems. (inset) A two level system (with ground level energy $\hbar 0$ and excited level energy $\hbar\omega_0$) split into Zeeman states in presence of (co-linear) magnetic field. (top) The instantaneous population fluctuations between ground level Zeeman states causes instantaneous difference in absorption co-efficient (ΔA) for σ^+ and σ^- light, that causes magnetic circular dichroism (MCD). (bottom) The instantaneous fluctuations in A causes fluctuations in the refractive index (n) in response to those components of light via Kramers-Kronig relation. The difference in n for these two components of light, Δn causes Faraday rotation (FR) of the input probe laser beam. The figure is reproduced from ref. [1].

region of the system with negligible optical excitation. Another important difference is that, in the MCD-based measurements, the spin system magnetization can be probed by measuring the frequency (near the atomic resonance frequency) dependent transmitted beam intensity of the circularly polarized light. However, in the FR-based measurement, a polarization-sensitive detection set-up is required, since practically the intensity of the transmitted beam is unchanged.

Another important point to note is that in the classical definition of FR, the probe light propagates along the external magnetic field direction. However, the light beam detects the magnetization of the spin system along with its propagation direction irrespective of the direction of the applied magnetic field. Therefore, the FR-based technique can be used to measure the optical orientation of the macroscopic magnetization [183] as well as to probe the coherently precessing transverse magnetization to

detect the magnetic coherence of the spin system [184]. The macroscopic magnetization fluctuations of a spin system along the light propagation direction (regardless of the direction of the applied magnetic field or whether its absence) alter the optical properties of the medium along the same direction. The component of the instantaneous magnetization of the spin system along the light propagation direction is detected in the polarization angle of a far-off-resonant probe light by the paramagnetic FR method.

On the contrary, in the measurements of Faraday rotation, the amount of polarization rotation angle of the linearly polarized probe light traveling through the medium is characterized by the Verdet constant (V) of the medium quantifying the magneto-optical effect. Simply, the polarization rotation angle (θ_F) can be written as

$$\theta_F = V(\omega)\, B\, l, \tag{2.4}$$

where B is the longitudinal magnetic field, and l is the length of the medium. $V(\omega)$ is the frequency-dependent Verdet constant. However, in the measurements of paramagnetic FR, the quantity Verdet constant is irrelevant, rather how many spins are contributing to give rise to this effect and how efficiently the magnetization along the light propagation direction is converted into the FR − is more appropriate. The work reported in [185] introduced a more convenient quantity, the FR cross-section σ_F, which defines the efficiency of the conversion of magnetization fluctuation to the detected FR of a paramagnetic system. The instantaneous polarization rotation ($\theta_F(t)$) can be quantified as

$$\theta_F(t) = \sigma_F\, s_x(t)\, l, \tag{2.5}$$

where $s_x(t) = (n_{x\uparrow}(t) - n_{x\downarrow}(t))/2$ is the difference in the spin population densities at time t along the light propagation direction $\hat{x}$. In the transparency region of the probe laser light, the dependency of σ_F on the laser frequency is nearly constant. σ_F quantifies the sensitivity of the FR to magnetization fluctuations of a specific spin system and differentiates the efficiency of the paramagnetic FR technique with respect to different spin systems.

2.2.4 Magnetic field and light propagation geometry

The magneto-optical effects, such as MCD or FR are used to investigate the dynamical properties and energy structure of a transparent magneto-optical medium by measuring the magnetic response function or ac magnetic susceptibility. Depending on the configuration of the external magnetic fields and the light propagation direction, the detected magneto-optical signal carries information about the various dynamical and

static magnetic properties of the medium. In the traditional SNS technique, the probe laser light propagates across the magnetic field to study the macroscopic magnetization dynamics and the temporal coherence of the system.

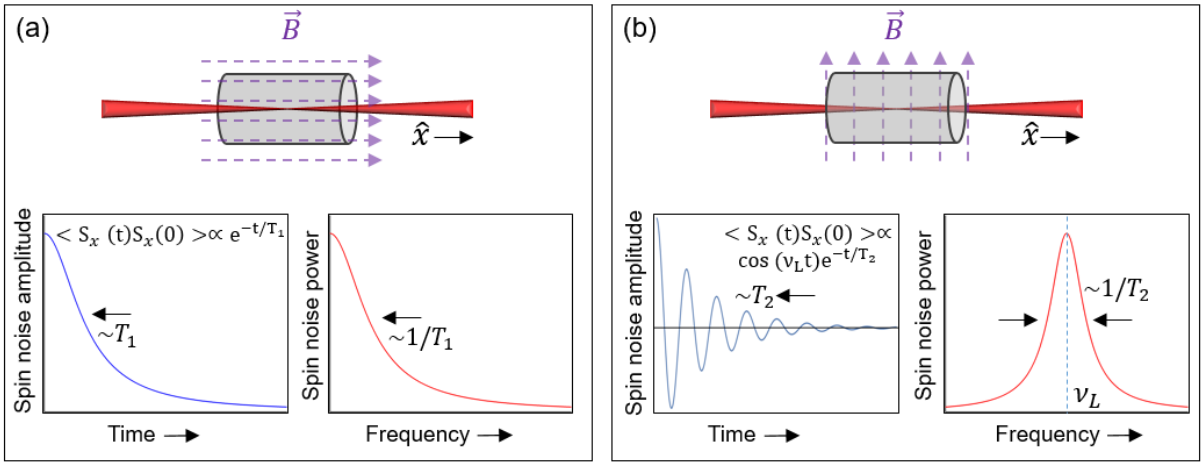

Figure 2.3: The light propagation and magnetic field configuration in Faraday (a) and Voigt (b) geometry. The light beam (red trace) propagates along $\hat{x}$ and the magnetic field direction is shown with the broken arrows. The spin noise amplitude (power) in time (frequency) domain in each configurations are shown in left (right) column in the bottom panel.

Nevertheless, depending on the interest of investigating the dynamics of the energy relaxation or coherence dissipation of a system, the geometry of the arrangements for the external magnetic field and the light propagation direction varies. However, to measure the energy relaxation dynamics and its characteristics relaxation times (T_1), the arrangement should follow the Faraday geometry. In the literature, T_1 is known as longitudinal spin-relaxation time. For the measurement of coherence and its characteristic times (transverse spin-relaxation time T_2) of the spin system, one needs to follow the Voigt geometry. In the traditional magneto-optical effect measurements, the magnetic field applied along or across the light propagation direction, probes the magnetic field induced circular or linear anisotropy, respectively. However, in the FR-based fluctuation measurement, this anisotropy may break the symmetry and the traditional SNS technique measures the anisotropy of circular birefringence. The following two basic geometries are:

Faraday geometry. In this geometry, the homogeneous magnetic field ($\hat{B}$) is applied on the spin system along the probe light propagation direction ($\hat{k}$), i.e. $\hat{B} \parallel \hat{k}$ as shown in Fig. 2.3 (a). Therefore, the probe light detects the longitudinal fluctuations of macroscopic magnetization of the spin system. More accurately, the dynamics of the

energy relaxation between various spin (Zeeman) states are measured in the steady-state condition. The characteristic time-scale for this dynamics is controlled by the longitudinal spin-relaxation time or lifetime in a particular energy state, T_1.

The diagonal density matrix elements ($|i\rangle\langle i|$) formed within the state-space spanned by the Zeeman states are measured in this configuration. Therefore, the modulation frequency associated with this detection technique in LIN spectroscopy is zero. The random fluctuations of the longitudinal magnetization, therefore, do not impart modulation on the probe intensity. However, the lifetime (T_1) related to this dynamics is revealed in the frequency spectrum of the magnetization. In the time domain, the detected longitudinal magnetization noise appears as the white noise at frequencies higher than that of the order of $1/T_1$. Therefore the auto-correlation function of this noise takes a shape of exponential with characteristic decay time T_1. The frequency spectrum of the longitudinal FR noise is therefore a Lorentzian in shape that appeared at zero frequency with full-width at half-maxima (FWHM) is proportional to $1/T_1$.

The measurements of magnetization noise in the Faraday geometry only provide information about the energy relaxation of the spin system, more precisely the linear magnetic response of the system in the parallel magnetic field configuration. However, this geometry does not provide any information about the various energy splittings of the spin system, which is very important not only to study the various interaction phenomenon causing such splittings but also to extend this technique to investigate the higher-order correlator. Another drawback of this geometry is that the spectrum appears at zero frequency where the measurement is highly dominated by the electronic $1/f-$noise. Suppressing such universal $1/f-$noise and detecting the longitudinal FR noise at zero frequency with a good signal-to-noise ratio (SNR) requires advanced hardware and very long acquisition times.

Voigt geometry. The drawbacks mentioned in the Faraday geometry can be overcome by changing the orientation of the magnetic field to the probe beam propagation direction in Voigt geometry. In this geometry, the magnetic field ($\hat{B}$) applied on the spin system is orthogonal to the probe light propagation direction ($\hat{k}$), i.e. $\hat{B} \perp \hat{k}$ as shown in Fig. 2.3 (b). Therefore, the probe laser light detects the spontaneous transverse magnetization of the system. In the density matrix formalism, the dynamics of the coherence between the Zeeman states (off-diagonal elements of the density matrix, $|i\rangle\langle j|$) are captured in the detected polarization angle of the transmitted probe laser through the spin system. In this configuration, the magnitude of the transverse magnetization vanishes. However, the spontaneous magnetization in time domain is still detected because its random fluctuations spontaneously breaks the symmetry of the

spin system.

Since in this geometry, the detection of spontaneous Zeeman coherence is involved, the spectrum will appear at the separation between two Zeeman states ($|(E_i - E_j)|/\hbar$, where $|i - j| = 1$) and discussed in details in the next chapter. The relevant timescale in this measurement is the coherence time (T_2) of the spin system.

An important point to note that, in the electron spin resonance (ESR/EPR), or nuclear magnetic resonance (NMR) spectroscopy the spin system is exposed to a resonant RF fields, which necessarily perturbed the system away from thermal equilibrium. However, in the optical FR-based SNS technique, the spin system is not perturb by any external oscillatory field. In the SNS technique, the relaxation in the coherence of spin system in thermal equilibirum induces atomic population to randomly fluctuate between available spin states. This random fluctuations of population between spin states is non-invasively detected by the off-resonant probe beam and a polarimetric detection set-up.

The thesis is organized as follows. In the previous chapter (chapter 1), we discuss the prerequisite for this thesis. In this chapter (chapter 2), the details of the basic ingredients for the formation and optical detection of spin noise in an atomic system are discussed. In chapter 3, we present the relevant equations describing SN in Voigt geometry in an ensemble of thermally equilibrium alkali atomic vapor. In this chapter, we describe the details of experimental arrangements and detection of intrinsic (equilibrium) SN signal and its characteristic features with various experimental parameters.

In chapter 4, we discuss the applications of SNS in precision measurements of atomic, magnetic, nuclear, and chemical properties of the Rb atoms. This method can be applied to any other spin system to measure those properties. We have also developed precision magnetometry using the SNS technique that can suppress the Hall probe magnetometer and discuss it in detail in this chapter. The measurements of SN from an optically pumped non-equilibrium but steady-state system are discussed in this chapter and its various applications are indicated.

In chapter 5, we present the SNS technique with coherent optical driving in thermal atoms. We have theoretically developed and experimentally demonstrated a million folds enhancement of the driven signal strength in comparison to the intrinsic SN signal. The theoretical derivation of intrinsic and Raman driven SN in an atomic system is discussed based on optical Bloch equations (OBEs). We also present how one can extract the information about intrinsic spin properties from such a driven spectrum. The generation of higher harmonics and detection of line-narrowing in the intrinsic SN signal due to Raman coupling are discussed.

In chapter 6, we discuss in detail the development of our low-cost real-time magnetometer system using the digital-receiver system (DRS) and SNS technique. In chapter 7, we present our state-of-the-art cold atom machine that magneto-optically traps (MOT) about ten million atoms at a temperature of 150 μK. The complete characterization of the cold atoms is discussed in detail in this chapter.

In chapter 8, we demonstrate, to the best of our knowledge, the first detection of spin noise from an ensemble of magneto-optically trap Rb cold atoms using the SNS technique and by employing Raman coupling. The relaxation in spin coherence between Zeeman states in such cold atoms is measured and presented in this chapter. In this proof-of-the-principle experiment, the details of the signal formation, detection, and characterization are presented. We finish the thesis with concluding remarks and outlook in chapter 9.

Chapter 3

Spin noise spectroscopy (SNS) in thermal atoms

In this chapter, we describe the detection of the intrinsic spin noise signal from thermal Rb atoms in equilibrium. The random fluctuations of the spin population between Zeeman states of ground hyperfine level lead to fluctuations in the macroscopic magnetization of the system in real-time. This fluctuation in magnetization is regarded as "spin noise" and is detected as a polarization fluctuation of a linearly polarized and far-detuned probe laser light as described in chapter 2.

We start with a simple equation (Eq. 3.1) that governs the dynamics of the spin systems' magnetization projected along the detection axis in presence of an orthogonal homogeneous magnetic field and dissipation due to the spin fluctuations. Afterwards, we present a detailed description of the experimental setup and relevant optical and electronic components. We show the spectrum of the intrinsic SN in thermal equilibrium and indicate the role of the magnetic field directions used in this technique. The characterization of this technique with various experimental parameters is presented towards the end of this chapter.

3.1 Spin dynamics and the spectrum in Voigt geometry

The intrinsic random fluctuations of the macroscopic magnetization reveal the characteristic relaxation times of the spin ensemble. In the presence of a constant magnetic field, the spontaneous transverse spin polarization precesses at the Larmor frequency (ν_L) about the magnetic field. Assuming a single exponential transverse spin relaxation (coherence) time T_2 and a magnetic field $B_\perp$ being orthogonal to the probe laser

propagation ($\hat{x}$), we can obtain the temporal correlation of magnetization along the probe beam from the Bloch equation

$$\langle M_x(t)M_x(0)\rangle \propto \cos(\nu_L t)e^{-t/T_2}, \tag{3.1}$$

where the Larmor frequency $\nu_L = g_F\mu_B B_\perp/h$, g_F is the g-factor of the hyperfine F-levels, μ_B is the Bohr magneton and h is the Planck's constant.

In practice, the random fluctuations in the macroscopic transverse magnetization precesses at frequency ν_L about the magnetic field with an "effective" spin coherence time T_2^*. Here, the system is subjected to various in-homogeneous broadening, such as spin-exchange and spin-destruction collisions, magnetic field in-homogeneity, collisions with the container walls and finite transit time. The spontaneous dynamics of $M_x(t)$ is pictorially depicted in Fig. 3.1. Note that this is a schematic representation of the spontaneous magnetization of an atomic system, and not an experimental measurement. The schematic shows the time average value of the magnetization is zero, however the variance – the strength of the noise – is non-zero. Here, the y-axis is the instantaneous magnetization of the system projected along the light propagation direction ($M_x(t)$) and does not have any unit. However, the experimentally measured quantity – Faraday rotation ($\theta_F(t)$) – is proportional to $M_x(t)$ and has a unit of radians. The proportionality constant between $M_x(t)$ and $\theta_F(t)$ contains the units radians. The x-axis is the time with unit of a sec. Therefore, the auto-correlation function of the spontaneous magnetization, as shown in Eq. 3.1, is an oscillatory envelope with exponential decay of time-scale T_2^*.

The measured Faraday rotation fluctuation $\langle\theta_F(t)\theta_F(0)\rangle$ ($\theta_F(t)$ is the Faraday rotation angle at time t) is a direct probe of the magnetization fluctuation $\langle M_x(t)M_x(0)\rangle$ of the system in thermal equilibrium and its Fourier transform to spectral frequency ν is the power spectral density $P(\nu)$ of the spin noise. Therefore,

$$\begin{aligned} P(\nu>0) &= \int_0^\infty dt\ \cos(\nu t)\langle\theta_F(t)\theta_F(0)\rangle \\ &\propto \frac{1/T_2^*}{(\nu-\nu_L)^2+1/T_2^{*2}}, \end{aligned} \tag{3.2}$$

where we have used Eq. 3.1 in the last line with T_2 replaced by T_2^*. So, the SN power spectrum has a Lorentzian lineshape centred at ν_L in frequency domain (refer to the peaks in the SN amplitude spectrum $\sqrt{P(\nu>0)}$ in Fig. 3.5 for ^{87}Rb or ^{85}Rb) and its full width at half maxima (FWHM) is proportional to $1/T_2^*$. The peak position of the SN spectrum, i.e. ν_L is the beat-note frequency between the consecutive Zeeman states

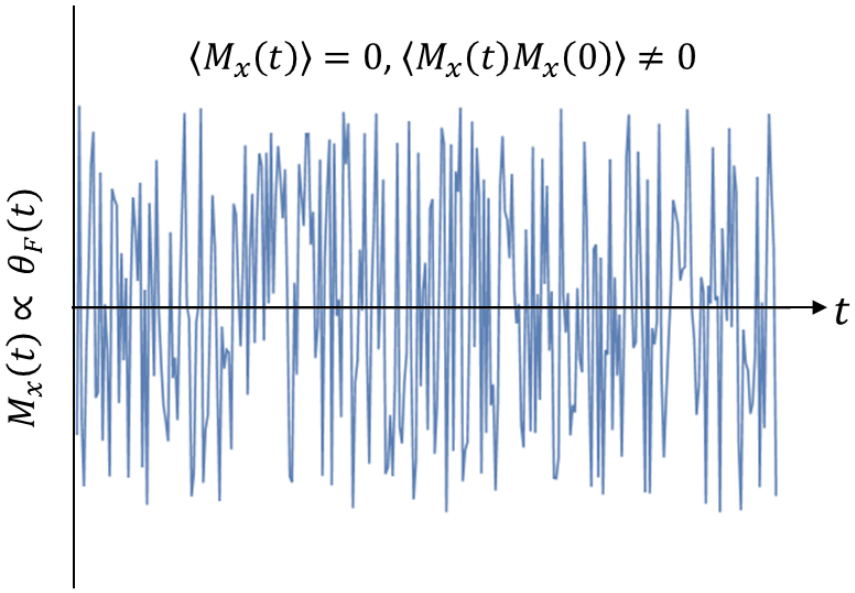

Figure 3.1: The trajectory of spontaneous magnetization ($M_x(t)$) of the spin system.

($\Delta m_F = \pm 1$). The intrinsic SN spectrum is the optically detected magnetic resonance signal of the spin system.

The energy of the Zeeman states E_{F,m_F} of hyperfine F-levels for alkali atoms in an arbitrary magnetic field $B_\perp$ has an exact expression following Breit and Rabi [186],

$$\begin{aligned} E_{F=I\pm\frac{1}{2},m_F} &= -\frac{h\Delta_{\rm hf}}{2(2I+1)} + g_I\mu_B B_\perp m_F \\ &\pm \frac{h\Delta_{\rm hf}}{2}\sqrt{1+\frac{4m_F}{2I+1}x+x^2}, \end{aligned} \tag{3.3}$$

where $h\Delta_{\rm hf}$, g_I and m_F are the zero-field hyperfine separation between the levels $F = I + \frac{1}{2}$ and $F = I - \frac{1}{2}$, the nuclear g-factor and the magnetic quantum number, respectively. Here, $x = (g_J - g_I)\mu_B B_\perp/(h\Delta_{\rm hf})$ where g_J is the Lande g-factor and the nuclear spin $I = 3/2(5/2)$ for ^{87}Rb(^{85}Rb). Since, the SNS detects the spin coherences between different Zeeman sub-levels ($\triangle m_F = \pm 1$), the frequencies of different magnetic resonance peaks have a nonlinear dependence on $B_\perp$ [22].

The SN signal strength. The integrated SN power over spectral frequency, $\Sigma \equiv \int d\nu P(\nu > 0)$, of the detected signal depends on various experimental parameters such

as probe laser detuning (δ_p), intensity (I_p) and cross-section (A), number density (n_0) of atomic spins and the length (l) of the cell, etc. This dependency can be written as [1, 4, 153],

$$\Sigma \propto \frac{I_p^2}{\delta_p^2}\left(\frac{n_0 l}{A}\right). \tag{3.4}$$

The details of the theoretical description of the SNS are discussed in [153, 171]. The theoretical derivation for spin noise in an atomic system is discussed in chapter 5 using master equations of the density matrix correlations between the Zeeman states manifolds. The integrated SN power Σ becomes asymmetric over δ_p for $\delta_p \approx 0$ due to the non-vanishing coherences between the ground and excited state hyperfine levels of the atoms [158]. This asymmetry in Σ is shown later in this chapter and discussed in detail. The asymmetry in Σ also depends on the homogeneous and inhomogeneous broadening present in the medium [158, 187] and discussed in chapter 4.

Note that, the various measurements shown throughout this thesis are performed using the light intensity noise (LIN) based SNS technique. We have performed and shown the temporal two-point correlation of the spontaneously fluctuating transverse magnetization ($M_x(t)$) of a spin system in various temperatures.

3.2 Experimental set-up for LIN based SNS technique

The schematic of the experimental set-up for intrinsic SN measurements of thermal rubidium atoms in equilibrium is shown in Fig. 3.2.

The probe beam. A linearly polarized probe laser beam (red trace) with tunable frequency ν_p is sent through a 20 mm long quartz cell containing enriched ^{87}Rb vapor. This probe beam is derived from a grating stabilized external cavity diode laser (ECDL) in Littrow configuration having an instantaneous linewidth better than 500 kHz (refer to Fig. 3.4 (a)). The probe beam with a Gaussian profile is focused inside the atomic vapor to a $1/e^2$ waist size of $\sim$ 50 μm at the focal plane and a Rayleigh range of 4 mm. In order to study the dependence of the SN spectra on the probe beam detuning δ_p, the probe frequency ν_p is varied over a large range of frequencies ($\sim$ 40 GHz). The relevant energy-levels of ^{87}Rb are depicted in Fig. 3.3. The detuning of the probe laser beam for addressing ^{87}Rb atom is defined as $\delta_p = \nu_p - \nu_{F=2\rightarrow F'=3}$, where $\nu_{F=2\rightarrow F'=3}$ is the frequency between $F = 2$ and $F' = 3$ hyperfine transition line. We have used the feed-orward mechanism to operate the laser in a mode-hop free regime. The frequency ν_p of the probe beam is measured using a commercial wavelength meter (HighFinesse,

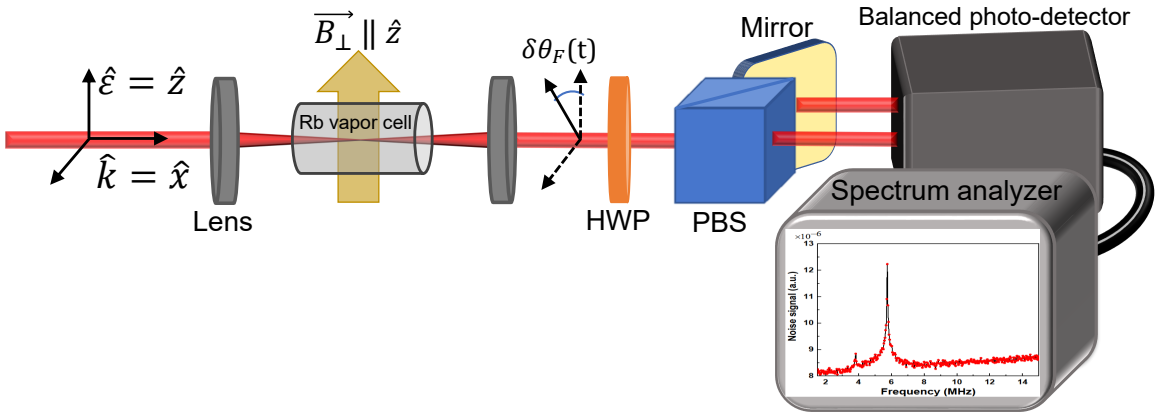

Figure 3.2: Schematic of the experimental set-up for measuring spin noise (SN) spectrum. A linearly polarized probe laser beam along $\hat{x}$ is focused by a plano-convex lens of focal length 20 cm before entering the vapor cell. The transmitted probe beam is sent through a polarimetric set-up comprising of a half-wave plate (HWP) and a polarizing beam splitter (PBS), and then it is collected by a balanced photo-detector which is connected to a swept-frequency spectrum analyzer (SFSA). A constant magnetic field $B_\perp$ along $\hat{z}$ is applied on the atomic vapor using two magnetic coils in Helmholtz configuration.

model-WSU2) with a relative accuracy of $\pm$ 1 MHz. The plane of polarization of the probe beam before the glass cell is controlled using a half-wave plate (HWP) and a polarizing beam splitter (PBS). We have managed to get the linear polarization quality of the probe beam better than 99%.

We have measured the linewidth of the probe laser beam by beating it with another laser beam generated from an independent ECDL source. We have taken an interferometry approach where the probe laser beam and a reference laser beam overlapped on a non-polarising beam splitter (NPBS). One of the outputs from NPBS is fed to a fast photo-detector, and observed a temporal interference pattern on the oscilloscope at the difference of the two laser frequencies (355 MHz). For the linewidth measurement of the probe laser, we have connected the output of the photo-detector to a swept frequency spectrum analyzer (SFSA) to investigate the spectral properties of the interfering beat signal. The spectrum of the beat signal is shown in Fig. 3.4 (a). The spectral width of the signal is $\sim$ 500 kHz, which infer that the linewidth of the probe laser beam is below 500 kHz. Another parameter of the probe laser beam which plays an important role in the measurement is the cross-sectional area at the center of the glass cell. As shown in Eq. 3.4, the total integrated noise power depends inversely on the probe laser cross-sectional area. Therefore, we tightly focus the probe beam at the center of the vapor cell to collect the SN signal with good SNR when the other

experimental parameters are fixed. To do such beam shaping of the probe laser, we first expand the beam using a telescope (the plano-convex lens pairs are: $f_1 = 5$ cm and $f_2 = 15$ cm) to generate a collimated beam with diameter 3 times larger than the initial beam (initial beam diameter ~ 1.3 mm). Thereafter, the expanded beam is sent through a plano-convex lens with a focal length of 20 cm, which generates the tightly focused beam at the center of the glass cell as mentioned earlier.

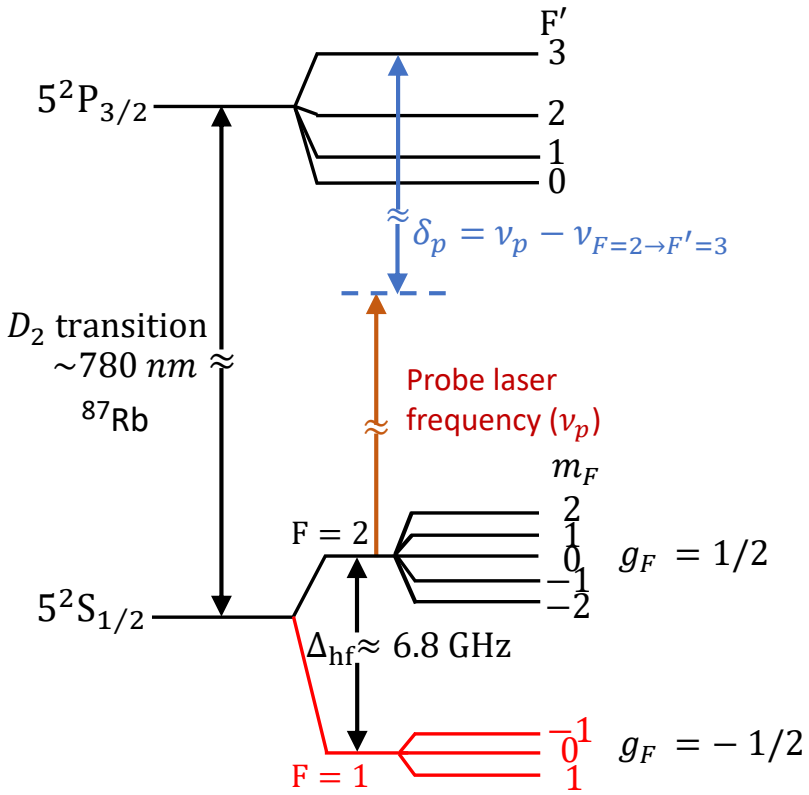

Figure 3.3: The relevant energy level diagram for D_2 transition ($5^2S_{1/2} \leftrightarrow 5^2P_{3/2}$ at 780 nm) of ^{87}Rb atoms and the frequency of probe laser beam. The two ground hyperfine levels ($F = 1$ and $F = 2$) are separated by ~ 6.8 GHz. The probe laser frequency ν_p is detuned by δ_p from the $F = 2 \rightarrow F' = 3$ transition, i.e., $\delta_p = \nu_p - \nu_{F=2\rightarrow F'=3}$, where $\nu_{F=2\rightarrow F'=3}$ is the frequency between $F = 2$ and $F' = 3$ hyperfine levels. The $g-$factors of the two ground hyperfine levels are also indicated. The Zeeman states of the ground hyperfine levels in the presence of external magnetic field are depicted.

The vapor cell. The quartz cell is filled with neon buffer gas along with enriched ^{87}Rb atoms at a pressure of 200 millibar in order to make the medium diffusive for Rb atoms. The inner surface of the cell is bare and anti-relaxation coating-free. The neon gas increases the transverse transit time of the atoms across the probe beam from

$\sim$ 200 ns to $\sim$ 100 μs providing sufficient time for acquiring time-resolved Faraday rotation signal for the accurate detection of the atomic properties. We collect each real-time Faraday rotation signal for a relatively long time duration compared to the transit time. The spin lifetime or coherence time of Rb atoms at room temperature [188] is longer than the transverse transit time ($\sim$ 100 μs). The inert gas neon is chosen because the collisions between Rb and neon do not change the spin state of the Rb atoms in the ground hyperfine levels. However, the presence of the buffer gas modifies the linewidth of the excited hyperfine levels via electromagnetic interaction. Buffer gas broadens the linewidth and shifts the level of the excited hyperfine levels. The nature of the broadening of the excited levels is the same for all the atoms in the cell irrespective of their velocity. This buffer gas-induced broadening of the excited level linewidth is known as pressure broadening and it is homogeneous in nature. This pressure broadening has various consequences in the measurements which will be discussed later in chapter 4.

We have heated the vapor cell during the experiment to increase the number density of the atoms. In order to study the dependence of the SN signal (see Eq. 3.4) and the effective transverse spin relaxation time (T_2^*) with various densities (i.e. temperature of the cell) of the atomic spins, one needs to vary the temperature of the cell in a controllable manner. To heat the quartz cell, we have made a 5 mm thick aluminium jacket and the vapor cell is inserted within it. We kept a 3 mm diameter circular opening on both sides of the jacket to pass the laser beams. The outer surface of the jacket is wrapped with a heating tape that is connected to the heating controller (OMRON, Model no. - E5CN-R2MT-500). We directly heat the aluminium jacket which passively heats the glass cell and controls the temperature of the atomic system. The typical time taken for the heating controller to reach a steady-state temperature is around 20-30 minutes and the temperature stability is $\pm$1.5°C.

The homogeneous magnetic field. The atoms are subjected to a uniform, constant magnetic field ($B_\perp \hat{z}$) orthogonal to the direction of propagation of the probe beam ($\hat{x}$) during the experiments. The magnetic field is generated using a pair of circular coils (both have several layers and several turns with a diameter of 17.6 cm) in the Helmholtz configuration. The generated magnetic field is uniform along the length of the cell within $\pm$0.4% as shown in Fig. 3.4 (b). The magnetic coils are connected to an Agilent power supply with current stability of better than 10 mA. The vapor cell and the magnetic coils are shielded with a mild-steel box ($\mu/\mu_0 = 2000$) to avoid any unwanted stray magnetic field, and undesirable frequency noise coming from other laboratory instruments.

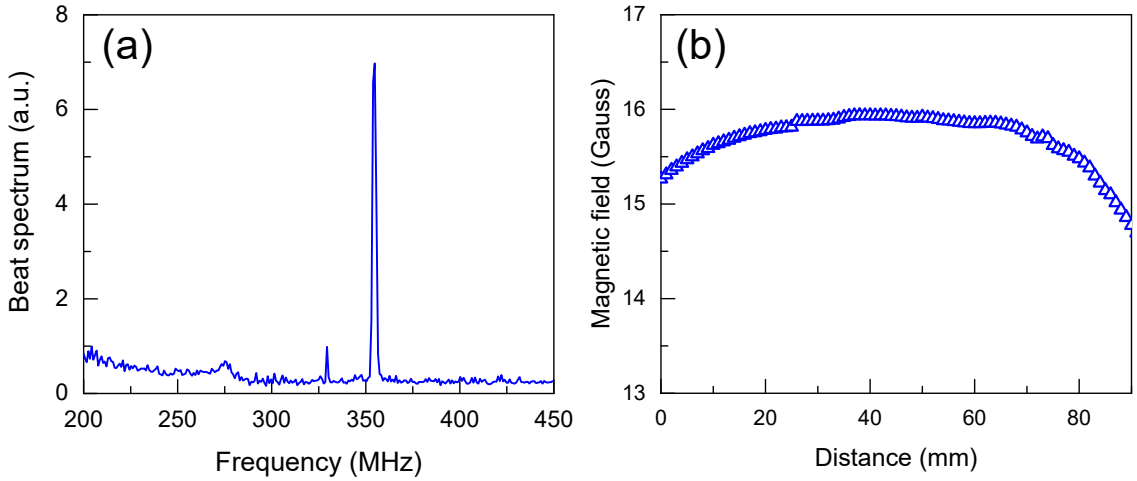

Figure 3.4: (a) Measurement of the laser line-width of the probe beam using the beat signal. We beat the probe laser beam with another external cavity diode laser (ECDL) beam on a non-polarising beam splitter (NPBS), and measure the spectrum of the beat in SA using high bandwidth photo-detector (PDA10A2, Thorlabs). The instantaneous (maximum) measured line-width of the ECDL beam is to be about 500 kHz. (b) The measured radial magnetic field profile of the Helmholtz coil using Hall probe magnetometer along the probe beam propagation direction. The 2 cm long Rb vapor cell is placed near the region of uniform magnetic field distribution.

The polarimetric set-up. The focused probe beam after passing through the glass cell is first collimated using a 20 cm long focal length plano-convex lens and then separated into $s-$ and $p-$polarized components using a polarization-sensitive set-up as shown in Fig. 3.2(a). The polarimetric set-up consists of an HWP and a PBS.

The detection set-up. The detection set-up comprises of a balanced photodetector (Newport model no. 1807-FS) and an SFSA (Agilent CSA Spectrum Analyzer Model no. N1996A, frequency range 100 kHz - 3 GHz). The two light components coming out from the polarimetric set-up are fed into the two ports of the balanced photo-detector which has a 3 dB bandwidth of 80 MHz and a good common-mode rejection ratio of 25 dB. The output of the balanced detector is directly connected to the SFSA whose resolution bandwidth (RBW) is adjusted between 100 Hz to 1 kHz. The spectrum analyzer was set on continuous averaging mode for one to three minutes for recording various SN spectra presented in this thesis. We have aligned the HWP of the polarimetric set-up by making the photo-current generated by the balanced photo-detector zero on the oscilloscope screen.

A general remark is that in this technique the separated probe beam after the polarimetric set-up first falls on the balanced photo-detector and generates a photo-

current in its electronic channel. In this process, the information of the electric field of the probe beam vanishes. However, the atomic properties that modify the polarization angle of the probe beam are only retained. Therefore, this technique can be called as detection of SNS using LIN-based spectroscopy.

3.3 The intrinsic spin noise (SN) signal

We have discussed earlier that the experimentally measured Faraday rotation angle ($\theta_F(t)$) is the measure to the instantaneous magnetization ($M_x(t)$) of the spin system along the probe beam propagation direction ($\hat{x}$). In the steady state of the system, the temporal auto-correlation function of $M_x(t)$ (i.e. $\langle M_x(t_1)M_x(t_2)\rangle$) depends on the difference of the two-time arguments ($t_1 - t_2$), and not their actual time stamps. This is because of the translational invariance symmetry of time. The auto-correlation function of this quantity can therefore be written as $\langle M_x(t)M_x(0)\rangle$, where we can fix the initial time argument as $t_2 = 0$, and $t = t_1 - t_2$ which in turn is proportional to the measured $\langle\theta_F(t)\theta_F(0)\rangle$.

In the experiment, during the recording of $M_x(t)$, the time steps (t) of the detection set-up should be much smaller than the characteristic relaxation time (in this case T_2, without in-homogeneous broadening) of the spin system, i.e., $t \ll T_2$. Another important timescale is the total length of the measurement time (T_m) which should be much longer than the T_2, i.e., $T_m \gg T_2$ to collect the complete trajectory of $M_x(t)$. Further averaging with repetitive measurements with large time scale T_m will increase further precision in the measurements of $\langle M_x(t)M_x(0)\rangle$. However, let us consider there are total N_m number of measurement data points within the single data collection time of T_m. Then it can be shown that the measurement of auto-correlation of $M_x(t)$ will require the calculation of $\sim N_m^2$ number of products of the auto-correlation function [3]. The most conventional and widely used approach is processing the data using the fast Fourier transform (FFT) and looking into its spectrum (i.e. Eq. 3.2). For the same number of data points N_m within the measurement duration of T_m, the typical FFT algorithm will require $\sim N_m \log(N_m)$ steps to perform, which is much lower than the N_m^2.

Therefore the measurement of the spectrum for spontaneous magnetization (noise) of the spin system along the probe beam direction is most convenient and useful, and the signal in the frequency domain provides valuable information about the physical parameters of the spin system. The balanced photo-detector and the SFSA used in the measurement of the SN spectrum of an "atomic spin system" satisfies the requirements mentioned above. A typical SN amplitude ($\sqrt{P(\nu > 0)}$) spectrum of Rb atoms in

thermal equilibrium at relatively low strength of the magnetic field $B_\perp$ (= 6.95 G) is presented in Fig. 3.5.

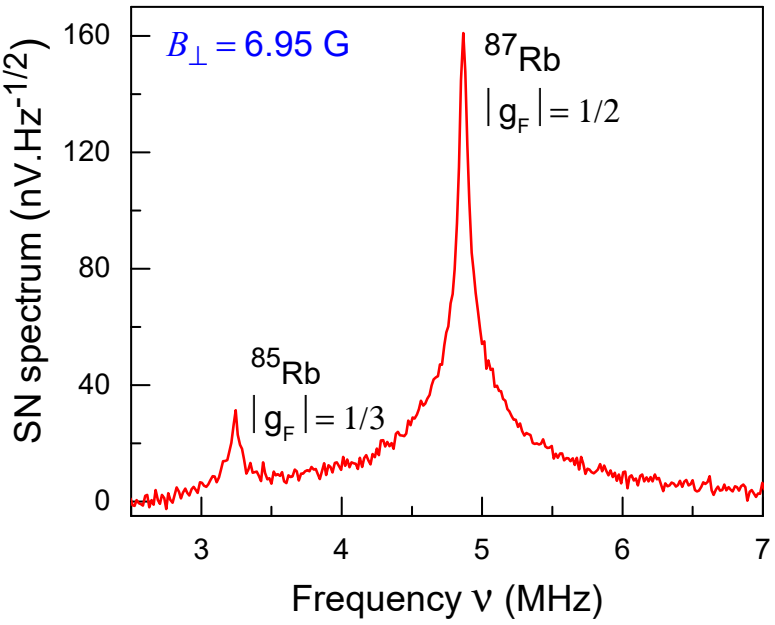

Figure 3.5: A typical SN amplitude spectrum at $B_\perp = 6.95$ G and vapor cell temperature of 105°C is shown for a probe beam detuning of $\delta_p = -10.2$ GHz. The stronger and weaker peaks are identified with ^{87}Rb ($|g_F| = 1/2$) and ^{85}Rb ($|g_F| = 1/3$), respectively.

This signal is obtained at vapor cell temperature of around 105°C with the atom density for ^{87}Rb is $(4.6 \pm 0.3) \times 10^{12}/\text{cm}^3$. The input probe beam is p-polarized ($\hat{\varepsilon} \parallel \hat{z}$) with total power of 600 μW. The probe beam is red-detuned by 10.2 GHz with respect to the D_2 transition (at $\sim$ 780 nm) of ^{87}Rb, $F = 2 \rightarrow F' = 3$. The detuning of the probe beam in the range of GHz frequency is achieved by tuning the laser current and the voltage on the piezo transducer attached to the grating in the ECDL. The absolute laser frequency is measured using a high-resolution wavelength meter (HighFinesse, model-WSU2) which has a frequency measurement accuracy of 1 MHz. First we locked the laser on the line $F = 2 \rightarrow F' = 3$ transition and noted down the laser frequency on the wavelength meter (384.228400 THz). Then we unlock the laser and adjust the current and piezo offset to move the laser frequency (for example, 384.218200 THz) to get the 10.2 GHz red detuned probe beam. While scanning the laser frequency, we continuously monitor the frequency of the laser in the wavelength meter. Two distinct noise peaks, one at 3.24 MHz and another at 4.87 MHz, are observed and identified as arising due to spin fluctuations among the intra-hyperfine Zeeman states ($\triangle F = 0$, $\triangle m_F = \pm 1$) of ^{85}Rb and ^{87}Rb, respectively. Note that, we have a glass cell filled with isotopically enriched ^{87}Rb atoms. However, there is a small contamination

($\sim 9\%$) of ^{85}Rb isotopes present in the cell along with the ^{87}Rb. Therefore the signal for ^{85}Rb is coming due to this contamination from the cell. The photon shot noise background of ~ 350 nV.Hz$^{-1/2}$ is subtracted from the noise spectrum. The photon shot noise is measured by removing the vapor cell from the set-up. We performed the measurement starting from 2 MHz to avoid the low-frequency electronic contribution in the photon shot noise. With our detection setup, we checked that the photon shot noise is broadband and flat after 1 MHz. The observed SN peaks are narrow ($\gamma' \sim 100$ kHz) compared to the excited hyperfine linewidth ($\gamma \sim 6$ MHz) and the peak positions (which occur at the ν_L) can be detected with a precision of ~ 1 part in 10^5. This makes it possible to employ SNS for a variety of precision measurements as we demonstrate in the subsequent chapters. Since the magnetic field is orthogonal to the probe laser propagation direction, the optical field effectively couples to the magnetization operator of the spin system with the selection rule of $\triangle m_F = \pm 1$, where m_F is the projection of the Zeeman states along the magnetic field direction.

The SN amplitude spectrum for the ^{85}Rb atoms are detected by the probe laser beam with different detuning ($\delta_p \sim -11.3$ GHz from $5^2S_{1/2}, F = 3 \rightarrow 5^2P_{3/2}, F = 4$ transition) that has been mentioned above. The relevant energy level diagram for ^{85}Rb atoms are presented in chapter 2. The SN signal corresponds to ^{87}Rb (^{85}Rb) are the contributions of a total six (ten) Zeeman coherence signal as can be seen by the Zeeman states of the ground hyperfine levels presented in Fig. 3.3. Since in this low magnetic field (= 6.95 G) the Zeeman energy separation between the consecutive states is similar, they all appear at the same frequency.

Note that the intrinsic SN spectrum corresponds to inter-hyperfine spin fluctuations ($\triangle F = 1$, $\triangle m_F = \pm 1$) of Rb atoms appear near the frequency of the ground hyperfine level separation for the corresponding atoms (~ 6.8 GHz for ^{87}Rb, and ~ 3.0 GHz for ^{85}Rb).

3.4 Units for the SN spectrum

We have presented the amplitude spectrum of the spin noise in Fig. 3.5, which is the square root of the power spectrum ($\sqrt{P(\nu > 0)}$) as shown in Eq. (3.2). According to the Eq. (3.2), the unit for the power spectrum ($P(\nu)$) is proportional to the second. However, here we clarify the fact that the experimentally measured power spectrum of the probe laser's Faraday rotation fluctuations is proportional to $P(\nu)$, and the proportionality constant (with a unit) depends on the atom-probe laser coupling parameters (e.g., probe intensity, probe detuning, oscillator strength, and so on). In the experiments, first, the optical field of the probe laser generates a photo-current in the balance

photo-detector. Thereafter, the generated photo-current produces a voltage through a transimpedance amplifier which is recorded in an SFSA. Therefore, the unit of the power spectral density is V^2/Hz. The SFSA has an input impedance of 50 ohm. If we divide the signal recorded in the SFSA by the load resistance (R = 50 ohm), then the unit of power spectral density becomes Watts/Hz (according to the relation: power = voltage^2/R).

Therefore, the unit for the power spectrum is W/Hz (or V^2/Hz) and the unit for the amplitude spectrum is $V/Hz^{-1/2}$, which are the two complementary representations of the unit for the spectrum. In this thesis, we will alternatively use both the units for the spectrum to represent the signal as well as to characterize and extract various atomic, nuclear, magnetic, and chemical parameters. A discussion regarding the usage of the units is discussed in Appendix E.

3.5 Characterization of the SN signal

In this section, we will discuss the SN spectrum and its dependence on various experimental parameters. We have studied the integrated SN power (in Watts unit) or amplitude (in Volts unit) as a function of various probe beam parameters (such as power, detuning, etc), the polarization state of the probe beam, magnetic field orientations, atom density, etc. We have also studied the FWHM of the SN signal as a function of those parameters. Before proceeding to these discussions, we will first present the SN signal where the atomic spins are subjected to in-homogeneous and laboratory stray magnetic fields.

3.5.1 SN spectrum with in-homogeneous and stray magnetic fields

The SN signal shown in Fig. 3.5 has been taken in presence of a uniform and homogeneous magnetic field. The square of the signal (i.e. $P(\nu)$) is Lorentzian and can be fitted with Eq. (3.2). However, the homogeneous magnetic field does not play any role in the spin-relaxation process by flipping the spins, or by spatially varying Larmor frequency.

SN spectrum in presence of in-homogeneous magnetic fields. When the atoms are placed in an in-homogeneous magnetic field produced by a pair of magnetic coils in anti-Helmholtz configuration, the recorded SN spectrum looks asymmetric as shown in Fig. 3.6 (a). The reason for this asymmetric nature of the SN signal is the magnetic

field variations (both magnitude and orientation). In this case, the atoms within the probe beam in a different position will precess about the local magnetic fields, which vary both in magnitude and orientation over space and give rise to different contributions in the spectrum at different frequencies. The details of this configuration and the detected SN signal from an ensemble of a cold Rb atomic cloud (T $\sim 150\mu$K) are presented in chapter 8.

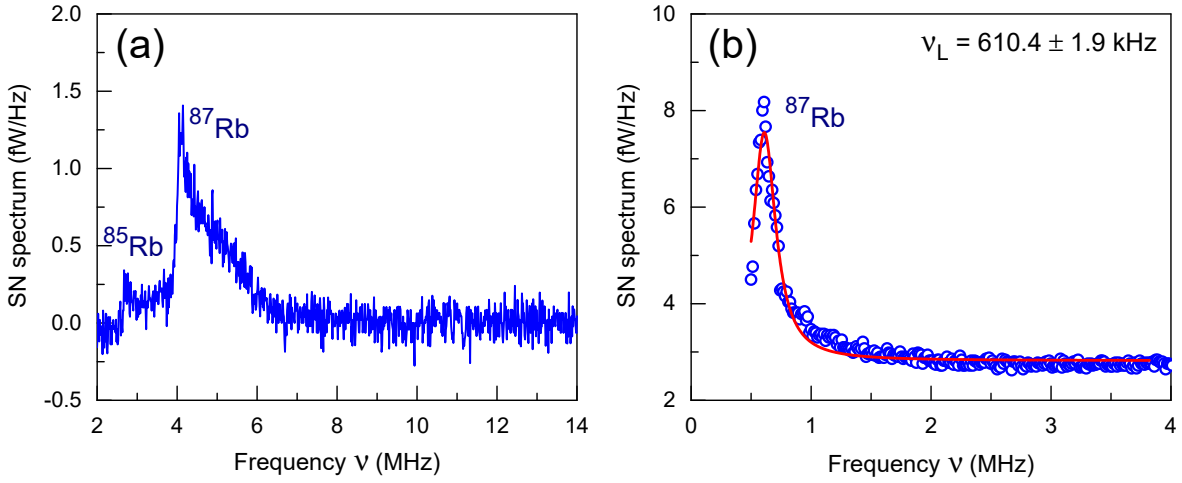

Figure 3.6: (a) The intrinsic spin noise (SN) spectrum in the anti-Helmholtz configuration of the current carrying coils. The probe beam was sent through 8 mm away from the centre of the two coils. The asymmetric nature of the SN spectrum signifies the variations of the magnetic field orientation and strength along the probe beam, and discussed in details in the text and in chapter 7. Total probe beam power = 500 μW, $\delta_p = -6.6$ GHz, cell temperature = 110°C, coil current = 2.9 A, and the data acquisition time is about 1 minute. (b) The SN spectrum at null coil currents. The cell was exposed to the earth magnetic field and the ambient magnetic field present in the laboratory due to various magnetic material on the optical table. The measured residual magnetic field near the focal point of probe beam is about 870 mG when the magnetic coils are switched off.

SN spectrum in presence of stray magnetic fields. The SN spectrum in the laboratory magnetic field around the atomic sample is presented in Fig. 3.6 (b). From the value of the peak position of the signal, one can measure precisely the ambient magnetic field (which includes the geomagnetic fields as well as other open sources in the laboratory which produce magnetic fields) near the atomic sample which is around 870 mG. Note that, for this measurement, we have removed the mild-steel box from the set-up. The red trace is the Lorentzian fit to the data.

3.5.2 SN signal strength with temperature

The raw SN spectrum of ^{87}Rb atoms at different temperatures of the vapor cell is presented in Fig. 3.7. During the experiments, we have kept all the other parameters fixed and varied only the temperature of the cell to collect the SN signal with different atom densities of Rb atoms.

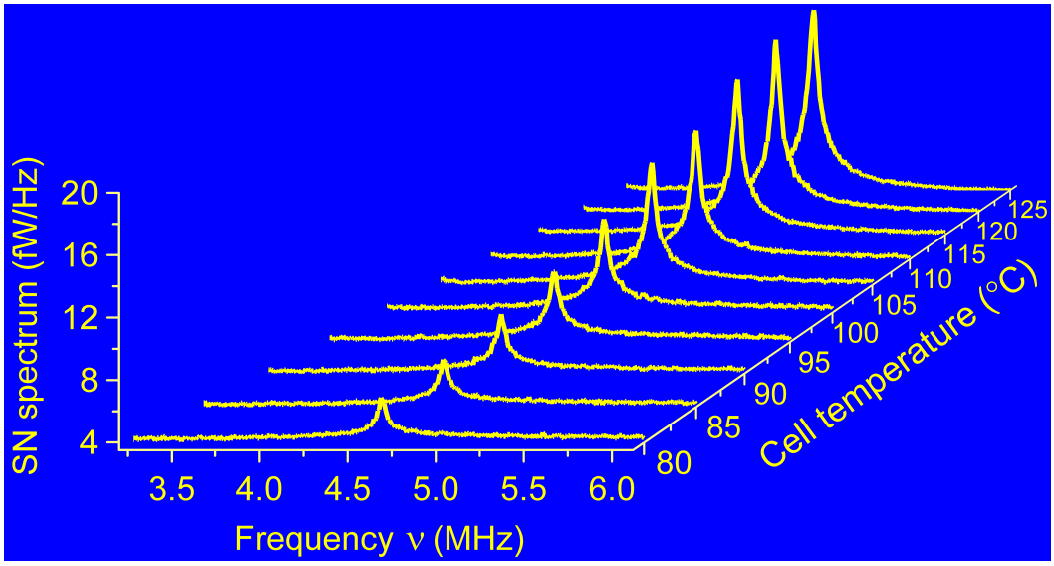

Figure 3.7: Raw spin noise (SN) spectrum of ^{87}Rb atoms at various temperature of the vapor cell. The ^{87}Rb atom density inside the probe beam volume increases with increasing the temperature of the cell. The strength as well as the FWHM of the SN signal increases with increasing the atom density within the cell and discussed in details Fig. 3.8 and in the text. Probe beam detuning $\delta_p = -8$ GHz, total probe beam power = 600 μW, and $B_\perp = 6.6$ G. The data acquisition time for individual spectrum is about 45 sec.

In the room temperature, the ^{87}Rb atom appears as a solid phase. We have heated the cell far above the melting point of the ^{87}Rb atoms (39.31°C [189]) into its vapor phase to perform the experiment. The partial vapor pressure of the ^{87}Rb atoms in the solid phase varies with temperature as [22, 190],

$$\log_{10} P_v = -94.04826 - \frac{1961.258}{T} - 0.03771687T + 42.57526 \log_{10} T, \tag{3.5}$$

where P_v is the partial pressure in Torr and T is the temperature in Kelvin. According to the ideal gas equation ($PV = nRT$, where P is the partial pressure, V is the volume of the container, n is the total number of atoms, and R is the ideal gas constant), and Eq. 3.5, the density of ^{87}Rb atoms inside the cell increases with temperature. The strength of the SN signal is enhanced with temperature as shown in Fig. 3.7, since

more number of atoms are participating in building up the signal.

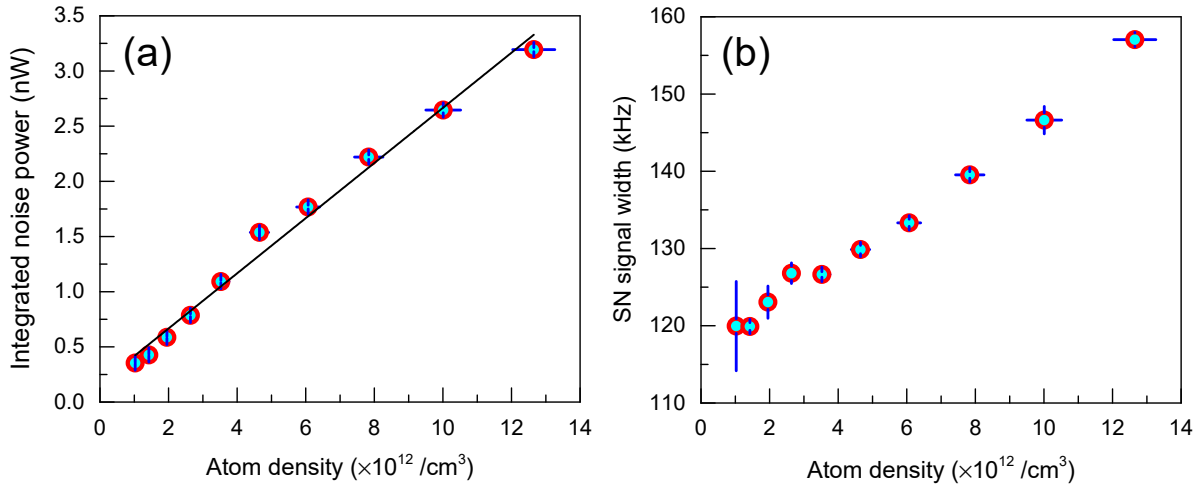

Figure 3.8: The integrated noise power (a) and the FWHM (b) of the intrinsic spin noise (SN) spectrum for various atom density inside the cell. (a) The noise power depends linearly with the atom density in the cell as expected from theory. (b) The FWHM increases with atom density in a linear fashion signifies the reduction of the coherence time (T_2) with increasing atom density. We have analyzed these observations from the raw spectrum presented in Fig. 3.7.

Fig. 3.8 (a) shows the dependence of Σ for ^{87}Rb atoms as a function of n. We have calculated the atom density inside the cell using the ideal gas equation and the temperature dependence of the vapor pressure equation shown in Eq. 3.5. The Σ presented in Fig. 3.8 (a) at each atom density is averaged over three independent measurements of the SN signal. We have observed linear dependence of Σ with atom density (n) as predicted by the theory in Eq. 3.4. The black solid line is the linear fit to those data points. Note that, we calculate the error in atom density using Eq. 3.5 by considering the temperature variations during the measurements.

Furthermore, we have investigated the Lorentzian FWHM of the SN power spectrum as a function of n in Fig. 3.8 (b). We have observed the FWHM of the measured SN signal increases with the temperature (or n) of the cell. This infers that the transverse spin-coherence time (T_2) is reduced with the atom density. As the temperature of the cell increases, more and more atoms gather together and the (two-body) collision rates enhance. Such collisions include hyperfine spin-exchange collision which is the most dominating, the spin-destruction collision with similar or other atomic species present in the system, and collision with the container wall. These all processes perturb the free evolution of the spontaneous transverse magnetization and reduce the coherence time. Apart from such collisions, the transit time of the moving atoms across the probe

beam also reduces with temperature. This effect can also broaden the line-width of the SN signal significantly.

3.5.3 SN signal strength with probe power

In this section, we demonstrate the integrated SN signal amplitude as a function of total probe beam power (I_p) with different value of detuning (δ_p) of the probe laser. Here the total power of the probe beam signifies the addition of the power of the two output laser beams ($s-$ and $p-$polarized) from the polarimetric set-up. As we have mentioned before the SNS can act as a relatively non-invasive detection technique if the photon scattering rate by the atoms is negligibly small. Both the photon scattering rate ($\propto I_p/\delta_p^2$) and the SN amplitude ($\propto I_p/|\delta_p|$) depend on the intensity and detuning of the probe beam. Therefore, the polarization fluctuation of a probe beam can reveal the intrinsic spin noise of a sample at thermal equilibrium only for a large detuning and a relatively low power of the probe beam.

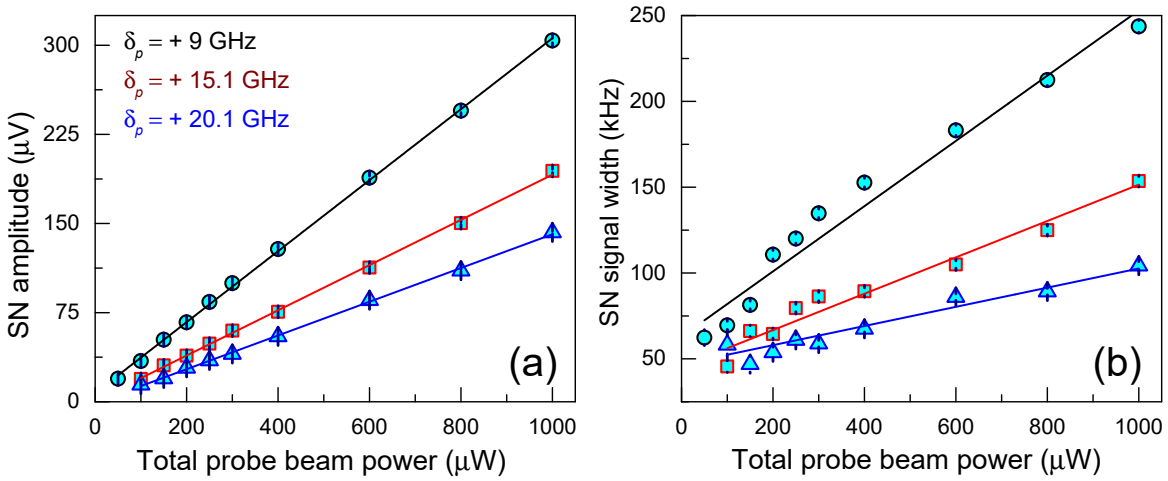

Figure 3.9: The integrated spin noise (SN) amplitude (a) and the FWHM (b) of the spectrum with the total probe beam power. The data has taken with three different detunings of the probe beam. The cell temperature (90°C) and $B_\perp = 4.6$ G were kept fixed during the measurements.

In order to explicitly measure the polarization fluctuation due to spin noise, the photon scattering rate due to the probe laser has to be minimized. It is true that for large detuning and low probe beam power the strength of the intrinsic SN signal is small. On the other hand, the photon scattering rate also goes down with detuning and intensity. Since the light scattering is proportional to the I_p/δ_p^2 and SN amplitude is proportional to $I_p/|\delta_p|$, for large detuning δ_p of the probe beam, the light scattering

falls rapidly, while keeping appreciable amount of detectable SN signal. Even in the case of large detuning, we observed an appreciable increase of the SN signal width with intensity of the probe beam. Therefore, to probe the SN signal intrinsically, probe beam power needs to keep low. The "intrinsic" SN signal can be detected in a better way in this near-nonperturbative regime of the probe beam parameters. Under this condition, the strength of the intrinsic SN signal can be enhanced by increasing the atom density. Therefore, experimentally, we need to play with the various parameters (such as probe beam diameter and power, atom density, probe beam detuning, and length of the sample) to find the "sweet-spot" parameter space that provides an appreciable amount of spin noise, with negligible perturbation to the spin system due to the probe beam.

Fig. 3.9 (a) shows the dependence of $\sqrt{\Sigma}$ as a function of the total probe beam power at a cell temperature of 90°C. We have repeated the data for three different detunings of the probe beam such as $\delta_p = +9$ GHz (black circles), + 15.1 GHz (red squares), and + 20.1 GHz (blue triangles). The solid lines are the linear fits to these data points. According to the Eq. 3.4, we have verified the linear dependence of the integrated SN amplitude with probe beam power.

The FWHM of the intrinsic SN power spectrum fitted with Lorentzian function as a function of probe beam power is presented in Fig. 3.9 (b) for these three detunings. Here the solid lines are the fits to the data points with a linear function. Apart from the basic spectral broadening mechanisms of the SN signal discussed in the last section, the spontaneous magnetization of the atomic system can also be perturbed by the optical scattering of the probe beam and broadens the signal. Fig. 3.9 (b) shows that for higher power and lower detuning of the probe beam, the atomic system is heavily perturbed by the optical scattering which contributes significantly to broadening the spectral width of the SN signal. However, for lower power and higher detuning of the probe beam, the optical scattering by the atom reduces significantly and probe the spontaneous evolution of macroscopic magnetization of the system nearly non-invasive way.

3.5.4 SN signal strength with probe detuning

Next we have investigated the dependence of SN spectrum with probe beam detuning of a wide range in both red and blue side from the resonance. Fig. 3.10 (a) shows the dependence of $\sqrt{\Sigma}$ in terms of δ_p of two different probe beam power.

We have observed a dependence of $|\delta_p|^{-1}$ in the measured $\sqrt{\Sigma}$ away from the resonance line $F = 2 \rightarrow F' = 3$ on D_2-line of ^{87}Rb atom ($|\delta_p| > 10$ GHz). This observation verifies the relation shown in Eq. 3.4. However, the SN amplitude $\sqrt{\Sigma}$ is not symmetric

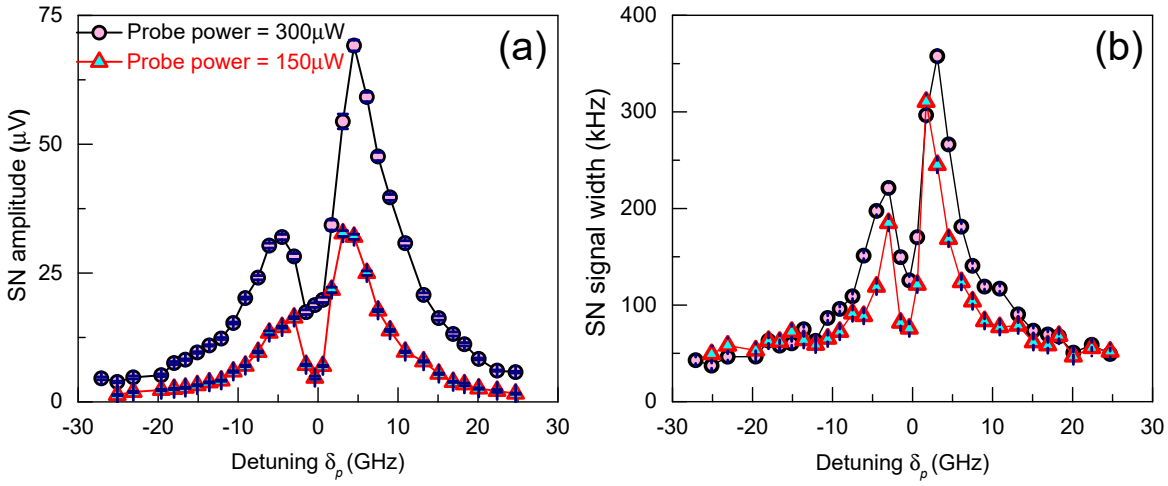

Figure 3.10: The dependence of the integrated spin noise (SN) amplitude (a) and the FWHM (b) of the intrinsic SN spectrum with the probe beam detuning (δ_p). For each measurements, the cell temperature and $B_\perp$ were kept fixed. (b) The fast decoherence rate near the vicinity of the atomic resonance line implies the effects of the optical excitation on the T_2.

in red and blue detune side near the resonance line. This happens due to the presence of another hyperfine level ($F = 1$) at 6.8 GHz away in the blue side from $F = 2 \rightarrow F' = 3$ line. Therefore, the strength of the measured $\sqrt{\Sigma}$ is higher on the blue side for a similar δ_p in comparison to the red side, since the atoms in both $F = 1$ and $F = 2$ levels are contributed significantly in the blue detune side.

The FWHM of the SN spectrum is presented in Fig. 3.10 (b). Around the vicinity of the resonance line, the Rb atoms are heavily perturbed by the optical scattering and broaden the spectral line-shape of the intrinsic SN signal. However, away from the resonance line, it has been observed that the width of the SN signal does not vary significantly due to the negligible optical scattering by the probe beam.

Whereas the data presented in Fig. 3.9 (a) and Fig. 3.10 (a) establishes the dependence of the measured integrated SN power (refer to Eq. 3.4) on the probe laser parameters, the results presented in Fig. 3.9 (b) and Fig. 3.10 (b) experimentally verifies the operating range of these parameters which makes this detection technique non-invasive in nature. We have seen from Eq. 3.4 that the Σ depends inversely on the probe laser cross-sectional area, A (the relative fluctuations of atom numbers (N) in a paramagnetic system is $\propto \sqrt{N}/N = 1/\sqrt{N}$, which increases with decreasing A). Therefore, in the experiment, the probe laser beam needs to be tightly focused inside the vapor cell to collect the SN signal with good SNR. However, focusing a laser beam tightly makes the intensity of the probe laser significantly huge within the Rayleigh

range. Therefore, the optical scattering is also enhanced. The most realistic experimental set-up for the non-invasive SNS technique is to focus the probe laser beam lightly, keep the detuning far away from the resonance line and perform the experiment with lower power of the probe beam.

3.5.5 SN signal with probe beam polarization angle

We have investigated the intrinsic SN power spectrum with various polarization angle of the incident linearly polarized probe beam. Any linearly polarized incident light is a linear superposition of the left- and right-hand circularly polarized light. Since the SNS technique relies on measuring the noise of the spin system, therefore the measured signal is independent of the polarization angle of the probe beam. The SN spectrum with various planes of polarization (θ) is shown in Fig. 3.11. Here, the angle θ signifies the angle between the plane of electric field oscillation of the probe beam and the applied homogeneous magnetic field. The integrated noise and FWHM of the individual SN signal shown in Fig. 3.11 are independent of θ, as expected.

In our SNS experiment, the measured instantaneous Faraday rotation is proportional to the instantaneous x-projection of the total atomic spins inside the probe beam. The linearly polarized probe beam that is propagating along the x-direction, detects this spin orientation on its polarization plane. The spin orientation changes the circular birefringence of the atomic system that can be detected using a linearly polarized light with a polarization plane oriented at any angle on the y-z plane. Therefore, the SN signal does not change with the polarization angle of the probe beam. Experimentally, to detect the SN spectrum using a probe beam with an arbitrary polarization angle (θ), the plane of the polarimetric set-up needs to be rotated by exactly the same amount.

3.5.6 SN signal in presence of a tilted magnetic field

So far we have demonstrated and characterized the intrinsic SN spectrum in the Voigt geometry where the applied homogeneous magnetic field (along $\hat{z}$) is orthogonal to the measurement axis ($\hat{x}$). However, the characteristic feature of the SN spectrum gets modified when the homogeneous magnetic field is applied at an angle with respect to the measurement axis. The dynamics of the spontaneous magnetization of a spin system about an external magnetic field and its relaxation time (τ_s) can be written

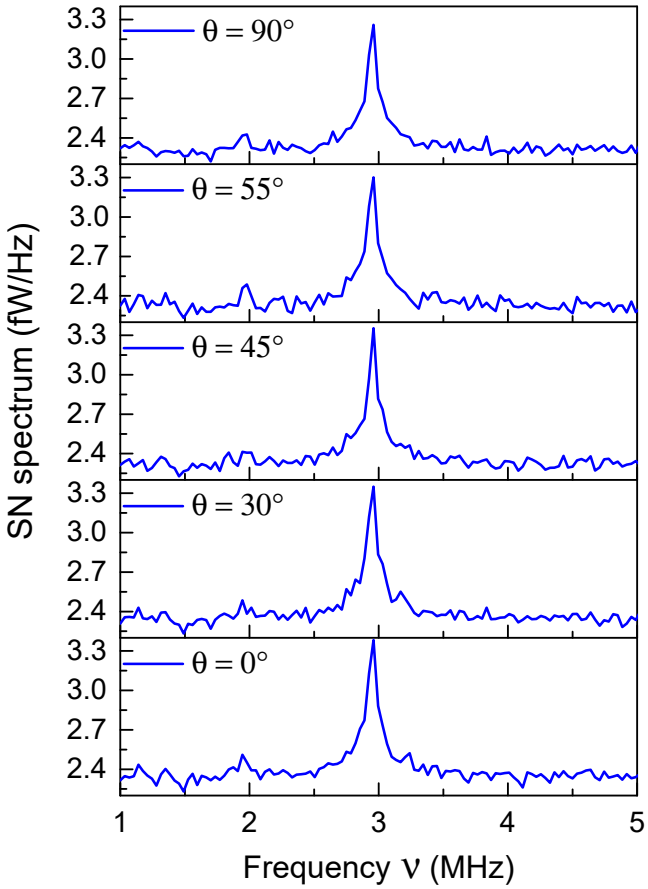

Figure 3.11: The spin noise (SN) spectrum with various combinations of the input linear polarization state of the probe laser beam. Here θ is the angle between the electric field oscillation plane of the probe beam and the applied homogeneous magnetic field. This observations shows that the SN signal strength does not depend on the polarization angle of the linearly polarized probe beam.

according to the Bloch equation as,

$$\frac{d\vec{M}(t)}{dt} = g\vec{M}(t) \times \vec{B} - \frac{\vec{M}(t)}{\tau_s}, \tag{3.6}$$

where g is the electron g-factor of the spin system. Let's now assume an isotropic relaxation rate $(1/\tau_s)$ along all axis of the magnetization, and the homogeneous magnetic field is applied on the $x-z$ plane at an angle θ_B with respect to the measurement axis x (see Fig. 3.14 (b-inset)). Now the solution of Eq. 3.6 for an arbitrary magnetization $(M(t=0) = M_{x0}\hat{x})$ of the spin system emerged at $t = 0$ along the measurement axis have a precession term about the magnetic field and a decaying term which can

be written as [3],

$$M_x(t) = M_{x0}\Big(\cos^2(\theta_B) + \sin^2(\theta_B)\cos^2(\nu_L t)\Big)e^{-t/\tau_s}. \tag{3.7}$$

The power spectrum for $M_x(t)$ can be obtained by doing Fourier transform of the auto-correlation function of Eq. 3.7, and can be written as,

$$P(\nu \geq 0) \propto \Big(\cos^2(\theta_B)\frac{1/\tau_s}{\nu^2 + 1/\tau_s^2} + \sin^2(\theta_B)\frac{1/\tau_s}{(\nu-\nu_L)^2 + 1/\tau_s^2}\Big). \tag{3.8}$$

Eq. 3.8 shows that the SN power spectrum in a tilted magnetic field has two peaks at zero and another at Larmor (ν_L) frequency. The strength of the SN signal appearing at these frequencies depends on the angle θ_B. However, in thermodynamic equilibrium, the total integrated noise of these two SN signals is always conserved. For the two extreme combinations of the magnetic field orientation, i.e. for co-linear magnetic field ($\theta_B = 0°$) the SN signal appears at zero frequency and for the transverse magnetic field ($\theta_B = 90°$) the SN signal appears at Larmor frequency (ν_L).

SN spectrum in presence of both co-linear and orthogonal magnetic fields. Let's consider a situation where a homogeneous co-linear magnetic field (B_x) and a homogeneous orthogonal magnetic field (B_z) is applied simultaneously on the atomic spin system. In this scenario, the total magnetic field is $B(=\sqrt{B_x^2 + B_z^2})$, which makes an angle along the $x-$axis as $\theta_B = \tan^{-1}(B_z/B_x)$. According to the Eq. 3.8, two SN signal will appear in the spectrum: one at zero frequency, and another at Larmor frequency ($\nu_L = g|B|$).

In the experiment, we have kept B_z fixed and varied the magnitude of B_x. We have recorded the intrinsic SN spectrum for each value of B_x and shown the signal at Larmor frequency in Fig. 3.12 with the angle θ_B. As the magnitude of B_x increases (i.e. θ_B decreases), the total magnetic field B also increases which in turn increases the ν_L. Therefore, for the higher value of the B_x (i.e. lower value of the angle θ_B), the SN peaks at ν_L shift towards higher frequency as can be seen in Fig. 3.12. Moreover, the angle θ_B decreases with B_x, which reduces the strength of the SN signal ($\propto \sin^2(\theta_B)$) as B_x increases to the higher values.

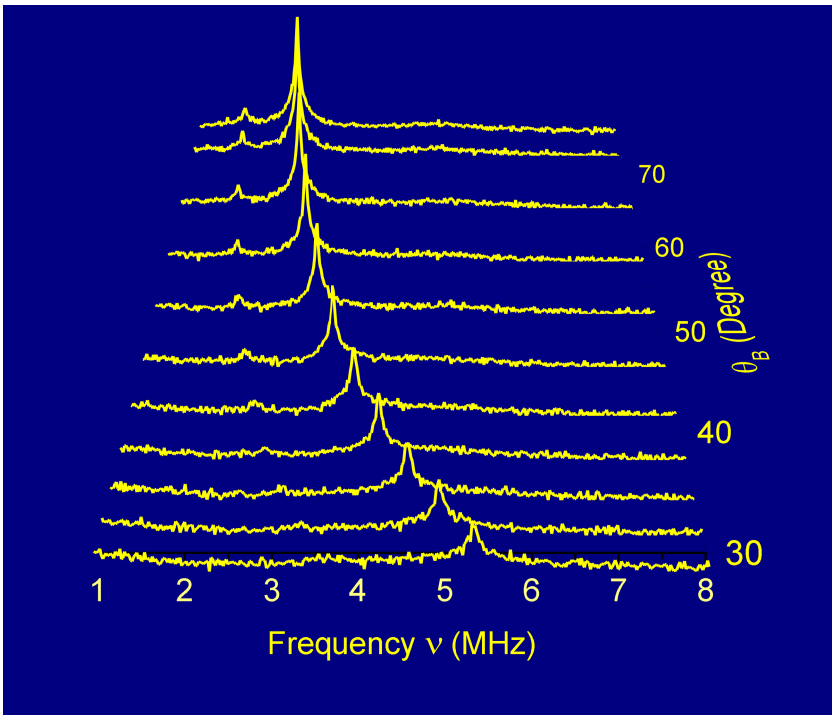

Figure 3.12: The measured spin noise (SN) spectrum in presence of homogeneous transverse and longitudinal magnetic fields. We kept the magnitude of the transverse magnetic field fixed, and vary the strength of the longitudinal magnetic field. Therefore, the total magnetic field, and its' orientation with respect to the light propagation (θ_B) changes for each measurements.

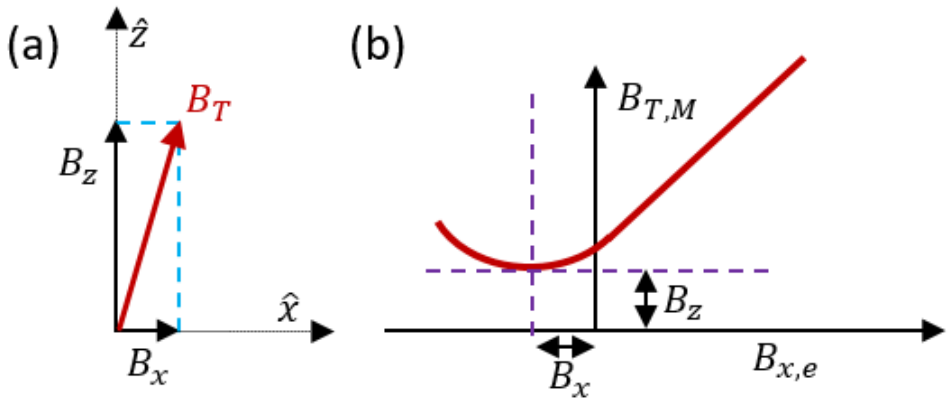

Figure 3.13: The development of precise atomic vector magnetometer. For details, see the discussion in text.

This measurement can find applications in developing the vector magnetometer using SNS technique. The results presented in Fig. 3.12 can precisely measure the strength of the individual components (B_x and B_z) of the total magnetic field (B) applied to the atomic system. Let's consider that the strength and orientation of

magnetic field B_T in a region is unknown, which has two components B_x and B_z as shown in Fig. 3.13 (a). Now to measure the components of B_T, one can apply an additional constant magnetic field ($B_{x,e}$) along the longitudinal direction and perform the experiment as presented in Fig. 3.12. The recorded SN signal with various values of $B_{x,e}$ (both positive and negative direction) gives the measured magnetic field ($B_{T,M}$) which can be written as, $B_{T,M} = \sqrt{B_z^2 + (B_x + B_{x,e})^2}$. The measured $B_{T,M}$ as a function of $B_{x,e}$ has a shape similar to the one shown in Fig. 3.13 (b). From this graph, one can precisely measure the components of the unknown magnetic field, B_T. The minimum value of this curve is a measure of B_z and for which value this minimum is achieved is a measure of B_x with opposite sign. This technique can be applied to measure the 3D orientation of an arbitrary magnetic field also.

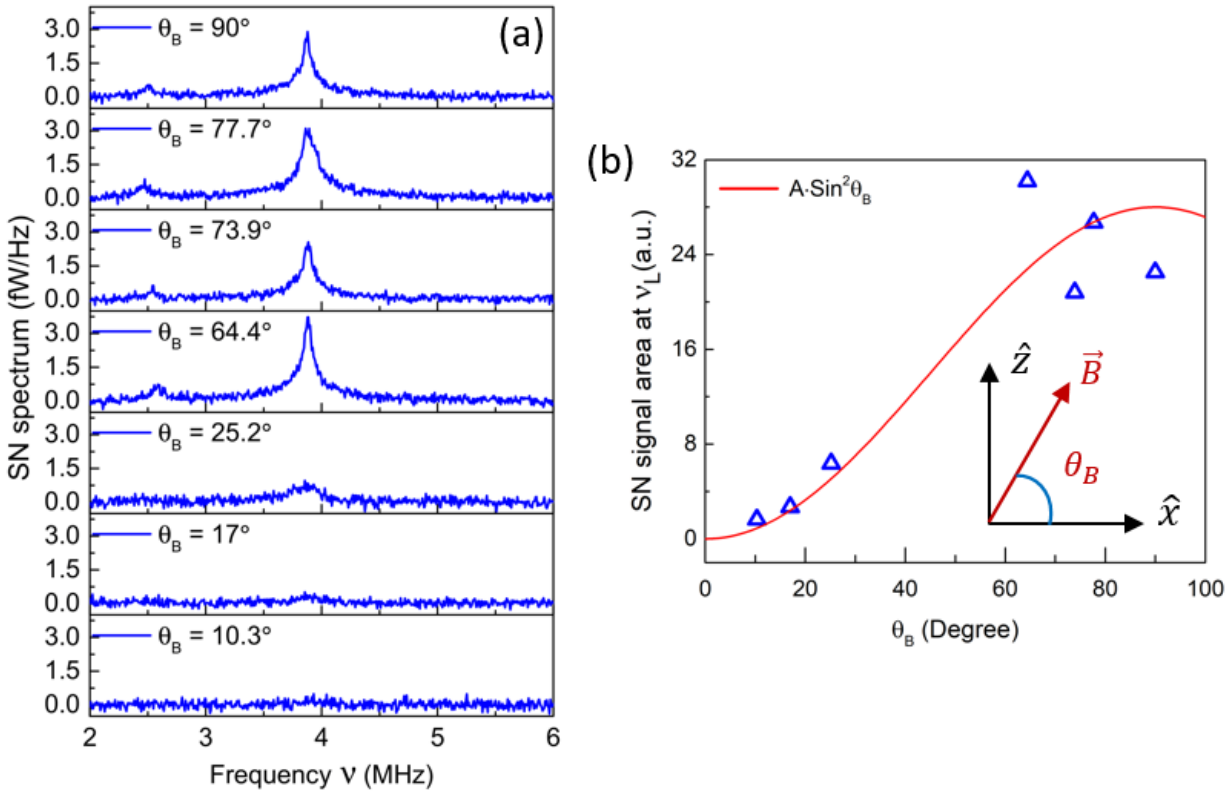

Figure 3.14: (a) The raw spin noise (SN) spectrum in presence of tilted homogeneous magnetic field. Here θ_B is the angle between the magnetic field direction and the probe beam propagation direction. (b) Total integrated noise power as a function of the angle θ_B discussed in Fig. 3.14. The measured data points (blue triangle) follow the $\sin^2(\theta_B)$ behavior as discussed in [3].

SN spectrum in presence of constant tilted magnetic field. Furthermore, we have applied a constant current through the Helmholtz coil to generate a constant

uniform magnetic field and varied the orientation of the coil with respect to the measurement axis to generate a constant tilted magnetic field. In this scenario, the SN signal at ν_L appears at the same frequency for all θ_B. However, the strength of the signal is modified according to Eq. 3.8. The raw SN spectrum is shown in Fig. 3.14 (a) for various values of θ_B.

For the sake of completeness, we have plotted the integrated power contained in SN signal (Σ) as a function of θ_B as shown in Fig. 3.14 (b), and fitted those data points with $\sin^2\theta_B$ to verify the Eq. 3.8.

Chapter 4

Applications of SNS with thermal atoms

In this chapter, we present the applications of spin noise spectroscopy (SNS) technique using thermal atomic vapors in equilibrium and optically driven out-of-equilibrium steady-state conditions. This chapter is mostly based on the publications [5]. First, the results of SNS using rubidium atoms in thermal equilibrium are presented. We have demonstrated accurate measurements of several physical quantities such as transverse spin-relaxation time (T_2), electron's $g-$factor, nuclear $g-$factor, isotope abundance ratios, and zero-field ground hyperfine splitting. We have also developed precision magnetometry using the SNS technique. While few of the measurements have been reported in [4, 85, 153] using SNS technique in thermal atoms and semiconductor systems, here we are able to refine some of these estimates especially for isotope abundance ratios, nuclear g-factor, and magnetometry. We then apply an optical pumping beam to control the relative spin population in the ground hyperfine levels of Rb atoms. This is realized using an on-resonance pump beam nearly co-propagating with the far-detuned probe beam. The optical pumping drives the system out of equilibrium. We then show that SNS can be used to measure the spin imbalance in different ground hyperfine levels without disturbing the non-equilibrium steady-state of the system. We also show that the SN spectra from the optically pumped atoms have better resolution than typical absorption spectra from the same system. Therefore, the SNS can be used in resolving spectral lines of a non-equilibrium system in the presence of various spectral broadening mechanisms. Next, we have presented the reduction in the width of the SN spectrum (increase in the coherence times) when the atomic vapor is subjected to the optical pumping beam with the correct frequency.

4.1 Measurements and results in equilibrium

The spectrum shown in Fig. 3.5 is the intrinsic SN signal of Rb atomic vapor at thermal equilibrium. In the subsequent sections, we will extract various physical, electronic, nuclear, magnetic, and chemical properties of Rb atoms using the intrinsic SN spectrum in a diverse range of the external magnetic field strength.

4.1.1 Measurement of effective transverse spin-relaxation rate $(1/T_2^*)$

The measurements of the transverse spin-relaxation rate $(1/T_2)$ of an atomic vapor are essential for many practical applications, especially in precision magnetometry [35] and investigations in the search for the origin of spin fluctuations and diffusion constant [191]. The FWHM of the intrinsic SN spectrum is a measure of the transverse spin-relaxation rate as described in Eq. 3.2. However, the accurate measurement of $1/T_2$ at a particular temperature is crucial in the thermal atomic vapor due to the presence of various spectral broadening mechanisms. Therefore in the experiments, we can measure the effective transverse spin-relaxation rate $(1/T_2^*)$ which includes all the broadening. Apart from the spin-exchange and spin-destruction collisions between similar and different atoms inside the cell, the most dominating factors for broadening the SN spectrum are the (short) transit times of the atom through the probe laser beam. There are several experimental studies with thermal atoms where researchers tried to reduce the sources of these broadening and measure the value of T_2^* which can be estimated as T_2. However, depending on the experimental consideration and the strength of the external magnetic field, the value of $1/T_2^*$ can vary from order of 1 s^{-1} to 10^6 s^{-1} [4, 154, 188, 191–195].

In the measurements using the SNS technique, we have estimated the value of $1/T_2^*$ of Rb atoms kept in our un-coated cell at the temperature of 100°C is $\sim 3{\times}10^5$ s^{-1}. As we have mentioned above, the transit times and the wall collisions mostly contributed to the measurement of this parameter. We put high-density neon buffer gas inside our vapor cell to increase the transit time of Rb atoms through the probe beam. Since the diameter of the vapor cell is 20 mm, and the waist size of the probe beam inside the vapor cell is ~ 50 μm, therefore the wall collision has a less contribution in broadening the SN spectrum than the transit time. Our measurement of T_2^* is basically bound to the diffusion of Rb atoms in the surroundings of neon gases. The magnetic field in-homogeneity has very little contribution in the measurement of $1/T_2^*$. However, the measurements for the contribution due to the spin-exchange and spin-destruction

collision are buried under the transit time broadening.

The peak position of the SN spectrum is a measure of the strength of the external magnetic field ($\nu_L \propto B$), and the width of the spectrum (for a particular SNR of the signal) defines the uncertainty. Since we have various control to reduce the width of the SN spectrum, the measurement of the magnetic field can be extremely precise using this technique and are discussed later in this chapter.

4.1.2 Measurements of isotope abundance of Rb atoms in the cell

The SNS were performed with an enriched ^{87}Rb vapor cell filled with ^{21}Ne buffer gas. The presence of Ne buffer gas broadens the excited hyperfine energy levels (F') of Rb atoms due to electromagnetic interaction between F' levels of Rb atoms and various energy levels of Ne atoms [196–198]. In this interaction process, the ground hyperfine levels (F) of Rb atoms are mostly unaffected. To detect the relative abundance of Rb atoms in our SNS vapor cell, we have performed an absorption spectroscopy experiment where a probe laser beam was passing through the cell with frequency scanned within a wide range covering both hyperfine transition line of Rb isotopes ($F = 2 \rightarrow F'$ for ^{87}Rb, and $F = 3 \rightarrow F'$ for ^{85}Rb). The transmission signal of the probe laser as a function of frequency is shown with the black solid trace in Fig. 4.1. As a reference, we sent another probe beam generated from the same ECDL through a normal Rb vapor cell (un-coated and absence of any buffer or quenching gases) simultaneously, and record the transmission signal as presented with blue trace in Fig. 4.1. For the transmission signal in the normal vapor cell, we have identified the hyperfine transition lines for both the isotopes of Rb atoms as indicated in the bottom with blue arrows.

The total integrated area under the individual transmission signal is proportional to the atom density for the corresponding Rb isotopes inside the cell. On the other hand, the spectroscopy signal captured in black trace is unresolved, and the estimation of the isotope abundance of Rb atoms will be imprecise. However, the SN spectrum shown in Fig. 3.5 clearly indicates the presence of both isotopes in the cell. In the spin-based measurements, the total integrated noise of the power spectrum is a measure of the atom density for both Rb isotopes according to Eq. 3.4. From the ratio of the total integrated SN power (Σ) of the two peaks, we estimate an abundance ratio of ^{87}Rb : ^{85}Rb = 11 : 1 from Fig. 3.5 at that temperature. This shows that SNS is a sensitive technique for detecting the abundance of various isotopes of an atom with high precision even when they are present in minute quantities.

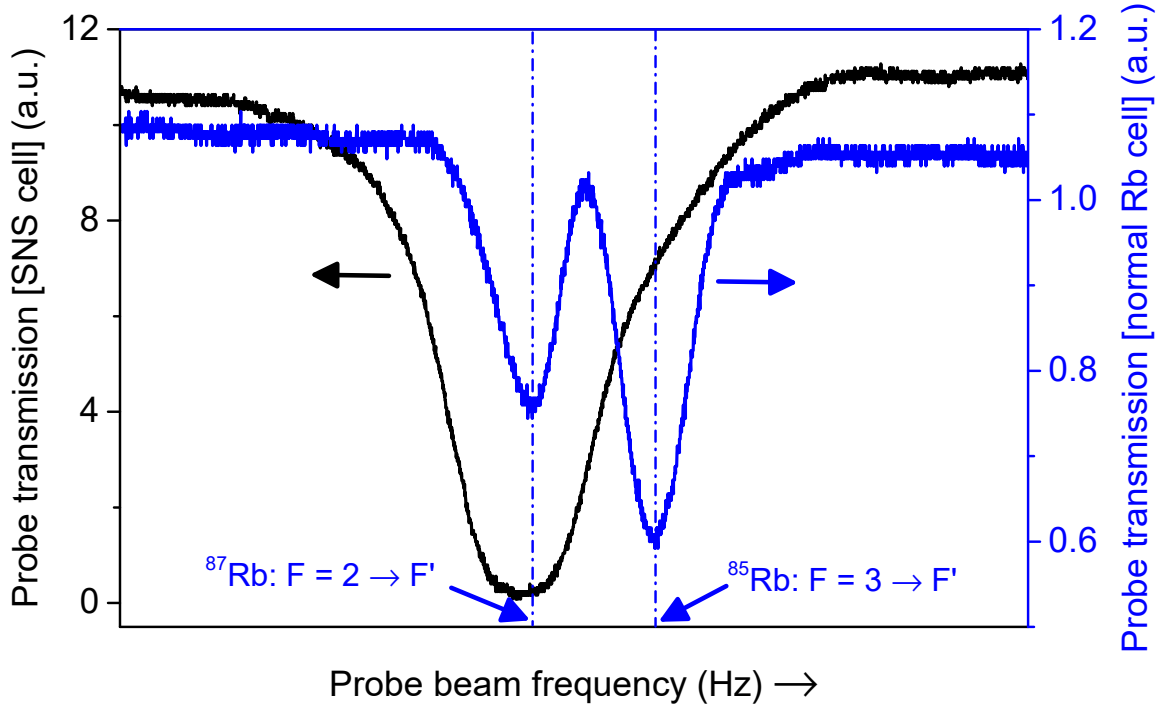

Figure 4.1: The measured probe transmission signal through enriched ^{87}Rb SNS (black trace) and normal Rb (blue trace) vapor cell. The SNS vapor cell is heated to T = 80°C to achieve enough vapor pressure for ^{87}Rb atoms to detect the transmission signal whereas the normal vapor cell was kept at room temperature. The laser light was scanning over a wide frequency range around the atomic transition lines of Rb atoms and were split into two parts and sent through two different cells. The black (blue) transmission signal is pressure (Doppler) broadened. The blue trace is shown here for reference to verify that the presence of ^{85}Rb atoms in the SNS cell is not detectable using traditional absorption spectroscopy shown in the black trace.

4.1.3 Measurement of electronic g-factors of Rb atoms

Linear Zeeman regime. The detected SN spectrum for Rb atoms in presence of a magnetic field in linear Zeeman regime (LZR) provides the Landé $g-$factors of the ground hyperfine levels (g_F). In the experiment, we have identified the range of LZR where the energy difference between two consecutive Zeeman resonances is much smaller than the detected SN signal width (such as energy difference between $(ii)-(i) \ll 1/T_2^*$). Therefore, in the LZR, all the six (ten) Zeeman coherence peaks appear at the Larmor frequency for ^{87}Rb (^{85}Rb) atoms as is evident from Fig. 4.2.

Measurements of g_F for Rb isotopes. Fig. 4.3(a) shows the SN spectra at three representative values of magnetic fields ($B_\perp$) illustrating that the two noise peaks, corresponding to ^{87}Rb and ^{85}Rb isotopes, shift in positions with $B_\perp$. Fig. 4.3(b) gives the variation in the position of these noise peaks in the frequency domain as a function

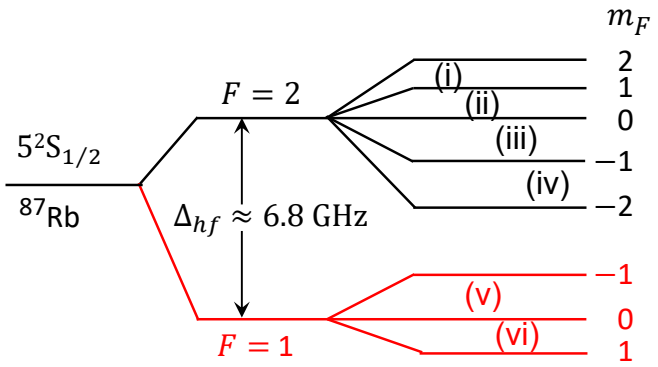

Figure 4.2: The Zeeman energy states of ^{87}Rb atoms in the ground hyperfine levels at arbitrary magnetic field.

of $B_\perp$. The bright (faint) trace corresponds to the spin noise peak positions of ^{87}Rb (^{85}Rb) atoms. The linear dependence of the peak positions on $B_\perp$ indicates that the atomic system is in the linear Zeeman regime. The slope ($g_F\mu_B/h$) of these lines give a measure of the magnitude of $g-$factor $|g_F|$ for the ground state hyperfine levels. The $g-$factors obtained from our measurements are $|g_F| = 0.500(\pm 0.001)$ for ^{87}Rb and $|g_F| = 0.333(\pm 0.001)$ for ^{85}Rb which are in excellent agreement with the theoretical values [22].

The theoretical value of $g-$factors for ground hyperfine levels are the same in magnitude, but opposite in sign for both the Rb isotopes. However, the SNS technique detects only the spin fluctuations between the consecutive Zeeman states and does not rely on their sense of rotation. Therefore, the measurements of the magnitude of g_F is a sufficient piece of information that provides the energy level splitting and their sense of precession in the energy space in the LZR.

4.1.4 Precision magnetometry

The SN signal that appeared in the LZR is a precise measure of the external magnetic field strength on the condition that the $g-$ factors of the atomic sample are provided. The g_F of an atomic system can be measured with extremely high accuracy using the SNS technique which in turn helps to measure the magnetic field with similar accuracy using the same formula of ν_L. The accuracy in the magnetic field measurements can be improved by performing repetitive measurements with a reasonable amount of data acquisition time. However, when the strength of the external magnetic field is beyond the LZR, the energy separation between two consecutive Zeeman states are not identical to the other Zeeman states energy separation (i.e. $(i) \neq (ii) \neq (iii)$..., and so on in Fig. 4.2). In this regime, the Zeeman energy state varies non-linearly with the

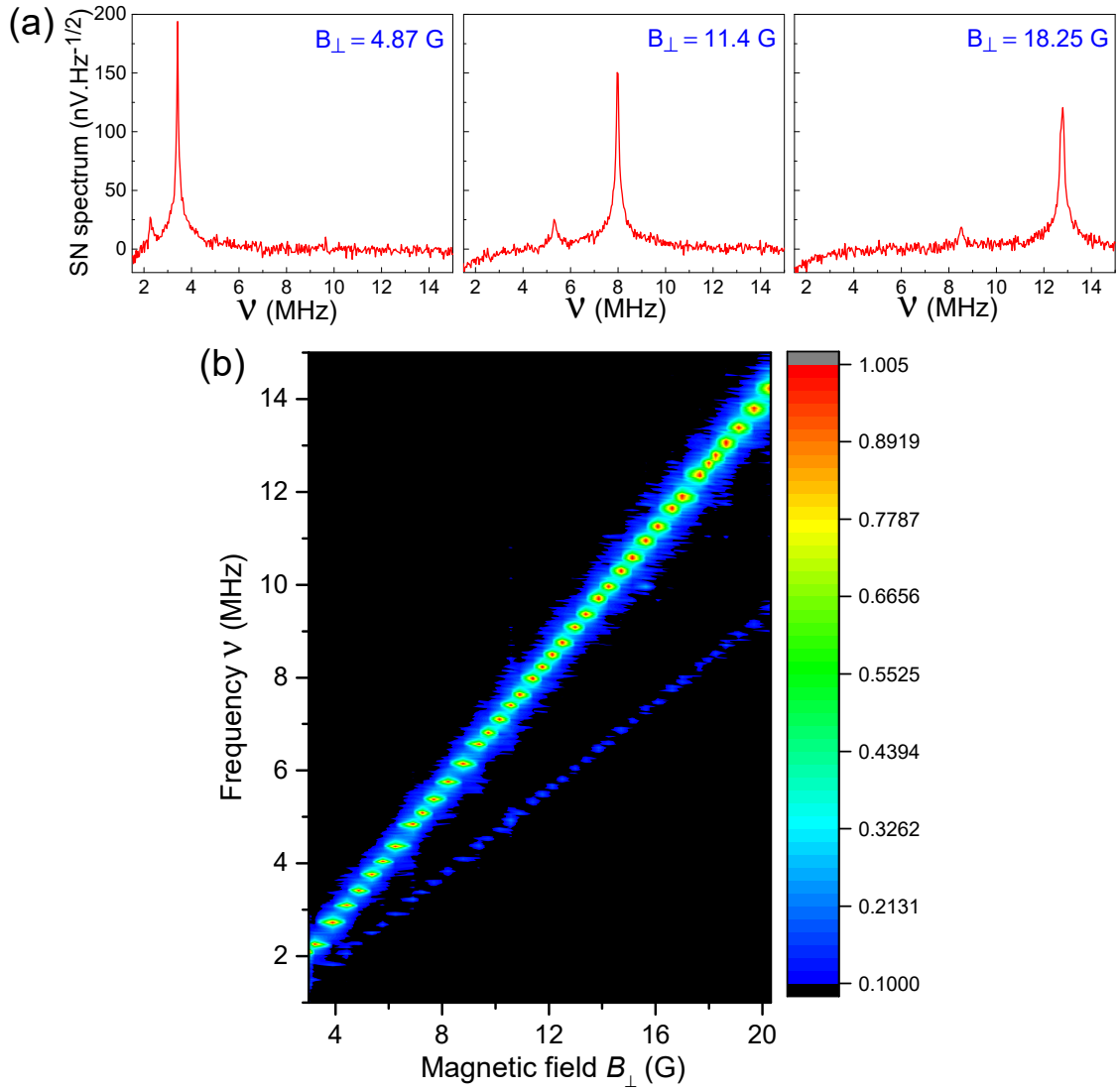

Figure 4.3: (a) Spin noise (SN) spectra at various $B_\perp$ are presented. The linear shift of the noise peaks with $B_\perp$ suggests a linear Zeeman effect of the ground state hyperfine levels in that $B_\perp$ range. (b) A 2-D false color mapping shows the SN peak positions for ^{85}Rb and ^{87}Rb as a function of $B_\perp$. The bright (faint) trace is for ^{87}Rb (^{85}Rb) SN signal. The noise signal strength of ^{87}Rb and ^{85}Rb for each spectrum is plotted after normalizing the signal by the SN peak strength of ^{87}Rb. The slopes of these traces reveal $|g_F|$ of Rb isotopes.

magnetic field according to the Breit-Rabi formula (refer to Eq. 3.3) and is called as non-linear Zeeman regime (NZR). In NZR, the energy difference between any two Zeeman separations (as an example, $(i) - (ii)$) is more or comparable to the $1/T_2^*$). Therefore in this regime, the detected SN signal gets split into multiple peaks in the spectrum and the notion of a single Larmor frequency is no longer valid.

In the experiments, while increasing the strength of the applied magnetic field ($B_\perp$), the spin noise spectra is observed (see Fig. 4.4(a)) to broaden (within a range of $B_\perp \sim 20 - 40$ G where $(i) - (ii) \simeq 1/T_2^*$) and to split into well-resolved peaks at even higher $B_\perp$ (> 60 G, where $(i) - (ii) > 1/T_2^*$). In this relatively high magnetic fields, the system is clearly in NZR (Eq. (3.3)) as discussed earlier. A false-color mapping of the measured nonlinear Zeeman splitting of the ground hyperfine levels of ^{87}Rb atoms as a function of $B_\perp$ is shown in Fig. 4.4(b).

Measurements of the magnetic field in NZR. In the NZR, the precise measurement of magnetic fields using an individual SN peak is difficult unlike the case in the LZR where the SN peak position is a true measure of the magnetic fields. However, in NZR, all the individual SN peaks collaboratively measure the magnetic field precisely and the method is described below.

The individual noise peaks in the SN spectrum for a higher $B_\perp$ (> 60 G) can be identified as the transitions between different Zeeman states of the ground hyperfine levels. These are shown in the inset of Fig. 4.5 where $P1$ denotes the magnetic resonance frequency between $(F = 2, m_F = 2) \leftrightarrow (F = 2, m_F = 1) \equiv (i)$ and $P2$ for the magnetic resonance frequency between $(F = 2, m_F = 1) \leftrightarrow (F = 2, m_F = 0) \equiv (ii)$ and so on (refer to Fig. 4.2). Fig. 4.4(b) shows the nonlinear dependence of each noise peak position on $B_\perp$ in the NZR. However, the sum of all four noise peak frequencies for $F = 2$ hyperfine levels,

$$S = P1 + P2 + P3 + P4 = \frac{\mu_B}{h}(3g_I + g_J)B_\perp, \tag{4.1}$$

depends linearly on $B_\perp$. Using the values of $P1, P2, P3, P4$ determined from the measured SN spectrum one can estimate $B_\perp$ using Eq. (4.1), substituting the values of μ_B, h, g_I [199], g_J [199], which are already known to high precision. Therefore the sum of all four noise peak positions for Rb atoms (in general for all alkali atoms) in a ground hyperfine level in NZR has similar straightforward dependence alike in the case of LZR. As the observed SN peaks are extremely narrow (FWHM $\sim$ 100 kHz) and the peak positions can be determined with an accuracy of one part in 10^5. We can therefore measure an external magnetic field within that same order of relative error,

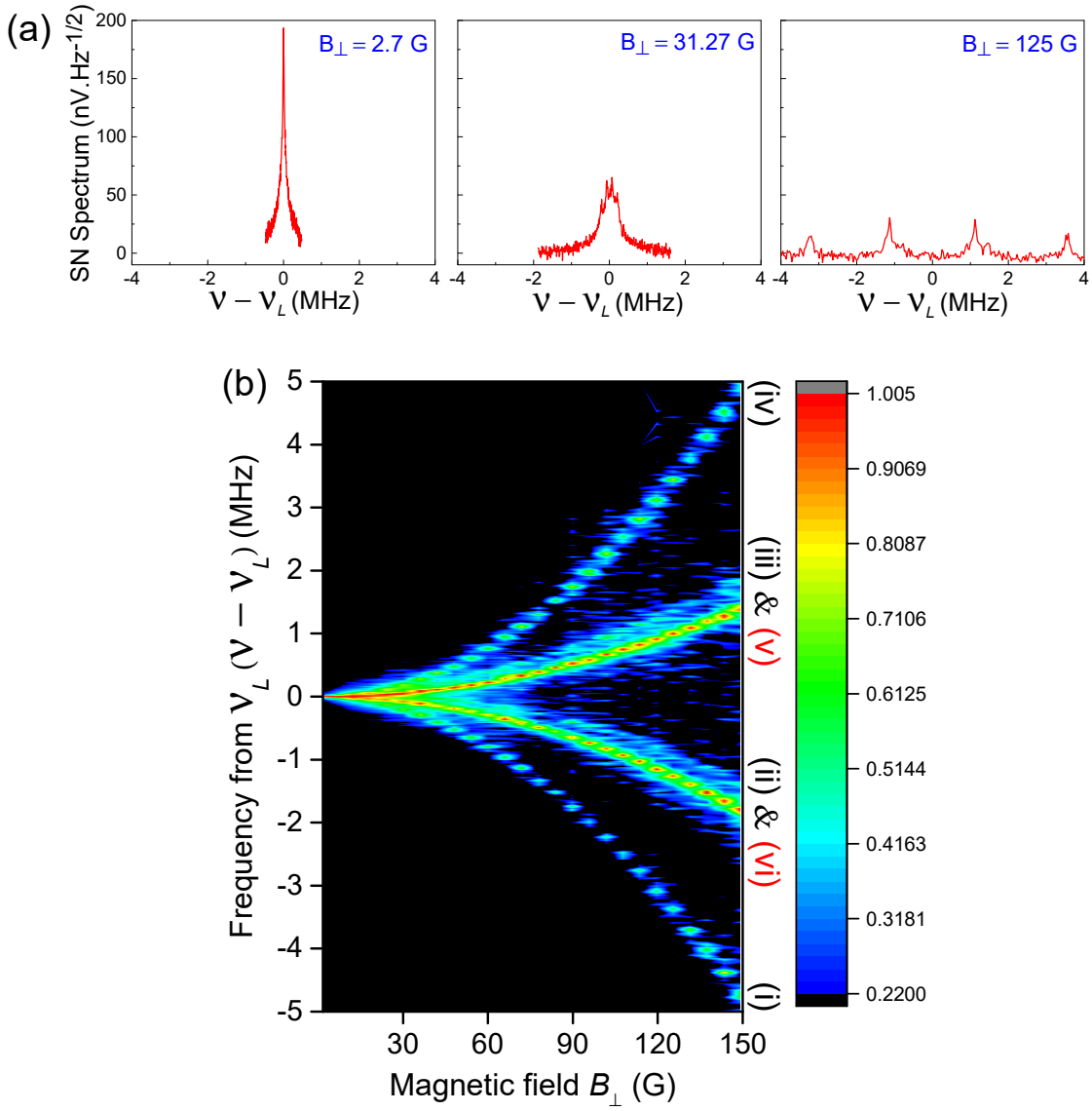

Figure 4.4: Broadening and splitting of the spin noise (SN) spectrum with increasing $B_\perp$. (a) SN spectra for ^{87}Rb at $B_\perp = 2.7$ G, 31.27 G, 125 G. The origin of the frequency in these spectra is shifted to the central Larmor frequency $\nu_L = g_F \mu_B B_\perp / h$. The other parameters are: probe power = 400μW, $\delta_p = -10.6$ GHz, cell temperature = 105°C. (b) Visual realization of the nonlinear Zeeman effect of ground state hyperfine levels with increasing $B_\perp$. Each spectrum is normalized by the strongest peak in the SN signal.

of one part in 10^5, for the range of $B_\perp$ where noise peaks are separable. Thus SNS provides a simple means of precision magnetometry.

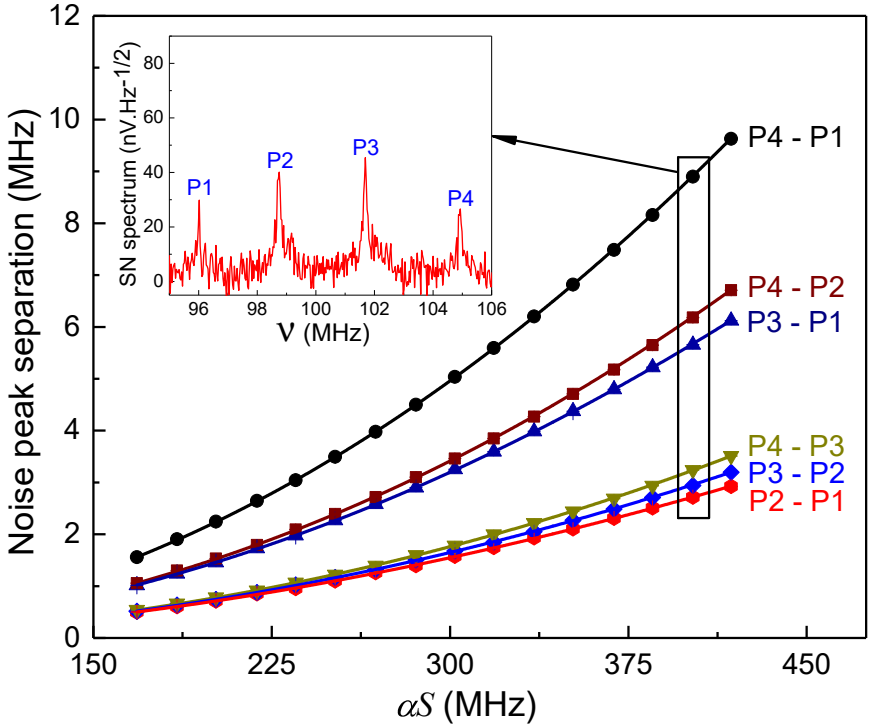

Figure 4.5: Measurement of magnetic field $B_\perp$ and $\Delta_{\rm hf}$ using spin noise spectroscopy. $P1, P2, P3$ and $P4$ indicate the position of spin noise peaks (corresponding to Zeeman sub-levels of $F = 2$) as can be seen from the raw data in the inset. The measured frequency separation between different noise peaks are plotted against measured αS (refer to the text). The bold lines are obtained from the Breit-Rabi formula in Eq. (4.2) with known parameters for error analysis in magnetic field measurements. The experimental parameters are the same as in Fig. 4.4.

Now we rewrite Eq. (3.3) for ^{87}Rb as

$$\begin{aligned} E_{F=2,m_F} &= -\frac{h\Delta_{\rm hf}}{8} + \frac{hg_I}{(g_J - g_I)}(\alpha S)m_F \\ &+ \frac{h}{2}\sqrt{\Delta_{\rm hf}^2 + \Delta_{\rm hf}(\alpha S)m_F + (\alpha S)^2}, \end{aligned} \tag{4.2}$$

where $\alpha = (g_J - g_I)/(g_J + 3g_I)$. In Fig. 4.5, we plot, as a function of αS, the noise peak separations $((P4-P1), (P4-P2)$ ... $(P2-P1))$ calculated from Eq. (4.2) using known values of $h, g_I, g_J, \Delta_{\rm hf}$. Superposed on the plot are the experimentally obtained noise peak separations shown as solid symbols with 1σ error bars. Then, we note down the x-errors between the experimentally obtained peak separations and those from the calculated curves. The root-mean-square value of the x-errors gives an estimate of the error in measuring the external magnetic field. We find that the error is within 500 μG

in our measurement range of $B_\perp$ between 60 G to 150 G. However, the upper bound of the unknown $B_\perp$ can be anything since the noise peaks are already separated after 60 G of the magnetic field. Therefore any strength of the external magnetic field above 60 G can be measured with this accuracy using the SNS technique. The measurements of the low magnetic field (below 20 G i.e. in the LZR) can also have similar accuracy as presented in the precision measurements of g_F. However, within the range of $20-60$ G magnetic field, where the SN peak gets broadened but not split into multiple peaks introduces errors in precise measurements of the magnetic field. In this range, both LZR and NZR are not easily applicable. However, bringing down the value of SN signal width ($\sim$ kHz) using hydrocarbon chain coated cells can help to split the SN signal in this regime and use the NZR formula to precisely measure the magnetic field. This accuracy surpasses the standard Hall probe-based magnetometers by nearly two orders of magnitude. Moreover, this high precision measurement of the magnetic field is an in-situ detection, without requiring the physical placement of a separate probe. A few recent studies [85, 200] are performed to indicate the potentialities of SNS to measure magnetic fields (both external and effective – "internal" ones). In the present work, we have provided a precise estimate for the accuracy of the measured magnetic field using the SNS technique. Further, the precision magnetometry using the SNS in atomic vapors is expected to work for a large temperature window including room temperature in contrast to the similar magnetometers with cooled semiconductors used in the previous studies [85, 200].

Note that, the measurement of magnetic fields using SN signal is absolute and does not require any calibration which is absolutely necessary for the Hall probe or other semiconductor device based magnetometers.

4.1.5 Measurement of zero-field hyperfine separation

In Fig. 4.5, we have also fitted the experimentally obtained values of $(P4-P1)$, $(P4-P2)$ ... $(P2-P1)$ using Eq. (4.2) keeping $\Delta_{\rm hf}$ as a free parameter. From these fittings, we extract the value of the zero-field hyperfine constant for ^{87}Rb as $\Delta_{\rm hf} \sim 6805.5(\pm 7.2)$ MHz with an error below 0.5% [201].

4.1.6 Measurement of nuclear g-factor

In the presence of $B_\perp$, the energy separations between similar magnetic (Zeeman) transitions from different hyperfine ground levels (F, m_F) such as, $(2,1) \leftrightarrow (2,0)$ and $(1,1) \leftrightarrow (1,0)$ or $(2,0) \leftrightarrow (2,-1)$ and $(1,0) \leftrightarrow (1,-1)$ in Fig. 4.2, are determined by the second term in Eq. (3.3) arising out of the nuclear spin. However, since the

value of nuclear g-factor (g_I) is small, the contribution of this term is negligible for low magnetic fields. Therefore, the SN peaks from $(2,1) \leftrightarrow (2,0)$ and $(1,1) \leftrightarrow (1,0)$ are almost unresolved for $B_\perp < 150$ G in our case. At high magnetic fields (> 150 G), we can resolve the SN peaks from all available Zeeman transitions when their separations are more than the width of the individual peaks. Six distinct SN peaks from the allowed $\triangle F = 0$, $\triangle m_F = \pm 1$ transitions of ^{87}Rb are observed in Fig. 4.6 at $B_\perp = 160$ G. The value of g_I can be precisely obtained by measuring the separation between $(2,1) \leftrightarrow (2,0)$ and $(1,1) \leftrightarrow (1,0)$ (also $(2,0) \leftrightarrow (2,-1)$ and $(1,0) \leftrightarrow (1,-1)$). From a series of such measurements, the experimentally estimated g_I for ^{87}Rb in our experiment is $-0.00100627(\pm 0.00002558)$, where the quantity in the bracket refers to the 1σ error.

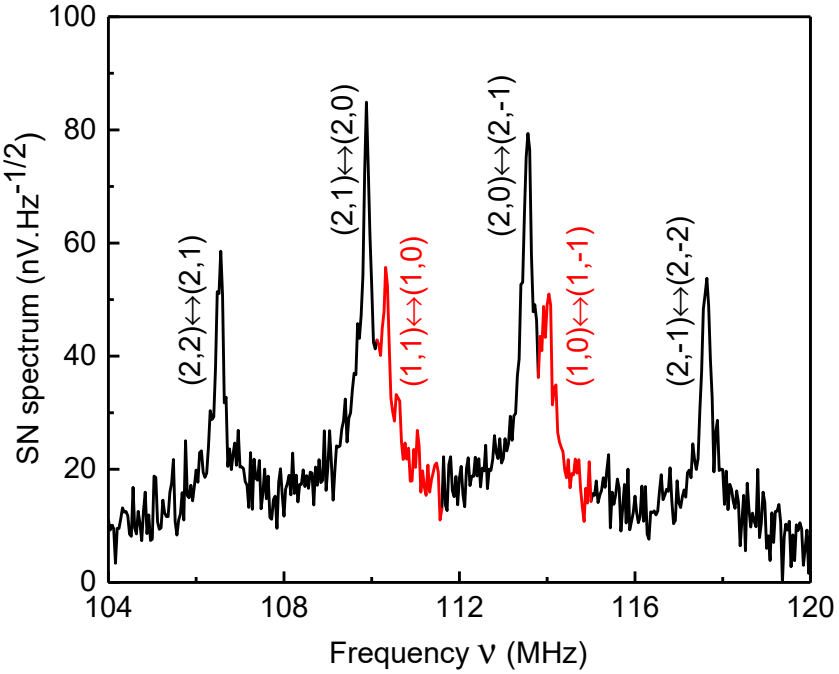

Figure 4.6: Spin noise spectrum with resolved all-allowed Zeeman transitions ($\triangle F = 0$, $\triangle m_F = \pm 1$) of ground state hyperfine levels in ^{87}Rb. The parameters are $B_\perp = 160$ G, probe power = 750 μW, $\delta_p = -10.6$ GHz, cell temperature = 105°C. The value of nuclear g-factor (g_I) is precisely obtained and reported in the text by measuring the separation between $(2,1) \leftrightarrow (2,0)$ and $(1,1) \leftrightarrow (1,0)$ (also $(2,0) \leftrightarrow (2,-1)$ and $(1,0) \leftrightarrow (1,-1)$) in a series of measurements.

Note that the middle two peaks are stronger in strength than the outer peaks for $F = 2$ level SN signal. This can be explained as the intermediate Zeeman states $m_F = -1, 0, 1$ are each connected to consecutive two m_F states (upper and lower), whereas, the outer $m_F = -2, 2$ states are only connected to one m_F state only (see Fig. 4.2).

4.2 Measurements and results in optically pumped atomic system

Thus far, we have explored the characterizations and applications of the SNS technique in an equilibrium thermal vapor. In conformity with the FDT, at thermal equilibrium, the SNS technique detects the two-point temporal correlations of magnetization ($\langle M_x(t)M_x(0)\rangle$) which provides a linear response characteristic of the spin system. However, the measurements of a similar spin-spin correlator in a non-equilibrium steady-state system give the additional non-equilibrium contributions in the linear response function which is beyond the topic of FDT and provides useful information about the non-linear characteristic of the system. In the following, we report the measurements of SN signal in an out-of-equilibrium steady-state atomic system where we use an additional optical field to manipulate spin populations in different ground hyperfine levels. In this non-equilibrium system, even if the externally applied perturbation is relatively weak − the detected spin noise signal provides useful additional information which can not be obtained in the equilibrium SN measurements. The higher-order spin-spin correlators and the cross-correlators between the atomic spin states are the fundamental studies in the out-of-equilibrium steady-state system that provides various properties of the system which is not accessible in the linear response measurements and using FDT.

Recently, theoretical investigations have been studied in the semiconductor system where a weak applied electric field can shift the spin noise peak of the conduction electron [94]. The shift in the SN peak is proportional to the spin-orbit coupling strength for the electron moving along the electric field direction. This study can not be performed within the equilibrium SNS technique. In another study where the SNS was employed to detect the couplings and correlations between different spin coherences in a non-equilibrium atomic vapor [162]. In the experiment in [162], the Zeeman states of the ground hyperfine levels of ^{41}K are driven by a weak radio-frequency magnetic field which brings the vapor out-of-equilibrium.

In contrast, we have applied an optical pumping (control) beam that connects the ground and excited hyperfine levels to drive as well as incoherently control the spin populations in the ground hyperfine levels. The pump beam is linearly polarized and almost co-propagating (within 5°) with the probe beam. The pump beam after the vapor is blocked with a beam blocker in order to avoid its falling on the photo-detector. The pump beam is derived from an independent tunable external cavity diode laser. The Rb atoms in the vapor cell are optically pumped to the desired ground hyperfine levels by tuning the frequency ν_c and the intensity I_c of the pump laser. We have

performed the SN measurements from such an optically pumped atomic system with the far-detuned linearly polarized probe laser beam after reaching the steady-state of the system. Substantial modifications of the SN signals are observed depending upon the relative ground hyperfine level populations of the ^{87}Rb atoms.

Optical pumping. Whereas the random spin-exchange collisions depolarise the atomic spin polarization at thermal equilibrium, the optical pumping (OP) [34, 202–206] method orients them in a preferred direction by transferring the angular momentum of light to the atomic spin states. OP is a well-established and efficient technique for initializing and maintaining the atomic spin polarization in a specific quantum state. In general, the atomic spins are oriented along the direction of the light propagation due to the selection rules of the light-matter (dipole) interactions. In this method, a particular atomic ground level is polarized by repeated cycles of light absorption in ground levels and spontaneous emission from excited levels. In an ideal case, the absorption of the pump photon stops when the atomic population is transferred to a specific ground state, known as a 'dark state'. For the optical pumping for the light with electric field vector, $\vec{E}(t) = E_0\, e^{i(k_L\, x - \omega_L t)}\, \hat{e}$, the dipole transitions depend on optical detuning ($\omega_L - \omega_0$, where ω_0 is the atomic transition frequency), the presence of an external magnetic and/or electric fields, and the polarization $\hat{e}$ of the light. For the circular polarization of the electric field $\hat{e}_\pm = \frac{(\hat{y} \pm i\hat{z})}{\sqrt{2}}$, the atomic spins orient along the propagation direction $\pm\hat{x}$ via the polarization selective allowed transitions $m_F = m_{F'} \pm 1$. For $F \leq F'$, the polarized state is $m_F = \pm F$ is dark. On the other hand, for linear polarized light $\hat{e} = \hat{y}$ or $\hat{z}$ the spin alignment happens along $\hat{x} \times \hat{e}$ with zero net orientation for the transition $F \to F' = F - 1$. In this case both the Zeeman states $m_F = F$ and $m_F = -F$ are dark.

Since OP method initializes the atomic spins in a desired atomic state, it has many practical applications using thermal atom in precision metrology [35, 207–211], quantum memory and information processing [212–216], noble gas hyper-polarization via spin-exchange collisions [33, 217, 218], and searches for new physics beyond standard model [149, 219–221]. However, in our work [5] we have demonstrated a controlled optical pumping of ^{87}Rb atoms between the ground hyperfine levels and detected the instantaneous spin population using SNS technique. In our experiments, we have addressed the atomic transitions $F \to F' \geq F$ by the linearly polarized pump laser beam propagating along the $x-$axis. Note that for simplicity we ignore the small angle made by the pump laser beam with respect to the $x-$axis (see Fig. 4.7(a)). Therefore at a steady state, the atomic spins orient along the $x-$axis with equally distributed amongst the possible Zeeman states, and no dark state has been formed. However,

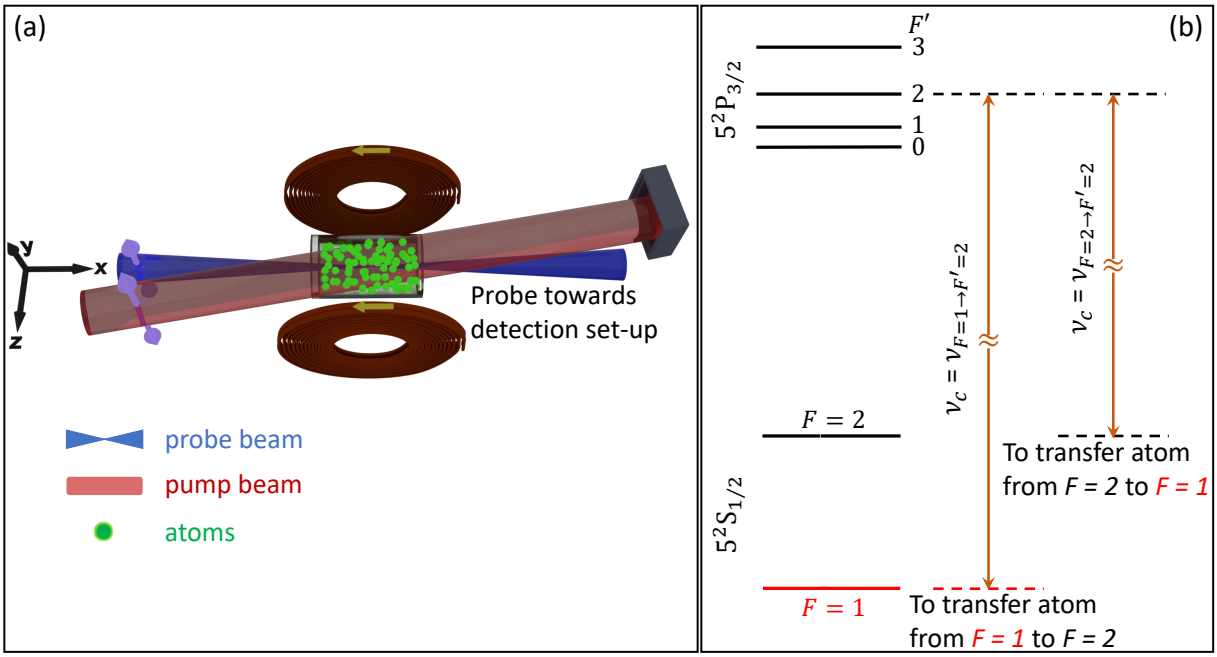

Figure 4.7: Schematic of the experimental arrangement (a) and frequency (ν_c) of the pump beam (b) used for optically pumped spin noise (SN) experiments of thermal ^{87}Rb atoms.

depending on the pump laser frequency connected to a particular atomic transition, the atoms accommodate in either in $F = 1$ or in $F = 2$ hyperfine levels as shown in Fig. 4.7(b).

4.2.1 Detection of spin imbalance

Here, we implement the non-invasive SNS technique to probe the instantaneous spin population, i.e. the spin imbalance between the ground hyperfine levels in an optically driven steady-state ^{87}Rb atomic system without applying further perturbation [28]. In particular, the SNS technique discussed in this chapter detects the spin imbalance of the system in its steady-state for a particular intensity of the optical pumping beam. The optical pumping timescale to attain the steady-state is much shorter than the measurement duration.

In the absence of the pump beam, six spin coherences at reasonably higher magnetic fields are seen in the SN spectrum in Fig. 4.8(b) as is expected from an ensemble of atoms with the population in both the ground hyperfine levels ($F = 1, 2$). The probe beam and other experimental parameters are the same as in Fig. 4.6. On setting the frequency ν_c of the pump beam on resonance to the $F = 1 \rightarrow F' = 2$ transition of ^{87}Rb, a fraction of atoms is pumped out of the ground $F = 1$ level depending on the

intensity I_c of the pump beam. This is evident in Fig. 4.8(a) where only four SN peaks related to $F = 2, \triangle m_F = \pm 1$ are observed at the highest I_c. We have kept the pump beam on during the measurements. On the other hand, when the atoms are pumped out of the ground $F = 2$ level using a pump beam resonant with the $F = 2 \rightarrow F' = 2$ transition, the SN spectrum reduces to two peaks related to $F = 1, \triangle m_F = \pm 1$ spin coherences. This is shown in Fig. 4.8(c) for different pump beam intensities. The false-color graph shown in Fig. 4.9 represents a more qualitative picture of the optical pumping schemes of ^{87}Rb atoms (see the caption of the figure for description). The probe beam is around -10 GHz detuned from the $F = 2 \rightarrow F' = 3$line, and -16.8 GHz detuned from $F = 1 \rightarrow F' = 2$line. We calculate the optical pumping rate by the probe beam is around 0.8 % for $F = 2$, and 0.3 % for $F = 1$ atoms in comparison to the on-resonance pumping beam. Therefore, in our study, we ignore the contribution of the optical pumping by the probe beam.

We have extracted the degree of spin polarization in different ground hyperfine levels as a function of pump beam intensity from a series of measurements similar to the ones presented in Fig. 4.8. The measured hyperfine spin polarization of $F = 1$ level $(n_{F=1}/(n_{F=1}+n_{F=2}))$ with pump beam (on resonance with $F = 2 \rightarrow F' = 2$ transition) intensity is presented in Fig. 4.10 (a). We fit the individual noise power spectrum using a Lorentzian function and take the ratio of the integrated intra-hyperfine spin noise power corresponding to $F = 1$ hyperfine level to the total SN power. Since, our probe beam detuning $\delta_p = -10.6$ GHz, the probe beam detuning with respect to $F = 1 \rightarrow F' = 2$ transition is -17.4 GHz. We had incorporated this factor while extracting the population ratio from the SN spectra. We observe a monotonic increase in the degree of polarization with increase in the pumping beam intensity saturating towards a complete polarization for very high pump beam intensity. A similar trend is observed for the pumping into $F = 2$ ground state hyperfine level.

We have also presented in Fig. 4.10 (b) the measured width of the intra-hyperfine $(F = 1)$ spin noise spectrum as a function of the pump beam intensity. We observe from our measurements a monotonic increase of the noise signal width (or the spin relaxation rate) with optical pumping beam intensity. In the context of spin fluctuations of non-equilibrium electrons and excitons in semiconductors [134], spin pumping can suppress spin fluctuations. However, in our measurements, the presence of a strong pump beam in the dilute atomic vapor can lead to (a) non-equilibrated electron's spins and (b) off-resonant pumping, leading to the reduction of spin lifetime, which manifests as an increase of the width of the SN spectrum.

These experiments indeed clearly show that the spin populations in different ground hyperfine levels subjected to optical pumping beam in the steady-state condition is

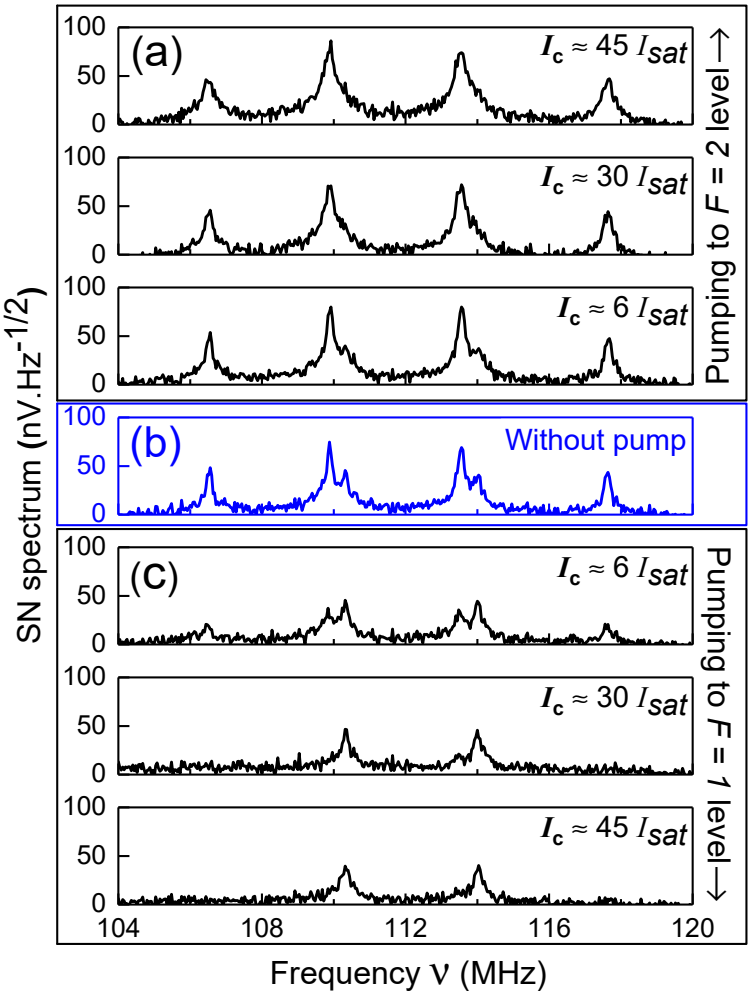

Figure 4.8: Spin noise (SN) spectra in and out of equilibrium ^{87}Rb atoms. (a) SN spectra with a pump beam on resonant to $F = 1 \rightarrow F' = 2$ optical transition for various pump beam intensities I_c. (b) SN spectrum in thermal equilibrium (without optical pump beam). (c) SN spectra with a pump beam on resonant to $F = 2 \rightarrow F' = 2$ optical transition for different pump beam intensities I_c. For all panels, $B_\perp = 160$ G, $\delta_p = -10.6$ GHz and cell temperature = 105°C. Note that, the parameter I_c is calculated using the CO-DATA [22] value of ^{87}Rb excited hyperfine level line-widths without considering the neon buffer gas inside the cell.

reflected in the SN spectra. Such relatively non-invasive detection of spin states in a non-equilibrium atomic system may find applications in atom interferometry [222], atomic clocks [223] and gravimetry [224].

4.2.2 Resolving spectral lines

The enriched ^{87}Rb vapor cell used in our experiments contained a buffer gas (neon) with a partial pressure of 200 millibars, and thus the conventional absorption spectra

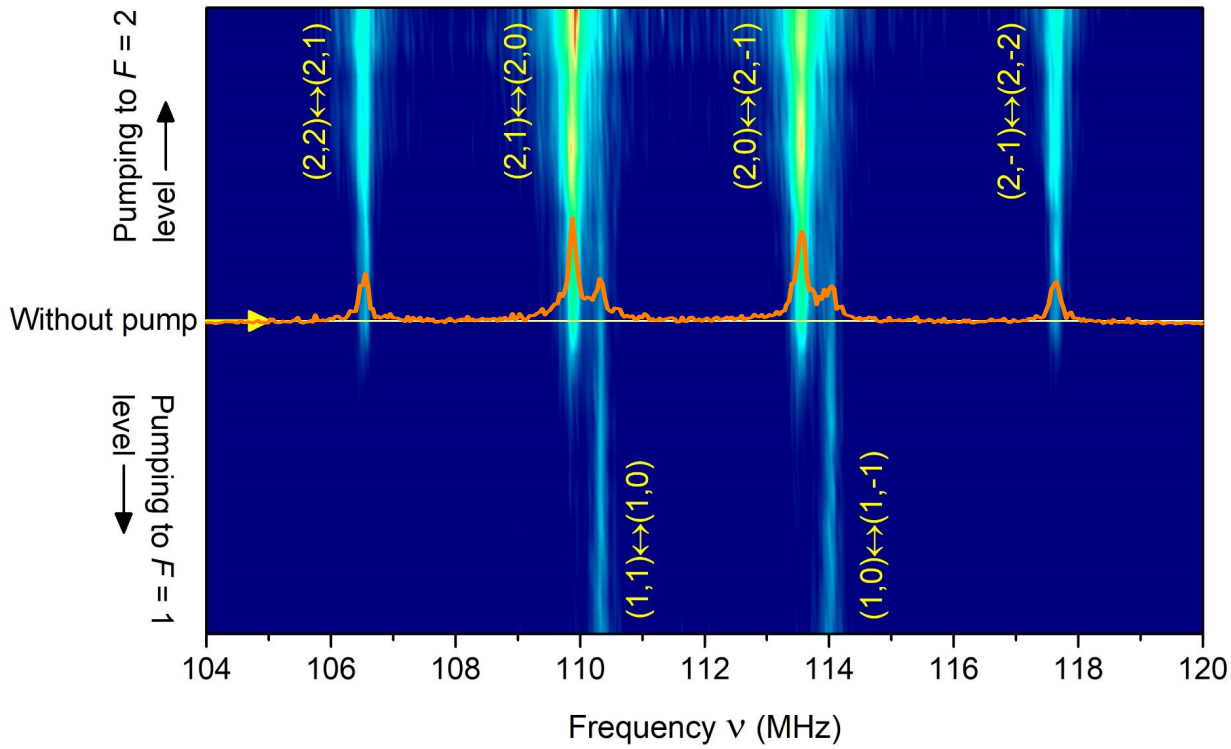

Figure 4.9: The false color map depicts the spin noise (SN) spectrum in presence of the optical pumping beam. The raw spectrum (orange color) represents the intrinsic SN signal where all six Zeeman coherence peaks are visible. The upper half corresponds to the driven SN spectrum with atoms optically pumped to $F = 2$ hyperfine level. The lower half represents the same for atoms optically pumped to $F = 1$ hyperfine level.

that we measure suffers broadening mainly due to homogeneous pressure broadening [196–198] and modestly due to inhomogeneous Doppler broadening. The transmission of the probe laser through the atomic vapor at 90°C is studied in the absence and presence of an optical pump beam as shown in Figs. 4.11(a) and 4.11(c). The detuning δ_p of the probe beam was varied over a wide range (−10 GHz to 12 GHz) which covers both the $F = 2 \rightarrow F'$ and $F = 1 \rightarrow F'$ transition lines of ^{87}Rb atoms. In the absence of a pump beam in Fig. 4.11(a), the probe transmission as a function of δ_p shows a single dip situated in-between those transition lines. In this experiment, we first allow the probe laser beam to pass through the cell and then let it fall on a power meter sensor. The measurement time for each detuning is of 5 seconds. The integrated SN power Σ from the Rb vapor also shows a single dip in Fig. 4.11(b) in the absence of optical pumping. Thus, both the absorption spectroscopy and SNS fail to detect $F = 2 \rightarrow F'$ and $F = 1 \rightarrow F'$ transition lines separately. Nevertheless, the dip in Σ (in Fig. 4.11(b)) seems to indicate a red-detuned $F = 2 \rightarrow F'$ transition as expected in the presence of neon buffer gas [198]. Therefore, the intrinsic spin noise measurements in buffer

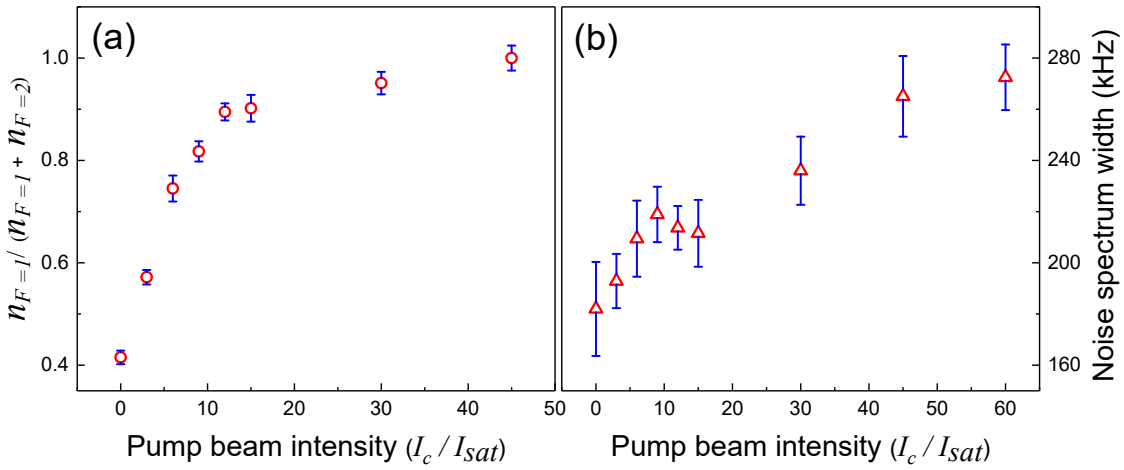

Figure 4.10: Plot of relative population in $F = 1$ hyperfine level (a) and width of the spin noise (SN) spectrum due to intra-hyperfine spin fluctuations in $F = 1$ hyperfine level (b) as a function of optical pumping beam intensity. Both the relative population and the width are extracted from a set of SN spectra recorded in presence of optical pumping beam, a few representative ones are presented in Fig. 4.8 (c).

gas filled neutral atoms can establish the fact that the buffer gas broadens the excited hyperfine level line-width as well as shifts the resonance line towards the red detuned side.

The comparison of the transmission and SN spectra has been recently reported for the Cs vapors in thermal equilibrium [170]. Here, the SNS revealed spin correlations present in the mostly Doppler broadened atomic ensemble. On the other hand, we investigate mostly pressure broadened atomic vapors. Our transmission spectra in Fig. 4.11(a), reveals a pressure broadened FWHM of $\sim (2\pi\times)$ 5 GHz, in contrast to a Doppler broadened FWHM of $\sim (2\pi\times)$ 0.7 GHz from a buffer gas free vapor cell. Therefore, we also expect that our optically driven atomic system is mostly homogeneously broadened. A priori, it is not obvious that the SNS will be able to resolve the different ground hyperfine levels of an optically driven system. In the following, we present our measurements to show that such additional information can be obtained from an optically pumped system.

In the case of an optically pumped atomic ensemble, the probe transmission (Fig. 4.11(c)) can detect the above two optical transitions independently. In Fig. 4.11(d), we show the integrated SN power Σ with the probe detuning δ_p when the atoms are optically pumped to either $F = 2$ or $F = 1$ level by a pump intensity $I_c > 50I_{sat}$. We observe a dip in each integrated SN power near (~ 1 GHz red shifted) $F = 2 \rightarrow F'$ or $F = 1 \rightarrow F'$ transition lines. Therefore, the SNS can also be used to resolve the spectral lines in

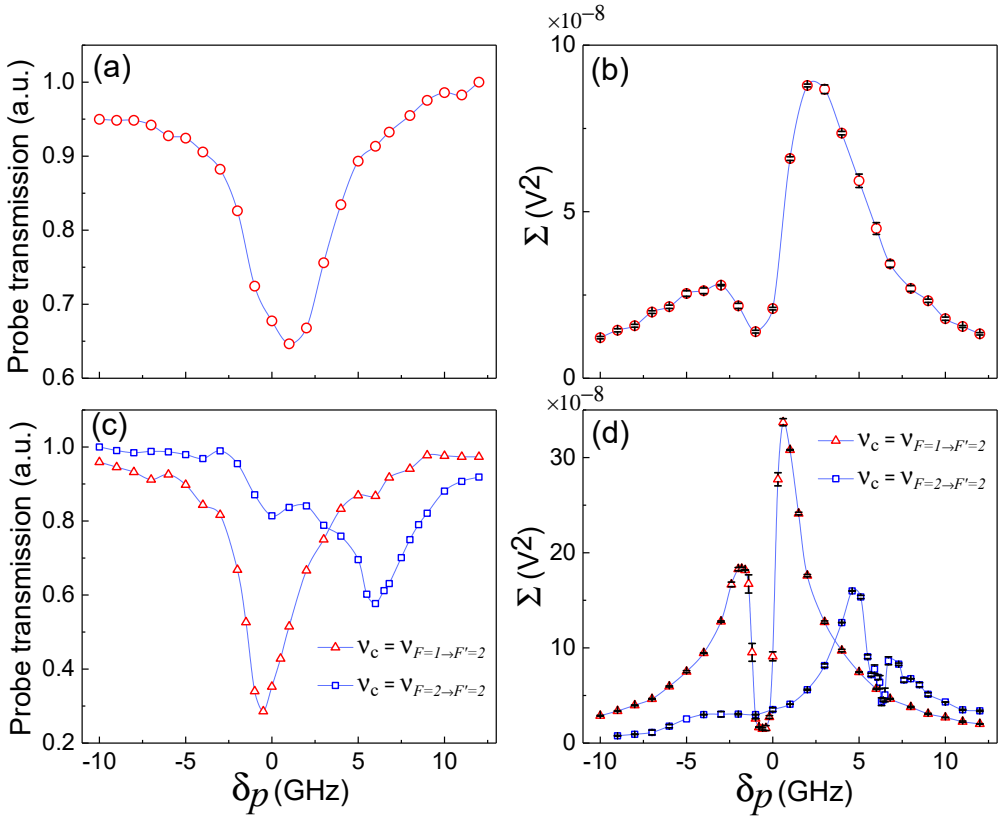

Figure 4.11: Comparison between absorption spectroscopy and spin noise spectroscopy in resolving spectral lines in a buffer gas filled Rb vapor cell in the absence [(a) and (b)] and presence [(c) and (d)] of optical pumping. [(a) and (c)]: Probe transmission vs. probe beam detuning, δ_p defined in Fig. 3.3. [(b) and (d)]: Integrated spin noise (SN) power Σ from ^{87}Rb atoms vs. δ_p. Red triangles (blue squares) depict probe transmission and integrated SN power Σ from optically pumped $F = 2$ ($F = 1$) atoms. The lines joining the data points are a guide to the eye. For all panels, $B_\perp = 7.12$ G and cell temperature = 90°C.

a driven atomic system [187]. Moreover, SNS has a better resolution (around three times in Fig. 4.11(d) than Fig. 4.11(c)) over the absorption spectroscopy [187]. This last finding could have potential application in driven systems with narrower separation between relevant transitions where the SNS would be more useful to probe such transitions separately.

We can also detect these transitions by tuning the frequency ν_c of the pump beam instead of the probe beam. Here we keep the probe detuning δ_p fixed at -10 GHz from $F = 2 \rightarrow F'$ transition (and around -16.8 GHz detuned from $F = 1 \rightarrow F'$ transition). Therefore, most of the contribution in the SN signal comes from the $F = 2$ level. We tune the frequency ν_c of the pump beam from -10 GHz to 10 GHz around $F = 2 \rightarrow F' = 3$ transition. We plot the integrated SN power Σ as a function of

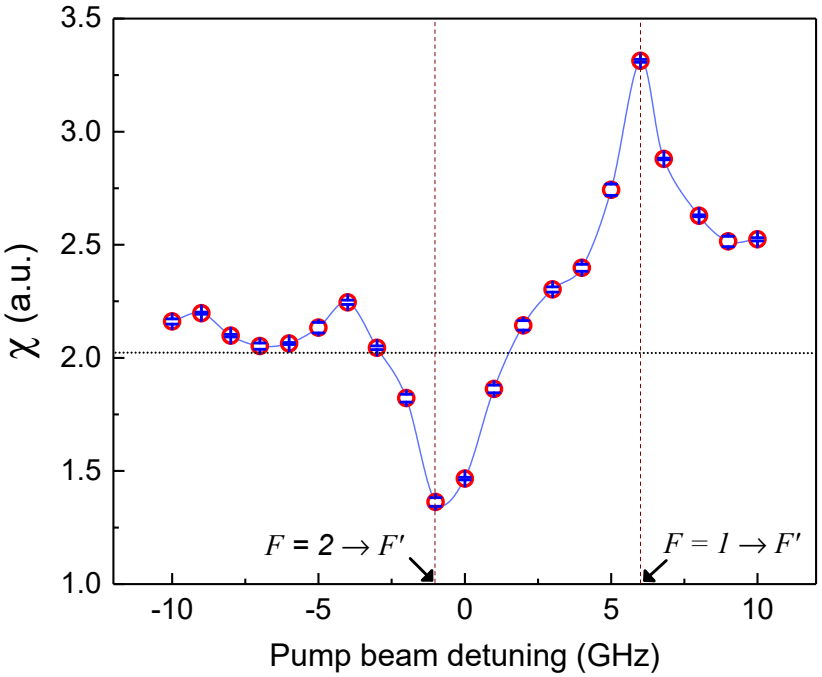

Figure 4.12: Resolving spectral lines of ^{87}Rb atoms in the presence of neon buffer gas by tuning the pump beam frequency ν_c. Here, the probe beam detuning $\delta_p = -10$ GHz and the pump beam intensity $I_c \sim 50 I_{sat}$. The black dotted horizontal line represents the integrated spin noise power χ without optical pumping. The line joining the data points are a guide to the eye.

the pump beam detuning in Fig. 4.12, and observe a clear dip near $F = 2 \rightarrow F'$ transition and a prominent peak near $F = 1 \rightarrow F'$ transition. Therefore, unlike conventional spectroscopy, in the case of SNS, we have the freedom to scan the pump beam for detecting the spectral lines instead of applying the pump beam at a particular known frequency as in Figs. 4.11(c) and 4.11(d). This, we believe, will be of particular advantage, when we wish to probe local environment-induced energy level shifts, or in resolving ground energy levels in complex molecular and condensed matter systems where one has incomplete knowledge of energy levels.

4.2.3 Reduction in width of optically pumped SN spectrum

So far we have discussed the basic features and applications of optically pumped SN spectrum by analyzing the integrated noise (Σ) measurements. However, the measurement of FWHM of the SN spectrum in presence of a pump beam conveys useful information about the characteristic relaxation rates of spin coherence in a non-equilibrium system. In this section, we present the modifications in FWHM of the ^{87}Rb SN signal with various pump beam power. The FWHM of the intrinsic SN spectrum shown in

Fig. 4.13 (first data point) is 222(±4) kHz (shaded horizontal region). The measurement is performed at cell temperature of 100°C and $B_\perp \sim 7.5$ G. We kept the probe beam detuning $\delta_p = -10$ GHz to detect the spin noise signal from $F = 2$ hyperfine manifolds. Note that in this experiment, the strength of the magnetic field is kept in the linear Zeeman regime and a single SN peak is observed in the spectrum.

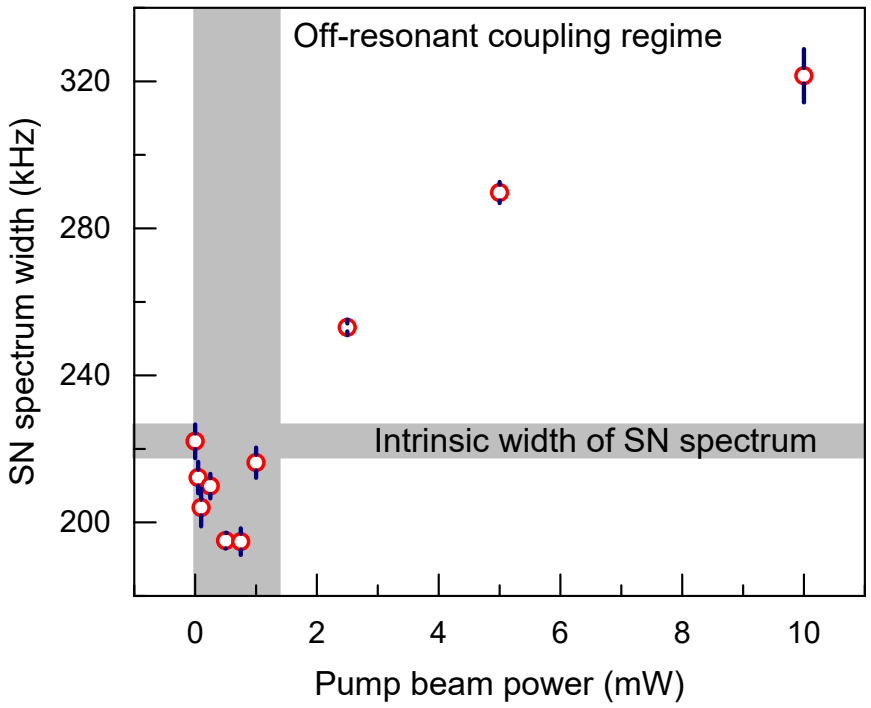

Figure 4.13: Variations of the FWHM of spin noise (SN) spectrum of ^{87}Rb atoms with control beam power. Control beam is kept on resonance to $F = 1 \rightarrow F' = 2$ transition of ^{87}Rb. The probe beam can detect only the SN signal from $F = 2$ Zeeman level manifolds ($\delta_p = -10$ GHz). The vertical shaded region shows the reduction in FWHM of the SN spectrum with control beam power. Right side of the shaded region, the FWHM increases with control beam power indicating the off-resonant coupling of the $F = 2$ atoms by the control beam. The horizontal shaded regions indicates the intrinsic width of the SN spectrum with error (1σ) for five measurements

In this optical pumping scheme, we have systematically transferred the atomic population from $F = 1$ hyperfine level into $F = 2$ level by fixing the pump beam frequency on $F = 1 \rightarrow F' = 2$ transition line. Thereafter we have detected the SN signal with various pump beam power and measured the FWHM of each of those spectrum. The dependence of measured FWHM with pump beam power is shown in Fig. 4.13. The error bars represent the 1σ uncertainty of the measured width for independent measurements taken completely randomly. In Fig. 4.13, we have observed a consistent reduction in FWHM (vertical shaded region) of the recorded SN signal at reasonably low power of the pump beam. This reduction is maximum ($\sim 15\%$ in

comparison to the FWHM of the intrinsic SN signal) at the saturation intensity of the pump beam. The reduction in FWHM of SN signal infers the longer spin coherence time of the optically pumped atoms in $F = 2$ hyperfine level. However, for higher pump beam power the FWHM is observed to be increased. According to the observations, we have divided the pump beam power into two regions namely: (a) Inter-hyperfine spin-exchange free region (the vertical shaded line) where the width has been reduced and (b) the off-resonant coupling region where the width is increased.

We have mentioned earlier that the ground hyperfine levels of ^{87}Rb atom possess same but opposite Landé $g-$factors ($g_{F=2} = 1/2$, and $g_{F=1} = -1/2$). This distinction in $g-$factors reduces the spin-coherence time after making a spin-exchange collision between two atoms in different hyperfine levels when $\nu_L \geq 1/T_2$. In our experiments, the Larmor precession rate is much faster than the spin-coherence rate, i.e. $\nu_L > 1/T_2$. Therefore, the spin-exchange collisions have a significant contribution in broadening the SN spectrum. However, such spin-exchange collisions can be reduced by transferring the atoms to a specific hyperfine level utilizing the optical pumping technique and synchronously precesses about the magnetic field for a longer time. This effect is shown in the shaded vertical column in Fig. 4.13 which can be recognized as region (a) of the pump beam. Nevertheless, the other spectral broadening sources such as spin-destruction collisions, wall collisions, transit times, and magnetic field in-homogeneity are unaffected by the optical pumping and contributed accordingly. Therefore at the saturation intensity of the pump beam, a maximum of 15% reduction in width has been observed in our experiments which is the sole contribution due to the spin-exchange collision.

In region (b), the width of the SN spectrum has been observed to be increased with pump beam intensity. Although in this region the entire population has been transferred to the $F = 2$ level, however, the presence of the strong pump beam during the experiment can optically excite these atoms via an off-resonant scattering process. Since we have observed a pressure broadened absorption line-width of the rubidium atoms in our cell is in a similar order of the ground hyperfine separation, the strong pump beam which is + 6.8 GHz away from $F = 2 \rightarrow F'$ line can significantly perturb the atomic spin precession. Such an optical scattering process on the optically pumped atoms is enhanced with the pump beam power. This process enhances the SN signal width with the pump beam power in the region (b). In conclusion, in region (a) the off-resonant scattering is insignificant on spin-coherence dynamics of optically pumped atoms, and the absence of spin-exchange collision makes the spin coherence time longer. Conversely, in region (b), the spin coherence time is reduced due to strong perturbation by the pump beam.

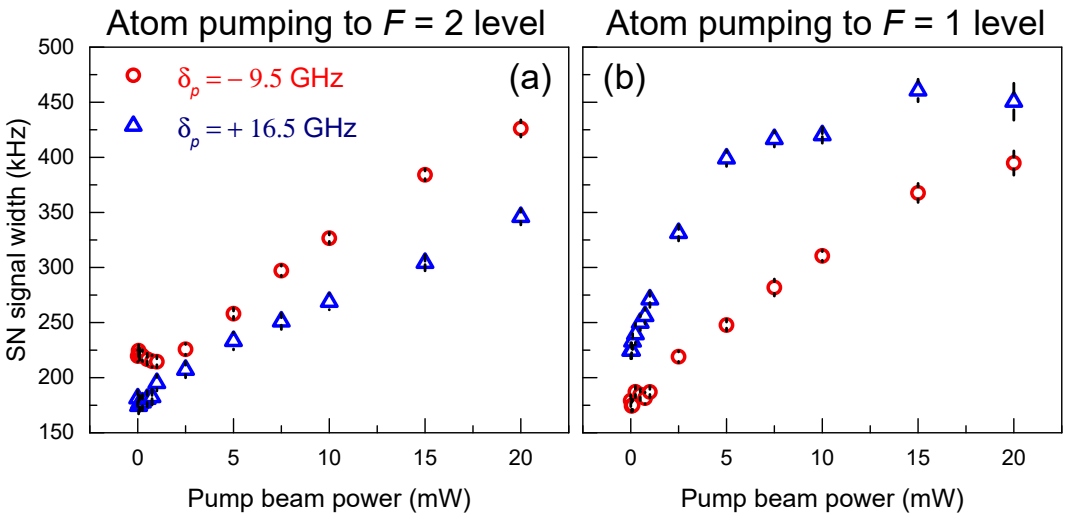

Figure 4.14: The reduction in FWHM of the spin noise (SN) spectrum from optically pumped atoms in $F = 2$ (a) and $F = 1$ (b) level. The red circular (blue triangular) data points are taken with probe beam close to $F = 2$ ($F = 1$) level. The reduction in FWHM of the SN spectrum have been observed for the atoms in optically pumped to $F = 2$ level, and probe beam close to $F = 2$ ($\delta_p = -9.5$ GHz). The width reduction is not observed from atoms in optically pumped to $F = 1$ level.

In another experiment, we have transferred the atoms into $F = 1$ hyperfine level and studied the FWHM as a function of pump beam power. However, in this case, we have not observed any detectable reduction in the width as shown in Fig. 4.14 (b). Here, the blue triangles (red circles) are the data that corresponds to the probe beam detuning kept on the blue (red) side with respect to the $F = 1 \rightarrow F'$ transition line (δ_p is the detuning as we defined earlier with respect to $F = 2 \rightarrow F' = 3$). Note that the red (blue) detuned probe beam detects the SN signal from $F = 2$ ($F = 1$) level. Since at thermodynamic equilibrium, the average population in $F = 2$ level is 5/3 (*i.e.* 1.67) times higher than $F = 1$ level, therefore more pump beam power is required to transfer the atoms from $F = 2$ to $F = 1$ level. In this case, before entering into the spin-exchange regime, the perturbation due to pump beam prevents increasing spin-coherence time as shown in Fig. 4.14 (b). In Fig. 4.14 (a), we have presented the similar study for optically pumped atoms in $F = 2$ level with probe beam kept on red and blue detuned side.

4.2.4 Optically pumped SN with different temperature

We have also investigated the optically pumped SN spectrum at various temperatures of the vapor cell. In this experiment, we detect the SN signal from spin imbalanced

$F = 2$ hyperfine level of ^{87}Rb atomic system at each pump beam power by keeping $\delta_p = -9.5$ GHz. The FWHM, signal strength and integrated spin noise for T = 80, 100 and 120°C are shown in Fig. 4.15.

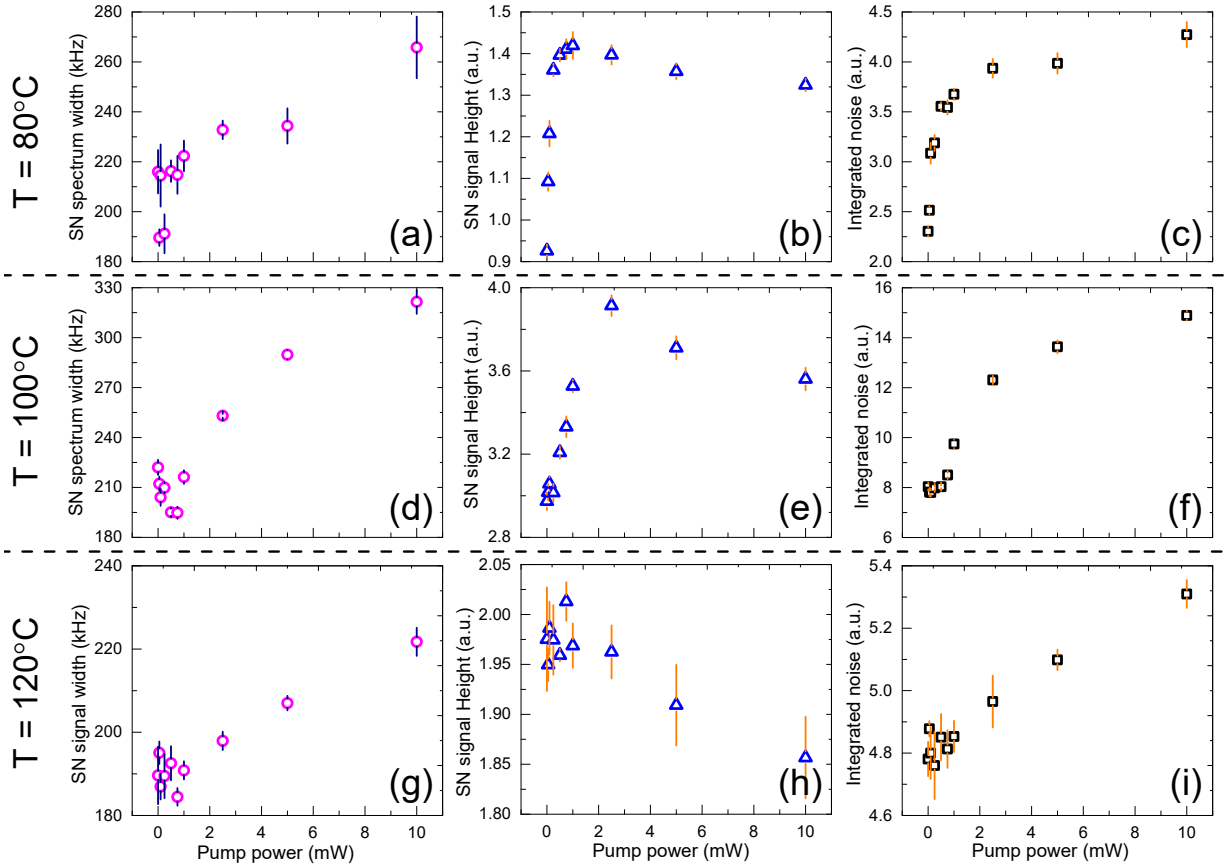

Figure 4.15: The FWHM, height and total integrated noise of the spin noise (SN) spectrum from the optically pumped atoms in $F = 2$ level at various temperature as a function of the pump beam power. The probe beam detuning was kept at $\delta_p = -9.5$ GHz.

Temperature controls the atom density inside the cell which manifests characteristic differences of these observations. These can be observed in the measured FWHM with pump beam power at these temperatures in the first column of Fig. 4.15 (a, d, g). We have observed a consistent trend of reduction in width for low pump beam power of all these temperatures. This part is explained in detail in the previous Sec. 4.2.3. However, the atom density is very less for 80°C, resulting in a dominating off-resonant coupling to the pumped atoms even at low pump beam power. The signal strength as a function of probe beam power is also investigated at these temperatures and shown in Fig. 4.15 (b, e, h), respectively. When the atoms are optically pumped to $F = 2$ level, the SN signal strength is expected to be higher with pump beam power due to

the accumulation of more number of atoms in this level. We have observed a similar trend as shown in Fig. 4.15 (b, e, h). After a certain value of the pump beam power, the height of the SN signal is observed to be reduced. This is due to the fact that our measurements are now entering into the off-resonant coupling domain. In this regime, due to the increase of the signal width (as evident in the first column of this Fig. 4.15 (a, d, g)), the SN signal smeared out − resulting in the reduction of height. Next, we study the integrated noise as a function of pump beam power at these temperatures. In a triangular approximation of the SN signal (recall the Lorentzian lineshape of the signal), the integrated noise is proportional to the multiplication of the first and second column for the relevant temperatures. Such integrated SN as a function of the pump power is shown in Fig. 4.15 (c, f, i) and is observed to increase with higher pump power for all these temperatures. This is quite intuitive to understand this observation by considering the fact that the optical pump beam accumulates more atoms in $F = 2$ level, and thereby increases the noise. We present these graphs to summarize the detailed picture of the dynamical SN signal parameters as a function of pump beam power at various temperatures.

Chapter 5

SNS with coherent optical driving in thermal atoms

This chapter is mostly based on the publication [17]. In the previous chapter, we have demonstrated the SNS technique in a non-equilibrium rubidium atomic system. Such a non-equilibrium system is achieved by optical pumping using a resonant and linearly polarized light. In this process of optical pumping, a population imbalance is created between the ground hyperfine levels. However, the populations are distributed equally in all possible Zeeman states within the resultant hyperfine level for a linearly polarized optical pumping beam. Therefore, the OP schemes do not induce any additional coherence between the atoms apart from manipulating them between ground hyperfine levels in a controlled manner. Nevertheless, the optical pumping is an incoherent process to randomly put the atoms in the accessible Zeeman states within the resultant ground hyperfine levels. The modifications in the SN spectrum and their FWHM in comparison to the intrinsic signal as described in chapter 4 reflect the population imbalance and its effect on the spin coherence rate, respectively. The enhancement of the SN signal strength of an optically pumped spin system can reach up to two times if the appropriate spin state is probed. Such a small enhancement in the strength of the SN signal is not enough to extract the information about the spin dynamics of a system where the intrinsic spin fluctuation is expected to be a few orders of magnitude less than the thermal atoms.

After the first detection of spin noise from thermal sodium atoms in 1981 [48], the fast Fourier transform (FFT) based spectrum analysis has improved tremendously to perform the experiment and extract the signal with good SNR in other spin systems such as conduction electrons, semiconductor quantum dots, and quantum wells, chemical compounds to name a few. The non-invasive detection of spontaneous spin fluctuations in cold (in the temperature range of μK) and ultra-cold (in the tempera-

ture range of nK) atomic ensembles are going to be useful to study various dynamical properties of the cold atoms. In order to detect the intrinsic spin fluctuations in a cloud of cold atoms, the signal strength improvement via improved electronics is required. In this chapter, we focus on the signal strength improvement via coherent optical drive which enables us to detect the intrinsic spin coherence from cold atoms, for the first time, using the existing electronics.

We coherently drive the atoms distributed in different Zeeman states within a ground hyperfine level using a pair of phase-coherent laser beams. The presence of this additional phase-coherent (we will call them Raman beams) laser beams drastically modifies the dynamics of the atomic spin system which in turn reflects in the spin noise signal. We have solved the master equations of the density matrix elements of the system using optical Bloch equations (OBEs) to investigate the modifications in the Raman driven signal. Experimentally we have demonstrated an enhancement of a million times of the Raman driven signal in comparison to the intrinsic spin noise signal with thermal atoms. Such a huge enhancement in the signal allows one to detect spin fluctuations in cold atoms and quantum gases. Note that, the probe beam and detection set-ups are kept the same while comparing the intrinsic and driven signal. We have investigated the driven signal in thermal atoms with various Raman beams parameters that will be discussed in detail in this chapter. The main goal in this work is to extract the information about the intrinsic spin coherence rate of the system by investigating the Raman driven signal using our developed theory.

When a lambda (Λ) type three-level system interacts with a pair of coherent laser fields, an existence of interference between different dipole transition pathways are proposed in [225]. They have observed a substantial modifications in the systems' susceptibility at the vicinity around the atomic (dipole) resonance frequency by analyzing the atom-light system based on density matrix treatment. The non-zero off-diagonal elements of the density matrix represent the existence of these various interference pathways. When the two near-resonant coupling laser fields are weak and similar in strength and other internal and external degrees of freedom of light and atoms are appropriate, a dark state is formed between the ground states. The atoms are observed to get trapped into the dark state via spontaneous emission, a phenomenon which is known as coherent population trapping (CPT) [226]. The existence of dark state and phenomenon of CPT is discussed in details in the articles [227–232]. The atoms which are trapped in the dark state are unaffected by the near-resonant laser fields and are free from other dissipation mechanisms present in the environments. Nevertheless, the net magnetization of such an atomic ensemble precess about the magnetic field coherently for a longer time, in principle for an infinite duration. In this chapter, we will

describe the contribution of these dark state atoms in the formation of SN signals based on Faraday rotation fluctuation measurements.

5.1 Theoretical Modelling

Let us consider the dynamics of valance electron of ^{87}Rb atoms in a Λ-type three level system (3LS) formed with two ground hyperfine levels within $5S_{1/2}, F = 2$ state and one excited level in $5P_{3/2}, F' = 3$ state. These are the Zeeman states within the hyperfine levels and we denote them as $|1\rangle, |2\rangle$ and $|3\rangle$ as shown in Fig. 5.1. These states are generated by applying a homogeneous magnetic field along the $\hat{z}-$axis. The optical dipole transitions connecting the levels $|1\rangle \leftrightarrow |3\rangle$ and $|2\rangle \leftrightarrow |3\rangle$ are driven by two off-resonant coherent laser (Raman) beams with Rabi angular frequencies Ω_{13} and Ω_{23}, respectively. Note that the dipole transition between the levels $|1\rangle \leftrightarrow |2\rangle$ are forbidden. In the following, we produce a microscopic model of the driven systems which we can solve exactly to find the correlations between the ground states. We will ignore the contributions of equilibrium thermal noise while deriving the spectrum for coherently driven 3LS. The equilibrium thermal noise form a background pedestal in the spectrum and we will show this in the experimental results part. The theoretical modelling for the Raman driven SN signal based on Heisenberg$-$Langevin equations are discussed in Appendix F. In the following section, we discuss the Raman induced ground state coherence using phenomenological master equations based on OBEs.

5.1.1 Phenomenological master equations for the driven 3LS

A pair of phase-coherent Raman radiation fields derived from ECDL interacts with a 3LS formed by two ground states $|1\rangle$, $|2\rangle$ and one excited state $|3\rangle$ as depicted in Fig. 5.1. The frequency, intensity, and polarization of the individual Raman beams are controlled using acousto-optic modulators (AOMs) and wave-plates.

The semi-classical interaction Hamiltonian of the 3LS in the presence of two Raman beams within the rotating-wave approximation (RWA) for semiclassical light-matter interaction can be written as [233]

$$\frac{\mathcal{H}_{int}}{\hbar} = (\Delta_{23} - \Delta_{13})\mu^{\dagger}\mu - \Delta_{13}\sigma^{\dagger}\sigma - \Omega_{13}(\sigma + \sigma^{\dagger}) - \Omega_{23}(\mu + \mu^{\dagger}), \tag{5.1}$$

where, we define the dipole transition operators of the 3LS by $\sigma^{\dagger} = |1\rangle\langle 3|$, $\mu^{\dagger} = |2\rangle\langle 3|$, $\nu^{\dagger} = |1\rangle\langle 2|$. Here, Ω_{13} and Ω_{23} are the resonant Rabi angular frequency of the Raman field 1 (R1) and Raman field 2 (R2), respectively. For simplicity, we have

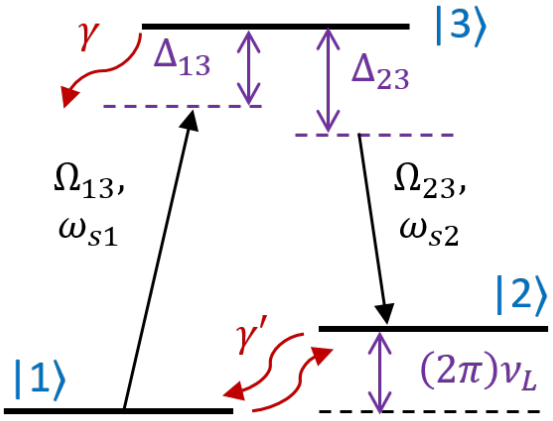

Figure 5.1: Energy level diagram used for coherent coupling between the Zeeman states ($|1\rangle$ and $|2\rangle$) within a ground $F-$level. Δ_{i3}, Ω_{i3}, and ω_{si} $(i = 1,2)$ are the optical detuning, Rabi frequency, and frequencies of the two Raman fields. γ is the excited state ($|3\rangle$, a Zeeman state in $F'-$level) linewidth, and γ' is the relaxation rate of spin coherence between the states $|1\rangle$ and $|2\rangle$. The Raman resonance condition is satisfied when the frequency difference between the Raman fields coincides with the frequency difference between the states $|1\rangle$ and $|2\rangle$ (i.e., $\omega_{s1} - \omega_{s2} = 2\pi\nu_L$), where ν_L is the Larmor frequency.

assumed that Ω_{13} and Ω_{23} to be real-valued. The detunings of the Raman fields from the related optical transitions are $\Delta_{13} = \omega_{s1} - \omega_3 + \omega_1$, $\Delta_{23} = \omega_{s2} - \omega_3 + \omega_2$, where $\omega_{s1}(\omega_{s2})$ is the angular frequency of the Raman field 1(2), and ω_i is that of the state $|i\rangle$ $(i = 1, 2, 3)$. The symbols s_1, s_2 denote the polarizations (linear or circular) of the two Raman fields.

In the presence of the Raman fields, the atoms are driven out of thermal equilibrium. The Raman beams are made to travel co-propagating to eliminate the Doppler effect of the thermal atoms during interacting with the Λ-system. The effect of interaction Hamiltonian $\mathcal{H}_{int}$ modifies the bare atomic eigenstates to a new set of eigenstates when analyzed from the rotating frame defined by the laser fields. One of this eigenstate is the so-called dark atomic state formed between two ground states $|1\rangle$ and $|2\rangle$ and can be represented as $|\psi_D\rangle = c_1|1\rangle - c_2|2\rangle$. Here the amplitudes c_i $(i = 1, 2)$ depends on the Rabi frequencies of the Raman beams. The dark state $|\psi_D\rangle$ does not contain any amplitude of the excited state $|3\rangle$ and can be effectively decoupled from the laser fields with the proper choices of the amplitudes c_is. Therefore the atoms in this coherent superposition state live longer (ideally for infinite time) and precess coherently around the applied magnetic field. The power spectrum for the coherently driven system will ideally be a delta function. In the following, we will experimentally demonstrate and theoretically show that this is in fact the case. However, the contributions of the

equilibrium thermal noise (i.e. intrinsic spin noise) and incoherent excitation of the atoms by the Raman radiation fields are ignored in the theoretical derivation.

We can directly write the phenomenological master equations (Lindblad equations) for the evolution of various components of the density matrix of the 3LS for the Hamiltonian $\mathcal{H}$ in Eq. F.1. These equations are similar to those obtained from the microscopic Heisenberg-Langevin equations but with some differences in the rates which we point out below. Since the intrinsic fluctuations (related to the equilibrium noise, e.g., $\eta(t)$ above) only form a broad background in the measured power spectrum for a relatively strong driving by the Raman fields, we drop these noise terms from the following master equations to be able to extract an analytical expression for the measured power spectrum. These master equations are written in the rotating frame by rewriting the elements of coherence as $\tilde{\rho}_{31}(t) = \rho_{31}(t)e^{-i\omega_{s_1}t}, \tilde{\rho}_{32}(t) = \rho_{32}(t)e^{-i\omega_{s_2}t}, \tilde{\rho}_{21}(t) = \rho_{21}(t)e^{-i(\omega_{s_1}-\omega_{s_2})t}$ where $\tilde{\rho}_{31}(t), \tilde{\rho}_{32}(t)$ and $\tilde{\rho}_{21}(t)$ are the density matrix elements in the laboratory frame and $\rho_{ij}(t)$ are those in the rotating frame. We study how the drive beams affect the coherence between the ground levels $|1\rangle$ and $|2\rangle$. We further take the following limits for the relaxation rates, $\gamma_{13} = \gamma_{23} = \gamma, \gamma_{12} = \gamma_{21} = \gamma', \gamma_{31} = \gamma_{32} = 0$ and $\gamma' \ll \gamma$, to simplify the master equations. We get,

$$\begin{aligned}
\frac{d\rho_{11}}{dt} &= \gamma(1-\rho_{11}-\rho_{22}) - i\Omega_{13}(\rho_{13}-\rho_{31}), && (5.2)\\
\frac{d\rho_{22}}{dt} &= \gamma(1-\rho_{11}-\rho_{22}) - i\Omega_{23}(\rho_{23}-\rho_{32}), && (5.3)\\
\frac{d\rho_{13}}{dt} &= -(\gamma+i\Delta_{13})\rho_{13} - i\Omega_{23}\rho_{12} \\
&- i\Omega_{13}(2\rho_{11}-1+\rho_{22}), && (5.4)\\
\frac{d\rho_{31}}{dt} &= -(\gamma-i\Delta_{13})\rho_{31} + i\Omega_{23}\rho_{21} \\
&+ i\Omega_{13}(2\rho_{11}-1+\rho_{22}), && (5.5)\\
\frac{d\rho_{23}}{dt} &= -(\gamma+i\Delta_{23})\rho_{23} - i\Omega_{13}\rho_{21} \\
&- i\Omega_{23}(2\rho_{22}-1+\rho_{11}), && (5.6)\\
\frac{d\rho_{32}}{dt} &= -(\gamma-i\Delta_{23})\rho_{32} + i\Omega_{13}\rho_{12} \\
&+ i\Omega_{23}(2\rho_{22}-1+\rho_{11}), && (5.7)\\
\frac{d\rho_{12}}{dt} &= -i(\Delta_{13}-\Delta_{23}-i\gamma')\rho_{12} + i\Omega_{13}\rho_{32} \\
&- i\Omega_{23}\rho_{13}, && (5.8)\\
\frac{d\rho_{21}}{dt} &= i(\Delta_{13}-\Delta_{23}+i\gamma')\rho_{21} - i\Omega_{13}\rho_{23} \\
&+ i\Omega_{23}\rho_{31}. && (5.9)
\end{aligned}$$

These master equations are exactly similar to those in Eq. F.13 when we identify the elements of the density matrix with the expectation of related operators. (i.e. $\rho_{13}(t) \equiv S_1(t), \rho_{12}(t) \equiv S_2(t), \rho_{32}(t) \equiv S_3(t), \rho_{33}(t) \equiv S_{11}(t), \rho_{11}(t) \equiv S_{22}(t)$). However, there are some differences arising from the identification of γ_{21} or γ_{12} with γ_3. We apply these equations to investigate how the Raman fields affect the coherence $\tilde{\rho}_{21}(t)$ between the ground levels. From the above set of equations, we find $\rho_{21}(t)$ at the steady-state by setting $d\rho_{ij}(t)/dt = 0$.

An off-resonant, linearly polarized probe laser field propagating along x-direction dispersively detects the temporal fluctuations of the population between the Zeeman states within a ground hyperfine level of rubidium atoms. The measured instantaneous Faraday rotation of the probe field is proportional to the instantaneous population difference between the consecutive Zeeman states. Therefore the autocorrelation of the Faraday rotation signal can be represented by a two-time correlation $\langle\tilde{\rho}_{21}^{\dagger}(t)\tilde{\rho}_{21}(0)\rangle$ of density matrix coherence ($\tilde{\rho}_{21}$) between these states in the laboratory frame. We write the power spectrum by taking the Fourier transform of such a correlation:

$$\begin{aligned} P(\omega) &= \frac{1}{2\pi}\int_{-\infty}^{\infty} dt\, e^{i\omega t}\tilde{\rho}_{21}^{\dagger}(t)\tilde{\rho}_{21}(0) \\ &= \frac{1}{2\pi}\int_{-\infty}^{\infty} dt\, e^{i(\omega-\omega_{s_1}+\omega_{s_2})t}\rho_{21}^{\dagger}(t)\rho_{21}(0), \end{aligned} \tag{5.10}$$

where the expectation is performed over equilibrium thermal noise. For a strong driving, we ignore the equilibrium noise in leading order to obtain a simple expression for the power spectrum of the strongly driven atoms at steady-state. When the driven atoms reach the steady-state at a long time, $\rho_{21}(t)$ becomes time-independent. Then, we can replace $\rho_{21}(t)$ and $\rho_{21}(0)$ by their steady-state value ρ_{21} to find,

$$\begin{aligned} P(\omega) &= \frac{1}{2\pi}\int_{-\infty}^{\infty} dt\, e^{i(\omega-\omega_{s_1}+\omega_{s_2})t}|\rho_{21}|^2 \\ &= \delta(\omega+\omega_{s_2}-\omega_{s_1})|\rho_{21}|^2. \end{aligned} \tag{5.11}$$

We can find a relatively simple formula for ρ_{21} by choosing $\Omega_{13} = \Omega_{23} = \Omega$,$\gamma_{13} = \gamma_{23} = \gamma, \gamma_{12} = \gamma_{21} = \gamma'$ and $\Delta_{23} = 0, \Delta_{13} = \Delta$:

$$\rho_{21} = -\frac{\gamma\Omega^2((\gamma'+i\Delta)(2\gamma+i\Delta)+4\Omega^2)}{\gamma(\gamma'^2+\Delta^2)(2\gamma^2+\Delta^2)+(2\gamma\gamma'(3\gamma'+4\gamma)+(\gamma'+2\gamma)\Delta^2)\Omega^2+4(3\gamma'+2\gamma)\Omega^4}. \tag{5.12}$$

$P(\omega)$ in Eq. 5.11 shows a delta peak at $\omega = \omega_{s_1} - \omega_{s_2} =: 2\pi\delta_{12}$, whose strength $|\rho_{21}|^2$ in Eq. 5.12 grows rapidly with increasing Ω before saturating at large Ω. Note, $A := B$ indicates that A (: towards A) is defined to be B, i.e. in the last line we defined δ_{12}

in terms of the Raman laser frequency difference, $\omega_{s_1} - \omega_{s_2}$. Therefore in the driven spectrum, the delta function peak will appear at the two photon frequency difference of the Raman beams which we define as δ_{12}. Further we can also express δ_{12} in terms of the optical detunings of the Raman beams (Δ_{13}, Δ_{23}) and the Larmor frequency (ν_L) of the atoms in the ground levels, in the following fashion: $2\pi\delta_{12} = 2\pi\nu_L - (\Delta_{23} - \Delta_{13})$ (see Fig. 5.1). Note also that, for our measurements, any relative phase difference between Ω_{13} and Ω_{23} is irrelevant. This point will be clear when we discuss the results.

The power spectrum in Eq. 5.11 gives a delta peak at spectral frequency $\omega = \omega_{s_1} - \omega_{s_2}$ whose strength is determined by $|\rho_{21}(\infty)|^2$ given in Eq. 5.12. The strength of the peak is maximum when $\Delta = 0$ ($\Delta_{13} = \Delta_{23}$ for general detunings), and the peak height falls with increasing $|\Delta|$ as shown in Fig. 5.2. When $\Delta_{13} = \Delta_{23}$, we get $\delta_{12} = \nu_L$ signifies that the driven spectrum strength is maximum when the two-photon difference of the Raman beams is equal to the Larmor frequency of the atoms. This is the Raman resonant condition ($\delta_{12} = \nu_L$), and in this situation, more and more atoms will trap into the dark state. For $\Delta_{23} = 0$, the envelope of the sharp delta peaks has a Lorentzian-like shape centered around $\Delta_{13} = 0$ when $\Omega < \gamma$ but it changes to Gaussian-like shape for larger Ω. We also present the simulated envelope spectrum of the Raman driven signal in a wide parameter range for Ω, γ and γ' in Fig. 5.3. In the inset of Fig. 5.2, we further show the dependence of the envelope width of the driven power spectrum as a function of the (scaled) driving Rabi frequency Ω/γ. As intuitively expected, the envelope width falls with decreasing driving Rabi frequency which we have also measured experimentally in thermal vapor. For $\Delta_{23} \neq 0$, the peak height is maximum around $\Delta_{13} = \Delta_{23}$.

The coherence between the ground levels is induced by the Raman beams, and its strength increases with increasing value of the Rabi frequencies of the Raman beams before saturating at higher $\Omega > \gamma$ as shown in Fig. 5.4. The dependence of coherence on Ω can be understood easily by taking resonant limit $\Delta = 0$ (i.e. $\delta_{12} = \nu_L$) in Eq. 5.12, and we get

$$|\rho_{21}(\infty)|^2_{\Delta=0} = \frac{\gamma^2\Omega^4}{(\gamma'\gamma^2 + (3\gamma' + 2\gamma)\Omega^2)^2}. \tag{5.13}$$

Intrinsic spin noise spectrum In the absence of driving by the Raman fields ($\Omega = 0$), the rubidium atoms are in thermal equilibrium, and the populations in their hyperfine ground level Zeeman states fluctuate over time due to thermal (and quantum) fluctuations. Such equilibrium population fluctuations generate an intrinsic SN in the atomic vapor as discussed earlier in this thesis. When $\Omega = 0$, only the lower two levels

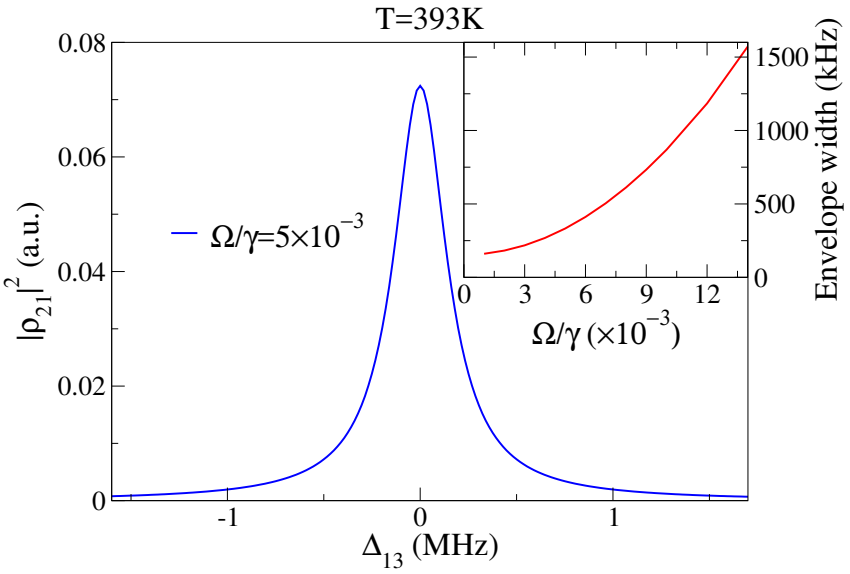

Figure 5.2: The envelope $|\rho_{21}|^2$ of the Raman driven power spectrum (in arbitrary unit) from rubidium atomic vapor with the Raman beam detuning Δ_{13} at relatively low driving Rabi frequency $\Omega/\gamma = 5 \times 10^{-3}$ and temperature T= 393K where $\Delta_{23} = 0$. The inset shows the dependence of the envelope width (with a factor of 2π) of the driven power spectrum as a function of the (scaled) driving Rabi frequency Ω/γ.

of the three-level system (3LS) participate in the equilibrium spin dynamics detected by the probe beam. Therefore, we can derive the SN spectrum by including a noise term in the master equations of the density matrix elements of these levels. Thus, we write

$$\frac{d\tilde{\rho}_{21}}{dt} = i(\omega_2 - \omega_1 + i\gamma_{21})\tilde{\rho}_{21} + \eta(t), \tag{5.14}$$

where we assume the noise $\eta(t)$ to be a Gaussian white noise with zero mean and $\langle \eta(t')\eta(t'')\rangle = N_2\gamma_{21}\delta(t'-t'')$, where N_2 is number of atoms within the measurement region. We then get the power spectrum $P(\omega)|_{\Omega=0}$ of the spontaneous spin fluctuations as:

$$\begin{aligned} P(\omega)|_{\Omega=0} &= \frac{1}{2\pi}\int_{-\infty}^{\infty} dt\, e^{i\omega t}\langle\tilde{\rho}_{21}^{\dagger}(t)\tilde{\rho}_{21}(0)\rangle \\ &= \frac{1}{\pi}\mathrm{Re}\Big[\int_{0}^{\infty} dt\, e^{i\omega t}\langle\tilde{\rho}_{21}^{\dagger}(t)\tilde{\rho}_{21}(0)\rangle\Big] \\ &= \frac{N_2}{2\pi}\frac{\gamma_{21}}{\gamma_{21}^2 + (\omega - \omega_2 + \omega_1)^2}. \end{aligned} \tag{5.15}$$

where γ_{ij} is the relaxation rate of the spin coherence between states i to j of the atoms and N_2 is the number of atoms in the observation region. $P(\omega)|_{\Omega=0}$ is

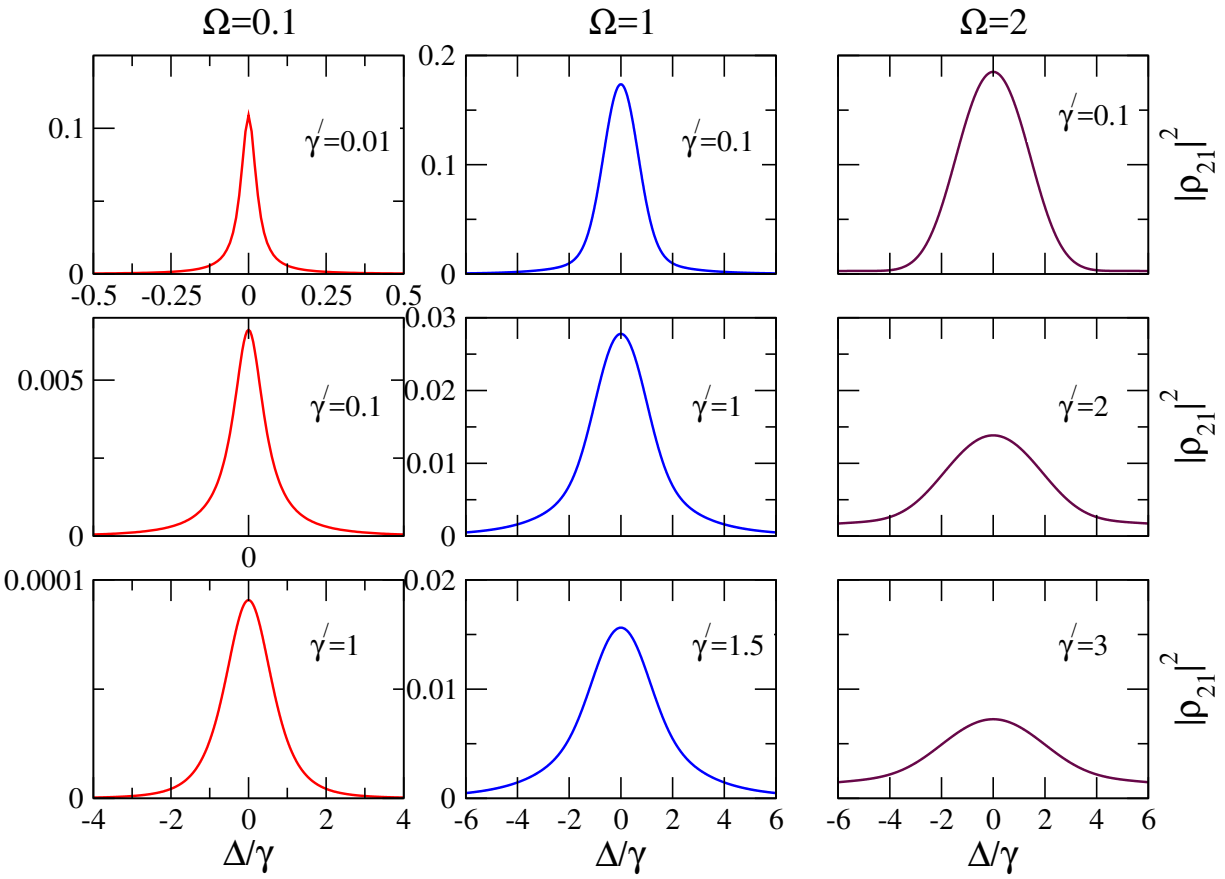

Figure 5.3: Features of symmetric $|\rho_{21}(\infty)|^2$ as a function of the detuning Δ ($\equiv \Delta_{13}$) of the Raman beam for various Raman beam driving Ω ($= \Omega_{13} = \Omega_{23}$) and decay rate γ' ($\gamma_{12} = \gamma_{21}$). Here, $\Delta_{23} = 0$. All parameters are in units of γ ($\gamma_{13} = \gamma_{23}$).

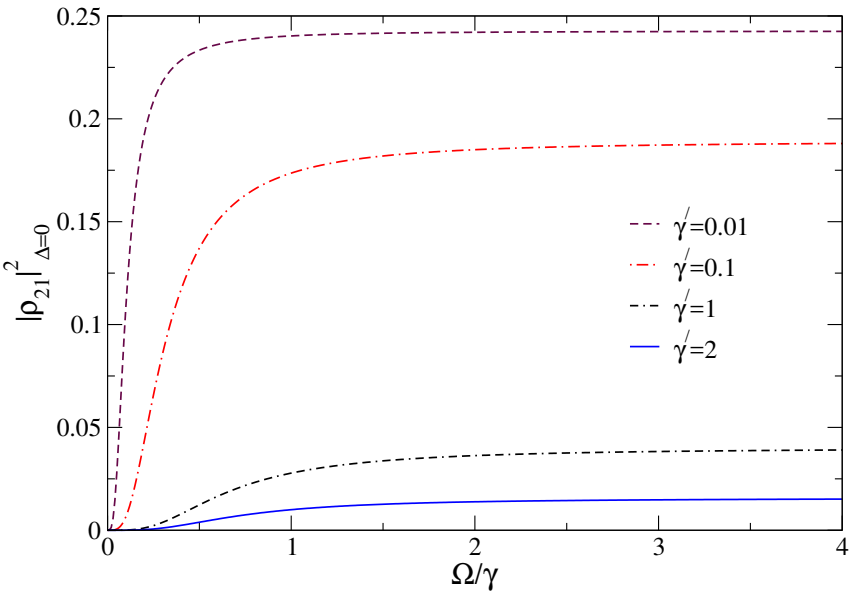

Figure 5.4: Dependence of the induced coherence $|\rho_{21}(\infty)|^2_{\Delta=0}$ between the ground levels on the Rabi frequency Ω of the Raman beams at resonance. All parameters are in units of γ ($\gamma_{13} = \gamma_{23}$).

a Lorentzian centered around $\omega = (\omega_2 - \omega_1) =: 2\pi\nu_L$ and with a full-width at half maximum (FWHM) of $2\gamma_{21}$.

5.2 Experimental results and discussions

In this section, we present the experimental results for the Raman driven spectrum of thermal ^{87}Rb atoms and compare them with the theory presented in the previous section. We will also extract information about the intrinsic spin-coherence of the atoms from the driven envelope spectrum. We will show the enhancement of the driven spectrum strength in comparison to the intrinsic SN signal. We also rigorously study the dependence of the driven spectrum strength on the relative polarization states of the Raman beams. A qualitative theory of polarization dependent on the driven spectrum that supports the experimental observations are also discussed. Next, we present Raman beam induced coherence transfer between homo-nuclear atoms with different $g-$factors. We also observe a generation of higher harmonics in the spectrum at multiples of δ_{12} frequency for the strong coupling of atoms by the Raman beams.

5.2.1 Details of the set-up

The details of the experimental set-up for intrinsic spin noise measurements of Rb atoms are presented in chapter 3. The arrangement of the Raman beams for the measurements of the coherently driven spectrum is shown in Fig.5.5 (a). A linearly polarized probe laser beam (blue) is sent through the vapor cell along $x-$direction and collected in the polarimetric and detection set-up. The laser beam is focused at the center of the cell. We use the same Rb atomic vapor cell for the measurements of Raman driven signal as mentioned in chapter 3. We kept the probe beam detuning $\delta_p = -4\gamma$ away from the relevant transition as shown in Fig.5.5 (b). We have independently measured the pressure broadened (due to the presence of neon buffer gas in the cell) line-width of the absorption signal of ^{87}Rb atom is $\gamma = 2\pi\times$ 1.79(0.02) GHz. A homogeneous magnetic field is applied on the atoms along the $z-$direction using a pair of magnetic coils in Helmholtz configuration.

For the detection of Raman driven signal, we sent a pair of phase correlated laser beams (red) through the vapor cell. We align the Raman beams with a small angle $\sim 3^\circ$ with respect to the x-axis to prevent them from falling on the photo-detector and block them after the cell. The Raman beams are generated from another ECDL with linewidth below 1 MHz. The frequency of the Raman beams are tuned in such a way to address the transition $5S_{1/2}, F = 2 \rightarrow 5P_{3/2}, F' = 3$ (D_2) transition of ^{87}Rb as depicted

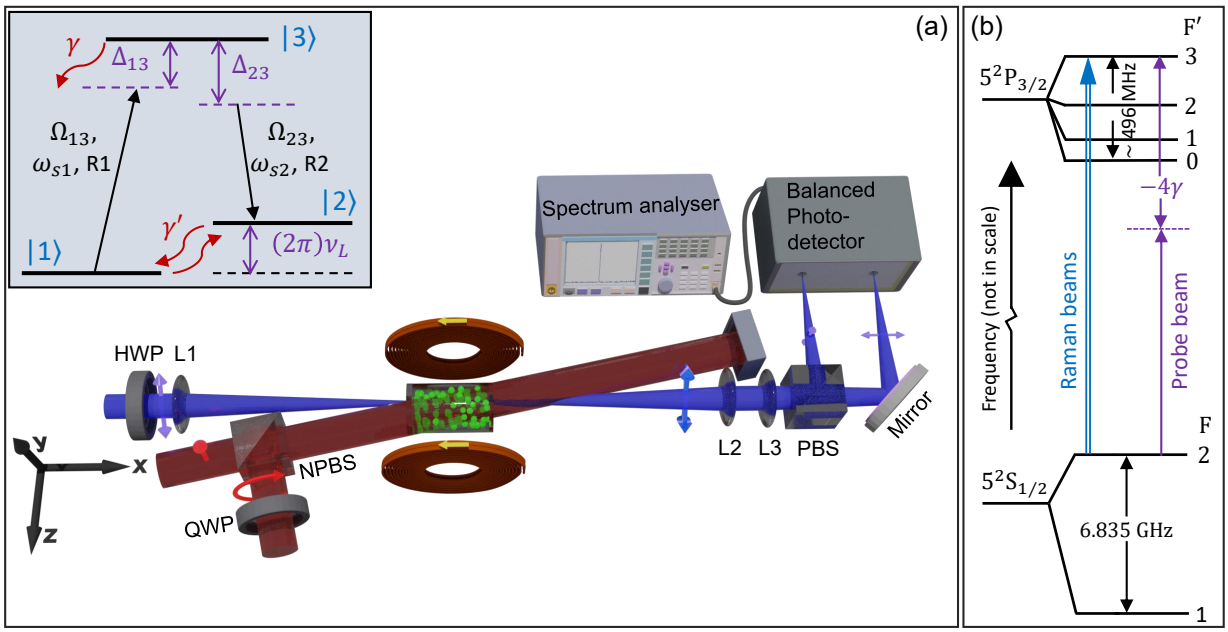

Figure 5.5: The schematic of the experimental set-up for the detection of Raman driven spectrum using Faraday rotation fluctuation measurements and the relevant energy levels of the ^{87}Rb atoms. (a) depicts the arrangements of the Raman beams (red), probe beam (blue), magnetic coils, vapor cell (filled with rubidium atoms and neon buffer gas) and detection set-up. The magnetic coils are arranged in Helmholtz configuration to produce a homogeneous magnetic field over the vapor cell. The red linear and circular arrows indicates the polarization states of the Raman beams. HWP: half-wave plate, QWP: quarter-wave plate, L1, L2, L3: lenses, NPBS: non-polarizing beam splitter, PBS: polarizing beam splitter. (b) The relevant electronic energy level diagram of ^{87}Rb atoms [22] and the probe and Raman laser frequencies used for the measurements. (a-inset) We indicate the Raman beams as Raman beam 1 (R1) and Raman beam 2 (R2). In the experiment, we select $|F = 2, m_F = -1\rangle \equiv |1\rangle$, $|F = 2, m_F = 0\rangle \equiv |2\rangle$ and $|F' = 3, m_{F'} = 0\rangle \equiv |3\rangle$ of the ^{87}Rb atoms.

in Fig.5.5 (b). The spatial mode of the Raman beams is cleaned to the Gaussian mode using polarization maintaining fibers. The fiber output laser beam is then split into two parts using an HWP and PBS. Thereafter, these two beams are sent through separate but similar AOMs. The frequency of the AOMs is tuned by the voltage control oscillator (VCO) in the radio-frequency (RF) range. The details of AOM is discussed in Appendix B. We have taken the -1^{st} order diffracted beam from each AOMs as a Raman beams. The diameter of the Raman beams is ∼3.4 mm. Before sending them into the vapor cell, the Raman beams are made to overlap using a non-polarising beam splitter (NPBS) to generate the beat signal. The instantaneous spectral width of the beat signal is ∼ 200 Hz with a 10 Hz resolution bandwidth (RBW) of the spectrum analyzer. However, the frequency jitter of beat signal over a second of integration time is ∼ 2 kHz which is the typical measurement time of the driven spectrum using Raman beams. This jitter in the frequency of the beat signal is originated from the voltage fluctuations which are fed into the VCO of the AOM. The polarization of the Raman fields can be independently varied, employing the combination of half-wave plates (HWPs) and quarter-wave plates (QWPs). We typically manage to obtain a polarization purity of the Raman fields > 99%.

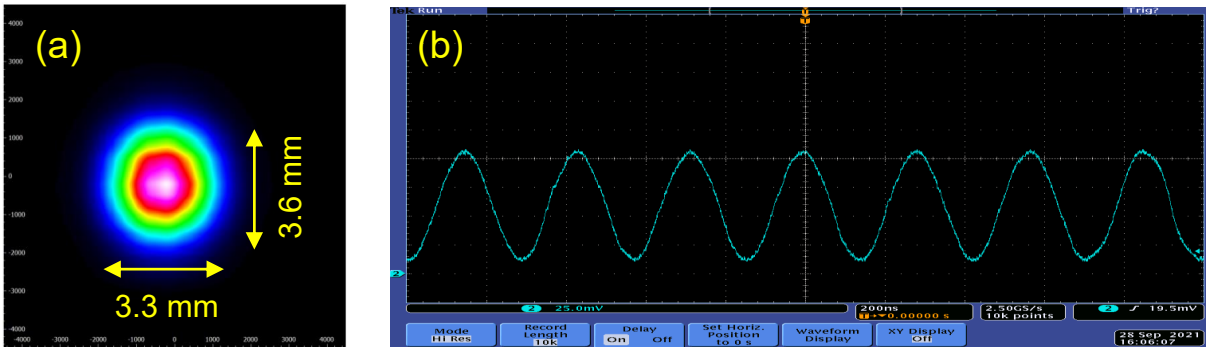

Figure 5.6: The spatial intensity profile (a) and the temporal interference pattern (b) of the combined Raman beams measured before the vapor cell.

We have also measured the temporal interference pattern of the combined Raman beams before sending them into the vapor cell. We have maximized the overlap between the Raman beams on the NPBS by maximizing the strength of the temporal interference signal on the oscilloscope as shown in Fig.5.6 (b). The spatial intensity profile of the combined Raman beams before the cell is shown in Fig.5.6 (a).

5.2.2 Enhancement of the signal using Raman driving

First we demonstrate the generation of the delta function peak (see Eq. 5.11) at frequency δ_{12} in the spectrum and the enhancement of that signal-strength with the Raman driving as compared to the intrinsic SN signal (i.e., $\Omega = 0$) in the thermal ^{87}Rb atomic vapor. In the experiment, we select the 3LS as $|F = 2, m_F = -1\rangle \equiv |1\rangle$, $|F = 2, m_F = 0\rangle \equiv |2\rangle$ and $|F' = 3, m_{F'} = 0\rangle \equiv |3\rangle$ (see Fig.5.5 (a-inset) and Fig.5.5 (b)). We choose the polarization of the Raman fields in the $(\pi_1)_x - (\sigma_2^+)_x$ configuration where the subscript 1(2) refers to R1 (R2), and x-axis is the propagation direction of the Raman fields. We keep the Raman beams continuously on during the measurements.

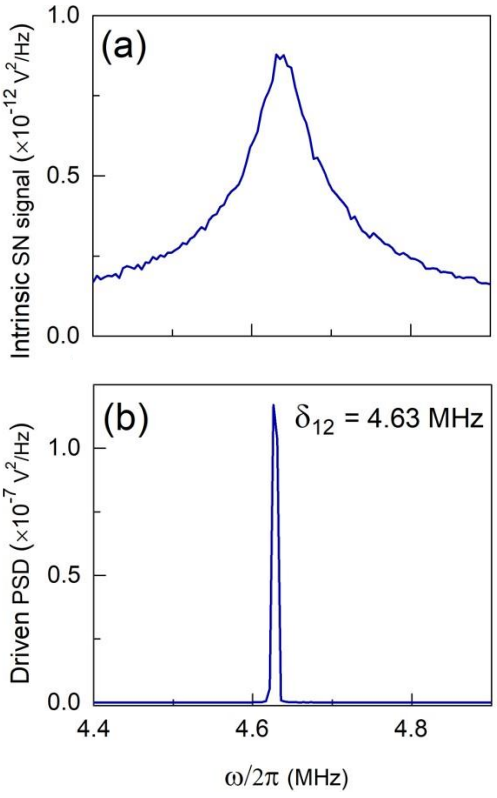

Figure 5.7: The formation of the delta peak at frequency δ_{12} when the Rb atoms are coherently driven by the Raman beams. (b) shows an extremely narrow peak (broadens by the experimental noise) in the driven spectrum at the Raman resonance condition (i.e. $\delta_{12} = \nu_L$) for the Raman beams intensity of Ω/γ =7.6 $\times$ 10^{-3}. An enhancement of the signal strength of 10^5 times in comparison to the intrinsic SN signal (a) has been observed as predicted by the theory.

The measured intrinsic spin noise power spectrum $P(\omega)|_{\Omega=0}$ is presented in Fig. 5.7(a), which shows the Lorentzian FWHM of $\sim 2\pi\times$ 150 kHz for ^{87}Rb atoms in thermal equilibrium at T = 388 K. We have experimented with a lower frequency span of the spectrum analyzer which detects the intrinsic SN signal at the Larmor frequency of $\sim$

4.63 MHz. The Faraday rotation is an angle having a unit of rad. Since we have performed a polarimetric measurement on a balanced photo-detector with output in volts, the power spectral density (PSD) has a unit of V^2/Hz [15, 174]. The data acquisition time for this measurement is 98 seconds.

Next, we employ the Raman beams ($\Omega \neq 0$) to pass through the atomic systems and detect the driven PSD at the Raman resonance condition, i.e. at $\delta_{12} \sim 4.63$ MHz. The detected driven PSD is shown in Fig. 5.7(b) for $\Omega/\gamma = 7.6 \times 10^{-3}$. Experimentally we observed a small but finite width ($\sim$ 2 kHz) of the detected signal instead of the delta function as predicted in Eq. 5.11. This width is due to the relative frequency jitter of the two Raman fields during the acquisition time of the signal which is derived from two independent AOMs. The data acquisition time for this signal is one second. Additionally, we have also observed an enhancement of the signal strength ($|\rho_{21}|^2$) for $P(\omega)|_{\Omega\neq 0}$ by 10^5 times in comparison to the intrinsic SN signal as shown in Fig. 5.7 (a).

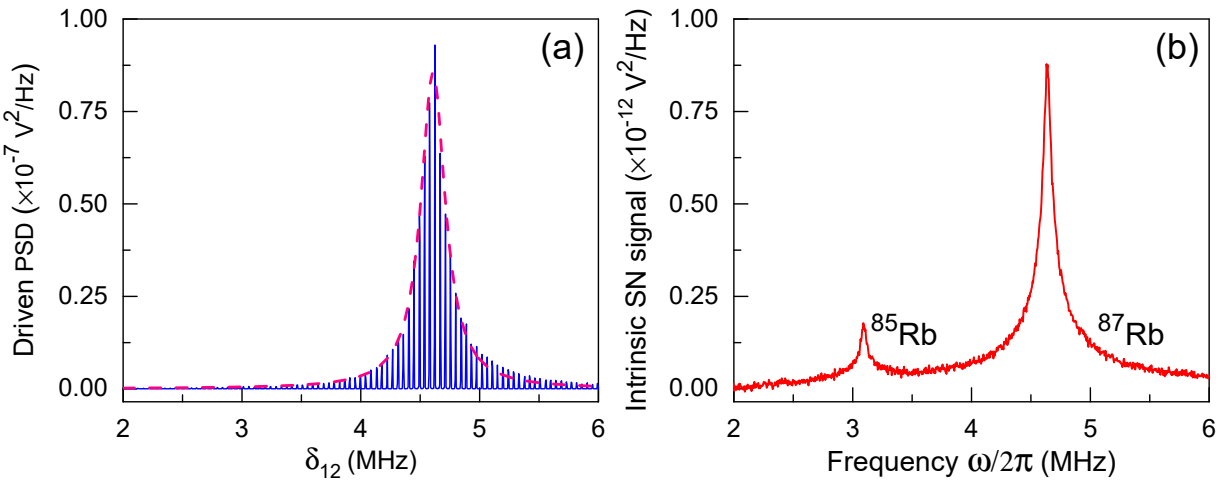

Figure 5.8: Raman driven envelope spectrum (a) and intrinsic spin noise (SN) spectrum (b) rubidium atomic vapor at T = 388 K. In (a), ^{87}Rb atoms were coherently driven by a pair of Raman fields, and the envelope of the series of spectra is fitted by $|\rho_{21}|^2$ shown in Eq. 5.12 (pink dashed line). The strength of the driven spectrum is enhanced by approximately 10^5 times in comparison to the intrinsic SN signal when the Raman field intensity Ω/γ =7.6 $\times$ 10^{-3} and $2\gamma' = 2\pi \times 118.6$ kHz.

In the subsequent experiments, we vary δ_{12} while keeping $\Delta_{23} = 0$ (i.e. we vary the frequency of the R1 centered around $\Delta = \Delta_{13} = 0$), and record a series of spectra shown in Fig. 5.8(a). The peak height is maximum when $\Delta = 0$ (i.e., $\delta_{12} = \nu_L$), and it decreases with increasing $|\Delta|$. The envelope of the narrow peaks with varying δ_{12}, as shown in Fig. 5.8(a), has a "Lorentzian−like" shape when $\Omega < \gamma$. But it switches to a "Gaussian−like" shape for larger Ω. For the experiments performed in this work, the

Ω/γ has always been less than 1, therefore we explored the "Lorentzian−like" regime. These series of spectra span an envelope that is fitted (pink dashed line) by the formula $|\rho_{21}|^2$ given in Eq. 5.12 with fitting parameters Ω/γ =7.6 $\times$ 10^{-3} and $2\gamma' = 2\pi \times 118.6$ kHz. This fitting gives a peak position of the envelope spectrum at ν_L and an envelope width of $\sim 2\pi\times$ 250 kHz. As a comparison to the undriven signal, we have also provided the intrinsic SN signal shown in Fig. 5.8(b) taken in the same experimental parameters (with $\Omega = 0$). In Fig. 5.8(b), we have observed a significant SN contribution of the ^{85}Rb atoms which are left undriven by the Raman beams in Fig. 5.8(a). Therefore, the enhancement of the Raman signal for ^{85}Rb atoms are not prominent in Fig. 5.8(a).

5.2.3 Measurement of intrinsic spin coherence using driven PSD

The dependence of $|\rho_{21}|^2$ on Ω can be understood by taking the Raman resonant limit $\Delta = 0$ ($\delta_{12} = \nu_L$) in Eq. 5.12, and we get Eq. 5.13. Eq. 5.13 shows that the coherence between the ground levels grows with increasing Ω before saturating for higher $\Omega > \gamma$. The on-resonance signal strength has a simple dependence on the three parameters, namely Ω, γ, and γ'. However, the value of γ is constant for the Rb atoms inside the cell. Therefore, for a particular temperature, the dependence of on-resonance signal strength with Ω provides information about the intrinsic spin-coherence rate (γ') according to the Eq. 5.13. In order to measure $|\rho_{21}|^2_{\Delta=0}$, we vary the intensities of the Raman fields keeping $\Delta = 0$. We have performed this measurement for two different temperatures of the cell in order to compare the value of γ' extracted from the driven PSD with the intrinsic spin-coherence rate.

The measured on-resonance peak strength $|\rho_{21}|^2_{\Delta=0}$ as a function of Ω/γ is plotted in Fig. 5.9. The black triangles (blue circles) are the data corresponding to T = 373 K (393 K) of the vapor cell. We fit these data by Eq. 5.13 (solid lines) keeping only γ' as a free parameter. We extract the value of $2\gamma'$ to be $2\pi\times(95\pm7)$ kHz and $2\pi\times(136\pm15)$ kHz for 373 K and 393 K, respectively. We have separately measured the FWHM of the intrinsic SN spectrum to be $2\pi\times(126\pm3)$ kHz and $2\pi\times(153.7\pm0.4)$ kHz for these temperatures, respectively. We attribute these small but finite (within 25 %) differences to two competing effects of different physical origins - the perturbation induced by the Raman driving to bring the atoms beyond thermal equilibrium and linear response, and the suppression of spin projection noise due to coherent coupling.

We have also extracted the value of γ' by fitting the recorded envelope spectrum with Eq. 5.12 with keeping γ' as a free parameter. For this, we have recorded the envelope of $P(\omega)$ by varying δ_{12} for a fixed value of Ω. We repeat these experiments for various values of Ω/γ and fit each spectrum with a Lorentzian function (since $\Omega/\gamma <$

1). The extracted FWHMs of the envelope for various Ω/γ are shown in Fig. 5.10. Black triangles (blue circles), shown in the inset, are the extracted values of $2\gamma'$ after fitting the envelope with $|\rho_{21}|^2$ given in Eq. 5.12 for T = 373 K (393 K), respectively. The average value of $2\gamma'$, extracted from these measurements is $2\pi\times(95\pm6)$ kHz and $2\pi\times(131\pm10)$ kHz for those two temperatures, respectively.

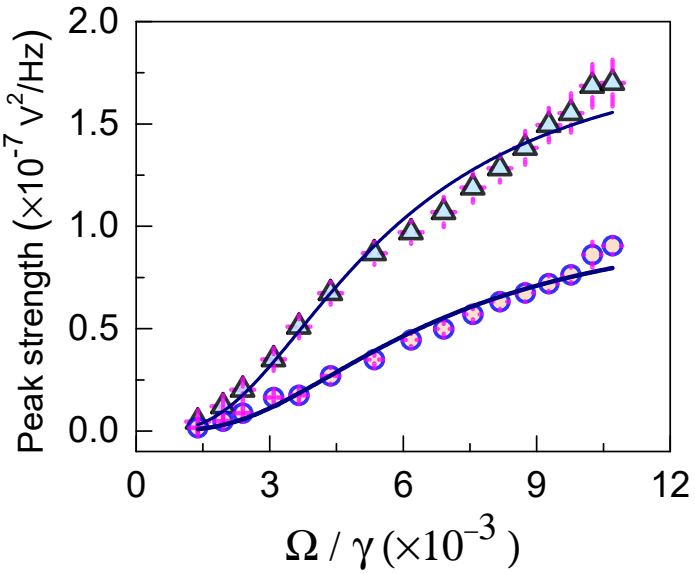

Figure 5.9: On-resonance ($\delta_{12} = \nu_L$) signal strength of the Raman driven signal from the thermal ^{87}Rb atoms as a function of Ω/γ. The black triangles (blue circles) are the on-resonance peak strength for temperature T = 373 K (393 K). The solid lines are the fits by Eq. 5.13.

In the measurements reported in Fig. 5.10 (inset), we notice consistent lower values of the extracted $2\gamma'$ than the intrinsic measurements ($\Omega = 0$), which indicates that the spin projection noise suppression is more significant for thermal vapors than the perturbation effects bringing the system beyond equilibrium.

We have further experimentally verified that the FWHM of the envelope can be smaller than the intrinsic width of the SN spectrum (indicated by arrows at the bottom-left side of Fig. 5.10). We have detected as much as 15% reduction in the width of the driven envelope than the intrinsic SN spectrum.

5.2.4 Dependence of driven power spectrum on Raman fields' polarization

We have also experimentally investigated the dependence of the Raman driven power spectrum on the polarization state of the Raman fields in the thermal ^{87}Rb atomic vapors.

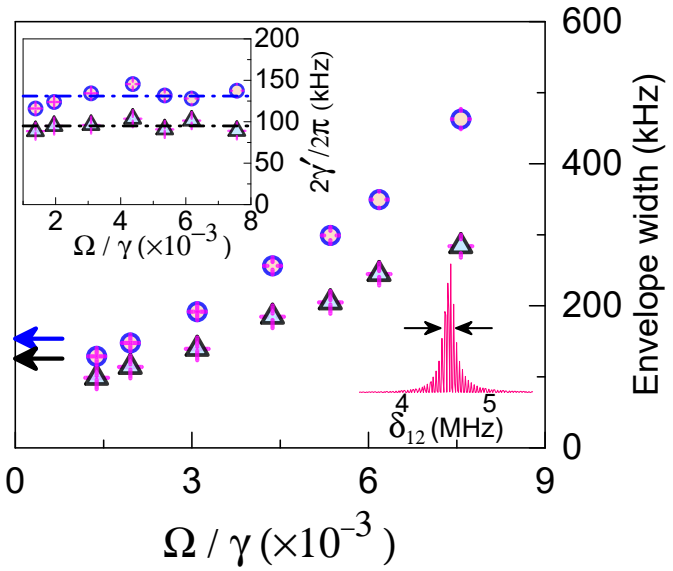

Figure 5.10: The FWHM of the envelope of $P(\omega)$ for the thermal ^{87}Rb atoms as a function of Ω/γ. The black triangles (blue circles) represent the FWHM (with a factor of 2π) of the envelope fitted with Lorentzian profile for T = 373 K (393 K). In the inset, the black triangles (blue circles) show the extracted value of $2\gamma'$ after fitting the envelope using Eq. 5.12. The black (blue) arrow indicated on the bottom-left side represents the measured FWHM of the intrinsic SN spectrum. The raw spectrum and its measured FWHM are indicated at the bottom-right corner.

In Fig. 5.11 (a), we show the driven power spectrum for various combinations of the polarization state of the Raman fields in thermal vapors. The polarization of the R1 field is linear ($(\pi_1)_x$), and kept fixed. We have tuned the polarization state of the R2 field, and recorded the driven power spectrum as shown in Fig. 5.11(a). The strength of the spectrum is maximum for $(\pi_1)_x - (\sigma_2^+)_x$ polarization of R1 and R2 fields, which corresponds to the angle $\theta = 45°$ or $225°$ between the optic axis of the QWP and the input polarization (p-polarized) of the R2 field. The Raman fields can not drive the atoms coherently between the states $|1\rangle$ and $|2\rangle$ for polarization combination $(\pi_1)_x - (\pi_2)_x$, which corresponds to $\theta = 90°$ or $180°$. This fact was experimentally confirmed and is presented in Fig. 5.11(a), which shows that we indeed coherently drive the entire atomic sample as opposed to incoherent driving. Note that we have observed an additional maximum at $\theta = 135°$. The appearance of this maximum can be explained in the above way by considering a Λ system with ground states $|F = 2, m_F = -1\rangle \equiv |1\rangle, |F = 2, m_F = 0\rangle \equiv |2\rangle$ and excited state $|F' = 3, m_{F'} = -1\rangle \equiv |3\rangle$. Such a combination of states is allowed for the alkali atom ^{87}Rb in our thermal vapor experiments.

We here demonstrate the role of angular momentum conservation in coherent coupling through our measurements. In Fig. 5.11(b), the normalized peak strength of the

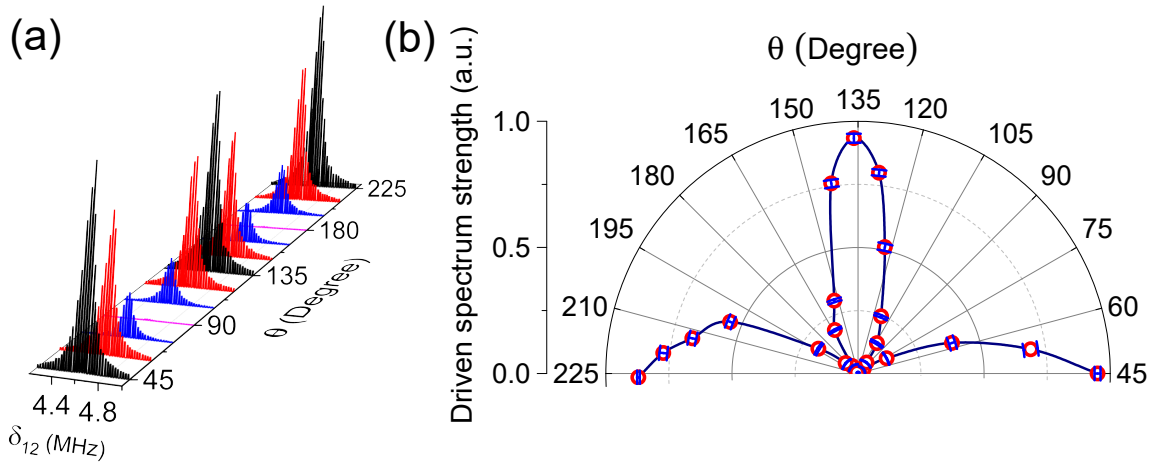

Figure 5.11: (a) The Raman driven power spectrum with detuning δ_{12} for various polarization states of the R2 field in thermal vapors. The R1 field is p-polarized ($(\pi_1)_x$). θ is the angle between the optic axis of the quarter-wave plate (QWP) and the input polarization (p-polarized) of the R2 field. The angular momentum conservation of light-matter interactions in Λ system is satisfied for $(\pi_1)_x - (\sigma_2^{\pm})_x$ polarization combinations of the Raman fields. These correspond to $\theta = 45°$, $135°$, $225°$, where a maximum in the spectrum is observed. The driven spectrum vanishes for $(\pi_1)_x - (\pi_2)_x$ polarization combinations ($\theta = 90°$and $180°$), implying no coherent coupling between the states $|1\rangle \leftrightarrow |2\rangle$ by the Raman fields. (b) The driven spectrum strength as a function of θ at Raman resonance condition. The solid line joining the data points are a guide to the eye.

driven power spectrum ($|\rho_{21}|^2_{\Delta=0}$) from thermal vapors is shown for various angle θ. The observation in Fig. 5.11(b) shows the fidelity of the coherent coupling of atoms by the Raman fields' polarization state. This can also be applied to control the atomic coherence between ground levels. The manipulation of atomic level coherence may find applications in quantum communications and quantum information processing using neutral atoms.

Raman coherence in the quantization basis The experiments in the vapor cell were performed in the presence of a homogeneous magnetic field (defining the quantization axis) applied along $\hat{z}$, and the Raman fields propagating along $\hat{x}$. The probe laser propagating along x-direction detects the x-component of the atomic spins. Here we neglect the slight angle between the probe and the Raman lasers, as schematically shown in the Fig. 5.12(a).

We consider the polarization state of the Raman fields propagating along $\hat{k} \parallel \hat{x}$ being linear ($(\pi_1)_x$) and circular ($(\sigma_2^+)_x$). In the presence of the Raman fields, the electronic spins align along the x-axis. However, due to the homogeneous magnetic

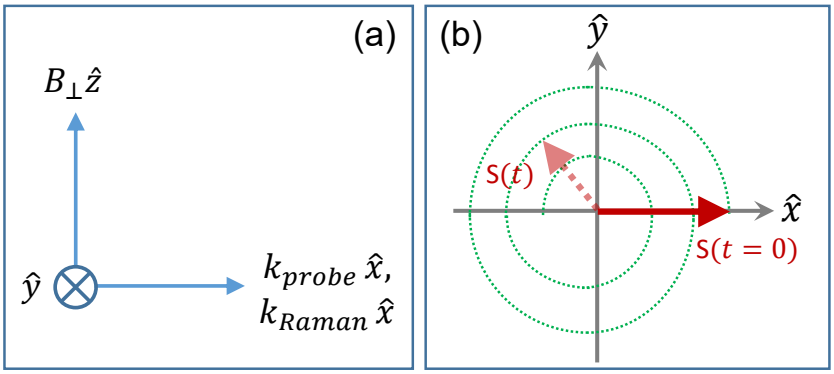

Figure 5.12: (a) Depicts the direction of the applied uniform magnetic field ($B\hat{z}$), the propagation direction of probe ($k_{probe}\hat{x}$) and Raman ($k_{Raman}\hat{x}$) lasers. (b) shows the precession of the system's magnetization on the $x-y$ plane about the magnetic field applied along the $z-$direction.

field along $\hat{z}$, the spins precess about z-axis on the $x-y$ plane. Since the Larmor precession rate (e.g., $\nu_L \sim 4.6$ MHz) in our experiments is typically much higher than the spin relaxation rate ($1/2\pi T_2 \sim 0.15$ MHz), the spins lie on the $x-y$ plane as shown in Fig. 5.12(b).

We further restrict our discussion for a system with ground hyperfine level $F = 1$ and excited hyperfine level $F' = 1$. In the following, we will describe the dependence of Raman-driven power spectrum strength on various polarization combinations of R1 and R2 fields presented in Fig. 5.11. Any spin component of F or F' on the $x-y$ plane can be written as a linear superposition of all possible spin components along $\hat{z}$, for an example [234],

$$|m_F = 1\rangle_x = \frac{1}{2}|m_F = -1\rangle_z + \frac{1}{\sqrt{2}}|m_F = 0\rangle_z + \frac{1}{2}|m_F = 1\rangle_z. \tag{5.16}$$

We can also decompose the polarization of the Raman fields in terms of their electric fields in the following fashion [204, 235]:

$$(\pi_1)_x \equiv \hat{e}_{1y} = \frac{1}{\sqrt{2}}\left(\frac{\hat{e}_{1y} + i\hat{e}_{1x}}{\sqrt{2}}\right) + \frac{1}{\sqrt{2}}\left(\frac{\hat{e}_{1y} - i\hat{e}_{1x}}{\sqrt{2}}\right), \tag{5.17}$$

and,

$$\begin{aligned}(\sigma_2^+)_x \equiv \frac{\hat{e}_{2z} + i\hat{e}_{2y}}{\sqrt{2}} &= \frac{\hat{e}_{2z}}{\sqrt{2}} + \frac{i}{2}\left(\frac{\hat{e}_{2y} + i\hat{e}_{2x}}{\sqrt{2}}\right) \\ &+ \frac{i}{2}\left(\frac{\hat{e}_{2y} - i\hat{e}_{2x}}{\sqrt{2}}\right),\end{aligned} \tag{5.18}$$

where, $\hat{e}_{1i}$ or $\hat{e}_{2i}$ is the ith component of the corresponding electric field with $i = x, y, z$.

In our experiment, we fix the frequency of R1 field (of $(\pi_1)_x$ polarization) on-resonance to $|m_F = -1\rangle_z \leftrightarrow |m_{F'} = 0\rangle_z$ transition, and that of R2 field (of $(\sigma_2^+)_x$ polarization) on-resonance to $|m_F = 0\rangle_z \leftrightarrow |m_{F'} = 0\rangle_z$ transition. According to our decomposition in the Eq. 5.17 and Eq. 5.18, the allowed optical transitions in the $\hat{z}$ basis can be shown in Fig. 5.13, where the field $\hat{e}_{2z}$ couples $|m_F = 0\rangle_z \leftrightarrow |m_{F'} = 0\rangle_z$ transition and the field $(\hat{e}_{1y} + i\hat{e}_{1x})/\sqrt{2}$ couples $|m_F = -1\rangle_z \leftrightarrow |m_{F'} = 0\rangle_z$ transition.

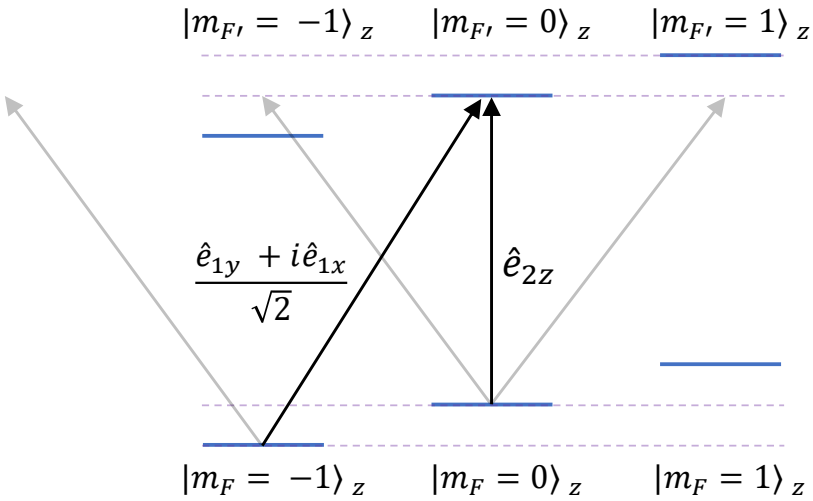

Figure 5.13: Formation of a Λ system in $\hat{z}$ basis within the Zeeman states for $(\pi_1)_x$ and $(\sigma_2^+)_x$ combination of polarization of the Raman fields. The generated Λ system is shown by black arrows.

The Fig. 5.13 shows that a Λ type 3LS is formed (indicated by black arrows) in $\hat{z}$ basis, and a coherence is built between the states $|m_F = -1\rangle_z \leftrightarrow |m_F = 0\rangle_z$. The coherence between $|m_F = 0\rangle_z$ and $|m_F = 1\rangle_z$ can also be explained in a similar fashion. This coherence in $\hat{z}$ basis in turn built a coherence in $\hat{x}$ basis via Eq. 5.16, and detected by the off-resonant probe laser. This case corresponds to $\theta = 45°$ and $225°$ in Fig. 5.11. The other maxima at $\theta = 135°$ can be explained by considering the $(\pi_1)_x$ and $(\sigma_2^-)_x$ combination of the polarization states of the R1 and R2 field.

Note that, in the Raman-driven SN experiment, two different kinds of atomic excitations happen simultaneously. First − coherent excitation − where the atoms will get trapped in the dark state formed between the two consecutive ground Zeeman states. Second − incoherent excitation − where the off-resonant $\sigma^\pm$ or π component leads to the random redistribution of the atoms in the ground Zeeman states. The atoms which are trapped in the dark state are free from incoherent excitations by the other off-resonant Raman fields components. The remaining atoms that are randomly distributed in various Zeeman states will participate in the coherent excitation in their

upcoming excitations. In this way, eventually, in the steady state, all the atoms will finally get trapped in the dark state and contribute to the coherent part of the spin noise. However, there may be some incoherent excitation that occurs due to the improper polarization and overlap mismatch of the Raman beams, frequency mismatch, etc. In this case, this incoherent excitation contributes as a background pedestal (broadband atomic white noise) in the spectrum.

For $(\pi_1)_x - (\pi_2)_x$ combination of R1 and R2 field polarizations ($\theta = 90°$ and $180°$), no Λ system is formed in $\hat{z}$ basis within the ground hyperfine level Zeeman states. Therefore, no amplification in the driven power spectrum has been observed.

However, it can be shown using Eq. 5.18 that when both the Raman fields are σ^+ polarized, a double Λ system is formed within the consecutive Zeeman states in F-manifolds. In this case, the signal strength is two times stronger than the case discussed in Fig. 5.13.

The Table 5.1 summarizes the Raman driven signal strength for various combinations of the Raman fields' polarizations.

Polarization of Raman fields	Comments on signal strength
$(\pi_1)_x - (\pi_2)_x$ and $(\sigma_1^{\pm})_x - (\sigma_2^{\mp})_x$	No amplification, Intrinsic
$(\pi_1)_x - (\sigma_2^{\pm})_x$ and $(\sigma_1^{\pm})_x - (\pi_2)_x$	$\lvert\rho_{21}\rvert^2$
$(\sigma_1^{\pm})_x - (\sigma_2^{\pm})_x$	$2\lvert\rho_{21}\rvert^2$

Table 5.1: Dependence of Raman-driven power spectrum signal strength on the Raman fields' polarization combination.

We have experimentally verified the dependence of the on-resonance Faraday rotation fluctuations signal strength on different polarization combinations of the Raman fields. The experimental results are shown in Fig. 5.14 for completeness.

5.2.5 Raman driven spin-exchange between homo-nuclear atoms with different $g-$factors

The spin coherence of an atom can enhance via spin-exchange collisions (SEC) with other atoms in the spin-exchange relaxation free (SERF) regime [36, 37, 39, 236] or using SEC to transfer coherence from one polarized atomic species to another unpolarized atomic species [237–239]. In general, the efficiency of the coherence transfer is maximum when they are resonantly coupled i.e. when their Lande$'$ g-factors are

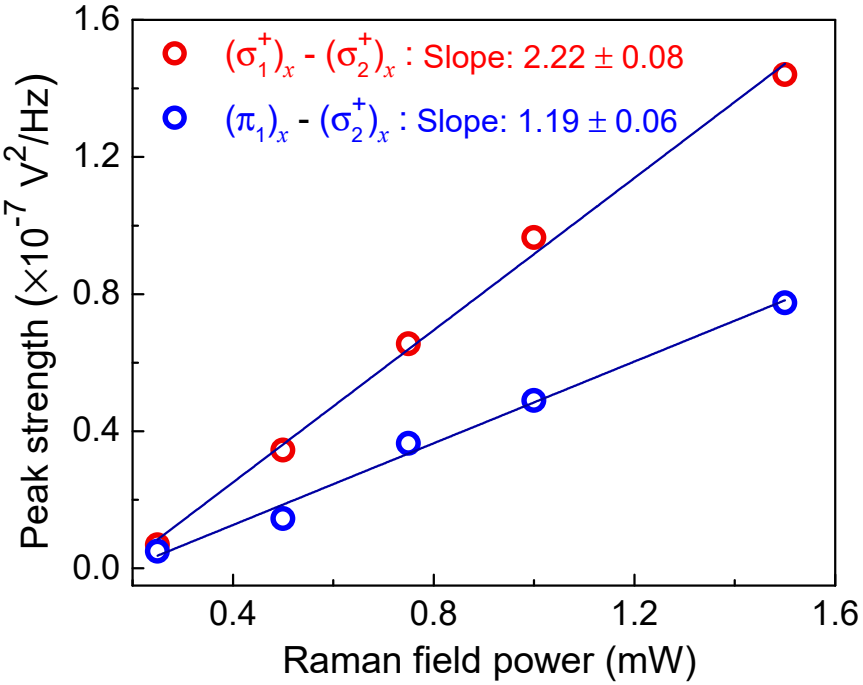

Figure 5.14: The on-resonance signal strength of the Raman driven spectrum for $(\sigma_1^+)_x - (\sigma_2^+)_x$ and $(\pi_1)_x - (\sigma_2^+)_x$ combination of the Raman fields' polarization with various driving intensities. The plots support the results summarized in Table 5.1.

similar. A coherence transfer between atomic species with different g-factors can be possible using RF dressing. The Lande$^{'}$ g-factor of different atoms vary differently depending on the strength of the applied RF field. For a certain value of the RF field strength the g-factors of the colliding pairs are same. Therefore the strength of the RF field can be tuned carefully to match the g-factors of the atoms and a transfer of maximum coherence can be possible between them. An example of such coherence transfer from major species ^{133}Cs to minor species ^{87}Rb has been shown in [240] at a non-zero constant magnetic field. The coherence transfer by spin-lock technique is presented in the work [241] where there is no need to tune the rf-field amplitude. Also, the coherence transfer between atoms with the same Lande$^{'}$ g-factors are observed in [19]. In all of these previous examples, an rf field has been used to transfer coherence between two atomic species. At a non-zero magnetic field, the coherence of an atomic system can be achieved by introducing a circularly polarized light beam with intensity modulated at the frequency of the Zeeman splitting. Such an atomic coherence can transfer to other atomic species with different Lande$^{'}$ g-factor and reported in [242].

In our experiment, we have also observed a coherence transfer via SEC when one atomic species is resonantly driven by the coherent Raman beams. Our vapor cell contains both the isotopes of rubidium atoms with abundance ratio of ^{85}Rb : ^{87}Rb

= 1 : 11 at 373K temperature. The $g-$factors of these two homo-nuclear atoms are different. However, in the experiment when we have resonantly driven the ^{85}Rb atoms by the Raman beams, a significant line-narrowing in the intrinsic SN has been observed for ^{87}Rb atoms. This line-narrowing is a signature of the coherence transfer from ^{85}Rb atoms to ^{87}Rb atoms via SEC.

We have tuned the δ_{12} of the Raman beams through the ν_L of ^{85}Rb atoms and observed the modifications in the intrinsic SN spectrum for ^{87}Rb atoms. We have kept the Raman beam polarization in $(\pi_1)_x - (\sigma_2^+)_x$ combinations. In Fig. 5.15 (a), the intrinsic SN spectrum of Rb isotopes for a magnetic field of 6.2 Gauss and temperature of 373K is presented. The intrinsic SN signal for Rb isotopes is indicated in the picture. Next, we have employed the Raman beams with δ_{12} varied around the SN peak of ^{85}Rb atoms. In Fig. 5.15 [(b) and (c)], δ_{12} is lower than the frequency of the SN peak of ^{85}Rb, and the SN spectrum of ^{87}Rb has not been significantly affected. When the Raman beams resonantly coupled to the ^{85}Rb atoms (i.e. δ_{12} = SN peak of ^{85}Rb), a strong modification of the intrinsic SN spectrum of ^{87}Rb has been observed which is shown in Fig. 5.15 (d). This leads to enhancing the coherence time for ^{87}Rb atoms by almost one order. The FWHM of the SN spectrum of ^{87}Rb has been reduced by almost **one order** and the signal strengths also increased by an order. When δ_{12} is on the other side of the SN peak of ^{85}Rb atoms, no such significant line narrowing is observed in the SN spectrum of ^{87}Rb (see Fig. 5.15 [(e) and (f)]).

5.2.6 High Harmonics generation at δ_{12} for strong driving

Furthermore, we have also observed the generation of second harmonics of δ_{12} in the driven power spectrum when the Rb atoms are strongly driven ($\Omega/\gamma > 0.01$) by the Raman beams.

In Fig. 5.16, we demonstrate the generation of second harmonics at $2\delta_{12}$ when δ_{12} is scanned around the ν_L for both the Rb isotopes. The intrinsic ($\Omega = 0$) SN signal of Rb isotopes in a particular magnetic field are indicated with the vertical broken yellow lines and red labels on the top of the graph. Since the density of the atoms for ^{85}Rb isotopes are an order of magnitude smaller than the ^{87}Rb isotope in the vapor cell, the trace for the intrinsic SN signal corresponds to ^{85}Rb atoms are not visible in the false-color map, whereas the SN signal for ^{87}Rb atoms are presented with the vertical blue trace. In the Raman driven experiments, we locked the R2 beam frequency on the $|2\rangle \leftrightarrow |3\rangle$ transition. The frequency of the R1 beam is varied near the $|1\rangle \leftrightarrow |3\rangle$ transition during the measurements. The Rabi-frequency of both the Raman beams are equal and kept Ω/γ =1.2 $\times$ 10^{-2}. In experiments, we first keep δ_{12} in the lower

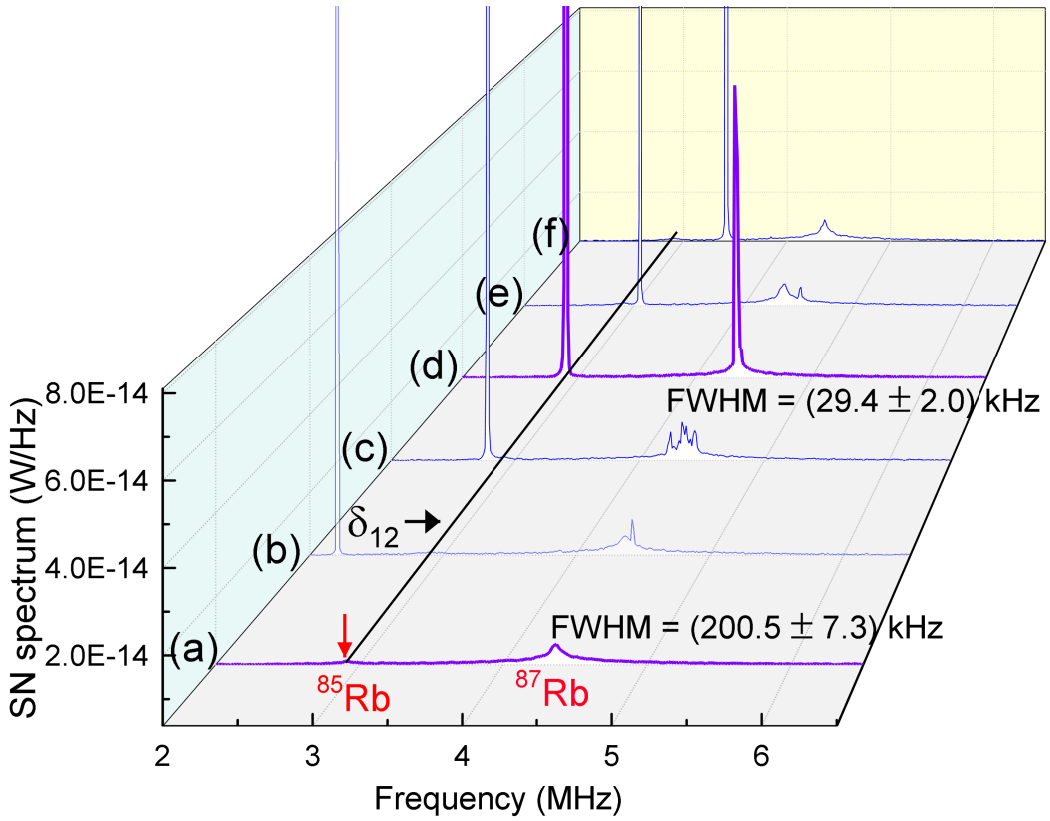

Figure 5.15: The coherence transfer between homo-nuclear atoms via spin-exchange collision (SEC) when one of them is subjected to the resonant Raman coupling. (a) the intrinsic spin noise (SN) spectrum of Rb isotopes present in the vapor cell. δ_{12} is varied around the SN peak of ^{85}Rb atoms. A reduction of one order in the FWHM of the intrinsic SN signal for ^{87}Rb atoms has been observed when δ_{12} is equal to the Zeeman splitting of ground hyperfine levels of ^{85}Rb atoms in (d). The plots in (b-c) and (e-f) show no significant effect in the SN spectrum of ^{87}Rb atoms has been observed when δ_{12} is different from the Zeeman splitting of ^{85}Rb atoms. The y-axes of the plots are truncated.

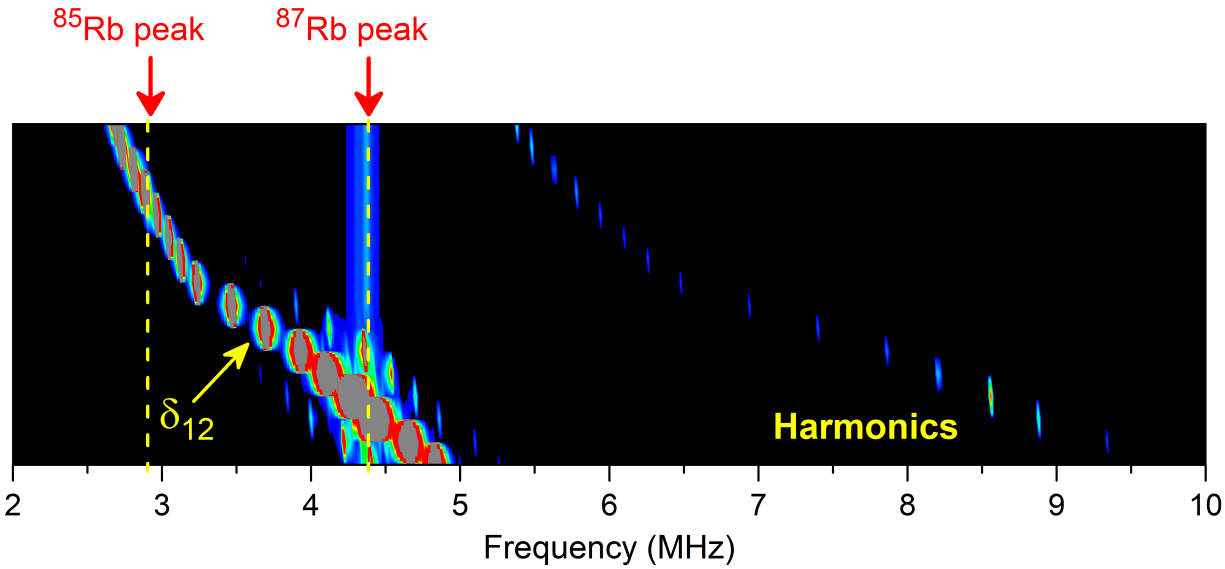

Figure 5.16: Second harmonic generation at δ_{12} frequency in the spectrum for strong Raman coupling. The spin noise (SN) peak positions of ^{85}Rb and ^{87}Rb are indicated using vertical yellow broken lines. The detuning δ_{12} is varied over the SN peaks of both ^{85}Rb and ^{87}Rb isotopes, and they are identified as the grey color trace on the false color map. The light blue color traces at $2\delta_{12}$ are identified as the second harmonics of δ_{12}.

side of ν_L of ^{87}Rb by keeping ω_{s1} red detuned with respect to $|1\rangle \leftrightarrow |3\rangle$ transition. The Raman beams were continuously kept on during the measurement of duration 10 s. We have recorded the spectrum in a wide spectral frequency range of (2-10) MHz. Next, we change δ_{12} towards the ν_L side and repeat the measurements. We have performed the measurement until δ_{12} crosses the ν_L on the higher frequency side. In Fig. 5.16, the grey color trace represents the position of δ_{12} in the spectral frequency domain, whereas the generated second harmonics correspond to each δ_{12} are shown on the right-hand side of the spectrum. The signal strength of the second harmonics is observed to be strong when δ_{12} of the Raman beams are crossed through the ν_L for both the isotopes. This is because the generation of second harmonics is more when any one of the Rb isotopes is resonantly driven by the Raman beams. When δ_{12} is far away from those SN peaks, the second harmonic is not observed in the spectrum.

Generation of higher harmonics for maximally coupled system. In section 5.2.4, we have demonstrated that the Raman driven signal strength is enhanced by two times when the polarization of the Raman beams are chosen as $((\sigma_1^{\pm})_x - (\sigma_2^{\pm})_x)$ configuration. In Fig. 5.17, we present the generation of higher harmonics until fourth order when Rabi frequency of the Raman beams are same as in Fig. 5.16, however the polarization is chosen as $(\sigma_1^{+})_x - (\sigma_2^{+})_x$. Moreover, we have performed this experiment

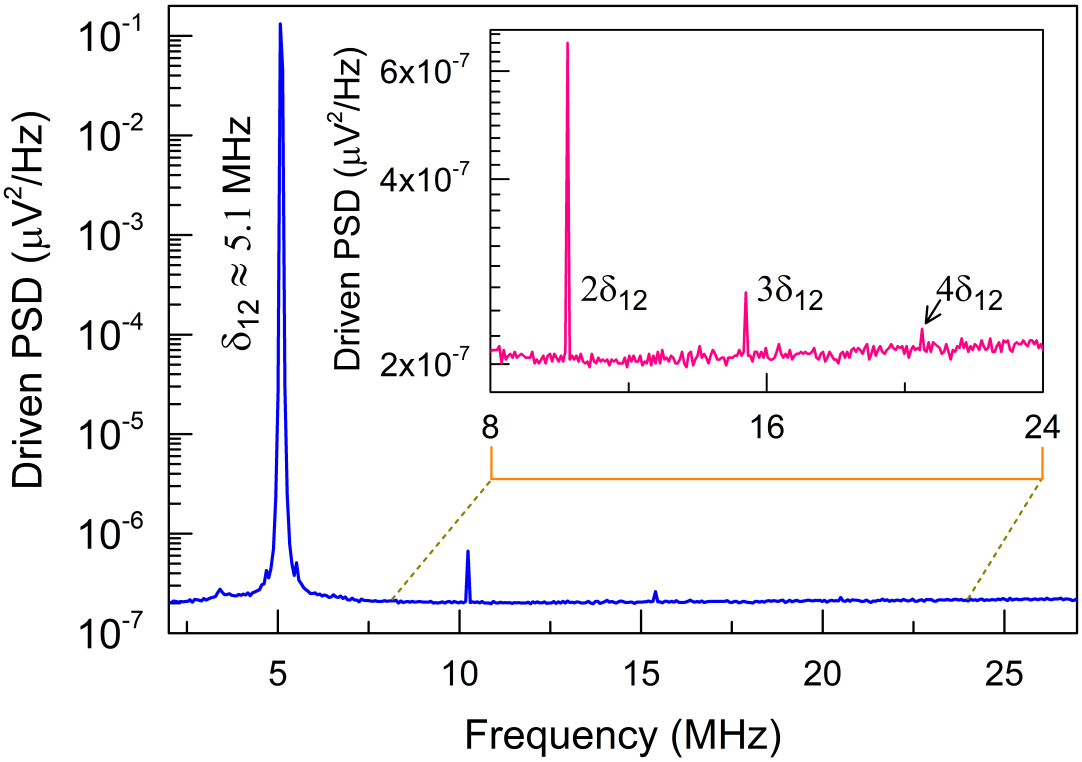

Figure 5.17: Generation of higher harmonics at δ_{12} from the coherently driven ^{87}Rb atoms. The Raman beams are relatively strong ($\Omega/\gamma > 0.01$) and resonantly couple to atomic 3L Λ-system. The polarization of the Raman beams used for this measurement is $(\sigma_1^+)_x - (\sigma_2^+)_x$ for maximum coupling. Inset shows the generation of higher harmonics of δ_{12} till fourth order.

at the Raman resonance condition for ^{87}Rb atoms, i.e. $\delta_{12} = (\nu_L)_{87}$. The inset shows the zoomed y-scale of the spectrum which verifies the presence of the higher-order harmonics in the Raman driven spin correlation signal. The relative strength of the higher harmonics (at $n\delta_{12}, n = 2, 3, 4$) are extremely weak (more than five orders) in comparison to the principle signal at δ_{12}.

The atoms in the dark state (ψ_D) coherently oscillates between the states $|1\rangle$ and $|2\rangle$ at a rate of frequency difference between those states (see Fig. 5.18, $\Lambda-$system designated as ②). However, when the Raman resonance condition is satisfied, the rate of oscillation is the Larmor frequency (ν_L) of the electron in the magnetic field. In the dark state, the oscillation of the atomic population between the ground states induce similar oscillation of the system's linear susceptibility ($\chi^{(1)}(\omega)$), where ω is the optical frequency) which is being detected by the far-off resonant probe laser beam. Nevertheless, in this case, the thermal fluctuations of the atomic population between these states are heavily suppressed and only the coherent oscillations persist. Therefore, we have observed a strong and extremely narrow spin coherence signal in spectrum at δ_{12} when $\delta_{12} = \nu_L$ as shown as the first (principle) peak in Fig. 5.16. The principal peak at δ_{12} is observed even if $\Omega \ll \gamma$. However, when the Rabi frequency increases, the higher-order peaks in the multiple of δ_{12} appear in the spectrum due to the multiple wave mixing between the various excitation channels in the coherently driven system as discussed in the following.

In Fig. 5.18, the coherent oscillation of atoms in the dark states formed within $|1\rangle \equiv |F = 2, m_F = -1\rangle$ and $|2\rangle \equiv |F = 2, m_F = 0\rangle$ are shown as a purple arrow in the $\Lambda-$ system designated by ②. In the experimental part, for simplicity, we have considered only one $\Lambda-$ system formed by atomic energy states and Raman beams. However, in actual cases, the other combination of Zeeman states will also form $\Lambda-$ system with varied optical detuning from the excited state as shown in Fig. 5.18. However, this detuning (order of MHz) is negligible compared to the γ. Therefore, all four $\Lambda-$ systems and the corresponding dark states have been contributed in the generation of the strong Raman driven spectrum at δ_{12} as indicated in Fig. 5.18 and shown in Fig. 5.17. Fig. 5.18 shows that at the Raman resonance condition, the coherent oscillation of the atomic population between adjacent Zeeman states ($\Delta m_F = \pm 1$) happens at a rate of the Zeeman splitting (ν_L) and so to say at δ_{12}. However, when the atomic vapor is driven with strong Raman beams, the non-linear susceptibility ($\chi^{(3)}(\omega)$) of the medium start to play a significant role in the constructive interference of the different transition pathways in the atom-light interactions at the Raman resonance condition. In this scenario, the atoms that coherently oscillates between $|m_F = -2\rangle \leftrightarrow |m_F = -1\rangle$ ($\Lambda-$ system①) can participate in the oscillation in the $|m_F = -1\rangle \leftrightarrow |m_F = 0\rangle$ (i.e. in $\Lambda-$

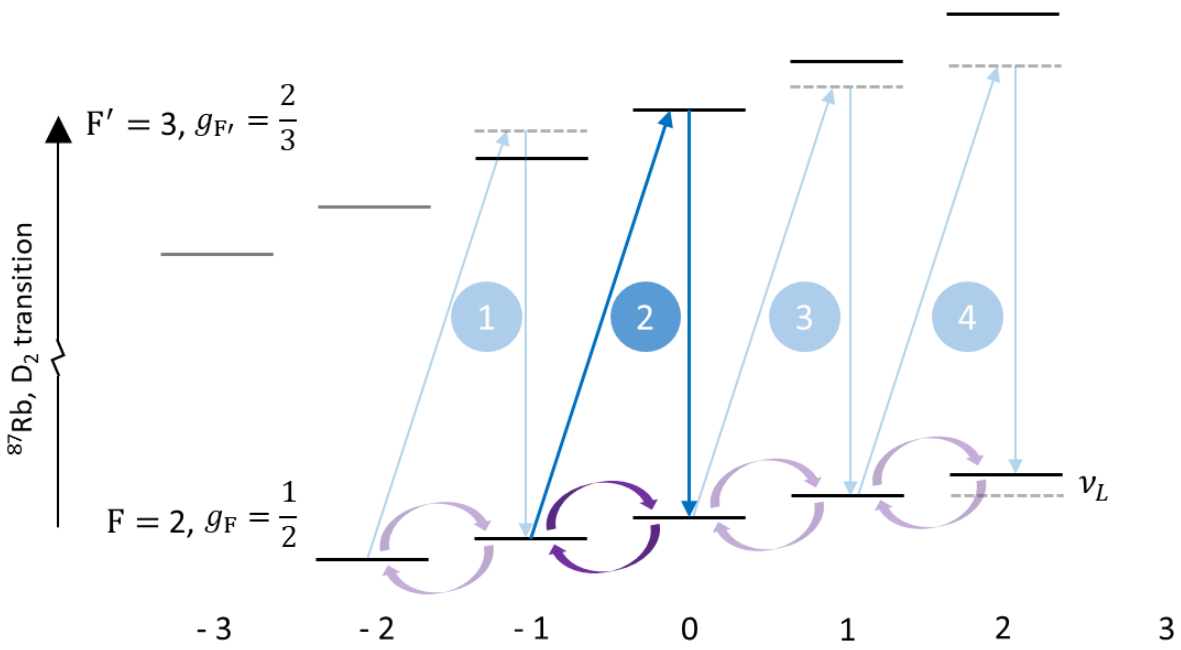

Figure 5.18: The coupling of Raman beams with atomic Zeeman states to explain the generation of higher harmonics.

system②). In this case, depending on the strength of the non-linear susceptibility, a small fraction of atoms can oscillate between the states with $\Delta m_F = \pm 2$ and frequency at $2\delta_{12}$. These states are: $|m_F = -2\rangle \leftrightarrow |m_F = 0\rangle$, $|m_F = -1\rangle \leftrightarrow |m_F = 1\rangle$ and $|m_F = 0\rangle \leftrightarrow |m_F = 2\rangle$. This observation is shown in Fig. 5.16. In this case, the intermediate ground state is not seen by those fraction of atoms due to the quantum interference effect of the transition amplitudes. The appearance of the other harmonics can also be explained in this way.

Chapter 6

Magnetometry using SNS technique

This chapter is based on the publication [20]. In this chapter, we present the development and characterization of a generic, reconfigurable, low-cost software-defined digital receiver system (DRS) for temporal correlation measurements in atomic spin ensembles. We demonstrate the use of the DRS as a component of a high resolution magnetometer. Digital receiver based fast Fourier transform spectrometers (FFTS) are generally superior in performance in terms of signal-to-noise ratio compared to traditional swept-frequency spectrum analyzers (SFSA). In applications where the signals being analyzed are very narrow band in frequency domain, recording them at high speeds over a reduced bandwidth provides flexibility to study them for longer periods. We have built the DRS on the STEMLab 125-14 FPGA platform and it has two different modes of operation: FFT Spectrometer and real time raw voltage recording mode. We evaluate its performance by using it in atomic spin noise spectroscopy experiments. We demonstrate that the SNR is improved by more than one order of magnitude with the FFTS as compared to that of the commercial SFSA. We will also demonstrate that with this DRS operating in the triggered data acquisition mode one can achieve SN signal with high SNR in a recording time window as low as 100 msec. We make use of this feature to perform time resolved high-resolution magnetometry.

6.1 Introduction

Digital receivers are a class of electronic systems where operations like amplification, filtering, integration etc. are performed as a series of mathematical operation on embedded components like FPGAs, Microprocessors or GPUs. Compared to their analog counterparts, digital receivers are immune to variations in gain and temperature. However, digital systems have quantization noise, sampling rate and phase noise which can

be minimized by choosing high bit-width ADCs and low drift clock sources. These characteristics make digital receivers an attractive option in applications where precision measurements are required [243, 244]. AMO experiments are one such example.

Digital receivers are being used in AMO experiments for process control [245] (e.g. temperature, current and wavelength control in lasers), synchronous detection [246] and in compact magnetic resonance spectroscopy systems [247]. However, synchronous detection may not be feasible in many AMO experiments including spin noise spectroscopy [1, 4, 5]. The typical strength of the raw SNS signal is $< 100\,\mathrm{nV}/\sqrt{Hz}$ which is far less compared to the previous studies[245–247]. Therefore, the SNS signal has to be recorded continuously (or on trigger) to improve the SNR.

In this chapter, we discuss the development and utilization of a versatile digital receiver to measure the SN in atomic vapor systems. We have performed a comparative study with the results presented in chapter 3 and 4 [5]. We then demonstrate its utility in real-time precision magnetometry. This digital receiver can also be used as a component of a novel, miniaturized magnetometer based on SNS techniques that will be discussed at the end of this chapter.

The chapter is organized as follows: We introduce SNS and the digital receiver system developed for its measurement in section 6.2. The firmware architectures of the former is described in section 6.3. The methods adopted to mitigate the effects of electro-magnetic interference (EMI) in the measurements are described in section 6.4. In section 6.5, we present the SNS data obtained by using our DRS as well as a comparison with the results obtained from SFSA. Further, we demonstrate triggered data acquisition and time resolved magnetometry using our DRS. We conclude in section 6.6 after a brief discussion on further applications and future scope of the developed receiver.

6.2 Digital receivers for spin noise spectroscopy

In this section, we describe the implementation of this detection schemes in spin noise spectroscopy technique by introducing our digital receiver.

6.2.1 Spectroscopy technique

Study of SN of an atomic ensemble has varied applications, ranging from precision magnetometry, non-perturbative optical detection to metrology and quantum sensing. Our SNS experimental set-up using DRS system is shown in Fig. 6.1. A probe laser beam which is red detuned by 10 GHz is used to probe the spin fluctuations of the

atoms in the vapor cell heated to temperatures ranging between 350 K and 400 K. The spin fluctuations causes polarization fluctuations of the probe laser. The polarimetric detection scheme employing a half wave plate (HWP), polarizing beam splitter (PBS), and a balanced photo-detector (BPD) is capable of measuring this polarization fluctuation. A uniform magnetic field ($B_\perp$), produced using a pair of magnetic coils in Helmholtz configuration, is applied on the atomic vapor which is perpendicular to the propagation direction of the probe laser beam. The output signal of the BPD is recorded using the digital receiver described in this chapter and reported in section 6.5.

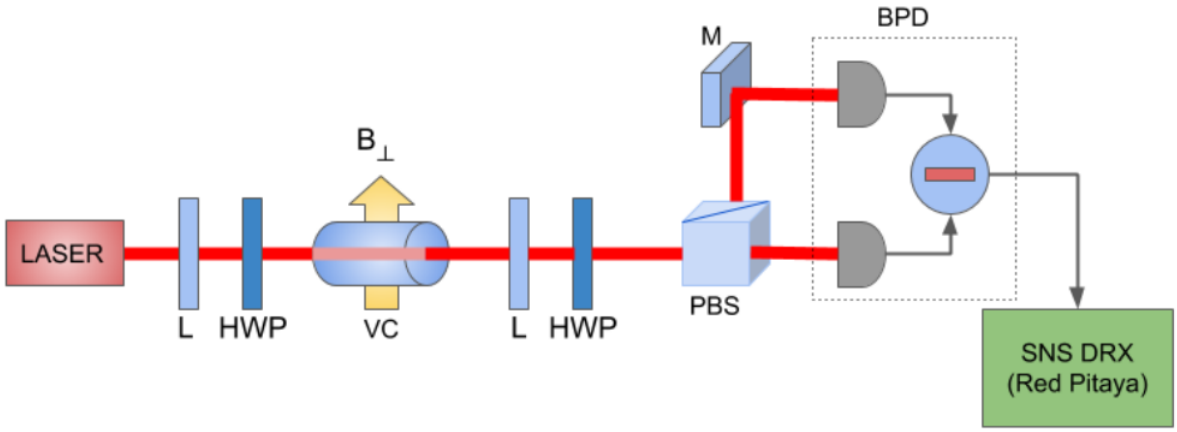

Figure 6.1: A typical spin noise spectroscopy (SNS) set-up of rubidium (Rb) atomic vapor. L- plano-convex lens, VC- vapor cell (contains Rb atomic vapor), M- dielectric mirror, HWP- half wave plate, PBS- polarizing beam-splitter, BPD- balanced photodetector, $B_\perp$- orthogonal magnetic field.

Previously we used a commercially available SFSA[1] to detect the SN signal from the balanced photo-detector. It has a superheterodyne stage whose mixer provided a local oscillator (LO) signal, such that the radio-frequency (RF) signal is translated to a fixed intermediate frequency (IF). Since the LO has to be swept across a range of frequencies, the sweep time increases with frequency span. This reduces the dwell time at each frequency resulting in a decreased sensitivity. From the experimental point of view, this leads to poor SNR. Moreover, if the signal is expected to show variations smaller than the sweep-time, it cannot be detected. SFSAs also have a low frequency cut-off (in our case 100 kHz) below which the output amplitude and frequency measurements are not possible. For performing the SNS on laser cooled atoms to investigate spin dynamics in quantum regime, where a triggered data recording of a SN signal over a short duration ($\sim$ few ms) is required, a SFSA can not be used. Therefore, we develop the DRS system described in this chapter.

[1] https://www.keysight.com/in/en/assets/7018-01953/data-sheets/5989-9815.pdf

There have been recent experiments reporting measurements of SNS in quantum dots [122] as well as in atomic vapors [165], where the use of non-reconfigurable and somewhat expensive digital receivers are reported. However, the digital receiver described in this chapter, allows us to overcome the aforementioned limitations of SFSA, with certain trade-offs.

6.2.2 Digital receivers for SNS

We developed a digital receiver capable of operating in two modes, as listed below.

(1) A fast Fourier transform spectrometer (FFTS) to probe the entire frequency range of interest,

(2) A real time data recorder (RTDR) with trigger capabilities.

Both the aforementioned modes are implemented on the STEMLab 125-14[2] development board. This board is selected for our application because it has two 14 bit analog-to-digital converter (ADC) channels, with each channel providing a dynamic range better than 80 dB. It has an analog bandwidth of 62.5 MHz, and is DC coupled. The heart of the board is a Xilinx Zynq 7010 System on Chip (SoC), with integrated programmable logic (PL) cells and ARM microprocessor based processing system (PS). The signal processing algorithms are implemented on the PL side, while user control and data transmission programs are implemented on the PS side.

6.3 Firmware Description

In this section, we describe the firmware architecture of the two operational modes of the DRS.

6.3.1 Fast Fourier transform spectrometers (FFTS)

Fourier transform is used to find the spectral content of a time domain signal [248]. Fast Fourier transform (FFT) is an algorithm which reduces the complexity involved in calculating the Fourier transform from a $O(n^2)$ to $O(n \log n)$ problem by using the periodicity and the symmetry properties of the former [249, 250]. This, in general, reduces the number of operations required to obtain the spectrum and results in resource savings when implemented in embedded devices e.g. FPGA or in Microprocessors.

The SNR is proportional to $\sqrt{\beta\tau}$, where β is the bandwidth, and τ is the integration time [251]. For a conventional spectrum analyzer, there are two time scales involved:

[2] https://www.redpitaya.com/f130/STEMlab-board

t_s, the sweep time, and t_d, the dead time. So, if a sweep contains N_s points, the amount of time required for obtaining the power at each frequency becomes t_s/N_s. In cases where the data is to be acquired using interfaces such as GPIB, USB, or ethernet, t_d includes the time taken for the spectrum analyzer to transfer the data to the DAQ system, during which time no new acquisition can occur.

In case of an FFTs, the estimation of the power spectrum involves summation of all time domain samples of the burst used to perform the FFT. If a streaming algorithm is used, data acquisition, performing FFT and data transfer can happen simultaneously resulting in zero dead time. Thus for a single spectrum, with the same spectral resolution, an FFTs ideally provides $\sqrt{N_s}$ improvement in the SNR as compared to SFSA [252].

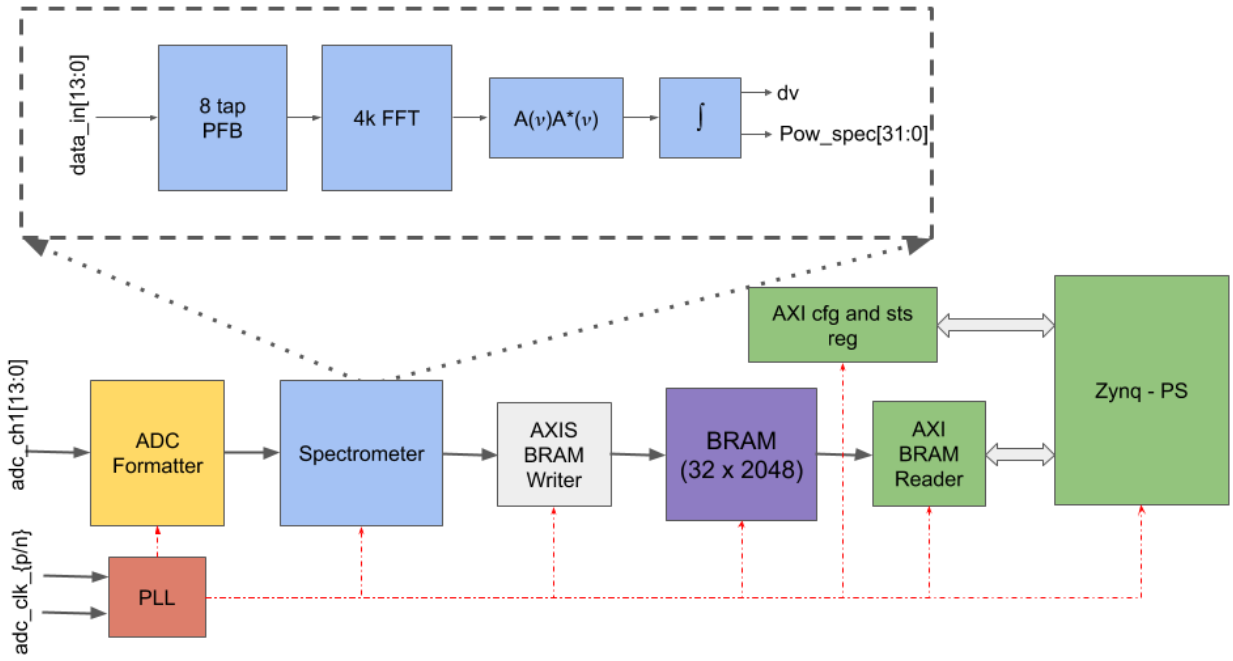

Figure 6.2: Top level block diagram of the FFTS. PS and related interfaces are shown as green blocks. The red dashed lines indicate the flow of the master clock at 125 MHz, which is derived from the ADC data clock. The data and clock inputs from the ADC to the FPGA are Low Voltage Complementary Metal Oxide Semiconductor (LVCMOS) signals.

The base firmware version of the Stem-Lab 125-14 provides a burst mode version of the FFTs. However, we required capability to perform this operation in streaming mode, and average the spectra on the FPGA itself. This allows us to keep data rates below 30 MBps, beyond which loss-less data transfer via ethernet becomes difficult, due to bottlenecks in communication between the PL and the PS sides of the SoC. The

block diagram of our FFTS implementation is shown in Fig. 6.2.

The analog signal is sampled by the on-board ADC at 125 MHz. The digitized data is captured synchronously on the FPGA, converted to 2's complement format and passed on to the spectrometer block.

The spectrometer block is implemented using Simulink System Generator. The signed data obtained so far is polyphase filtered using an 8 tap FIR filter [253]. The output of the filterbank is an 18 bit fixed-point number. This is input to the biplex FFT block IP core [254], available from the CASPER signal processing library [255, 256]. A 4096 points FFT is performed resulting in a spectral resolution of $\approx$ 30.5 kHz. As the data to the FFT block is real-valued, the power spectrum is estimated by computing the magnitude of the positive half of the spectrum. After the integration of a programmable number of spectra, the power spectrum is presented to the subsequent blocks for transmission to the DAQ. For example, if 1000 such spectra are summed, the resulting integration time is $\approx$ 32 ms.

The output spectra is recast as an Advanced eXtensible Interface (AXI) stream and is written to a Block RAM (BRAM) through the `AXIS BRAM WRITER` IP block [257]. Once the spectrum is written into the BRAM, a `finished` signal indicating this is asserted and posted to the `sts` register.

The FPGA present on-board provides access only to the PS Ethernet, therefore the transfer of data to the DAQ is mediated by executing a C code on the PS. The `sts`, `cfg` and `AXI BRAM READER` provide memory mapped access to the PL. `cfg` register is used to provide a master reset and configuration information to the PL. `sts` register provides information on the BRAM address pointer and holds the state of the `finished` signal. On the assertion of the `finished` signal, the PS starts reading the contents of the BRAM. The BRAM data is packetized as `UDP` packets with packet and spectrum count information and is transmitted to the DAQ using linux socket functions.

We characterize the developed spectrometer using continuous wave (CW) and SN signals. For the CW tests, signals at different frequencies and different powers are fed to the system and recorded. These tests are carried out to estimate the SNR of the spectrometer at different frequencies and to identify the linear regime. The power measured by the FFTS is found to linearly vary with the input power.

6.3.2 Real time data recorder (RTDR)

The FFTs discussed thus far, provides a simple and compact measurement option for SNS. In scenarios where the SN signal is short lived in time, a real time triggered data acquisition and processing protocol is required.

Table 6.1: The different options available in the RTDR firmware.

Option	Description
baseband	Records signal in dc - 625 kHz base-band; LO is disabled
IF	Records signal in an IF band spanning from f_{lo} to $f_{lo} + 625$ kHz
triggered	Records a signal burst for a programmable predefined time on rising edge of trigger pulse
continuous	Records data continuously

We developed a low bandwidth, raw voltage recorder. In Fig. 6.3, we show a top-level block description of the same. Table 6.1 outlines the various options available in the data recorder. Here, we use both the input channels, where one is from the BPD and the other is a signal generator (BK PRECISION Model no. 4040B), which is used as the local oscillator (LO). The IF signal is usually close to dc and tracking the variations in the former using the master clock operating at 125 MHz would result in sub-optimal usage of resources. Hence, we use a cascaded integrated comb (CIC) filter for down-sampling the signal [258, 259]. When the factor by which the signal has to be down-sampled is large, CIC filters, used as a front end for FIR filters result in decreased number of filter taps required for anti-aliasing.

The data from the multiplier as it enters the CIC filter is at 125 MSPS. This is decimated by 50, resulting in a data rate of 2.5 MSPS at the output of the CIC filter and an aggregate data rate of 1.25 MSPS after the FIR filter, resulting in a base-band data of 625 kHz.

We use four counters in the firmware for timekeeping purposes: a trigger counter (TC), a free running counter (FRC) at 125 MHz rate, a over- flow counter (OC) and a packet counter (PC). The TC keeps track of the triggers received by the RTDR, while the FRC keeps track of the time since the power on. The 32 bit OC counts the number of FRC overflows. These counters allow us to obtain the time between two trigger events and also its occurance instances since the start of acquisition. The PC helps us to ensure no data was missed during packet framing and transmission.

The data, along with the counter values, is written to a BRAM and read out by the PS and transmitted using ethernet.

CW signals at various frequencies within the 0-62.5 MHz band were injected at different power levels from -90 to 10 dBm. As shown in Fig. 6.4, the output power scales linearly with the input power, irrespective of the frequency.

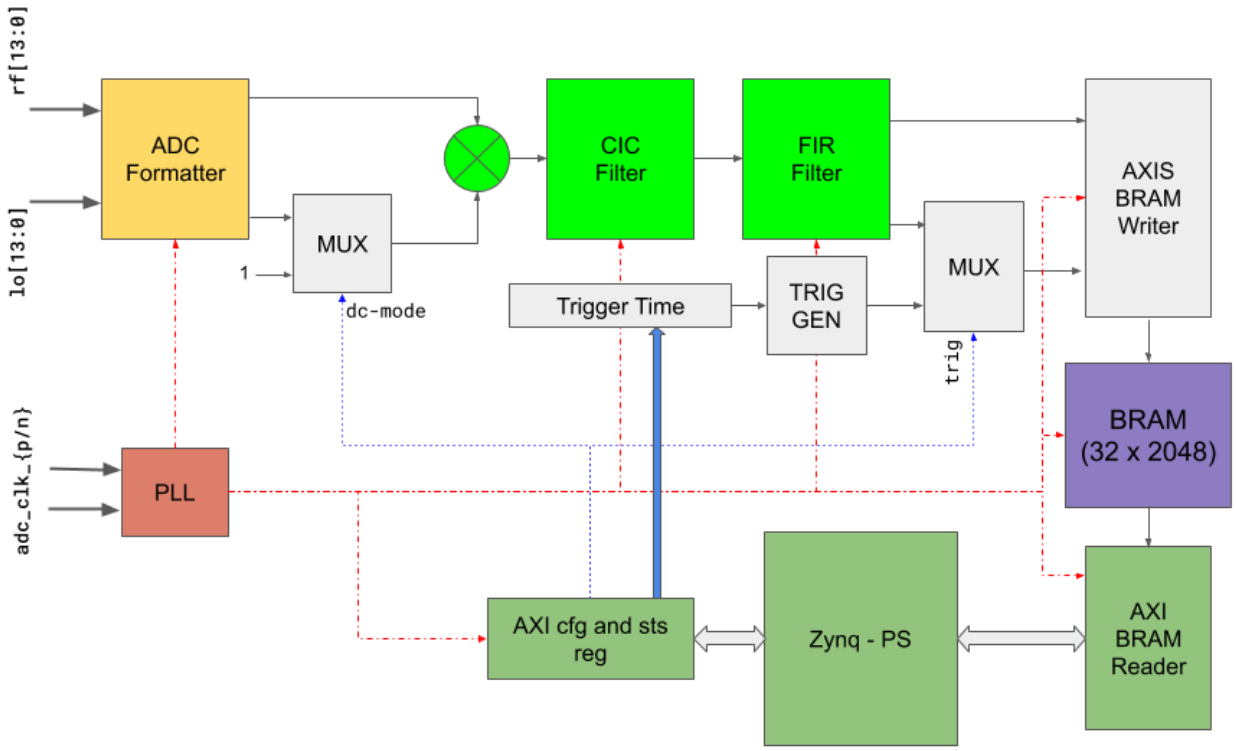

Figure 6.3: Firmware description of the triggered raw voltage recorder. The dotted blue lines represent the flow of control signals and status signals to and from the memory mapped AXI registers. The green blocks represent signal processing elements of the design.

6.4 Electromagnetic interference (EMI) and its mitigation

The ambient EMI can hinder the detection of weak signals. Some common sources of unavoidable EMI are 50/60 Hz AC lines, switching regulators and LO harmonics. Strong EMI affects the dynamic range of the receiver system at frequencies < 1 MHz. EMI can be mitigated during pre- and post-processing stages. We describe the techniques adopted, during these stages of EMI mitigation, in this section.

During our measurements, we found that the strong 50 Hz AC signal and its harmonics were getting coupled into the system through the AC adapter of the FPGA evaluation board. To overcome this, we replaced the power adapter with a commercially available battery-bank of similar specifications.

A second prominent source of EMI were the switching circuits associated with the magnetic coil current driver. This gave rise to strong peaks in the low frequencies. The SNS setup is located in a laboratory environment with multiple sources of EMI.

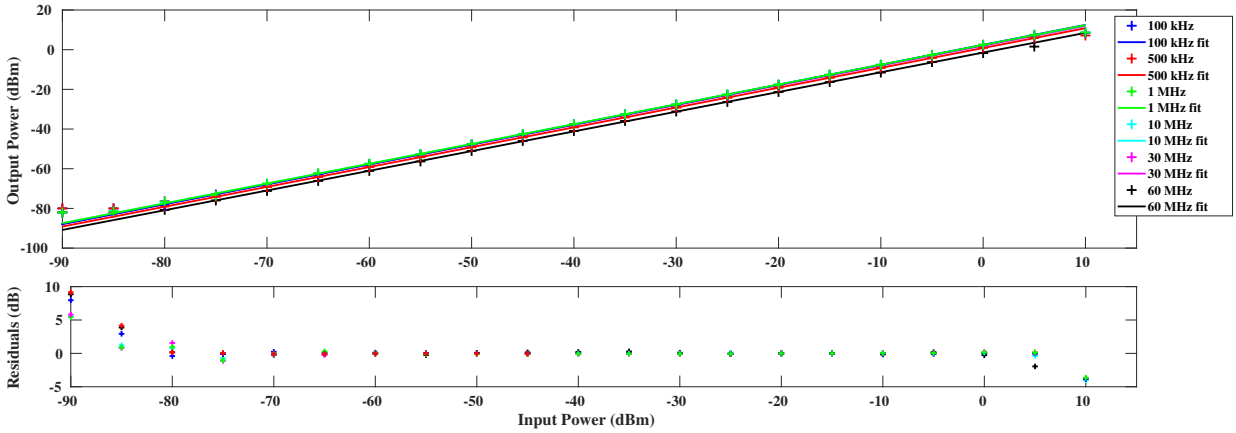

Figure 6.4: Characterization of the DRS (in both RTDR and FFTS modes) with signals of various power fed across the frequency range of operation. The '+' markers indicate the data and the solid lines represent the first order polynomial fits. The bottom plot shows the residuals. The black dashed lines encompass the linear range of the DRS.

Therefore, we custom designed a mild-steel enclosure for the DRS. In Fig. 6.5 we show the significant mitigation of EMI by ≈ 20 dB after adopting the aforementioned schemes. We performed further processing on the archived data to excise low-level narrow-band and impulsive broad-band EMI [260, 261]. For EMI that was stationary in frequency, we used a combination of background and median subtraction. Impulsive, broadband EMI, when present, was clipped from each channel when its value exceeded the 3σ threshold.

6.5 Results and Discussions

Our experimental set-up is shown schematically in Fig. 6.1. A uniform transverse magnetic field ($B_\perp$) was produced by the current flowing through a pair of magnetic coils in Helmholtz configuration. The signal from the BPD was recorded either with our digital receiver system (DRS) or a commercial spectrum analyzer (SFSA) for the purpose of performance comparison.

In Fig. 6.6, we show the SN spectrum of Rb atomic vapor with $B_\perp \sim 5.1$ G obtained using SFSA (top panel) and the FFTs (bottom panel). These sets of data were recorded under similar experimental conditions. In each of the panels, we observe two peaks appearing at ~ 2.4 MHz and ~ 3.6 MHz corresponding to SN signal due to ^{85}Rb and ^{87}Rb, respectively. The RBW of the SFSA has been kept the same as the channel width of the FFTs which is 30 kHz. The integration time for the SFSA

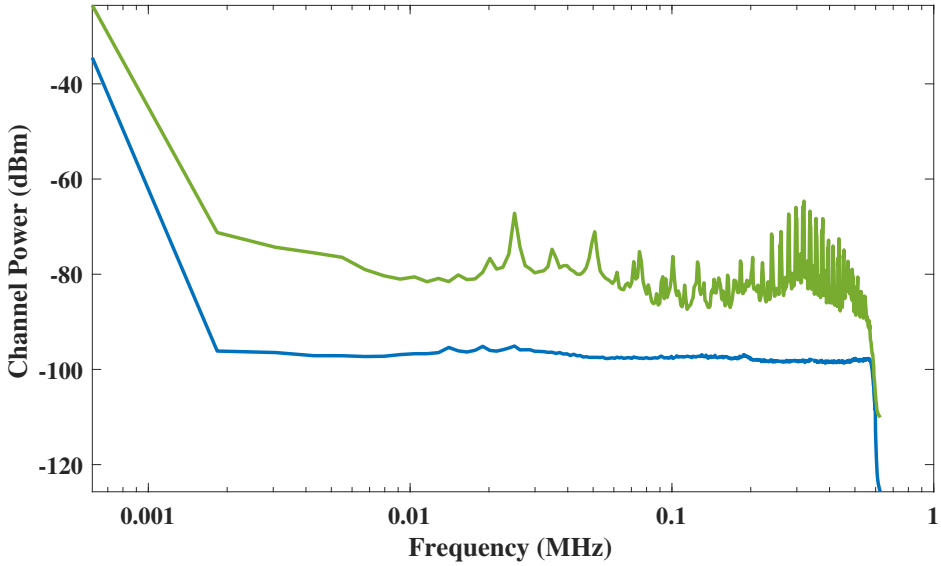

Figure 6.5: The effect of EMI on the measured spectrum (green trace) and after its mitigation (blue trace). The effect of EMI mitigation is clearly visible through the absence of spikes and a reduction in the noise floor by $\approx$ 20 dB in the blue trace.

to obtain the data presented in Fig. 6.6 (top panel) is 45 seconds whereas the same for the FFTs presented in Fig. 6.6 (bottom panel) is 10 seconds. In both the cases the spectrum is background subtracted and normalized to it's peak value. The SNR of the SN signal is defined as the ratio of the strength of the strongest signal to the rms value of the background signal. The background signal is obtained by recording the SN signal at zero magnetic field. Comparing these two spectra, we note that the SNR for the DRS is more than an order of magnitude better than that for the SFSA for the same integration time. This improvement in the SNR along with the fact that our DRS is light weight, portable, low-cost, low-power ($<$ 10 Watts) consuming as compared to a commercial SFSA, makes it preferable for both laboratory and field measurements.

Since the SN spectrum peak position is the Larmor frequency ν_L, by precisely measuring the peak position of the spectrum we can estimate the strength of $B_\perp$. Therefore, this measurement technique can be used as a precision magnetometry tool. Since the developed DRS described in this chapter is easily field deployable, it can have application in constructing a robust miniaturized magnetometer. As an example, the SN spectrum recorded at various magnetic field strengths are shown in Fig. 6.7. By fitting a Lorentzian to the individual spectrum, we can estimate the Larmor frequency and in turn, the magnetic field.

Another advantage of using this DRS is that the device is re-configurable, which

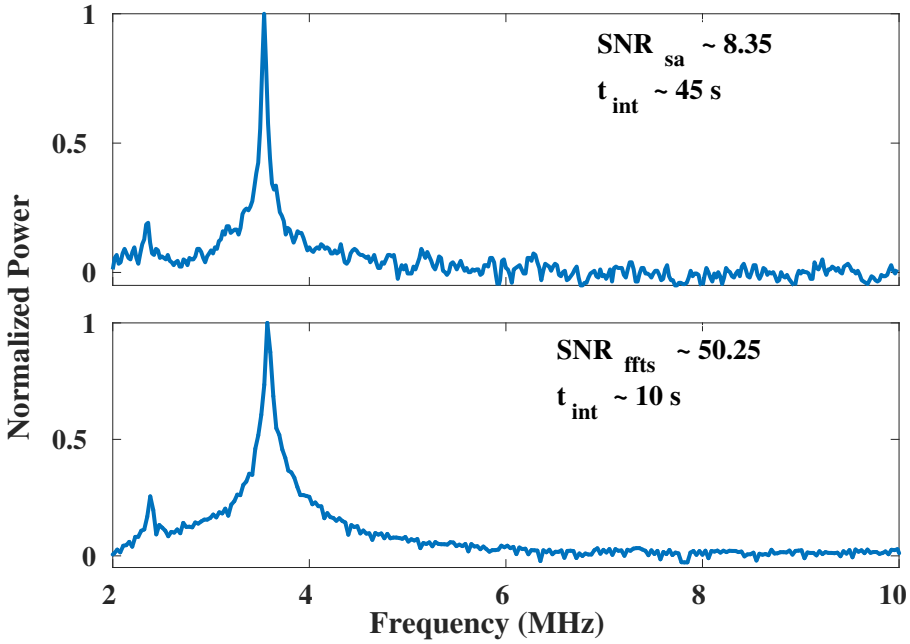

Figure 6.6: Spin noise (SN) spectrum acquired from SFSA (top panel) and FFTS (bottom panel). Note that the SNR is $\approx$ 50 for the FFTS for an integration time 5$\times$ lower than SFSA. These two spectra were recorded under the same experimental conditions, at $B_\perp \sim 5.1$ G.

enables triggered real time measurements of the SN spectra. In Fig. 6.8, we show an example of real time data acquisition. In each of the four panels we show SN spectrum obtained using our DRS with an integration time of as low as 100 ms after the TTL trigger pulse. The magnetic field strength was also changed after each trigger pulse. Hence, we can sample the magnetic field with a time resolution of 100 ms. The integration time of the data shown in Fig. 6.8 is 100 ms and the corresponding spectral resolution is $\approx$ 610 Hz resulting in an SNR $\sim$ 5. Whereas for the data shown in Fig. 6.7 the integration time was 1 s and the spectral resolution was 30 kHz, hence an SNR $\sim$ 15.

For testing and verification of the triggered mode acquisition, we generated an external trigger TTL pulse from a function generator and fed this into a SMA-to-GPIO board, which was connected to the Red-Pitaya using a ribbon cable and connector assembly. For this, the acquisition time was set to $\approx$ 100 ms. The trigger rate was $\approx$ 10 per minute.

The output from the BPD is fed to the DRS. The triggered acquisition works as follows: (a) The FPGA waits for a rising edge on the trigger input port, (b) On the rising edge of the trigger input, a `dv` signal is asserted, upon which the BRAM starts to store the data, (c) Once 256 such samples are written, the data is packetized and

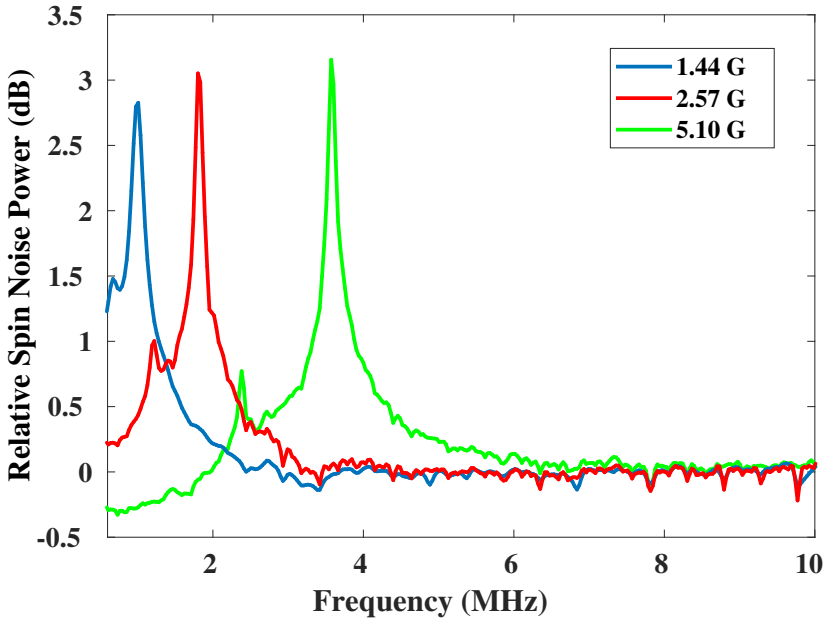

Figure 6.7: Background subtracted spin noise (SN) spectra measured for different magnetic field values. The error in the measurements are ≈ 0.02 G, which is limited by the spectral resolution ≈ 30 kHz of the FFTS.

transferred to the DAQ server. The trigger count and an absolute time stamp is included in the header data of the Ethernet packet for assisting in data analysis.

Another application of using this device is the temporal and spatial correlation measurements in a system with laser cooled atoms and ions. Intrinsically the correlation signals are expected to be extremely narrow in frequency domain and are promising candidates for various quantum technology applications. However, the measurement duration is typically limited to few milliseconds. Therefore, it is difficult to perform the SNS in cold atoms using traditional SFSA and therefore the DRS emerges as a promising candidate for this purpose. Also, since in the RTDR configuration, the DRS records the voltage samples directly, it gives us the flexibility to achieve high frequency resolutions, which is only limited by the timing jitter of the on-board clock.

The DRS in the RTDR mode, allows for a minimum time resolution of 800 ns when the data is treated in its raw form. When spectral analysis is carried out with a N point fourier transform, the channel width and the time resolution is $\frac{1.25\,\mathrm{MHz}}{N}$ and $N \times 800$ ns, respectively. Therefore, when the signal is inherently strong, higher time resolutions can be obtained at the cost of reduced frequency resolution. However, for intrinsic SN signal from atomic vapor, the SNR deteriorates for shorter integration times which affects the precision of the measurements. Therefore, for the purpose of demonstration, we integrate the SN signal for 100 ms time window and obtain a precision in measured

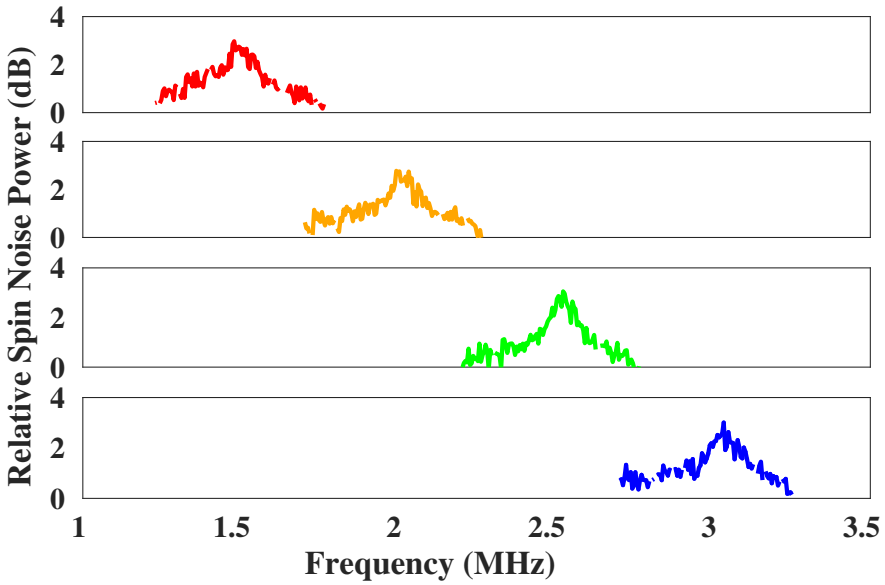

Figure 6.8: Spin noise (SN) spectrum at various magnetic field strengths from the RTDR. These series of spectra has an SNR ≈ 5, and the peak positions can be determined within an accuracy of $\approx 5\%$.

magnetic field of the order of 800 μG.

To demonstrate the response of the detection system to fast varying magnetic fields, we conducted an experiment [17], where we added a coherent drive [232] using a pair of Raman beams, which enhanced the SN signal strength million fold, improving the SNR. We then varied the magnetic field from 3.35 G to 3.85 G, synchronously with the coherent drive field frequency (i.e. δ_{12}), and recorded the signal using the DRS. The results from this experiment is shown in Fig. 6.9, where each pixel along time and frequency axis is ≈ 800 μs and 610 Hz, respectively. We see that the DRS simultaneously tracks the "step" changes in the magnetic field, as well as its drifts in milli-second timescales.

We highlight that a time resolved measurement of magnetic field has applications ranging from geophysics [262] to physiology [263, 264]. The time stamp contained in the received data (see section 6.3), can be used to determine the absolute time variation of the magnetic field strength.

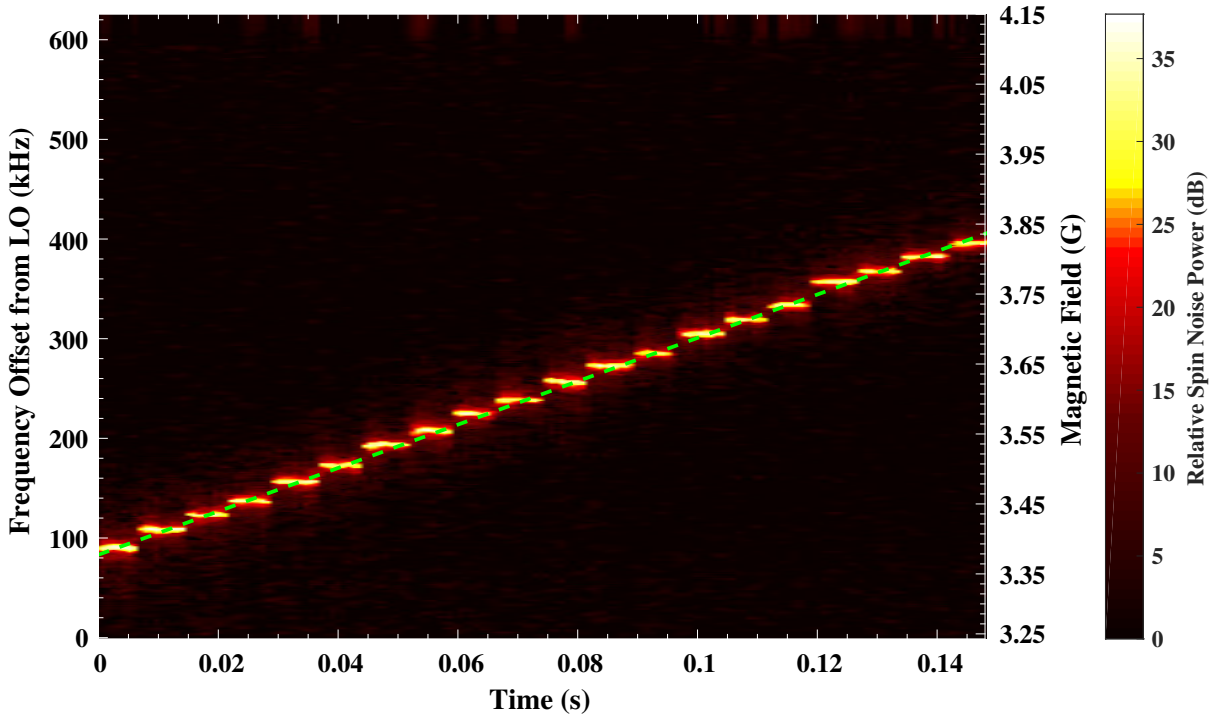

Figure 6.9: Waterfall plot of the DRS output when the magnetic field was swept from $\sim$ 3.35 G to 3.85 G. We have synchronously varied the coherent drive frequency (see text). The yellow patches represent the spin noise signal in the time-frequency plane, the green dashed line is a fit to the centroids of the yellow patches and its slope indicates the rate of variation of the magnetic field in time.

6.6 Conclusions and outlook of this chapter

We present the development of a software defined digital receiver system (DRS) with two operating modes for spin noise spectroscopy (SNS) experiments. We also show the applicability of the SNS technique in precision magnetometry and measure fast temporal variations in the magnetic field using DRS system. This device is fully reconfigurable.

The FFTs mode allows for user programmable integration times. The RTDR mode is specifically developed for studies of spin noise (SN) signals from cold atoms and for fast varying magnetic field measurements. Such a mode, where high time resolution voltage data can be recorded, does not exist in SFSA. The FFTs can also be used to supplement the RTDR mode as follows: using the FFTs, the user will be able to explore the spectrum over a wide range of frequencies and once the peak location is known, the RTDR can be used to obtain a time-frequency resolved picture of the signal of interest.

Future directions for the system development include using a DDS core which can internally generate the LO signals to facilitate a two channel implementation, replace the DAQ computer with a ARM based microprocessor system viz. Raspberry Pi for system miniaturization.

The receiver described in this chapter is developed to be a part of a compact, portable SNS magnetometer. While we have demonstrated the application of the digital receiver using the SNS experiments, it can be easily adapted for use in other experiments as well.

Chapter 7

Laser cooling and trapping of neutral atoms for spin dynamics studies

Primarily, the main objective of this thesis work was to develop a non-invasive and spin-sensitive imaging technique for ultra-cold quantum gases and molecular systems. Quantum gases are a clean and isolated system that provides ideal testbeds for exploring a wide range of fundamental physics. Since the observation of Bose-Einstein condensation (BEC) in dilute atomic vapor [265, 266], quantum gases have been used as a tool to create and study the controllable analogs of a wide variety of physical systems. This ranges from simulating various condensed matter Hamiltonians to understanding the fundamental interactions in the universe. The following Fig. 7.1 tries to capture the intersection of this field with other areas in physics.

Quantum gases exhibit properties that cannot be observed in a classical gas. The large de-Broglie wavelength of constituent particles compared to inter-particle separation causes overlap of wavefunctions and particles start to obey different statistics depending on their spin. This now allows one to mimic real physical systems in which these statistics are obeyed. The reason to mimic those systems with quantum gases is the precise control that can be exerted over the various experimental parameters using quantum gases. Another point is the time scales associated with various processes which might be very short in real systems and might not be controllable in real-time. These observations make quantum gases an ideal testbed to investigate physical phenomena covering large temporal and spatial scales.

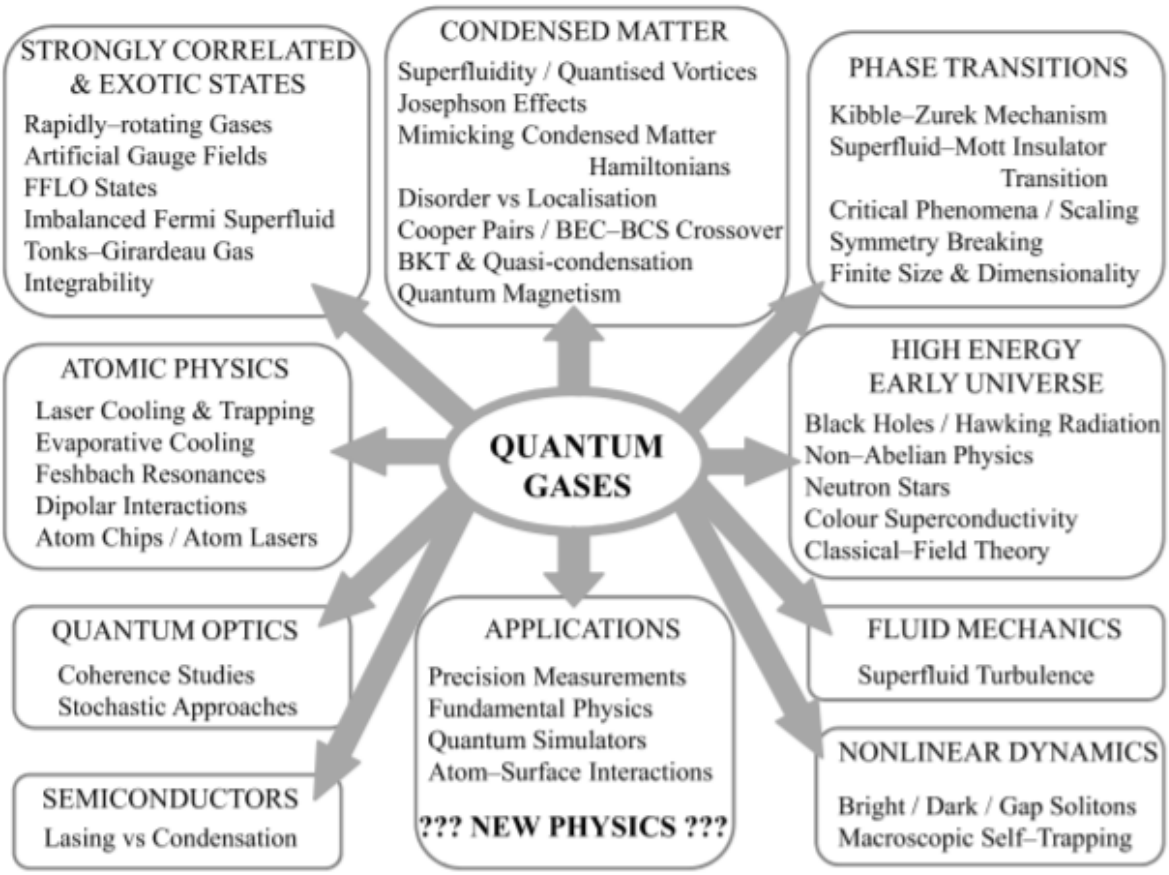

Figure 7.1: Quantum gases as an emerging interdisciplinary research field.

Quantum simulation [267–270] of a physical system is achieved by building another system that follows a model reproducing the same physics as the physical system. A good example is the Hubbard model which describes the system of interacting particles in a lattice. A quantum simulator of this model is the system of ultracold atoms in an optical lattice which can now be used to study the physics of interacting particles in a lattice. On these ideas, there has been immense progress in simulating a wide variety of physical systems. Comprehensive reviews of quantum simulation with ultracold gases can be found in [271–274].

However, in this chapter, we will discuss the laser cooling and trapping technique of neutral atoms to cool down their temperature in the range of 100's of μK. The atoms are trapped inside an ultra-high vacuum chamber using multiple laser lights and spatially in-homogeneous magnetic fields. This technique is known as a magneto-optical trap (MOT). This is the pre-cooling stage of neutral atoms to achieve the quantum gases in the temperature range of nK regime. In the following, we briefly describe the basic concepts of laser cooling and trapping [275–284] technique.

7.1 Doppler cooling of neutral atoms using laser light

Laser cooling uses the momentum associated with photons to decelerate atoms by shining laser beams that are red-detuned with respect to a particular atomic transition. For an atom moving in the opposite direction to the light propagation, the Doppler shift can compensate for the detuning and the atom can see the light resonant with the atomic transition. This leads to an increase of photon scattering rate, thus giving a retarding kick to the atom. The atom excited by photon absorption soon decays to its ground state by spontaneously emitting a photon in a random direction. Iterations of this preferential absorption of photons counter-propagating to atomic motion followed by spontaneous emission in random direction lead to a net deceleration of an atomic motion.

As shown in Fig. 7.2, if the absorbed and emitted photons have momentum $\hbar\mathbf{k}$ and $\hbar\mathbf{k}'$, respectively, then the average change in atomic momentum after N fluorescence cycles is N$\hbar\mathbf{k}$ because the average of $\hbar\mathbf{k}'$ is zero. This change is in direction of the absorbed photon which is opposite to atomic motion, hence the atom experiences a damping force. The damping force (i.e. rate of momentum change) is given by [284, 285]:

$$\mathbf{F} = \hbar\mathbf{k}\, R_{sc}(I, \delta), \tag{7.1}$$

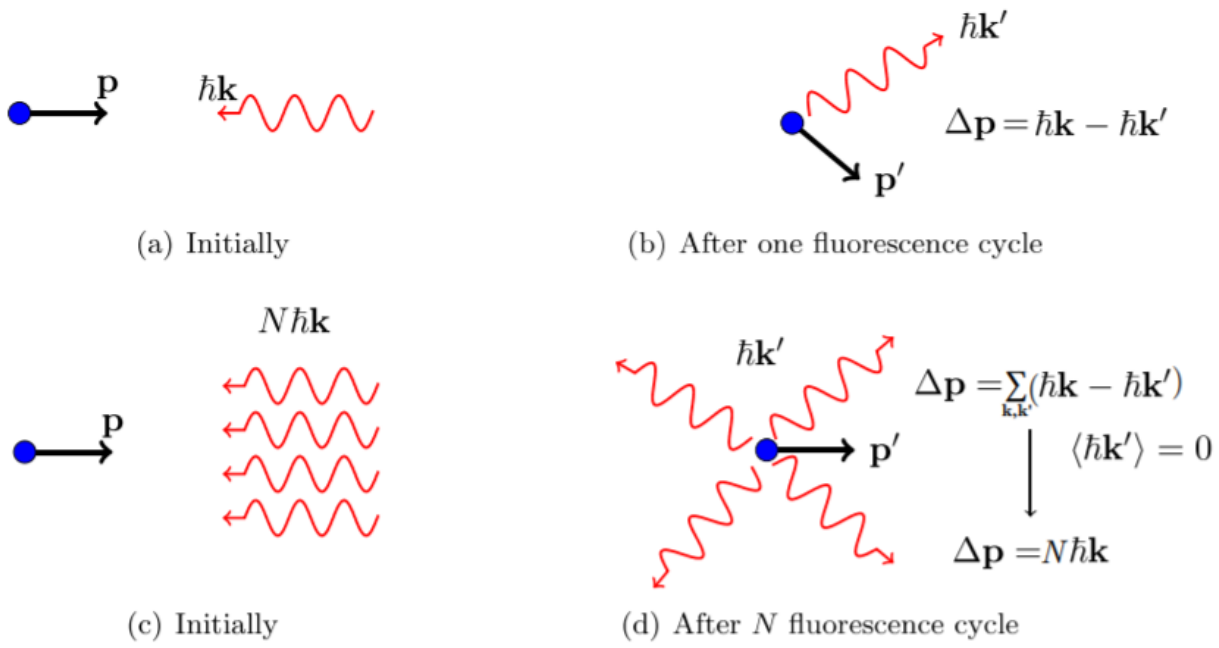

Figure 7.2: The schematic of the Doppler cooling mechanism.

where $R_{sc}(I, \delta)$ (called the scattering rate) is the net absorption rate which is equal

to absorption rate minus stimulated emission rate. I and δ are the intensity and detuning of the laser, respectively. In the above case of a two level system, $R_{sc}(I,\delta)$ can be written as [284]: $R_{sc}(I,\delta) = \gamma \times$ fraction of atomic population in excited state

$$R_{sc}(I,\delta) = \frac{\gamma}{2}\frac{s_0}{1+s_0+\left(\frac{2\delta}{\gamma}\right)^2}, \tag{7.2}$$

where γ is the natural line-width of the excited state and $s_0 (= I/I_{\text{sat}})$ is the saturation parameter of the atomic transition. I_{sat} is the saturation intensity for the corresponding atomic transition of the atoms. $\delta = \omega - \omega_0$ is the detuning of the laser from the related transition, where ω and ω_0 are the laser and atomic transition frequency, respectively. Therefore together with Eq. 7.1 and Eq. 7.2, the damping force is

$$\mathbf{F} = \hbar\mathbf{k} \times \frac{\gamma}{2}\frac{s_0}{1+s_0+\left(\frac{2\delta}{\gamma}\right)^2}. \tag{7.3}$$

In the above analysis, only one laser beam was considered which damps the motion of atoms only opposite to beam direction. For damping velocities parallel or antiparallel to a given direction, two oppositely directed beams are required. To cool atoms moving in 3−D, three mutually orthogonal pairs of counter-propagating beams along each of the x, y, z axes are required. Such an arrangement as shown in Fig. 7.3 (b) is called optical molasses (OM).

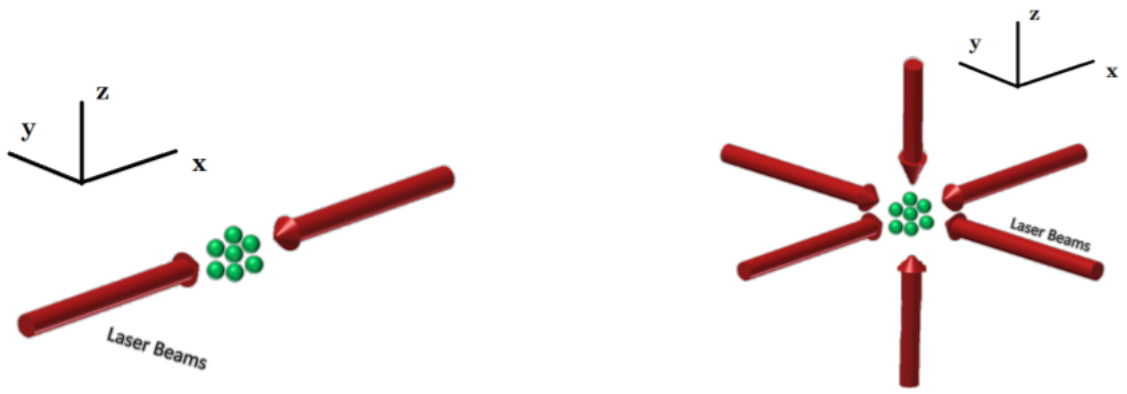

(a) Cooling in 1-D **(b)** 3-D Optical Molassses

Figure 7.3: The laser beam configuration for 1-D and 3-D optical molasses (OM).

As shown in Fig. 7.3 (a), an atom moving along the x axis receives separate forces

from two oppositely directed beams on the x axis, giving a net force of [284]:

$$\mathbf{F}_x = \mathbf{F}_+ + \mathbf{F}_-, \tag{7.4}$$

where $\mathbf{F}_\pm$ refers to the force from the laser beam propagating in the $\pm x$ direction. At low velocities ($\mathbf{v}$), where $|\mathbf{k}\cdot\mathbf{v}| \ll \gamma$, the net force is:

$$\begin{aligned} F_x &= F_+ - F_- \\ &= F(\omega - \omega_0 - kv) - F(\omega - \omega_0 + kv) \\ &\approx \left[F(\omega-\omega_0) - kv\frac{\partial F}{\partial \omega}\right] - \left[F(\omega-\omega_0) + kv\frac{\partial F}{\partial \omega}\right] \\ &= -2kv\frac{\partial F}{\partial \omega}. \end{aligned} \tag{7.5}$$

This is a damping force of the form:

$$F_x = -\alpha v, \tag{7.6}$$

where $\alpha = 2k\frac{\partial F}{\partial \omega}$. Using Eq. 7.3, the expression for α is

$$\alpha = 4\hbar k^2 s_0 \left[\frac{-2\delta/\gamma}{\left(1 + s_0 + \left(2\delta/\gamma\right)^2\right)^2}\right]. \tag{7.7}$$

In Eq. 7.7 we can as well ignore s_0 in the denominator, because the above treatment holds for $s_0 \ll 1$. Also for a damping force, we require a positive value of α and hence a red-detuning (i.e. $\delta < 0$). At low intensities, the damping force is largest when $\delta = -\gamma/\sqrt{12}$, but this is not the detuning at which the lowest temperature is achieved, as we shall show below.

7.1.1 Doppler cooling limit

The random nature of the spontaneous emission gives a random recoil to the atom after each emission. Also, the atom does not absorb the same number of photons in a given time interval δt. The fluctuations imposed onto the atomic motion due to these uncertainties cause a random walk of the atomic velocity on top of the damping in OM. This competition between diffusion and damping culminates into a steady-state velocity for the atoms. This limits the minimum achievable temperature of the Doppler cooled atoms.

To find a mathematical expression for the Doppler cooling limit we have to equate

the heating and cooling rates at steady state condition of the system. The cooling rate due to damping is [284, 285],

$$\left(\frac{dE}{dt}\right)_{\text{cooling}} = \mathbf{F}\cdot\mathbf{v} = -\alpha v_x^2 \tag{7.8}$$

where we are considering the 1−D case of two counter-propagating beams along $x-$axis. The heating rate associated with the repeated absorption and emission of photons is,

$$\left(\frac{dE}{dt}\right)_{\text{heating}} = \frac{1}{2m}\frac{d}{dt}\left\langle p_x^2\right\rangle = \frac{D_p}{m}, \tag{7.9}$$

where m and p_x are the mass and instantaneous momentum component of atom, respectively. D_p is the momentum diffusion coefficient. On solving for v_x^2, we get

$$v_x^2 = \frac{D_p}{\alpha m}. \tag{7.10}$$

The corresponding temperature (T) can be calculated by equi-partition theorem as,

$$\frac{1}{2}k_B T = \frac{1}{2}m v_x^2 \Rightarrow T = \frac{D_p}{\alpha k_B}, \tag{7.11}$$

where k_B is the Boltzmann constant and m is the mass of the atom. Thus, the limiting temperature is achieved by minimizing the ratio of D_p to α. To calculate D_P, we analyze the random walk of the atomic velocity which prevents the atom from coming to a complete standstill.

In a given time t an atom scatters a mean number of photons N given by, $N = R_{sc}t$. A random walk of N steps gives a mean displacement proportional to $\sqrt{N}$, or equivalently the mean square displacement equals N times the square of the step length. Of course, we have assumed Poissonian statistics.

Considering motion along $x-$direction only, spontaneous emission causes the mean square velocity to increase as [284],

$$\left\langle v_x^2\right\rangle_{spont} = N\eta_{sc}v_r^2 = \eta_{sc}R_{sc}\, v_r^2\, t. \tag{7.12}$$

The factor $\eta_{sc} = \langle\cos^2\theta\rangle$ represents the contribution of spontaneous emission along $x-$direction which depends on $\cos^2\theta$. Here θ is the angle between the $x-$axis and direction of emitted photon. In the case of two counter-propagating beams, for isotropic spontaneous emission we have $\eta_{sc} = 1/3$.

The fluctuations in absorption also cause a similar heating as above but without the factor η_{sc}, because all absorbed photons have the same direction. So,

$$\left\langle v_x^2 \right\rangle_{abs} = N v_r^2 = R_{sc}\, v_r^2\, t. \tag{7.13}$$

Although the above absorption was considered from a single laser beam, however, in the case of two counter-propagating beams, the effect of fluctuations is cumulative and the atom performs a random walk along the laser beams. To account for two counter-propagating beams, we change $R_{sc} \to 2R_{sc}$.

Finally in the 3−D case of three mutually orthogonal pairs of counter-propagating beams, the above analysis still holds with the modification $\eta_{sc} \to 3\eta_{sc}$ assuming that an atom scatters photons three times faster than in a single pair (this neglects any saturation). The net velocity due to heating is then,

$$\begin{aligned} \left\langle v_x^2 \right\rangle_{total} &= (1 + 3\eta_{sc})\, v_r^2\, (2R_{sc})\, t \\ &= 4\, v_r^2\, R_{sc}\, t. \end{aligned} \tag{7.14}$$

The momentum diffusion coefficient can now be calculated as:

$$D_p \;=\; \frac{1}{2}\frac{d}{dt}\left\langle p_x^2 \right\rangle \;=\; \frac{1}{2}\, m^2 \frac{d}{dt}\left\langle v_x^2 \right\rangle \;=\; 2m^2\, v_r^2\, R_{sc}. \tag{7.15}$$

Therefore the expression for temperature,

$$T \;=\; \frac{D_p}{\alpha\, k_B} \;=\; \frac{2\, m^2\, v_r^2}{k_B}.\left(\frac{R_{sc}}{\alpha}\right) \tag{7.16}$$

Using Eq. 7.2 and Eq. 7.7, we get the expression for temperature,

$$T \;=\; -\,\frac{\hbar\gamma}{8k_B}\left(\frac{1 + s_0 + \left(2\delta/\gamma\right)^2}{\delta/\gamma}\right). \tag{7.17}$$

The temperature is minimum when $\delta/\gamma = -1/2$ and for $s_0 \ll 1$,

$$T_{min} \;=\; \frac{\hbar\gamma}{2k_B}. \tag{7.18}$$

So far we have discussed the Doppler cooling mechanism and the minimum achievable temperature T_{min} of two-level atoms in presence of three pairs of co- and counter-propagating laser lights. However, multilevel atoms, such as alkali metal atoms constitute many ground and excited hyperfine levels, and multiple dipole transitions can

possible due to the Doppler effect. Moreover, the degenerate Zeeman states within the ground hyperfine levels experience dissimilar light shifts due to the interactions with the laser beams. This permits the atoms to cool further down below Doppler temperature, and this is known as Sub-Doppler cooling mechanism [286, 287].

7.2 Principle of magneto-optical trap

The cooling techniques discussed so far although damp the atomic motion, but cannot trap atoms in space. The reason is that velocity-dependent force can only confine the atoms in momentum space (i.e. cooling). To confine atoms in position space, position-dependent force is required. The combination of both forces achieves cooling as well as trapping for the atoms. A routine technique employed for this purpose in cold atom labs is the use of a magneto-optical trap which uses the multilevel structure of atomic energy levels to create a position-dependent force along with a damping force.

As shown in Fig. 7.4 (a), a MOT consists of the optical molasses arrangement (with $\sigma^+ - \sigma^-$ polarizations) in addition to a pair of magnetic coils carrying current in opposite directions (in anti-Helmholtz configuration). This pair of coils creates a quadrupolar magnetic field with the net field zero at the center between the coils and linearly increasing for small distances away from the center. The resultant magnetic field (near to the center) of the coils can be expressed as:

$$\vec{B}(x, y, z) = b'(x\hat{x} + y\hat{y} - 2z\hat{z}), \tag{7.19}$$

where b' is the magnetic field gradient.

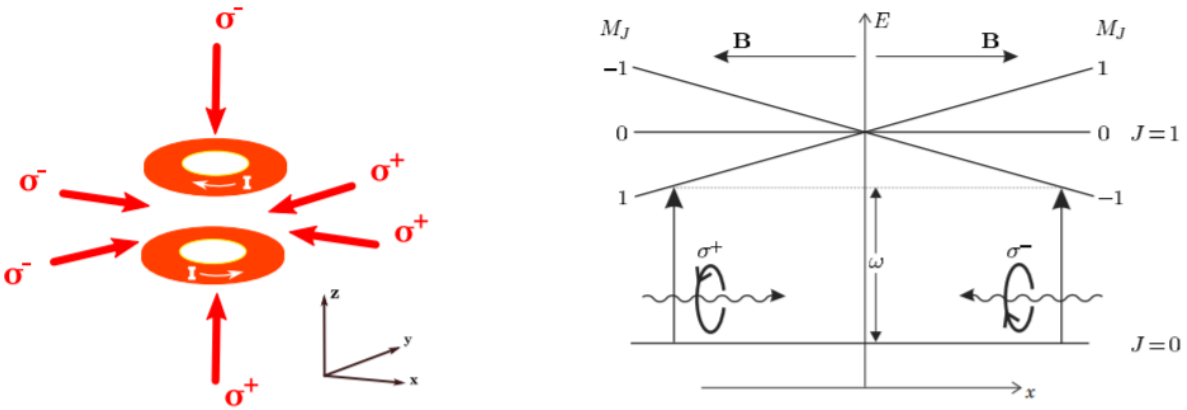

Figure 7.4: (Left) the propagation direction and polarization of the laser beams and the magnetic coil configuration for 3-D optical MOT. (Right) the basic principle of the 1-D MOT.

To explain the trapping force, we consider a simple atomic transition from $J = 0$ to $J = 1$. In presence of magnetic field given by Eq. 7.19 the excited state $J = 1$ splits into Zeeman states $m_J = 0, \pm 1$ whose degeneracy is lifted (as shown in Fig. 7.4 (b)) according to the relation

$$\Delta E = g_J \mu_B m_J B, \tag{7.20}$$

where, g_J is the Landé factor of level J. Now, consider an atom at the MOT center moving along $x-$axis. As it moves towards $x > 0$, the transition $J = 0 \rightarrow J = 1, m_J = 1$ comes closer to resonance with the red-detuned σ^- light. For $x < 0$, the transition $J = 0 \rightarrow J = 1, m_J = +1$ comes closer to resonance with the red-detuned σ^+ light. So the atom is always pushed back to center due to the light scattering. Note, however, that the forces exerted by the beams have not lost the velocity dependence, rather an additional position dependence (linear) has emerged. Thus the system now resembles a damped harmonic oscillator.

The mathematical formulation of MOT can be done similar to Doppler cooling in Eq. 7.21 with the addition of Zeeman shift along with Doppler shift. The force equation for MOT can therefore be written as [284, 285],

$$\begin{aligned} F_x &= F_{\sigma^+} - F_{\sigma^-} \\ &= F(\omega - (\omega_0 + \beta x) - kv) - F(\omega - (\omega_0 - \beta x) + kv) \\ &\approx -2\,kv\,\frac{\partial F}{\partial \omega} + 2\,\beta x\,\frac{\partial F}{\partial \omega_0} \\ &= -2\,kv\,\frac{\partial F}{\partial \omega} - 2\,\beta x\,\frac{\partial F}{\partial \omega}. \end{aligned} \tag{7.21}$$

In last the step we used the fact that since force depends on detuning, so $\frac{\partial F}{\partial \omega_0} = -\frac{\partial F}{\partial \omega}$. Also the term βx is the Zeeman shift of energy at position x. The expression for βx is given by,

$$\beta x = \frac{g_J \mu_B}{\hbar}\,\frac{dB}{dx}\,x. \tag{7.22}$$

7.3 Experimental set-up for MOT

In our laboratory, we have the option to capture both the rubidium isotopes in MOT once at a time by tuning the frequency of the relevant trapping lasers. So far we have discussed the principles of MOT for two-level atoms. However, the alkali atoms have multiple hyperfine levels in the ground and excited states due to the hyperfine interactions. The relevant energy level diagram for ^{85}Rb atom is shown in Fig. 7.5 (a). Therefore the requirement of the trapping laser beams, as well as the Doppler cooling

limit, has been modified due to these multiple energy levels of the atoms.

In Fig. 7.5 (a), the cooling laser beams connecting the cyclic transition $5S_{1/2}, F = 3 \rightarrow 5P_{3/2}, F' = 4$ (D_2) transition (detuning $= -2\gamma$) are used for slowing down the atom's velocity. However, a small fraction of atoms can also get excited to the other hyperfine levels such as $F' = 3$ and $F' = 2$ with reduced probability. After the spontaneous emission, some of these atoms gather into the ground $F = 2$ hyperfine levels depending on the branching ratio of the related transitions. These atoms (in $F = 2$ level) are lost from the cooling cycles since the ground hyperfine separation is much higher than the Doppler shift at the room temperature and they are no longer excited by the cooling beams. To participate those atoms in the cooling cycles, another laser beam co-propagating to all six directions along with the cooling beams is used to transfer them into the $F = 3$ level through optical pumping. For this purpose we have used another laser beam, called "repumper beam" generated from an independent ECDL and the frequency is chosen to resonance on the $5S_{1/2}, F = 2 \rightarrow 5P_{1/2}, F' = 3$ (D_1) transition.

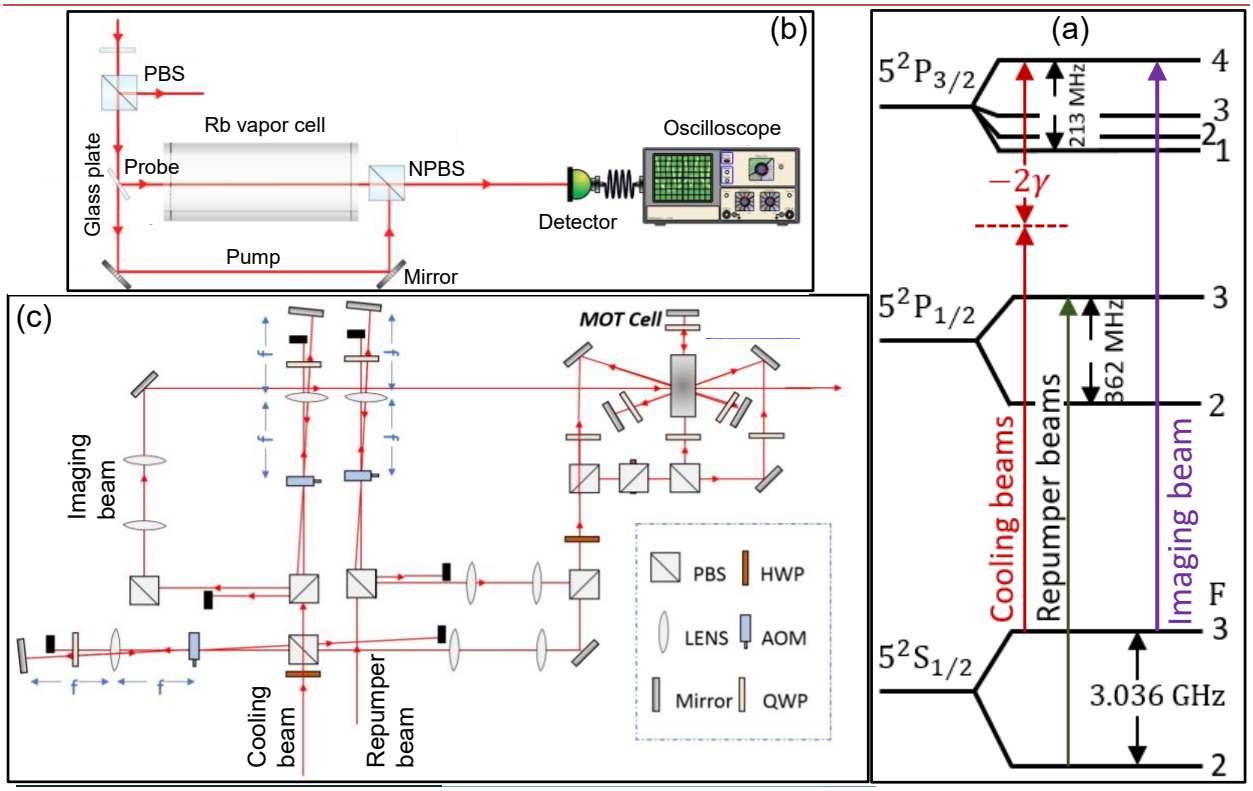

Figure 7.5: (a) The relevant energy level diagram and frequency of the cooling, repumper, and imaging beam to trap (in MOT) and detect ^{85}Rb atoms. (b) the saturation absorption spectroscopy (SAS) setup for frequency locking of the relevant lasers. (c) depicts the schematic of the optical arrangements for MOT.

We have used Doppler-free saturation absorption spectroscopy (SAS) [147] as a

frequency reference for locking the laser on a particular atomic transition line for both the cooling and repumper beams. The experimental arrangements for SAS is shown in Fig. 7.5 (b). The details of the SAS of Rb atoms are discussed in Appendix A. We have modulated the laser frequency at 2.4 kHz using the lock-in amplifier module which generates the dispersion-like error signal. Using the PID controller, we lock the laser frequency on the atomic transition line. The stability (below 500 kHz) of the laser frequency after locking is much better than the excited level line-width ($\sim$ 6 MHz) of the Rb atoms. The detuning and intensity of the cooling and repumper laser beams are controlled using AOMs and wave-plates. The arrangement of the cooling and repumper laser beams for MOT are shown in Fig. 7.5 (c).

The fiber coupled laser beams are expanded to have a Gaussian waist diameter of 8 mm and combined in a non-polarizing cube beam splitter. Thereafter, the combined cooling and repumper beams are split into three pairs of beams using a combination of half-wave plates and polarizing cube beam splitters. Each of the cooling beams is sent through the UHV glass cell (pressure $\sim 10^{-10}$ mbar) and retro-reflected via a quarter waveplate and a mirror. The incoming cooling beams are kept slightly converging to account for the losses in the optical elements and to ensure that any radiation-pressure imbalance between the incoming and the retro-reflected beam is eliminated. The restoring force required to confine the cold atoms is provided by a pair of current carrying coils in a near ideal anti-Helmholtz configuration. The magnetic field gradient generated by the anti-Helmholtz coil is separately measured using a Hall probe magnetometer. The (axial, $\frac{dB_z}{dz}$) magnetic field gradient used for making the cold atoms is around 2.9 G/cm/A, and we have used 8$-$12 A current for various measurements reported in this thesis. This is the traditional method to trap the neutral atoms inside an ultra-high vacuum chamber. Another laser beam, called an imaging beam, is used to probe the size and atom number of the trapped atomic cloud. The frequency of the imaging beam is chosen on-resonance to the cyclic transition i.e. $5S_{1/2}, F = 3 \rightarrow 5P_{3/2}, F' = 4$ (D_2) line as shown in Fig. 7.5 (a). Here, the frequency of the laser beams is shown for the trapping of neutral ^{85}Rb atoms, however, in the same experimental set-up ^{87}Rb atoms can also be trapped by tuning the laser frequency to the related transition corresponding to the ^{87}Rb atom. Using time-of-flight (TOF) and in-situ absorption imaging techniques, we measure the characteristic parameters (atom number, temperature etc.) of the cold atoms.

7.4 Detection techniques

Most of the quantitative measurements with the cold atoms in our experiments are done using absorption and fluorescence images of the atomic cloud. The number of trapped atoms, size of the atomic cloud, and the temperature - the three most important quantities relevant to our experiments are measured using these imaging techniques.

7.4.1 Fluorescence imaging

Alkali atoms have low optical saturation intensity and hence high photon scattering rate when subjected to near resonant radiation. The fluorescence emitted by trapped atoms can be used to find the size of the atom cloud and the number of atoms trapped in MOT. The number of atoms in the MOT can be determined using

$$N = \frac{1}{G\, R_{sc}(I,\delta)\, \Omega_s\, \eta\, \tau} \sum_{i,j} n_{i,j}, \tag{7.23}$$

where G is the gain of the camera, $R_{sc}(I,\delta)$ is the photon scattering rate per atom, Ω_s is the imaging solid angle within which the scattered photons are collected, η is the quantum efficiency of the camera chip, τ is the exposure time of the camera and $n_{i,j}$ is the number of counts at pixel labeled by pixel position (i,j). The photon scattering rate per atom is given by Eq. 7.2.

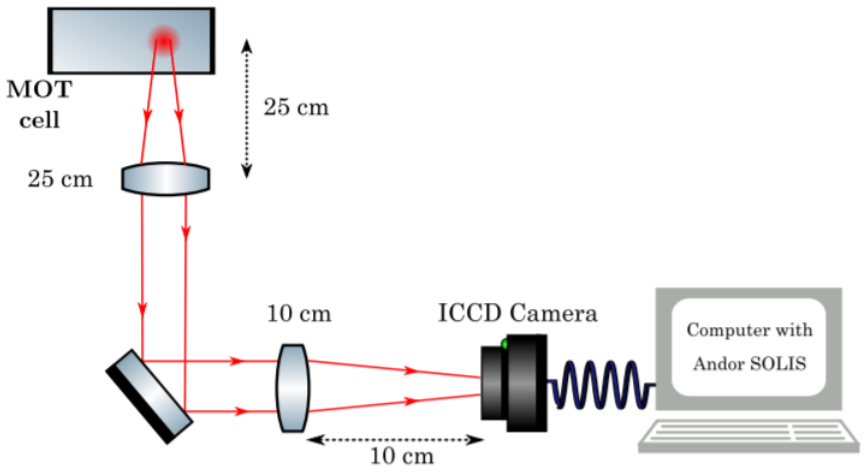

Figure 7.6: The arrangement of the lens used for fluorescence imaging of magneto-optically trapped ^{85}Rb atom.

The background trapping lights can also fall onto the detector chip and thus contribute to the counts $n_{i,j}$. we eliminate this by taking two separate images: one with MOT cloud and the background lights, and the second only with the background lights

after switching off the trapping magnetic fields. Subtraction from the first to the second gives the contribution of only MOT atoms.

The arrangement of the optical components for fluorescence imaging of magneto-optically trapped ^{85}Rb atom is shown in Fig. 7.6. 1-inch diameter and 25 cm focal length lens is placed at 25 cm below from the position of MOT cloud. The fluorescence emitted by the trapped atoms is captured by the first lens and then subsequently collected on another 1 inch and 10 cm focal length lens as depicted in Fig. 7.6. The collected fluorescence light in the second lens is then allowed to fall on an ICCD camera and computer for further image processing. A typical fluorescence image of $\sim 10^7$ magneto-optically trapped atoms is shown in Fig. 7.7.

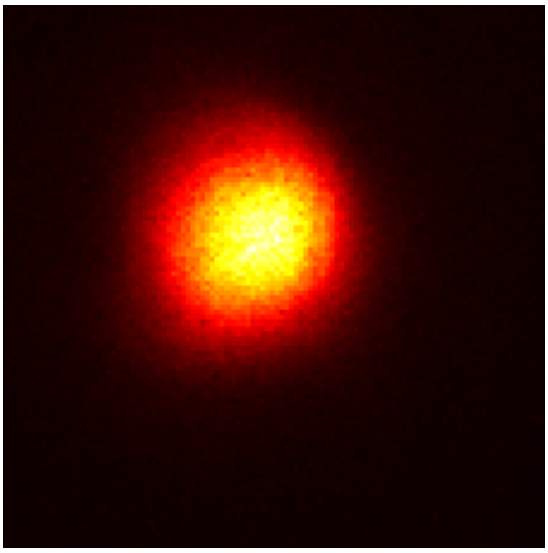

Figure 7.7: Typical fluorescence image of $\sim 10^7$ magneto-optically trapped ^{85}Rb atoms. For this background subtracted image, the detuning of the cooling beam is -12 MHz, axial magnetic field gradient is 30 G/cm and exposure time of the camera is 20 ms. The total power of the cooling beams are 14.5 $I_{\rm sat}$ and repumper beams are 1.8 $I_{\rm sat}$. The dimension of the frame is 6 mm $\times$ 6 mm.

The cloud size and the number of captured atoms in MOT are varied with various experimental parameters such as cooling and repumper beam power, cooling beam detuning, trapping magnetic field gradient, etc. In the following, using fluorescence imaging, we study the number of trapped atoms in MOT as a function of cooling beam detuning (in terms of δ/γ) and axial magnetic field gradient which is shown in Fig. 7.8 as a false-color map. In this measurement, we have fixed the cooling and repumper beam power to be 14.5 $I_{\rm sat}$ and 1.8 $I_{\rm sat}$, respectively. The repumper laser is locked on the $F = 2 \rightarrow F' = 3$ repumper line. For a particular magnetic field gradient, we have varied the detuning of the cooling beams using AOM and recorded the fluorescence

and background images in each of the detunings of the cooling laser. We have repeated and recorded the same measurements in a wide range of the magnetic field gradient. We have estimated the trapped atom numbers using the formula shown in Eq. 7.23 for each value of magnetic field gradient and detuning of the cooling beams.

As shown in Fig. 7.8, the maximum trapped ^{85}Rb atoms in our cold atom machine is around 2×10^7 for cooling beam detuning of around $\delta = -2.5\gamma$ and axial magnetic field gradient of around 40 G/cm. The MOT cloud is usually a source of dilute cold atomic samples and in our system, the density of atoms is measured to be $\sim 10^9/\text{cm}^3$.

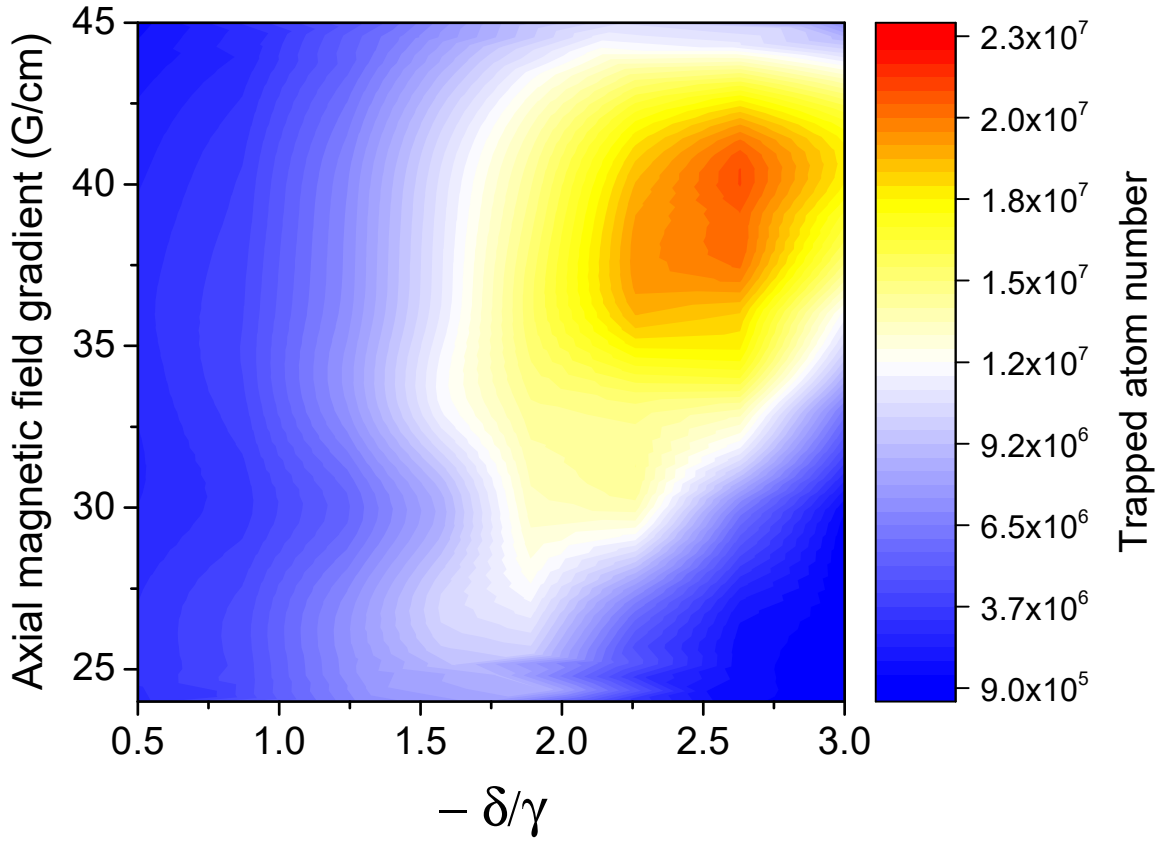

Figure 7.8: 2D false color plot of trapped MOT atom numbers as a function of detuning of the cooling beam (δ) and the trapping magnetic field gradient. The power of cooling and repumper beams are similar as mention in Fig. 7.7.

7.4.2 Absorption imaging

Methods. Absorption imaging technique is the most reliable method to measure the size, atom number, and temperature of the cold atomic cloud. However, the experimental sequences are different for the measurements of these quantities which will be discussed in the following section.

The absorption imaging technique relies on imaging the shadow of the cold atomic cloud on a weak, linearly polarized, and resonant light beam passing through the cloud. When the imaging laser beam (tuned to $5S_{1/2}, F = 3 \rightarrow 5P_{3/2}, F' = 4$ (D_2) transition) is sent through the ^{85}Rb cold atomic cloud, a shadow is cast on the detected profile of the imaging beam due to the optical absorption. In this method, the imaging beam is expanded to a much higher Gaussian FWHM in comparison to the dimension of the MOT cloud to avoid the variation in the intensity profile of the image beam in the region of the MOT cloud where they interact. Note that, the imaging beam is on-resonance to an atomic transition line and therefore this detection technique is destructive. The absorption imaging technique, in general, does not capture the dynamical information as well as microscopic behavior of the trapped atomic cloud.

In this technique, first, the trapping lasers such as cooling and repumper beams and the trapping magnetic fields are switched off. As a result, the atoms start falling under gravity, and simultaneously the atomic cloud also expands ballistically. It is during this fall that the imaging beam is pulsed at the atoms for a short duration of time. This is called time-of-flight (TOF) absorption imaging.

Basics of the light absorption by atoms. Let us consider a weak laser beam with intensity I_0 and frequency ω is propagating through an atomic medium. The transmitted intensity of the laser beam can be written according to Beer-Lambert's law as

$$I(\omega) = I_0\, e^{-\,C_d\,\sigma_{eg}} = e^{\,-\text{O.D.}\,\dfrac{\gamma^2}{4(\omega-\omega_0)^2+\gamma^2}}, \tag{7.24}$$

where σ_{eg} is the absorption cross-section. C_d and O.D. are the column density and optical density, respectively of the atomic cloud integrated along the laser beam propagation direction. These parameters are calculated using the following formulae:

$$\sigma_{eg} = \frac{3\lambda^2}{2\pi}, \tag{7.25}$$

$$C_d = \int n\, dx, \tag{7.26}$$

$$\text{O.D.} = C_d\,\sigma_{eg}\frac{4(\omega-\omega_0)^2+\gamma^2}{\gamma^2} = \ln\Big(\frac{I_0}{I(\omega)}\Big)\frac{4(\omega-\omega_0)^2+\gamma^2}{\gamma^2}. \tag{7.27}$$

Where λ is the wavelength (780 nm) of the laser. Here, n is the density profile of the atomic cloud and the probe beam is considered to propagate along $x-$direction. At

resonance (i.e. $\omega = \omega_0$), Eq. 7.27 can be written as,

$$\text{O.D.} = C_d\,\sigma_{eg} = \ln\Big(\frac{I_0}{I(\omega_0)}\Big). \tag{7.28}$$

According to Eq. 7.28, the column density of the atoms can be written as,

$$C_d = \frac{\text{O.D.}}{\sigma_{eg}}. \tag{7.29}$$

Absorption Imaging technique. To calculate the O.D. profile of the MOT cloud, we have to measure the ratio of $I_0/I(\omega_0)$ when the imaging is on-resonant. The ratio $I_0/I(\omega_0)$ can be measured by taking a ratio of the intensity profiles of the imaging beam without and with the absorbing atomic cloud. For this purpose, two images on the CCD camera are required. First, an image is taken with the atoms in the probe beam (let us call this image as Output) and after allowing the atomic cloud to fall out of the field of view of the probe beam another image is taken (let us call this image as Input). All images are taken with cooling beams, repump beams and the magnetic field switched off.

In practice, this way of finding relative transmission and hence the optical density is prone to error since the scattered light falling on the CCD camera at the time of taking these two images and the electronic noise (dark-current in CCD) are not taken care of. Therefore, we take three frames. The first two frames contain Output and Input, respectively and the third frame is a dark frame (let us call this image as Dark) where the camera is exposed for the same duration as in the case of the other two frames, but the probe is not pulsed within this time window.

The resulting optical density is then obtained as,

$$\text{O.D.} = \ln\Big(\frac{I_0}{I(\omega_0)}\Big) = \ln\left(\frac{\text{Input} - \text{Dark}}{\text{Output} - \text{Dark}}\right). \tag{7.30}$$

Note that, all the profiles i.e. Input, Output, and Dark are 2D arrays and thus is O.D., with each element obtained by entry-wise execution of the above formula on Input, Output, and Dark arrays.

Atom number measurement. From the O.D. array we can calculate the number of atoms in the cold atomic cloud. The number of atoms N can be calculated using,

$$N = \int C_d\,dy\,dz = \frac{A_{pix}}{\sigma_{eg}} \sum_{pix} \text{O.D.}, \tag{7.31}$$

where *pix* refers to pixels of the CCD camera and A_{pix} is the pixel area which is same for each pixel.

Temperature measurement. To calculate the temperature of the atomic cloud we perform a time-of-flight (TOF) measurement. For this, the delay between switching off the MOT cooling beam, repumper beam, and the magnetic field and the first image (i.e. Output) is varied. We set the delay for the first set of images to be 1 ms, then we increase these delays in convenient steps say 0.5 ms or 1 ms for the subsequent sets. We continue this till the time the atoms are still in the probe beam and we see a good absorption. Note that, after each set of imaging (i.e. Input, Output, and Dark) the MOT has to be re-prepared as this imaging technique is a destructive method.

Now for each imaging set, the O.D. array is found. The O.D. array is summed along its rows to get a 1D row vector. Similarly, it is also summed along its columns to get a 1D column vector. Now we fit a Gaussian on both these row and column vectors (called as x-direction and y-direction, respectively in the later discussion) independently. From the fit, we get the value of Gaussian width for both vectors. This Gaussian width increases if the atoms are allowed to fall for a larger time. It is because of the ballistic expansion due to the kinetic temperature which increases the Gaussian width according to the following formula,

$$\sigma^2(t) = \sigma^2(0) + \left(\frac{k_B\,T}{m}\right) t^2. \tag{7.32}$$

where σ^2 and T are the Gaussian widths and the absolute temperature of the cold atomic cloud.

Thus by performing a linear fit on the measured expansion of σ^2 of the MOT cloud vs. t^2, we can get the temperature of the atoms from the slope of the fit. Note however that the above equation is written for the MOT atoms but we are working with the MOT images. All lengths in the images are a scaled version of the real lengths in MOT (by the magnification factor of the imaging lens system). So the modified equation for the images becomes:

$$\sigma_i^2(t) = \sigma_i^2(0) + \left(\frac{\alpha_m^2\,k_B\,T}{m}\right) t^2. \tag{7.33}$$

where σ_i^2 is the Gaussian width in images and α_m is the magnification factor of the imaging system. Generally, σ_i^2 is obtained in pix^2, so unit conversion must be done carefully.

7.4.3 Imaging system and set-up

The imaging lens system and detection set-up for absorption imaging technique are shown in Fig. 7.9. For this method, we have generated an imaging laser beam from the same cooling laser source and passed it through an AOM for frequency tuning. After the AOM, the imaging beam is fiber-coupled for mode cleaning and sent through a 1-inch fiber collimator to get an expanded beam. The expanded imaging beam is shown with the red arrow in Fig. 7.9. The frequency of the imaging beam is chosen on-resonance ($\delta = 0$) to the cyclic transition of ^{85}Rb atoms to get maximum absorption cross-section so that minimum power can be used to image the MOT cloud with good SNR. We have chosen the frequency $\delta = 0$ of the imaging beam by performing an absorption image experiment which produces the transmission spectra through the MOT cloud in the vicinity of $\delta = 0$ as shown in Fig. 7.10.

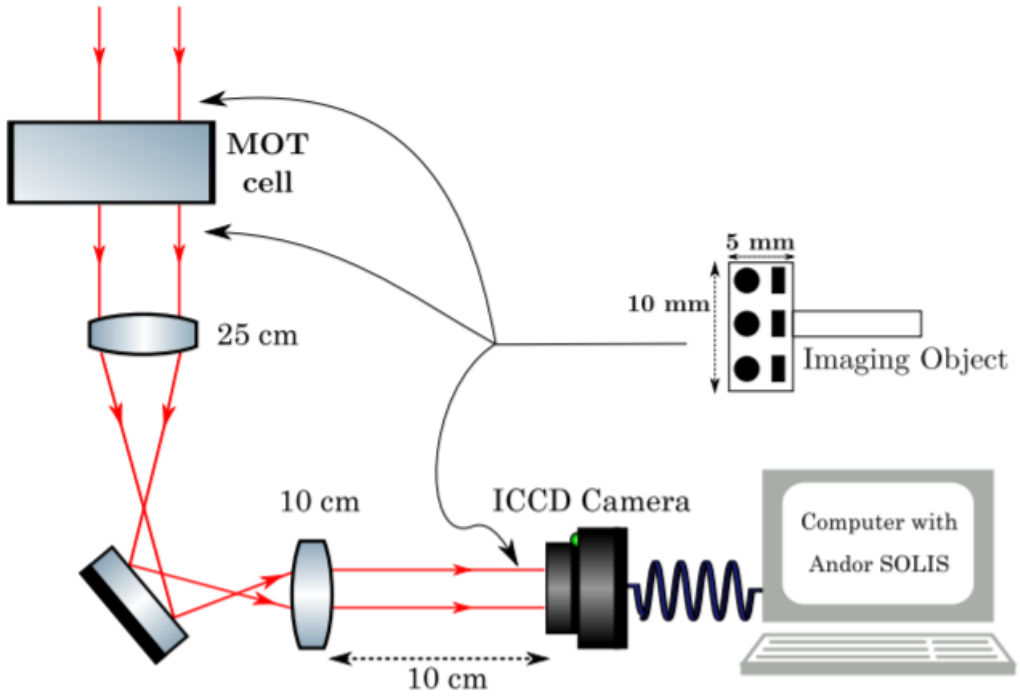

Figure 7.9: The lens system for absorption imaging technique magnification factor (α) measurement. The expanded and on-resonant image beam after passing through the MOT cloud is sent through the imaging lens set-up. The final is collected by an ICCD camera. The data analysis has been performed using python programming language.

In the absorption imaging technique, the most crucial factor is to precisely determine the magnification factor (α_m) of the lens system. In our set-up, the two lens system gives a magnification factor of about 0.4. To measure this factor we design an object in Inkscape (a graphics editing software) and print it on a transparent sheet.

This object with various length scales is shown in Fig. 7.9. This imaging object is first placed just in front of the camera while the absorption probe is ON. the shadow cast gives the real dimensions of the object in pixels. This calibration is required because although in Inkscape we may design a length of 1 cm but there might be an error in printing. Once we have calibrated our imaging target, we place it just in front of the MOT glass cell (absorption probe entry side) and record its image. This image is now formed by the lens and is magnified accordingly which gives the value of the magnification factor. Since we get lengths in terms of pixels the measurement is accurate.

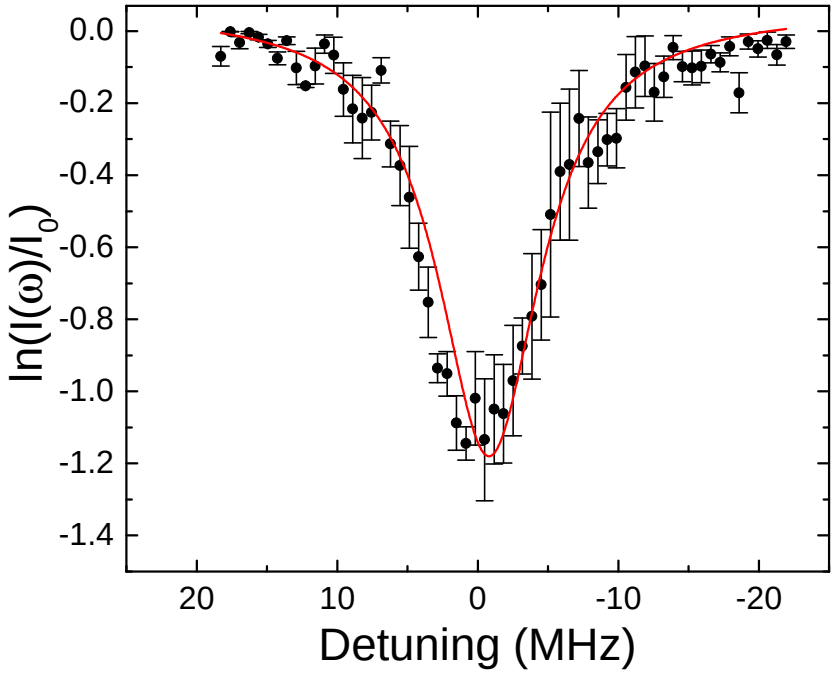

Figure 7.10: Variation of relative transmission of the imaging beam through the MOT cloud with detuning ($\delta = \omega - \omega_0$). The black dots show the experimental data points and red solid line is the fit according to 7.24.

Ideally, this imaging target should have been placed exactly at the MOT position to get the correct magnification value. But this is practically not possible, so we instead take another measurement by placing the imaging target just after the MOT glass cell (absorption probe exit side) and record its image. This gives us another magnification factor. To approximate the magnification factor we take the average of the two measurements at the probe entry and exit sides. The variation in magnification factor (α_m) also tells us about the quality of probe beam collimation, alignment of the imaging system, etc.

In the experiments, an 80 μW imaging beam is pulsed for a duration of 100 μs

using the AOM that record the Input, Output, and Dark profile. A typical processed absorption image (density profile) of the MOT cloud is shown in Fig. 7.11 in 2D color map. From the Gaussian fit to the column density data, we have estimated the FHWM of the MOT cloud to be around 4 mm.

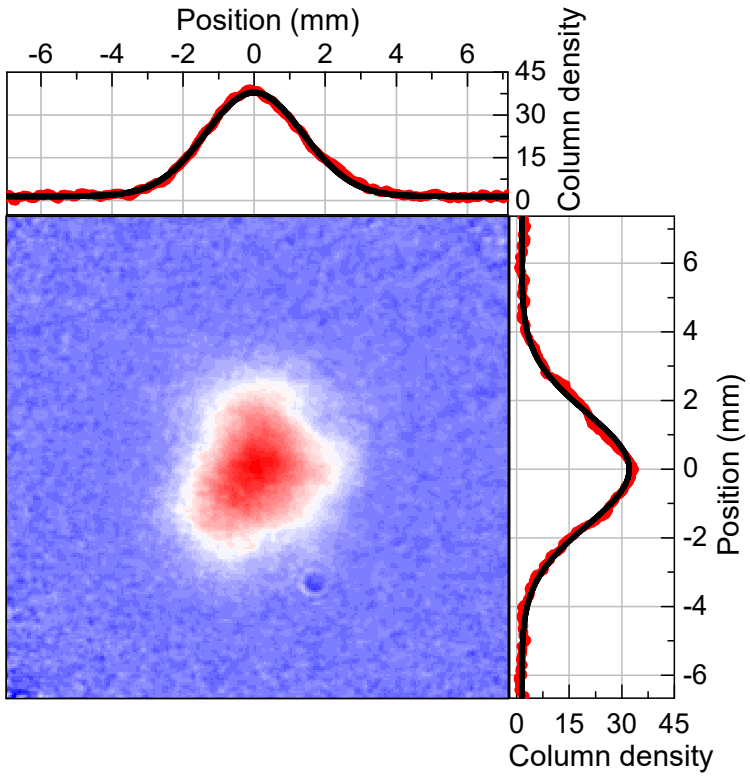

Figure 7.11: Representative O.D. profile. To calculate the 1D row density, we have summed the 2D O.D. along its row. Similarly, it is also summed along its columns to get a 1D column vector. The black solid line shows the Gaussian fit to the row density as well as column density. The area under the fitted curve is proportional to the number of atoms.

7.5 Characterization of MOT

To understand the performance of the cold atomic system, we have performed a few characterization measurements. A complete characterization of the cold atomic sample as a function of its various trapping parameters is necessary to carry out further experiments with the cold atom. We have optimized those parameters to trap the maximum number of atoms with a temperature close to the Doppler limit for the corresponding isotopes of the Rb atoms. In this section, we discuss the trapped atom numbers and temperature with cooling beam detuning using the absorption imaging technique. Repumper beam power and detuning do not play a significant role when the power is

chosen above some critical value (in our case $>$ 1 mW). For a particular cooling beam detuning, the variation of the number of trapped atoms with magnetic field gradient is discussed in the fluorescence imaging section (see Fig. 7.8). We have also varied the cooling beam power and detuning simultaneously (while the trapping magnetic field is off) to perform sub-Doppler cooling on the trapped atoms. We have discussed the optimum time required for efficient sub-Doppler cooling at the end of this section.

7.5.1 Number of trapped atoms with detuning

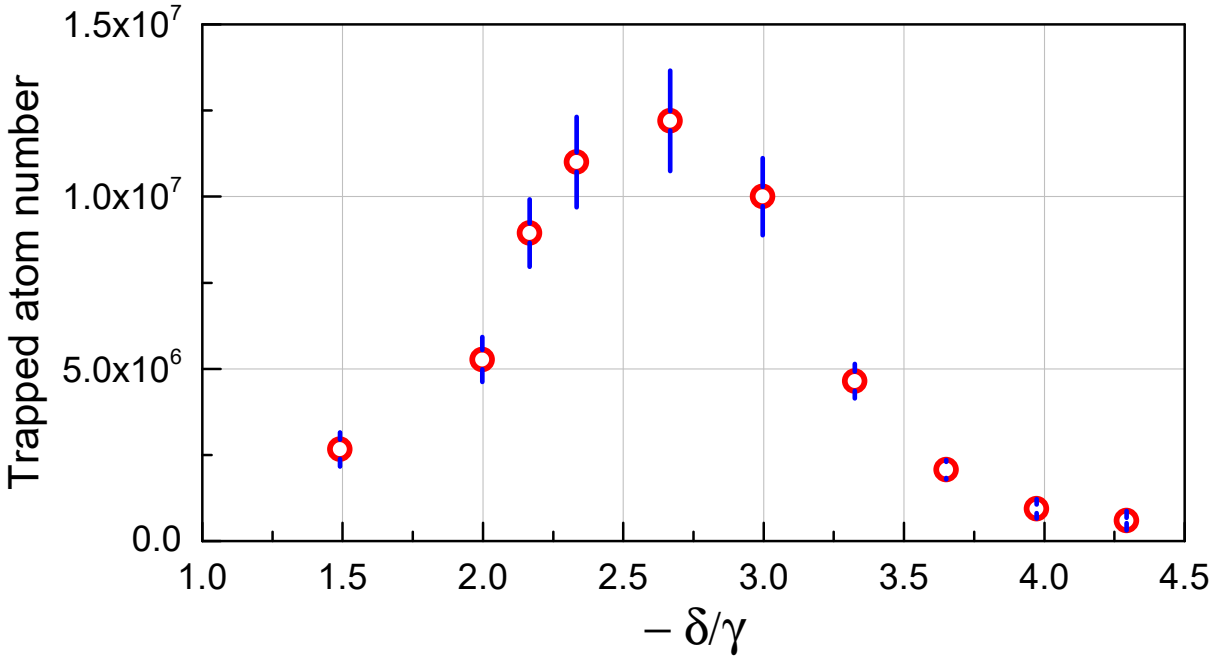

Figure 7.12: Variation of number of trapped atoms with cooling beam detuning measured using absorption imaging. The error bars represent $\pm\frac{1}{2}\sigma$ of five independent measurements.

The variation of the number of trapped atoms with cooling beam detuning (δ/γ) is shown in Fig. 7.12. The experiment is performed with an optimized (axial) magnetic field gradient of 40 G/cm that has been verified in section 7.4.1. The cooling and repumper laser beam power is fixed to 14.5 $I_{\rm sat}$ and 1.4 $I_{\rm sat}$, respectively. For each detuning of the cooling beam, first, we get the column density of the MOT absorption profile as shown in Fig. 7.11 and calculate the number of trapped atoms using the formula given in Eq. 7.31. We have repeated the measurement in each detuning five times and the average atom number with $\pm\frac{1}{2}\sigma$ error bars are presented in Fig. 7.12. This measurement is in good agreement with our fluorescence measurement results.

7.5.2 Temperature measurement

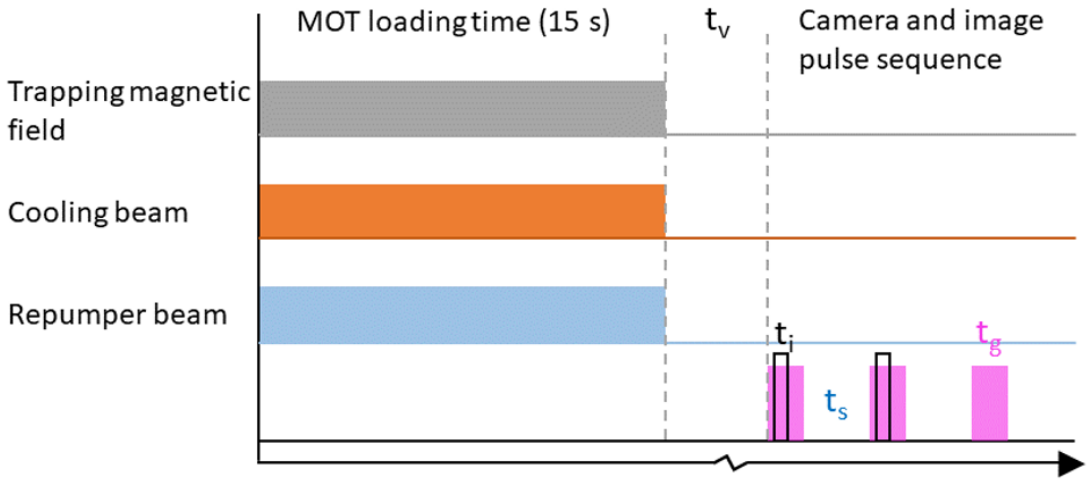

Figure 7.13: The time sequence for temperature measurement. The atoms are loaded in MOT for 15 s. The magnetic fields and laser beams are switched off to allow the MOT to ballistically expand and freely fall under gravity. t_v is the free-fall time of the atom cloud before getting hit by the first image pulse of duration $t_i = 100\,\mu$s. Three sets of images has been taken for the estimation of temperature of the MOT cloud. $t_s(= 1\,\text{s})$ and $t_g(= 1\,\text{ms})$ are the separation between two image pulses and the camera gate time, respectively. In TOF measurement, t_v is the time which is varied to probe the ballistic expansion of the cloud at various time.

The temperature of the cold atomic cloud is determined from the kinetic expansion rate after the release from MOT. One can measure this expansion rate by recording the absorption images of the ballistically expand and free-falling MOT with the different time intervals from initial time $t = 0$. $t = 0$ is the time when both the magnetic and optical fields are switched off. For MOT clouds, the ballistic expansion is governed by the thermal motion of the cold atoms. As we have discussed in Eq. 7.33, the temperature of the MOT atoms can be calculated using the slop of $\sigma^2(t)$ vs t^2 graph. The dependence of $\sigma^2(t)$ of the free-falling MOT cloud in terms of TOF is shown in Fig. 7.14. The temperature of the MOT cloud is measured to be $132 \pm 4\,\mu$K after fitting these data points with Eq. 7.33, and considering $\alpha_m = 0.4$.

Next, we vary the cooling beam detuning in a wide range (from -0.5γ to -4γ) to trap the atoms in MOT and measure the temperature at each detuning. The variation of temperature of the MOT cloud with detuning is shown in Fig. 7.15. The optimal temperature of around 150 μK of the MOT cloud is achieved below the detuning of $\delta = -2\gamma$.

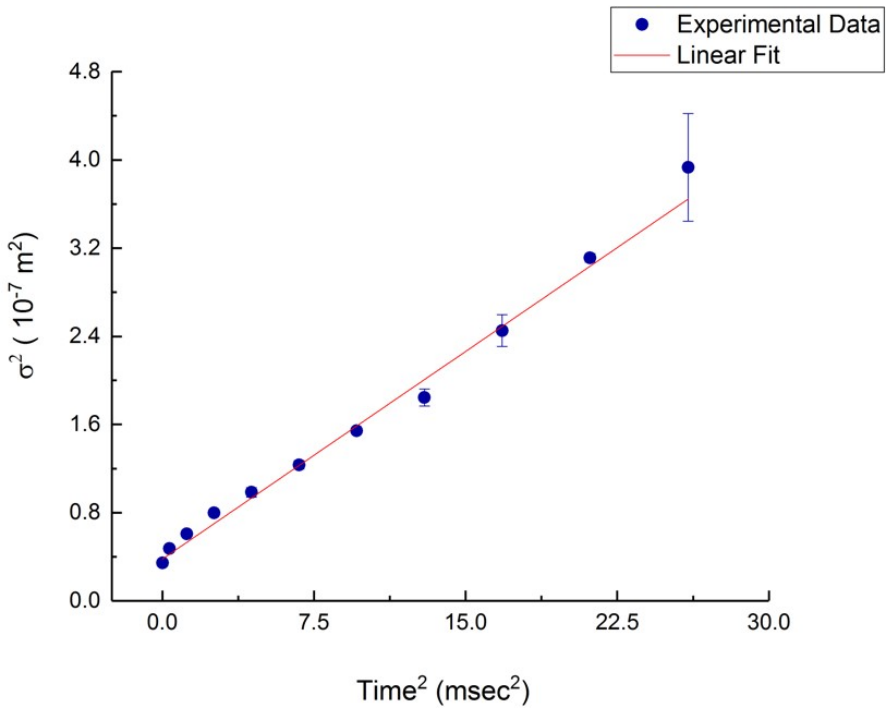

Figure 7.14: Typical ballistic expansion of cold cloud in time. The linear fit, according to Eq. 7.33 gives the temperature as 132 $\pm$ 4 μK .

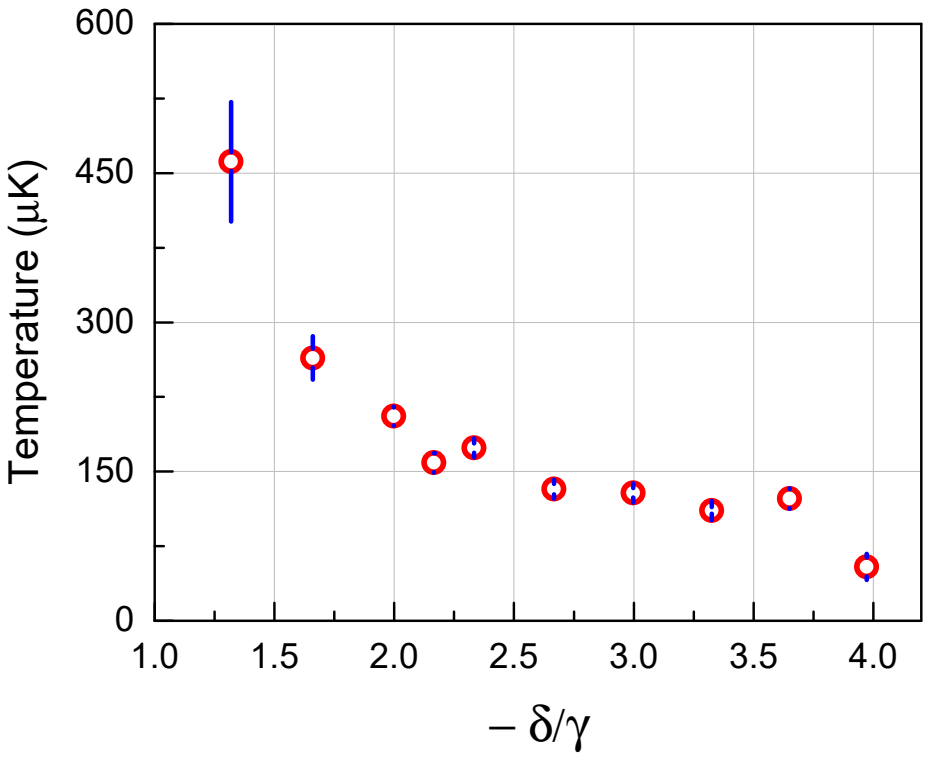

Figure 7.15: The variation of temperature of the cold atom cloud with detuning of the cooling beam.

7.5.3 Sub-Doppler cooling

The Fig. 7.14 shows the ballistic expansion of cold atomic cloud after releasing from MOT. However, if we keep the cold atoms for some finite duration in the optical molasses, the resulting temperature of the cloud is observed to be much lower than the Doppler temperature. This mechanism is called sub-Doppler cooling [287] and happens due to the multilevel structure of atomic energy level and polarization-dependent light shifts. Although the minimum attainable temperature in the sub-Doppler cooling process is the single photon recoil limit, however, before reaching this limit, the temperature of the atomic cloud depends on how much time the cloud spent in the optical molasses. The efficiency of the sub-Doppler cooling depends strictly on the cooling beam power and detuning. The reduction in the temperature of the MOT cloud depends on how much time the cloud spent in the molasses.

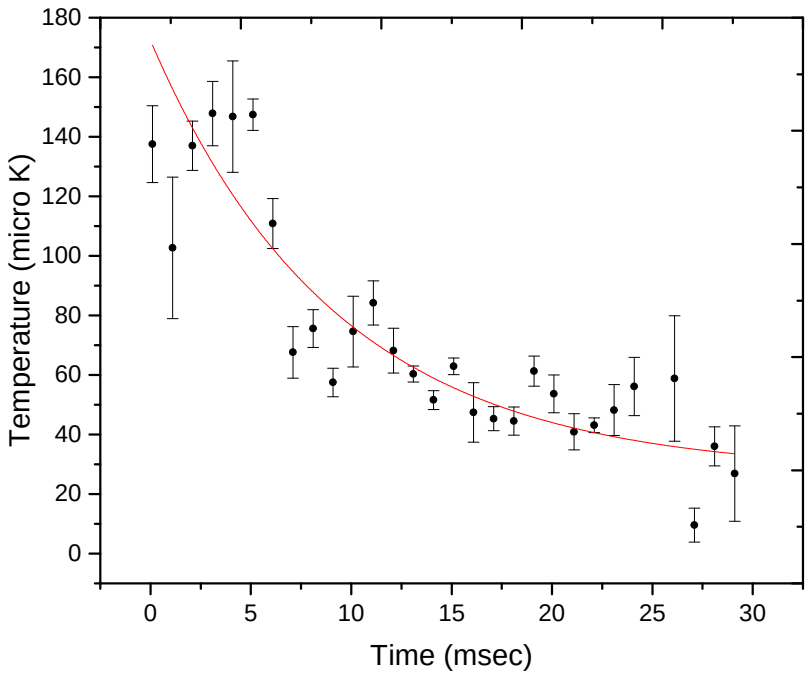

Figure 7.16: Representation of reduction of temperature with time spent in optical molasses. The solid red line is the fit to the Doppler cooling theory.

We have performed a systematic experiment to measure the temperature of the sub-Doppler cooled atoms for varied sub-Doppler times. For this, we first switched off the trapping magnetic field, and the cooling beam power is reduced to 6 mW and detuning is changed to -6γ. We keep atom cloud in variable times in the molasses and release

by switching off the cooling laser beams. Next, we perform an absorption imaging technique to measure the temperature of the cloud in each step of the sub-Doppler cooled atoms. We have shown the lowering down the temperature of the sub-Doppler cooled atoms as a function of sub-Doppler time in Fig. 7.16. This shows that the 30 ms is the minimum time required to reach the steady-state sub-Doppler cooling temperature of 20 μK.

7.6 Bulk properties of cold atoms: response to external dc stimulus

The optical molasses damping the motion of atoms is an excellent situation to study the diffusion of the cold cloud in the molasses beam [288, 289]. The diffusion can also be investigated by studying the response of the cold atoms to an external stimulus. We have theoretically developed and experimentally investigated the position response function (PRF) of cold atoms in a MOT by applying a transient homogeneous magnetic field as a perturbing force that is presented in our recent article [18]. We observe a transition from a damped oscillatory motion to an over-damped relaxation, stemming from a competition between the viscous drag provided by the optical molasses and the restoring force of the MOT. We also present the diffusion of the atomic cloud in the optical molasses by studying the PRF. This study shows the collective transport properties of the cold atoms as a bulk when exposed to an external perturbation. However, the direct measurement of the dynamics of the internal degrees of freedom (DOF) of the system, such as spin, that also contributes in the detected PRF, are discussed in the next chapter.

The work presented in [18], start with a simple Langevin equation to describe the cold atomic cloud in MOT and in presence of an externally applied force, $f(t)$. We have incorporated the dissipation kernel $\alpha(t)$ related to the random microscopic fluctuations $\zeta(t)$ via the FDT. In this analysis, we choose the OM in the cold-atom experiments as Ohomic bath since the force is proportional to the velocity with a fixed coefficient of proportionality or friction coefficient. We have derived the PRF of the cold atoms in response to the external force $f(t)$ by solving the Langevin equation. We show that the PRF have a shape of oscillatory or damped motion in time depending on the value of α of the molasses beams and the spring constant (k) of the trapping magnetic fields. Experimentally, we have measured the PRF by measuring the mean position of the cold cloud as a function of time after applying and switching off an external homogeneous magnetic field. The velocity response function is also measured, and various MOT

parameters are extracted precisely by measuring the PRF. The details of the paper [18] is not discussed in this thesis. It will be discussed in the subsequent thesis from the same group.

Chapter 8

SNS in cold atoms

This chapter is based on the publication [17]. Here, we demonstrate, for the first time, the measurement of spin coherence in cold atoms using Faraday rotation fluctuation technique.

Magneto-optical trap (MOT) is an experimental technique that reduces the atomic velocity distribution by almost three orders of magnitude and works as a pre-cooling stage to achieve ultra-cold atoms in the quantum regime. Therefore, the MOT is an essential step to get quantum (atomic) gases and a fully spin-based characterization of the MOT atoms is also of fundamental interest. It is a very interesting stage of cooling where the thermal effect reduces significantly and the quantum effect starts to appear. Note that the MOT is a dynamical system where repetitive cycles of capture and escape of thermal atoms continue within the volume of the trapping region. Since the atoms trapped in an MOT behaves classically, the system can be considered as a paramagnetic spin ensemble where the long time average of the magnetization along an axis is zero. Studying spin fluctuations and hence the spin coherence of an ensemble of cold atoms trapped in an MOT provides insightful information about the dynamical nature of the cold spin system. Such information will help to control and preserve the atomic spin states for further applications and implications.

In this chapter, we will present the detection of intrinsic spin-coherence from an ensemble of cold atoms trapped in a MOT using Faraday rotation fluctuations measurements. However, the MOT is a source of extremely dilute atomic gases at 100's of μK temperatures where the atom density is more than three orders of magnitude lower in comparison to the thermal atomic vapors at 373K temperature. Additionally, for a traditional vapor-loaded MOT, the typical diameter of the capture volume to trap the atoms is also limited by a few mm. Since the strength of the power spectrum for intrinsic SN signal depends linearly on the atom density ($\Sigma \propto n_0$) and the length of the atomic sample ($\Sigma \propto l$), the measured intrinsic SN signal is expected to be four orders

of magnitude lower in strength than the atomic vapors. Additionally, the cold atoms are more prone to get scattered by the weak and off-resonant probe beam and the intrinsic spin fluctuations of the ensemble can optically be perturbed. To avoid such optical excitation of the atoms by the probe beam, a relatively weak and far-detuned probe laser beam is used to detect the SN signal from cold atoms. Therefore the probe beam intensity and detuning dependent term in the detected SN signal ($\Sigma \propto I_p^2/\delta_P^2$) is also orders of magnitude lower for the cold atoms in comparison to the thermal atoms for a similar beam diameter (i.e. A) of the probe laser. In combination with all these contributions, we can expect at least four to five orders of magnitude weaker signals from cold atoms than thermal vapors with reasonable parameters of the probe beam and spin systems.

Furthermore, the atoms inside the MOT are a non-equilibrium system because of the presence of in-homogeneous magnetic fields and the quasi-resonant trapping laser beams. Therefore, in principle, to probe the intrinsic SN signal from the cold atoms in equilibrium requires releasing the MOT from the trapping volume, and detecting the signal only while the atoms are falling freely under gravity and free from trapping laser beams and in-homogeneous magnetic fields. The probe laser beam can be kept below the MOT cloud. During the time of data acquisition from the free-falling cold atomic cloud, the in-homogeneous magnetic field can be switched off, and simultaneously the homogeneous magnetic field can be applied perpendicular to the probe laser. However, in this technique, the cold atoms take a few ms to pass through the probe laser, which is insufficient to collect the long-time behavior of the spin dynamics of the system. All of these above disadvantages make it difficult to detect the intrinsic spin coherence signal from the cold atoms with the existing detection set-up.

Therefore, the intrinsic spin noise signals have not been detected so far in cold as well as ultra-cold atoms and quantum gases, where direct measurement of spin fluctuations is predicted to be extremely useful in understanding quantum phases [13, 14, 16, 163] and precision magnetometry [6, 7, 290]. Moreover, the cold atomic systems are ideal testbeds for demonstrating quantum effects due to their ultra-low temperatures [291].

Since the cold atoms spend a very short duration inside the probe beam in the free-falling measurements, as a proof-of-principle detection of intrinsic spin coherence from such a system, we have performed the in situ measurement by sending the probe beam through the captured atoms inside MOT. In this method, the measurement duration can be much longer than the system's characteristic relaxation times which gather sufficient data for the long-term behavior of the spin dynamics. Additionally, the strength of the intrinsic SN signal from in situ cold atomic cloud is extremely feeble to detect within SNS technique with good SNR as discussed earlier. Therefore, we have

coherently driven the in situ cold atoms with a pair of coherent Raman lasers to detect the driven PSD and extract the information about the intrinsic spin coherence of the same system as discussed in chapter 5. We have demonstrated an enhancement of the signal strength as much as million folds in thermal atoms using coherent Raman drive, which allows us to detect the spin coherences in cold atoms trapped in a MOT.

8.1 Detection of spin coherence in cold atoms

In this section, we first discuss the implementation of the coherent Raman drive technique to an in situ magneto-optically trapped cold ^{85}Rb atomic ensemble to extract the intrinsic spin relaxation rate γ'. We mostly focus on the detection of the driven PSD from the coherently driven cold atomic systems. To keep focus on the measurements, the details about the experimental set-up and data analysis procedures are provided in section 8.2 and section 8.3, respectively. Note that, we choose ^{85}Rb cold atoms for the detection of spin-coherence signal for the following reasons (a) We loaded the atoms in MOT from natural abundant background Rb vapor. The abundance ratio for the two isotopes of the Rb atoms are ^{85}Rb: ^{87}Rb 3:1. Therefore, the vapor pressure for ^{85}Rb atoms are three times higher than ^{87}Rb atoms in the vacuum chamber, that leads to higher atom density in the MOT for ^{85}Rb atoms, and (b) we have experimentally observed that the size (Gaussian FWHM) of the ^{85}Rb MOT is around 1.5 times higher than the ^{87}Rb MOT. The bigger MOT width is advantageous for the in-situ measurement of SNS experiment, since the tunability range of the probe scan is higher and the spatial resolution is more accurate.

In the recent past, the measurements of Faraday rotation as well as atomic number fluctuations have been demonstrated in cold atomic systems [10, 292–295]. However, we apply the Faraday rotation fluctuations technique to study, for the first time, spin coherence produced by a coherent Raman excitation in the cold atomic system. Our experimental system typically traps more than 10^7 atoms at a temperature of 150$\pm$10 μK in a standard vapor-loaded MOT with a typical Gaussian width of $\sim$ 4 mm. We take sufficient care to ensure that the center of the atomic cloud is overlapped with the zero of the quadrupole trapping field within 30 μm (see Fig. 8.1(a-inset)). Additionally, we align a pair of Raman fields with waist diameter of 6 mm, blue detuned by 2γ ($\gamma = 2\pi\times$6.1 MHz) from $5S_{1/2}, F = 3 \rightarrow 5P_{3/2}, F' = 4$ (D_2) transition. A collimated probe laser field along $\hat{x}$ with a waist diameter of 70 μm and blue detuned by 20γ from the same transition is sent through the cold atomic cloud (see Fig. 8.1(a) and Fig. 8.1(b)). We kept Raman beams detuned by $+2\gamma$ to ensure the minimal optical scattering imparted on the trapped atoms while maintaining significant coherent cou-

pling between the Zeeman states. The value of $+2\gamma$ is chosen after performing the following experiment. We vary the detuning of the Raman beams from 0 to higher values on the blue side. We noted down the atoms loss in the MOT in each detuning of the Raman beams. The atoms loss is saturated at $+2\gamma$ detuning. On the other hand, we have also performed the strength of the driven SN signal in each of the Raman beam detuning. We have observed that at $+2\gamma$ detuning the SN signal strength is significantly large, while the atoms loss is significantly less. The probe beam detuning is chosen to $+20\gamma$ to reduce the optical scattering. For the probe beam detuning of $+20\gamma$, the optical scattering reduces to 1600 times in comparison to the on-resonance probe beam. The probe field position with respect to the cloud center is independently measured using high precision absorption spectroscopy and absorption imaging within a precision of 10 μm. The quadrupole magnetic field profile creating the MOT is separately characterized using a Hall magnetometer probe, and it is shown schematically in Fig. 8.2(b).

To measure $P(\omega)$ at a finite Larmor frequency in the presence of the Raman fields, we have shifted the probe laser by 900 μm from the trap center in the $z-$direction on the $x-z$ plane. Also, due to the Raman fields, the cloud center shifts in the x-direction depending on the Raman fields intensity and the detuning (see Fig. 8.2(b)). In Fig. 8.2(a), we show a representative spectrum detected in this condition at $\delta_{12} = 2.73$ MHz for $\Omega/\gamma = 0.35$. In the absence of the Raman fields - unlike in the vapor case - we do not observe any detectable intrinsic SN signal as we have discussed earlier.

We record a series of $P(\omega)$ by varying δ_{12}. For a fixed value of Ω/γ and probe field position, we obtain composite spectra (see Fig. 8.2(c)) by repeating the above procedure and recording the peak height of each individual $P(\omega)$. The acquisition time for each data point (at δ_{12}) is 8 seconds for a signal run of the experiment. We analyze our experimental results using the earlier modeling for thermal vapors after including corrections due to magnetic field variations, atom density distributions, and multilevel contributions (see section 8.3 for details). The asymmetric nature of the spectrum in Fig. 8.2(c) arises mostly due to the magnetic field variations within the trapped MOT cloud and the Gaussian atom density distributions of the cloud. However, for the probe beam position $|z| < 1$ mm on the $x-z$ plane as in the case shown in Fig. 8.2(c), the magnetic field orientation ($\theta_B(x)$) with respect to the z-axis is the most dominating factor for the asymmetric nature of the envelope spectrum over the Gaussian atom density distribution of the MOT. The multilevel corrections have a negligibly small contribution in this asymmetric nature. We fit the data in Fig. 8.2(c) (solid red line) with a free parameter γ'. We get an estimate for the value of $2\gamma'$ from this fitting as $2\gamma' = 2\pi\times(1.0\pm0.7)$ kHz.

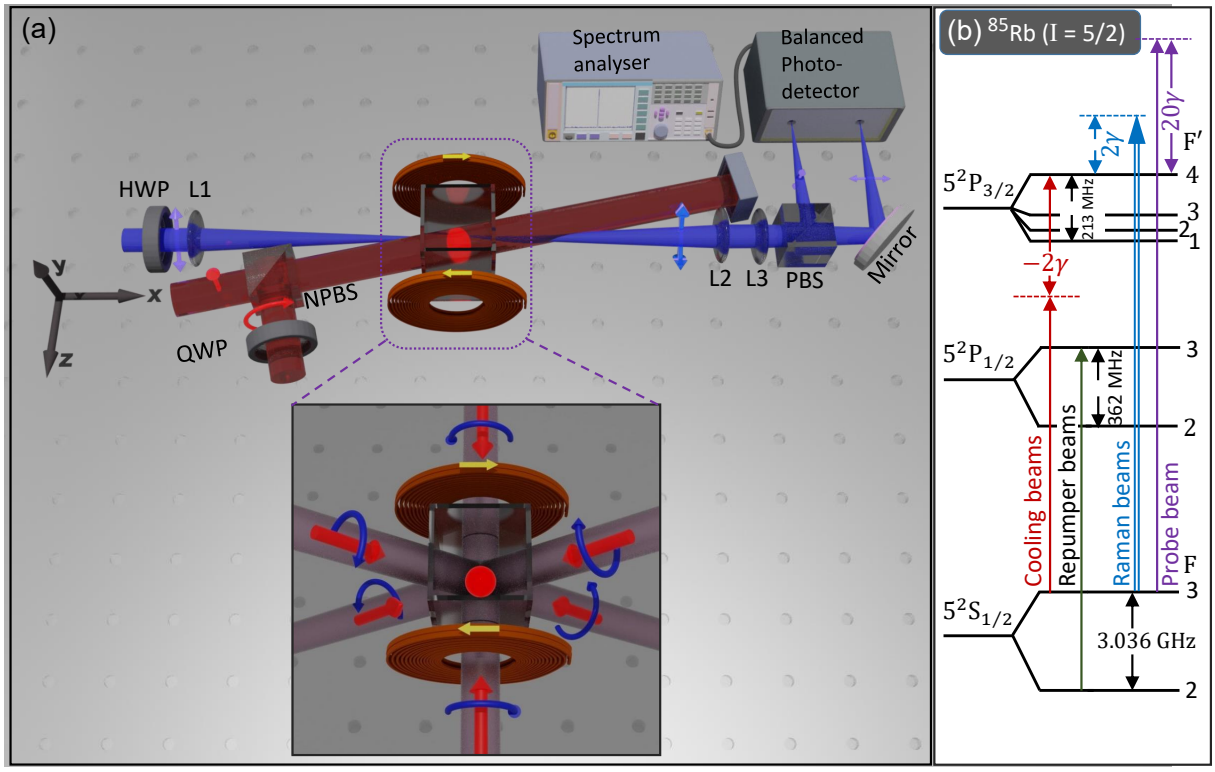

Figure 8.1: The schematic of the experimental set-up and the relevant energy levels for the spin noise (SN) detection of an in situ magneto-optically trapped (MOT) cold ^{85}Rb atomic ensemble. (a) depicts the arrangements of the Raman beams (red), probe beam (blue), magnetic coils, and detection set-up. (a-inset) in-situ magneto-optically trapped (MOT) ^{85}Rb atoms inside an ultra-high vacuum glass cell in presence of inhomogeneous trapping magnetic fields. The faint beams in (a-inset) are the cooling and repumper laser radiation fields used to capture the ^{85}Rb atoms in a MOT. Here the red arrows and blue circular arrows represent the direction of the laser beams and their polarizations. The red blob at the center of the glass cell represent the cold ^{85}Rb atomic cloud. HWP: half-wave plate, QWP: quarter-wave plate, L1, L2, L3: lenses, NPBS: non-polarizing beam splitter, PBS: polarizing beam splitter. (b) represents the electronic (dipole) transition lines for ^{85}Rb atom [23] and the frequencies of the cooling and repumper, Raman and the probe beams. I is the nuclear spin, $F(F')$ represents the ground (excited) hyperfine levels, and γ is the linewidth of the $F'-$levels of the respective atoms.

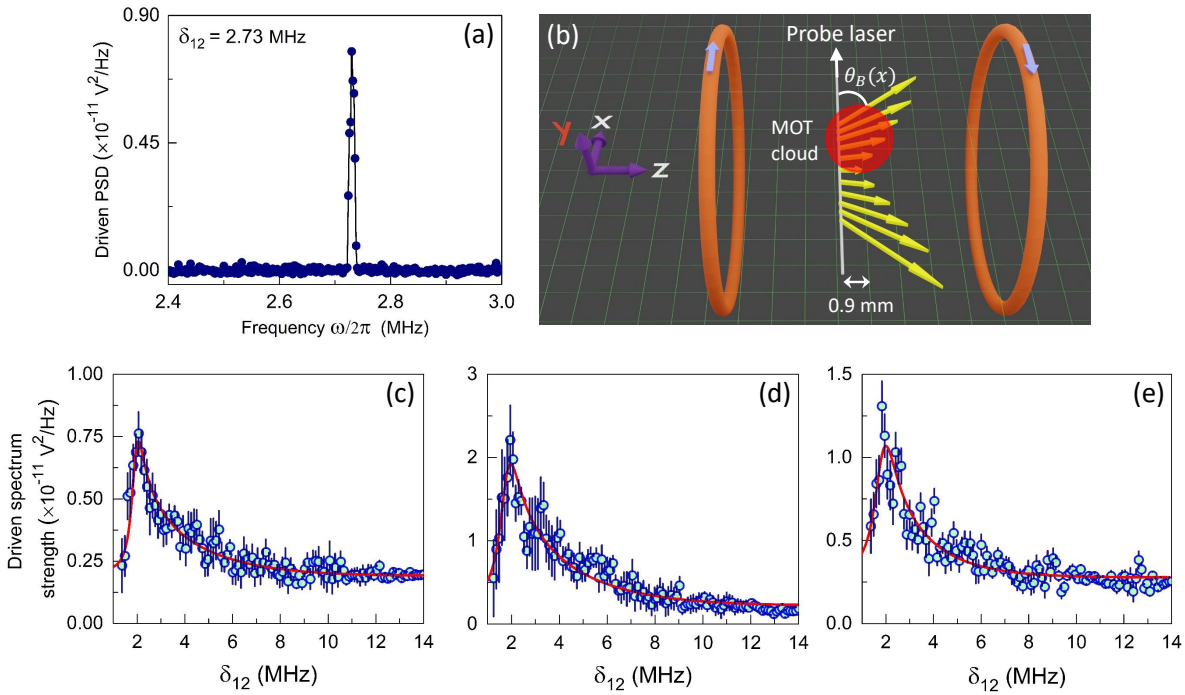

Figure 8.2: Measurement of spin coherence in Raman driven cold ^{85}Rb atoms at 150 μK. (a) $P(\omega)$ recorded at $\delta_{12} = 2.73$ MHz. (b) A schematic representation of our experiment including local magnetic field profiles (yellow arrows), the position of the cold atomic cloud (red blob), and the probe laser. (c-e) The recorded envelope spectra (blue open circles) for the various sets (check the text for details) of experimental parameters.

We have repeated the above measurements for various z-positions of the probe laser. Another representative data is shown in Fig. 8.2(d) for $z = 700$ μm, which gives $2\gamma' = 2\pi\times(2.3 \pm 0.7)$ kHz. We have also performed the experiment in the presence of balanced Raman fields, which minimize the shift of the cloud center as shown in Fig. 8.2(e). The extracted value of $2\gamma'$ is $2\pi\times(1.3 \pm 0.7)$ kHz. Our present experiment is limited by several factors, e.g., magnetic field in-homogeneity, off-resonant scattering, the effect of strong driving fields, and relative frequency stability of the Raman fields, which can significantly change the measured spin coherence rate. At this low temperature (150 μK), the above perturbation effects are typically far more important than the suppression of spin projection noise mentioned in chapter 5 where we have consistently obtained a lower value of the extracted spin coherence rate than the intrinsic SN measurements. Nevertheless, the observed reduction in extracted spin relaxation rate by two orders of magnitude as compared to the thermal atoms, which can be attributed to the six-order lowering of the temperature that substantially reduces thermal coupling, collisions, and transit times.

This experiment can further be extended to study spin coherences in cold atomic

ensembles confined in a far-off-resonant optical dipole trap. This would avoid the presence of an in-homogeneous magnetic field. Additionally, a free-falling cold atomic cloud provides a clean system unconfined by the trapping magnetic and quasi-resonant optical fields. The measurement of the transverse spin coherences in such a system can be performed by applying a homogeneous magnetic field along a preferred direction. However, the data acquisition time for such a measurement is limited by a few milliseconds and requires a high temporal resolution detection set-up to probe the signal as discussed earlier. In the future, such a measurement can be performed using, for example, our recently developed time-resolved digital receiver system (DRS) [20].

The detection method developed and described in this chapter can have significant applications in precision magnetometry, high-resolution imaging, non-perturbative probing of quantum phase transitions in cold atoms, and other similar systems such as cold ions and cold molecules.

8.1.1 Polarization dependence

We have also studied the strength of the driven power on the polarization state of the Raman beams in the cold rubidium atoms as shown in Fig. 8.3. We have fixed $\delta_{12} = 2.73$ MHz to resonantly drive the atoms located at $x = 1.9$ mm, $y = 0$, and $z = 900$ μm where $\theta_B \approx 45°$. The dependence of $P(\omega)$ on the Raman fields' polarization for cold atoms is similar to the previous case with thermal vapors (shown in Fig. 5.11). While the peak signal strength of $P(\omega)$ reduces exactly to zero at 90° and 180° as expected, the magnitude at $\theta = 135°$ reaches only half of the observed values at $\theta = 45°$ and 225° in cold atoms inside the MOT, which is very different from the thermal vapors in a homogeneous magnetic field.

8.2 Details of the experimental set-up

In chapter 5, we have reported the results in a thermal atomic vapor to develop and characterize the measurement of Faraday rotation fluctuations signal from a coherently driven system. In this chapter, we have provided one of the main studies of this thesis to extract the intrinsic spin coherence rate from a cloud of in situ cold ^{85}Rb atoms. In this section, we provide the details of the cold atomic setup that has been used for the measurement. We have discussed extensively the making and probing of cold atoms in an MOT in chapter 7, however here we provide the parameters used for the measurements.

We magneto-optically trap neutral ^{85}Rb atoms inside a glass cell maintaining back-

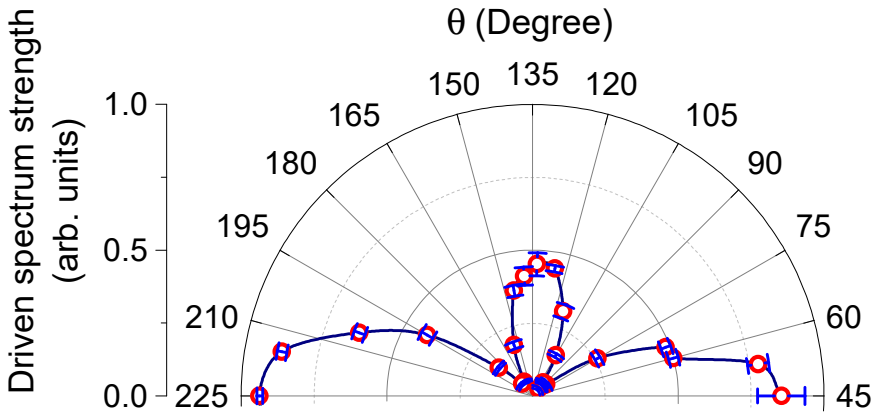

Figure 8.3: The driven power spectrum strength at $\delta_{12} = 2.73$ MHz for various angle θ in cold atoms. The signal strength at $\theta = 135°$ is about 1/2 of that at $\theta = 45°$ and 225°. The polarization sensitivity at each δ_{12} carries its unique signature for atoms in the MOT, unlike atoms in a homogeneous magnetic field. The solid line joining the data points are a guide to the eye.

ground pressure less than 10^{-10} millibar using standard laser cooling and trapping techniques (see Fig. 1(a-inset)). The cooling beams were generated from an external cavity diode laser (ECDL) and frequency stabilized to the 12 MHz red detuned (-2γ) with respect to $5S_{1/2}, F = 3 \rightarrow 5P_{3/2}, F' = 4$ (D_2) transition. The "repumping" laser beams were derived from another ECDL and frequency stabilized to the $5S_{1/2}, F = 2 \rightarrow 5P_{1/2}, F' = 3$ (D_1) transition (see Fig. 8.1 (b)). A pair of magnetic coils in near ideal anti-Helmholtz configuration produces the required spatial magnetic field gradient. We coincided the optical and magnetic field centers with the center of the vacuum chamber with an accuracy of ~ 30 μm. We use three independent detection techniques: absorption imaging, fluorescence imaging, and probe absorption for characterizing the cold atoms as discussed in chapter 7 and alignment of the optical fields for the experiments.

In Fig. 7.11, we show a typical absorption image of our cold cloud, which gives a good measurement of the total number and the spatial distribution of the atoms. Using a separate time-of-flight measurement, we obtain the temperature of the atomic cloud to be ~ 150 μK. We typically trap more than 10^7 atoms with a Gaussian FWHM of ~ 4 mm.

The strength and orientation of the magnetic field B vary within the atomic cloud along the probe field direction (x-axis) as shown in Fig. 8.4 and Fig. 8.2(b). In this configuration, the magnetic field exists only on the $x - z$ plane, and we calculate the magnetic field at each position using a solution of the elliptic equations [296]. See Appendix C for more details. We separately measure the field components (B_x, B_y, B_z) using a Hall probe magnetometer (LakeShore) for comparison and calibration purposes.

The angle $\theta_B(x)$ between the local magnetic field and probe laser propagation direction is position-dependent as shown in Fig. 8.4(right).

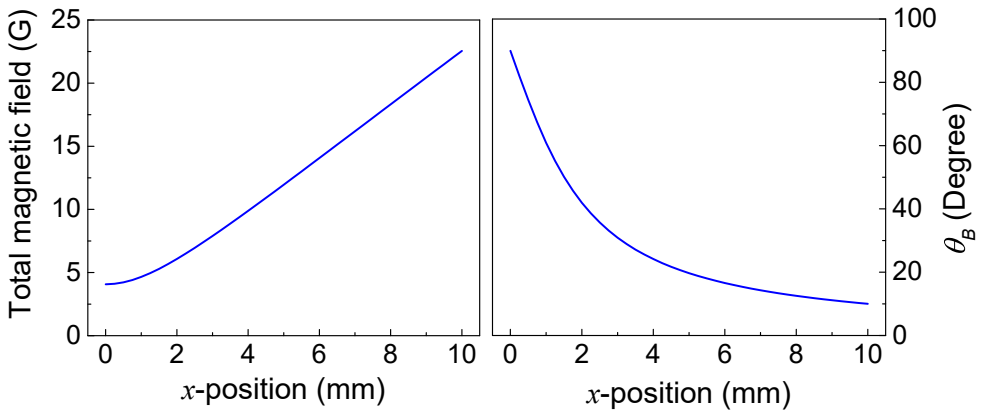

Figure 8.4: The x-dependence of the total magnetic field and the angle $\theta_B(x)$ between the local magnetic field and the probe laser propagation at $y = 0$ and $z = 900$ μm.

The Raman radiation fields for coherent driving were derived from the same ECDL, which provides the cooling laser light. Two independent acousto-optic modulators (AOMs) were applied to produce the Raman fields with controllable frequency difference (i.e. δ_{12}). The radio frequency signal sent into the AOMs can be tuned using two voltage-controlled crystal oscillators. The control voltage was sent using an FPGA board with a vertical resolution of 12 bits. A brief discussion on FPGA is provided in Appendix D. The long-term relative frequency 'jitter' of δ_{12} was measured to be $\sim$ 7 kHz (for measurement duration of 8 seconds). This 'jitter' limits our measurement precision, which can be reduced to a few Hz level using ultra-stable reference sources in the future upgrading of the experimental set-up. However, this relative frequency stability is adequate for the first sets of measurements of the Faraday rotation fluctuations signal from the cold atoms. The Raman fields were spatially mode cleaned using PM fibers, expanded to a Gaussian waist diameter of 6 mm, and combined in an NPBS before sending through the cold atomic cloud. The polarization of the Raman fields can be independently varied, employing the combination of half-wave plates (HWPs) and quarter-wave plates (QWPs). We typically manage to obtain a polarization purity of the Raman fields $> 99\%$. The Raman lasers are optically detuned by 2γ in blue side from $5S_{1/2}, F = 3 \rightarrow 5P_{3/2}, F' = 4$ (D_2) transition (see Fig. 8.1(b)) to minimize the radiation pressures on the trapped atomic cloud. However, we have separately measured the little shift of the cold cloud in presence of the off-resonant Raman beams using fluorescence imaging by keeping the camera on the $y - z$ plane. We have also taken sufficient care to align the center of the MOT cloud with the center of the Raman

beams.

Next, we align the probe beam through the MOT in a specific z position on the $x-z$ plane in presence of the Raman beams. The probe laser field is generated from another ECDL, and its frequency is monitored using a high precision wavelength meter (Highfinesse, WSU2) with an absolute frequency accuracy of 1 MHz. First, we clean the spatial mode of the probe laser using a PM fiber and then expand the beam diameter to 12.5 mm using two pairs of telescope. Next, we send the expanded probe beam through a plano-convex lens with a focal length of 40 cm before sending it into the MOT cloud in presence of Raman beams. The lens is placed on a three-stage transnational (x, y and z) mount and positioned exactly 40 cm away from the center of the MOT cloud. The Gaussian waist diameter of the probe beam is 70 μm at the focal point with a Rayleigh length of 12 mm. Since the diameter of the MOT cloud is much smaller than the Rayleigh length of the focused probe beam, we have considered that the probe beam diameter is constant within the cloud. We have sent the probe beam through the atomic cloud along $\hat{x}$ at $y = 0$, and the z position of the probe beam was varied for different sets of measurements. The exact position of the probe beam with respect to the MOT center is determined by performing a high-precision probe transmission spectroscopy experiment. After the MOT cloud, the probe beam is captured on another plano-convex lens and sent through the polarimetric set-up and fed to the balanced photo-detector.

8.3 Details of the data analysis procedure

In this section, we discuss the data analysis procedure to fit the cold atom driven spectrum using our developed theory and extract the value of γ'. For a homogeneous magnetic field as in the thermal vapor measurements, the Faraday rotation fluctuations signal (both the intrinsic and the Raman driven) is centered around a single Larmor frequency ν_L determined by the magnetic field strength B. However, for the cold atoms inside an MOT, the Larmor frequency $\nu_L(x)$ varies over space along $\hat{x}$. Therefore, the Zeeman splittings of the ground hyperfine levels are determined by the magnitude of the local magnetic field, and the Raman resonance condition is also position-dependent, i.e., $\delta_{12}(x) = \nu_L(x)$. In our numerical modeling, we take this position-dependent local magnetic field into account to calculate the strength of the Faraday rotation fluctuations signal at different spectral frequencies.

Moreover, the orientation ($\theta_B(x)$) of the local magnetic field also varies along $\hat{x}$ inside the MOT. The SN signal strength at $\nu_L(x)$ also gets modified by a factor of $\sin^2\theta_B(x)$ [3]. We have experimentally verified this correction factor by performing a

separate calibration measurement of the intrinsic SN spectrum in thermal atoms (see Fig. 3.14).

The atom density distribution within the MOT cloud addressed by the probe laser is not uniform, which is evident from the absorption image in Fig. 7.11. We incorporate this density distribution in the modelling of the SN signal strength ($\propto n(x)$, where $n(x)$ is the number density of atoms at position x) from the MOT [4, 21]. Note that $n(x)$ can be measured precisely using absorption imaging.

Another minor correction to the SN signal strength can be from the definition of the quantization axis, which also varies along x-direction on the $x-z$ plane. Since the local magnetic field alters over space, the coupling of the Raman fields with the atoms in the MOT also depends on x-position. Such correction can be incorporated in our modelling by an x-dependent Rabi frequency defined as $\Omega(x) = \Omega(1 - \sin^2\theta_B(x)/2)$.

So far, we have discussed the Raman-driven spin coherence between the ground states involving a single Λ system formed by states $|i\rangle$, where i = 1,2, and 3. Ideally, in cold atom experiments, six Λ systems are involved in giving rise to the driven power spectrum generated from $F = 3$ and $F' = 4$ hyperfine levels of ^{85}Rb atoms. However, the value of Landé g-factor is different for those two hyperfine levels, resulting in dissimilar contributions in building the signal strength from individual Λ system through the optical detuning of the Raman fields.

Incorporating the above factors and corrections, we get the strength $|\rho_{21}(x)|^2$ of the Faraday rotation fluctuations signal from the atoms at position x inside the MOT,

$$|\rho_{21}(x)|^2 = |\rho_{21}(\Omega(x))|^2 n(x) \sin^2\theta_B(x). \tag{8.1}$$

For a fixed position x within the MOT, we consider the contributions of all six Λ systems and add them up to get the total driven spectrum strength. The six Λ systems contribute differently via the optical detuning $\Delta_{23}(n)$ of the Raman fields from the excited state, i.e.,

$$\Delta_{23}(n) = 2\gamma + (3-n)(g_{F'} - g_F)\mu_B B(x)/h, \tag{8.2}$$

where n runs from 1 to 6 and $g_{F'}$ is the Landé g-factor of the excited level. We fix the detuning $\Delta_{23}(n) = 2\gamma$ for $n = 3$ in our experiment as shown in Fig. 8.5.

In Fig. 8.2 (c,d,e), we present some plots for the Faraday rotation fluctuations signals as a function of δ_{12} from a driven cold rubidium cloud. We have fitted the experimental data using the Eq. 8.1 along with $\rho_{21}(\Omega(x))$ from Eq. 8.3, where Ω is replaced by $\Omega(x)$ and we employ Δ_{23} from Eq. 8.2. The only free parameter in this fitting is the relaxation rate γ' of the hyperfine ground level Zeeman states, and all

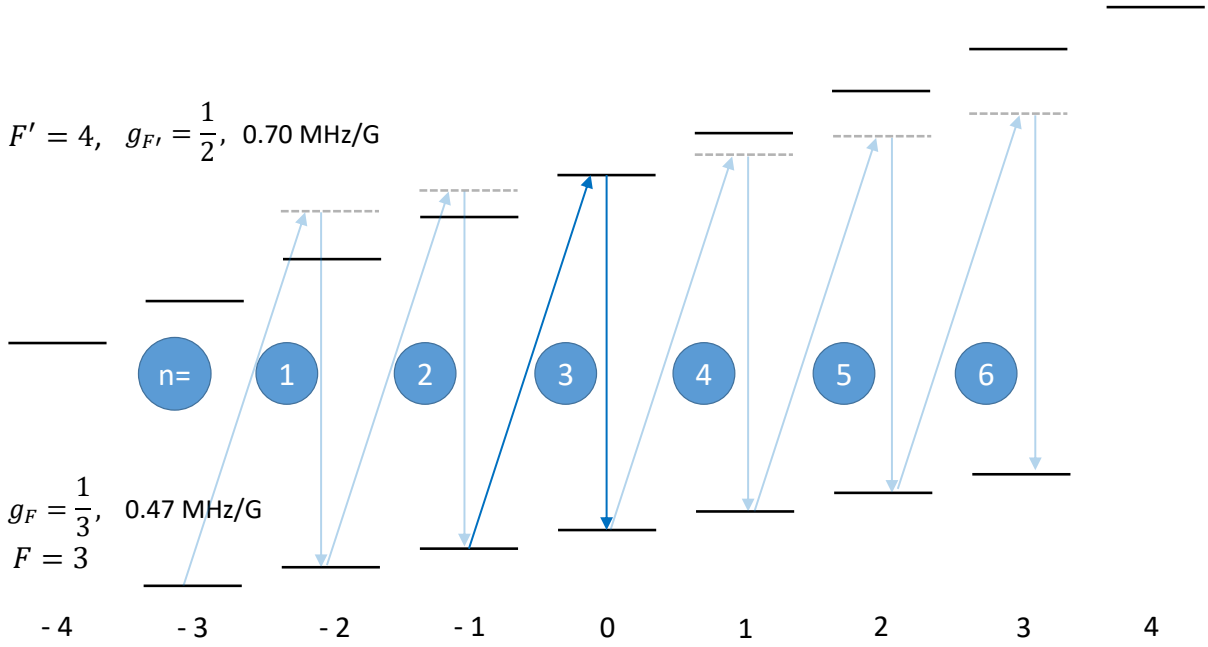

Figure 8.5: The six Λ systems formed in the ^{85}Rb cold atomic system. For simplicity the optical detuning of the Raman beams from relevant transition is shown here as zero. The extra term added to the detuning mentioned in Eq. 8.2 can be understood with this picture.

other parameters are measured in our experiment.

Here we provide the formula for $\rho_{21}(\Omega(x))$ mentioned in Eq. 8.1. In the atomic vapor case, we provide a relatively simple formula for ρ_{21} by choosing $\Omega_{13} = \Omega_{23} = \Omega$ and $\Delta_{23} = 0, \Delta_{13} = \Delta$, and that formula is employed for the driven thermal vapors. Here, we give a more general formula when $\Delta_{23} \neq 0$, which is our experimental condition for the driven rubidium cold atoms.

$$\rho_{21} = \frac{\gamma\Omega^2(\tilde{\Delta}(2i\gamma + \tilde{\Delta}) - 4\Omega^2 + (-2\gamma + i\tilde{\Delta})\gamma')}{\gamma(\tilde{\Delta}^2(2\gamma^2 + \Delta_{23}^2 + \Delta_{13}^2) + 2\Omega^2\tilde{\Delta}^2 + 8\Omega^4) + \Omega^2(8\gamma^2 + (\Delta_{23} + \Delta_{13})^2 + 12\Omega^2)\gamma' + \\ + \gamma\gamma'^2(2\gamma^2 + \Delta_{23}^2 + \Delta_{13}^2 + 6\Omega^2)} \tag{8.3}$$

where $\tilde{\Delta} = \Delta_{23} - \Delta_{13}$.

Chapter 9

Conclusions and outlook

We have measured the intrinsic spin coherence of cold atoms using Faraday rotation fluctuation measurement for the first time. This experiment opens up new possibilities to probe intrinsic spin dynamics and their interactions with various potentials in similar cold and ultra-cold atomic, molecular and ionic systems. Traditional non-invasive spin noise spectroscopy (SNS) technique have been used, along with Raman driving to the atoms, to probe the spin-correlation of the cold atomic system. We have also developed a theory of Raman driven SNS based on optical Bloch equations (OBEs). First we characterize this technique with thermal atoms, and later implement to cold atoms to extract the intrinsic spin coherence rate. We have shown a consistent measurement of spin coherence rate of thermal atoms using intrinsic and Raman driven SNS technique. A coherence transfer from one atomic species to another via spin-exchange collision has also been observed when the one of the atomic species is subjected to Raman coupling. We have developed and characterized the SNS technique with thermal rubidium atoms and extract atomic, magnetic, nuclear and chemical properties of atomic systems. We make use of the SNS technique to precisely measure the real-time external magnetic field strength with our developed digital receiver system (DRS). We have also implemented the optical pumping (OP) method to precisely control the spin population between the ground hyperfine levels of rubidium atoms and detect them non-invasively using SNS technique.

This novel detection technique along with Raman coupling scheme can be applied to diverse quantum materials, such as semiconductor hetero-structures, quantum dots, photonic crystals, atomic vapors, and Bosonic and Fermionic ultra cold gases to probe the spin correlations. The techniques developed during this thesis work promises to advance our knowledge about the origin of quantum magnetism. In the context of cold atoms in optical lattices, an analogue simulation of Hubbard Hamiltonian can be performed. The ground state solution can have either superfluid or insulating phases.

In the case of cold atoms with a particular spin state, this implies a phase transition between a spin fluctuating state to a "frozen" spin state. This phase transition can be investigated using the technique of SNS.

On the application front, these techniques can be utilized to develop high precision, real-time, and miniaturised magnetometers for quantum sensing. Reliable measurements of spin fluctuations as described in this thesis, can be a promising experimental tool for quantum information processing and computation. In recent past, a spin noise measurements had been performed to demonstrate the generation of entanglement between two distant (thermal) atomic spin ensembles in their quadrature components [213, 297]. In this experiment, the polarization of the two atomic systems is initially prepared in the opposite orientation ($+x$ for system 1 and $-x$ for system 2) using optical pumping. The instantaneous magnitude of the quadrature spin components, such as $y-$ and $z-$, is proportional to $\sqrt{N}$ where N is the number of atoms in each cell. The temporal evolution of these quadrature components is driven by quantum fluctuations, i.e. spin noise. Measurements of the spin noise of one system with respect to another (negative mass) system allow to detect the noise variances below the standard quantum limit set by the Heisenberg uncertainty principle [214, 215, 297] or by the stroboscopic back-action-evading measurement [298]. Apart from the atomic systems, the generation of entanglement in material systems by measuring the spin noise is achieved in many systems including trapped ions and atoms [299], quantum defects in crystals [300], and high-quality mechanical oscillators [301].

The entanglement between two non-local objects provides extra correlation that gives valuable resources for enabling the teleportation of quantum states and exponential speed-up in quantum computing [302] and precision metrology beyond standard quantum limits [303]. Generating and maintaining entanglement in material systems play a crucial role in many practical applications and fundamental research interests since the massive particles are an ideal system for the storage of quantum information. At the same time, the information can be transferred from one location to another using an optical state, since light is the best long-distance carrier of information. Therefore, in the context of quantum technology development, we expect, the studies and information contained in this thesis will be valuable for active and future researchers.

Appendix A

Saturation absorption spectroscopy (SAS)

The narrow linewidth lasers have to be precisely tuned for addressing the atomic transitions. This can be done by scanning the frequency of the laser beam passing through an atomic sample while simultaneously monitoring its absorption. At the resonance, the absorption should be the maximum. However, the precision of this technique of determining the resonance is limited by the sharpness of the absorption profile by the atomic sample. At room temperature, the velocity distribution, in an ensemble of atoms, can be described by the Maxwell-Boltzmann (MB) distribution function:

$$f(v) = 4\pi \left(\frac{m}{2\pi\, k_B\, T}\right)^{3/2} v^2\, e^{-mv^2/2k_BT}, \tag{A.1}$$

where m is the mass of the atom and v its velocity. This thermal motion of atoms broadens the atomic transition absorption line due to the Doppler effect.

We perform Doppler-free spectroscopy known as saturation absorption spectroscopy (SAS) technique which involves using an intense pump beam and weak probe beam derived from the same laser. The pump and probe are aligned in a counter-propagating layout as shown in Fig. 7.5 (b). The probe absorption is monitored while scanning the frequency of the laser (both pump and probe have this same frequency). Now the Doppler-shift in frequency due to atomic motion is given by:

$$\omega = \omega_0 - \vec{k} \cdot \vec{v}, \tag{A.2}$$

where ω is the shifted frequency, ω_0 is the actual frequency, k is the wave-vector of the light beam. The Doppler-shift for counter-propagating beams is different unless $\vec{k} \cdot \vec{v} = 0$. While scanning, the frequency of the laser comes to resonance with an atomic

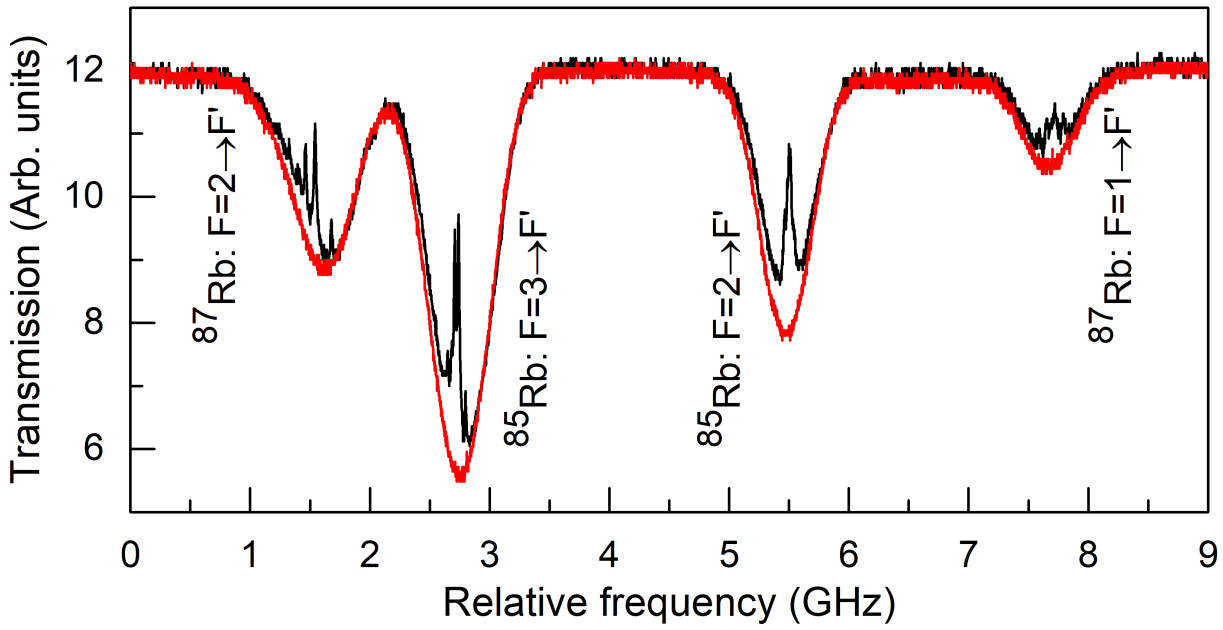

Figure A.1: The probe transmission signal near D_2-line of Rb isotopes in presence (black trace) and absence (red trace) of pump beam. The saturation absorption peaks (real and crossover) identifying various hyperfine transitions are observed in the black trace.

transition, a simultaneous absorption of pump and probe occurs only for atoms having $\vec{k} \cdot \vec{v} = 0$ i.e. for atoms moving perpendicular (or at rest) to beam propagation. This group of atoms is called the zero velocity class of atoms. At resonance, the pump due to its high intensity will saturate the transition only for this zero-velocity class. So there will be no absorption of the weak probe, rather it causes a sudden decrease(increase) in probe absorption(transmission). Since the simultaneous absorption of pump and probe happens only for the zero velocity class, the sharpness of resonance is only limited by the natural Lorentzian linewidth, pressure, and power broadening effects whereas it is independent of Doppler broadening. So we get a precise determination of the resonance frequency. A contrast between the Doppler-broadened profile with no hyperfine peaks and the SAS signal is shown in Fig. A.1. The hyperfine multilevel structure of atoms gives extra peaks in a SAS signal known as crossover peaks. This happens due to a particular velocity component of atoms along the beam propagation direction that is simultaneously excited by both pump and probe beams. However, both pump and probe excite different transitions. Here two types of systems are worth discussing, a) those with two excited states and one ground state (called $V-$system) and b) those with two ground states and one excited state (called $\Lambda-$system). In a $V-$type system, let an atom has velocity $\vec{v}(-\vec{v})$ along pump(probe). Let the pump and probe excite transitions with angular frequency ω_1 and ω_2 respectively and let the laser frequency

be ω_0 at crossover. So for simultaneous excitation:

$$\begin{aligned} \omega_1 &= \omega_0 - \vec{k} \cdot \vec{v} \\ \omega_2 &= \omega_0 + \vec{k} \cdot \vec{v} \\ \Rightarrow \omega_0 &= \frac{\omega_1 + \omega_2}{2} \end{aligned} \tag{A.3}$$

A similar phenomenon happens in a $\Lambda-$system but the crossover is a dip instead of a peak in this case [304]. This happens due to the optical pumping of atoms amongst the two ground states. Let the pump and probe excite transitions with angular frequency ω_1 and ω_2, respectively. Since the pump beam is very intense, all the atoms will be pumped to the ω_2 ground state which is excited by the probe. This entails probe absorption giving rise to a dip instead of a peak. In short, the cross-over between the excited hyperfine levels are a peak, and that between the ground hyperfine levels are a dip. The cross-over dip between the ground hyperfine levels are observed when the Doppler broadening is similar or more than the ground hyperfine level separation. The dip in the absorption spectrum is not observed when the Doppler broadening is much smaller than the ground hyperfine level separation.

A.1 Frequency modulation spectroscopy

Frequency modulation (FM) spectroscopy is a powerful tool that helps to lock the laser on the atomic transition line with stability much better than the exited level line-width of the atoms. It involves modulating the frequency of a laser generally by applying a variable sinusoidal voltage to the grating of the ECDL. The laser beam is passed through a sample which can respond to frequency changes say a SAS setup.

Now the SAS signal will have modulation as per the frequency modulation of the laser. Two points are worth mentioning : a) For SAS itself the frequency of laser is changed, but that modulation is very slow (few Hz) and its amplitude is large (called ramp amplitude). This is different from the modulation given to the laser current whose frequency is high (few kHz) but amplitude is less. b) The SAS signal has symmetric profile about resonance so we do not know if we are above or below a resonance just by measuring the SAS signal. It is actually the derivative of SAS signal which is anti-symmetric about the resonance and can tell if we are above or below a resonance. Such a derivative or error signal is shown in Fig. A.2 for Rb isotopes of cooling transitions.

To extract the derivative signal, we need to understand a simple mathematical treatment. If the laser frequency ω is sinusoidally modulated with modulation amplitude p

and frequency f, then the transmitted intensity I through the SAS cell is,

$$I(\omega + p\sin ft) = I(\omega) + p\sin ft\,\frac{dI}{d\omega} + \frac{p^2\sin^2 ft}{2!}\,\frac{d^2I}{d\omega^2} + ... \tag{A.4}$$

This can be re-written as,

$$I(\omega + p\sin ft) = \Big[I(\omega) + \frac{p^2}{4}\,\frac{d^2I}{d\omega^2} + ...\Big] + \sin ft\,\Big[p\,\frac{dI}{d\omega} + \frac{p^3}{8}\sin^2 ft\,\frac{d^3I}{d\omega^3} + ...\Big] + \\ +\cos 2ft\Big[-\frac{p^2}{4}\,\frac{d^2I}{d\omega^2} + ...\Big] + ... \tag{A.5}$$

So, the transmitted intensity contains a DC term, a term oscillating at f, a term oscillating at $2f$, and so on. Since we have assumed that$p$ is small, the coefficient of the $\sin ft$ term is essentially p multiplied by the first derivative of the transmitted intensity. So the derivative can be extracted by performing a phase-sensitive detection at f.

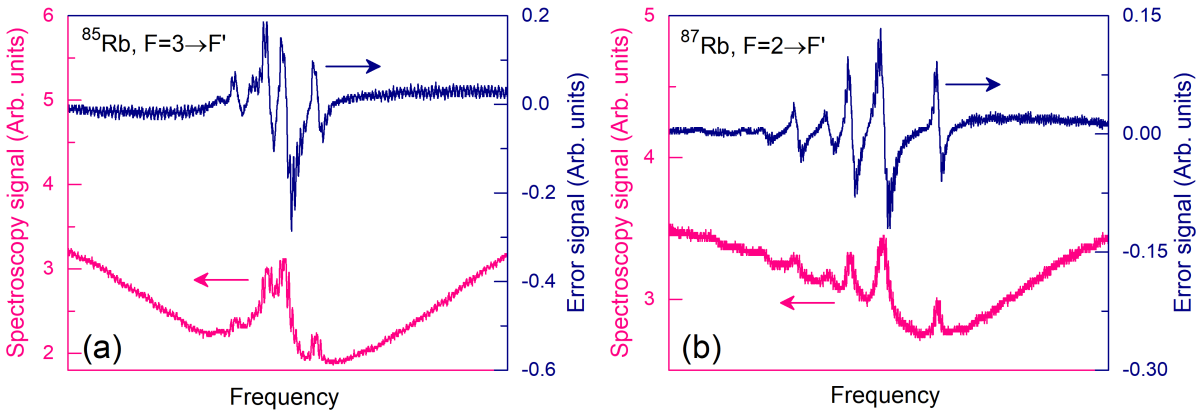

Figure A.2: The derivative (error) signal corresponds to the SAS signal of cooling lines Rb isotopes.

Appendix B

Acousto-optic modulator (AOM)

An AOM is a device used to change typically the frequency of light by a controllable amount generally of the order of several tens or hundreds of MHz. It is also used to vary the beam intensity. It consists of a crystal through which sound waves produced by an RF transducer travel to create modulation of density in the crystal. This density modulation leads to variations of refractive index which travel with the speed of the sound. So acoustic wavefronts are generated inside the crystal from which Bragg-diffraction of the beam occurs when:

$$2\Lambda \operatorname{Sin}\theta = n\lambda, \tag{B.1}$$

where Λ and λ are the wavelengths of sound and light, respectively and θ is the angle made by light with the acoustic wavefront. A schematic diagram of an AOM is shown in Fig. B.1.

To explain the frequency shift we can use wave-vector diagrams to illustrate the basic light-sound interaction [305]. These diagrams refer quantum-mechanically to the conservation of momentum in photon-phonon collisions and classically to phase-synchronous interaction. The assumption in the Bragg-diffraction that the incoming and scattered light has the same wavelength is good enough because of a huge difference in frequencies of light and sound.

This allows the wave-vector representation of the Bragg condition as shown in Fig. B.2. which can either be an upshift or downshift in the frequency of light by the amount same as the frequency of sound. So for an $n-$th order diffraction, we have :

$$f_n = f + n\nu_s, \tag{B.2}$$

where f is the frequency of light and ν_s frequency of sound. A practical problem

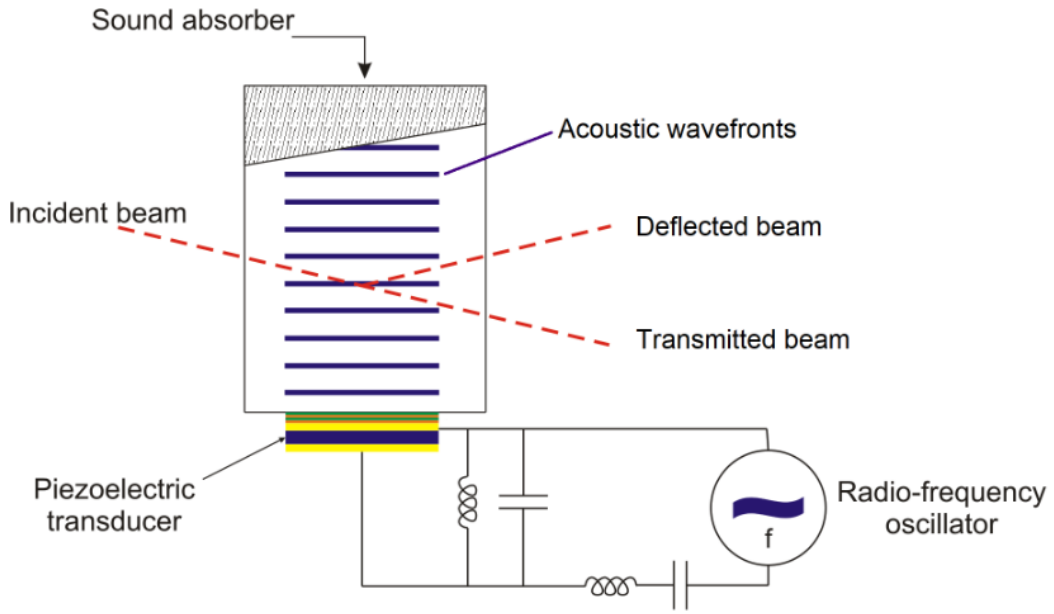

Figure B.1: The schematic of AOM.

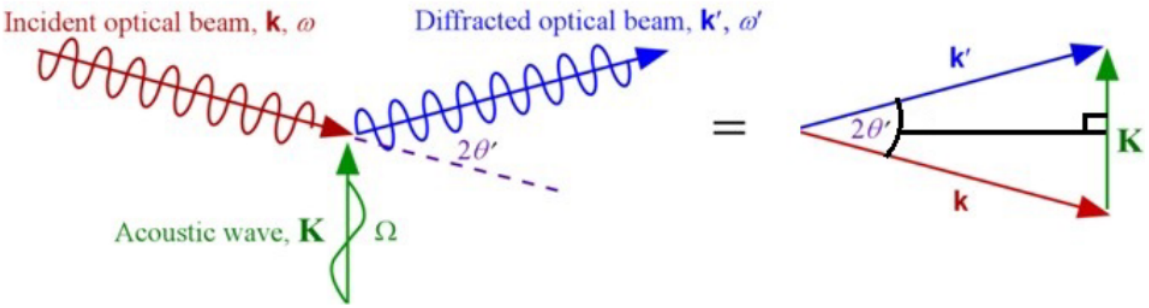

Figure B.2: Bragg condition as a wave vector diagram.

that arises when using AOMs to scan the laser frequency is the dependence of the beam diffraction angle on the modulation frequency. The alignment problems caused by AOM frequency sweeps can be practically eliminated by using the double-pass configuration [306], in which the laser beam travels through the AOM twice and the beam deflection is compensated in the second pass. Modulating the light with the AOM twice also means that the total frequency shift is twice the modulation frequency. For an optimized double-pass a cat's eye retroreflector [306] should be used instead of a flat mirror retroreflector. The double-pass configuration employs an extra QWP to separate the spatially overlapping input and output beams by making their polarizations mutually orthogonal which can be separated using a PBS.

Appendix C

Field profile of magnetic coils

C.1 Magnetic field expressions for circular current loops

The magnetic field generated by a current carrying element is given by Biot-Savart law as,

$$d\vec{B} = \frac{\mu_0}{4\pi}\frac{Id\vec{l}\times\vec{r}}{|r|^2} \tag{C.1}$$

where $\vec{dl}$ is the infinitesimal length vector of the current element (I) and $\hat{r}$ is the unit vector in the direction of the measured point from the current element.

For a single current loop of radius R perpendicular to z axis and centered at $z = A$, the magnetic field components in cylindrical polar coordinates is given by [307],

$$B_z = \frac{\mu I}{2\pi(R+\rho)^2+(z-A)^{2}{}^{1/2}}\Big\{K(k^2)+\frac{R^2-\rho^2-(z-A)^2}{(R-\rho)^2+(z-A)^2}E(k^2)\Big\}, \tag{C.2}$$

$$B_\rho = \frac{\mu I(z-A)}{2\pi\rho(R+\rho)^2+(z-A)^{2}{}^{1/2}}\Big\{-K(k^2)+\frac{R^2+\rho^2+(z-A)^2}{(R-\rho)^2+(z-A)^2}E(k^2)\Big\}, \tag{C.3}$$

and,

$$B_\phi = 0. \tag{C.4}$$

The argument in the complete integrals K and E is $k^2 = \frac{4a\rho}{(a+\rho)^2+(z-z_0)^2}$, where a is the radius of the coil. In air, $\mu = \mu_0 = 4\pi\times10^{-7}$ N/A^2. These equations are needed to

calculate numerically to get the total magnetic field of a thick circular coil by summing the fields produced by many single loops which make the large coil.

C.1.1 Helmholtz coil configuration

The standard technique for generating a uniform magnetic field is to use a pair of circular coils with equal currents flowing in the same sense. The magnetic field on the axis of a circular current loop of radius a with current I can be written as,

$$B(z) = \frac{\mu_0 I a^2}{2(a^2+z^2)^{3/2}} \tag{C.5}$$

at a distance z above the center of the loop. We can generate a nearly uniform field near the midway ($z = 0$) between the coils, using two such loops with distance d apart. The field as a function of z is,

$$B(z) = \frac{\mu_0 I a^2}{2}\left(\frac{1}{\{a^2+(z-d/2)^2\}^{3/2}} + \frac{1}{\{a^2+(z+d/2)^2\}^{3/2}}\right). \tag{C.6}$$

C.1.2 Anti-Helmholtz coil configuration

For trapping atoms in a MOT, we need a locally uniform field gradient to provide a spatially dependent Zeeman shift for neutral atoms. To do this, one simply reverses the current in one of the Helmholtz coils. Such coils were first used to trap neutral atoms by Migdall *et. al* [308]. The MOTs have a typical field gradient of 10-40 G/cm along the symmetry axis. A calculation of the magnetic field B along the z-axis (axis of symmetry) of a pair of anti-Helmholtz coils yields

$$B(z) = \frac{\mu_0 I a^2}{2}\left(\frac{1}{\{a^2+(z-d/2)^2\}^{3/2}} - \frac{1}{\{a^2+(z+d/2)^2\}^{3/2}}\right). \tag{C.7}$$

The currents in each coil are flowing in the opposite directions. The field components of anti-Helmholtz coils near the origin up to third order can be written as,

$$\begin{aligned} B_\phi &= 0, \\ B_z &= \frac{3\mu I d a^2}{2\{a^2+(d/2)^2\}^{5/2}} z + \frac{15\mu I a^2(d^2-3a^2)}{24\{a^2+(d/2)^2\}^{9/2}}\left(4z^3 - 6z\rho^2\right), \\ B_\rho &= -\frac{3\mu I d a^2}{4\{a^2+(d/2)^2\}^{5/2}}\rho + \frac{15\mu I a^2(d^2-3a^2)}{16\{a^2+(d/2)^2\}^{9/2}}\left(4\rho^3 - 4\rho z^2\right). \end{aligned} \tag{C.8}$$

The maximum field gradient of B_z obtained when $z = a$, which is $\frac{\partial B_z(0)}{\partial z} = \frac{48\mu_0 I}{25\sqrt{5}a^2} = 2\frac{\partial B_\rho(0)}{\partial \rho}$.

C.1.3 Spherical quadrupole coils

For magnetic trapping of cold atoms, the simplest magnetic field geometry with a local minimum is the quadrupole field is generated by two co-axial current loops (along $\hat{z}$-axis) with current flowing in opposite directions. In this configuration, the magnetic field near the quadrupole center is approximated by

$$\vec{B} = b(x, y, -2z). \tag{C.9}$$

b is the field gradient along the radial direction of the coils. The magnetic field is zero at the center and grows linearly in all directions. This shows that the quadrupole trap is much steeper near the center than the quadratic dependence trap.

Appendix D

FPGA control

The accurate characterization of the cold atomic samples requires a precise control over the time sequence of events. This is achieved by interfacing the experimental setup with a LabVIEW program implemented on a FPGA architecture. The 40 MHz onboard clock of FPGA provides a timing jitter of 25 ns.

D.1 LabVIEW

LabVIEW (acronym for Laboratory Virtual Instrument Engineering Workbench) is a system design platform and development environment for a graphical programming language from National Instruments. The programming language used in LabVIEW, also referred to as G, is a dataflow programming language. Execution is determined by the structure of a graphical block diagram (the source code) on which the programmer connects different function nodes by drawing wires. These wires propagate variables and any node can execute as soon as all its input data become available. Since this might be the case for multiple nodes simultaneously, G is inherently capable of parallel execution. Multi-processing and multi-threading hardware is automatically exploited by the built-in scheduler, which multiplexes multiple OS threads over the nodes ready for execution.

LabVIEW ties the creation of user interfaces (called front panels) into the development cycle. LabVIEW programs/subroutines are called virtual instruments (VIs). Each VI has three components: a block diagram, a front panel, and a connector panel. The last is used to represent the VI in the block diagrams of other, calling VIs. Controls and indicators on the front panel allow an operator to input data into or extract data from a running virtual instrument. However, the front panel can also serve as a programmatic interface. Thus a virtual instrument can either be run as a program, with

the front panel serving as a user interface, or, when dropped as a node onto the block diagram of other VIs, the front panel defines the inputs and outputs for the given node through the connector pane. This implies each VI can be easily tested before being embedded as a subroutine into a larger program.

D.2 The CompactRIO system

The CompactRIO platform features a range of embedded controllers with two processing targets: (1) a real-time processor for communication and signal processing and (2) a user-programmable FPGA to implement high-speed control and custom timing and triggering directly in hardware. Both these requirements are critical in cold atom experiments where the relevant time scale are usually less than few milliseconds. The various modules embedded in a CompactRIO refer to the same onboard FPGA clock and hence the sequence of generated signals is automatically synchronized.

The control of the experiment involves switching ON/OFF of the MOT beams, magnetic fields, imaging beams, Raman beams etc. The trigger pulses for this control were generated using the digital input-output (DIO) module NI-9403 embedded in a CompactRIO 9012. Apart from this the frequency and intensity of the beams can be changed by producing voltage ramp from the analog output module NI-9263. The delay between various events is controlled via the in-built wait function.

The CompactRIO is extensively used for controlling the rubidium lab experiments. A practical problem with directly using interactive front panel communication on FPGA is that if any change to the program is done (either in terms of logic or by mistake), it requires a recompilation. This can be daunting if the experimentalist wants to try out various combinations of same steps in the experiment. Our method of solving this problem culminates into building a centralized control interface for the upcoming Na-K experiment. This controls a PXI system with various modules for generating the required signals

Appendix E

Units of the SN spectrum

To compare the units used for the spectrum in this thesis, we have performed a separate experiment where the spectrum for photon shot noise (PSN) of the probe laser beam has been detected with various RBW (such as 0.1, 1, 10, 50, and 100 kHz) of the SFSA. We have performed the experiment with a reasonable scanning span of the internal local oscillator (LO) of 20 MHz of the SFSA in the vertical unit of Watts. Thereafter, we have normalized each detected spectrum with their corresponding RBW (let's say n kHz), in the unit of W/Hz and designate it as PSN ("n" kHz). We took the ratio of consecutive normalized PSN and shown in Fig. E.1 (b), and turns out that the ratio is always one for the five measurements shown in this picture. This experiment verifies that the spectrum detected in the Watts unit is linear and gets normalized with respect to the RBW of the spectrum analyzer, which clearly verifies that the unit for it is W/Hz. However, we have performed a similar experiment for amplitude spectrum (spectrum detected in volt unit) and observed that the normalized spectrum is obtained when the detected signal is divided by the square root of the RBW. This confirms that the units for the amplitude spectrum is $\mathrm{V/Hz^{-1/2}}$. We have also verified the fact that these two units are connected by the load resistance of the SFSA.

The absolute noise floor of generated noise from all sources. All the independent noise sources contributing to giving rise to the final spectrum are uncorrelated. Therefore, the cross-term vanishes while processing the data using the FFT algorithm, and the contributions from individual noise sources are added up separately in the detected spectrum. Such an observation is shown in Fig. E.1 (a). In this graph, we have shown a series of spectrum contributing from various sources related to the experiment. The navy spectrum shows the electronic noise floor of the SFSA and the red trace shows the spectrum when the detector is connected to the SFSA without exposing it to the probe laser beam. The blue spectrum shows the PSN floor of the

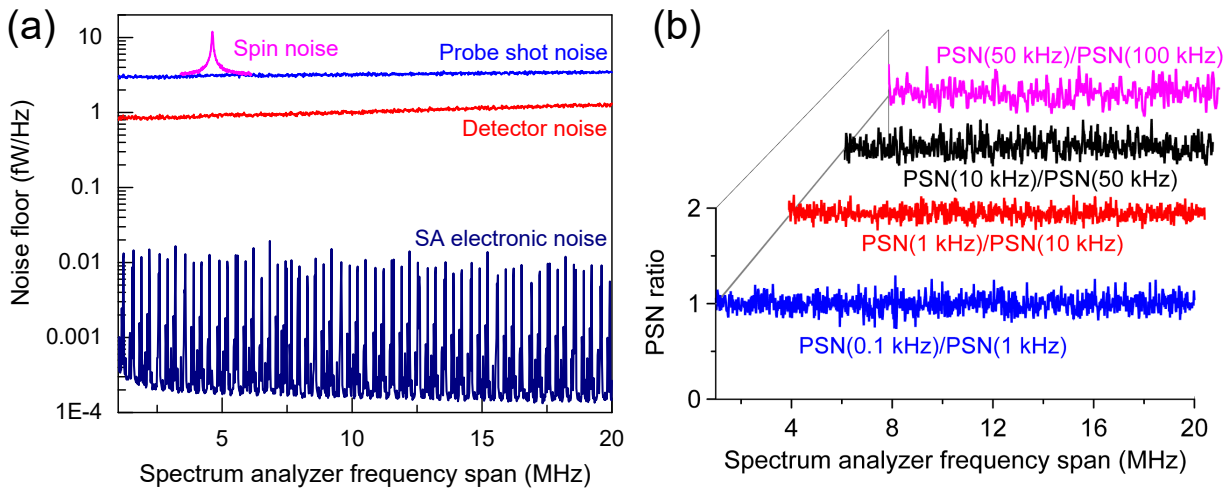

Figure E.1: (a) Depicts the individual noise floor from all sources of the experiments, such as, spectrum analyzer (navy), detector (red), probe photon shot noise (blue), and atomic spin noise (pink). (b) Clarify the units used for SN power spectrum in Watts/Hz. In this unit, the detected power spectrum is normalized with respect to the resolution bandwidth (RBW) of the spectrum analyzer (SA). Here the PSN ("n" kHz) signifies the photon shot noise of the probe beam measured with "n" kHz RBW of the SA, and normalized with respect to that RBW. The ratio of such PSN with different RBW is shown to confirm the unit of the power spectrum is W/Hz (see text).

probe laser beam when the atoms and magnetic fields are not present. In the end, the magenta spectrum shows the spin noise (SN) of the thermal atomic spins that give rise to the top of the PSN floor. The data shown here is in units of W/Hz. Therefore, the SN signal of the spin system can be extracted by subtracting the magenta trace from the blue trace.

Appendix F

Derivation of the driven SN signal using Heisenberg−Langevin equations

F.1 The Hamiltonian

The Hamiltonian ($\mathcal{H}$) of the 3LS ($\mathcal{H}_{3LS}$), the Raman beams ($\mathcal{H}_R$), and their interactions ($\mathcal{H}_{int}$) within the RWA can be written as [233]:

$$\begin{aligned}
\mathcal{H} &= \mathcal{H}_{3LS} + \mathcal{H}_{int} + \mathcal{H}_R, && \text{(F.1)}\\
\frac{\mathcal{H}_{3LS}}{\hbar} &= \omega_1|1\rangle\langle 1| + \omega_2|2\rangle\langle 2| + \omega_3|3\rangle\langle 3|, && \text{(F.2)}\\
\frac{\mathcal{H}_R}{\hbar} &= \sum_{k,s=s_1}^{s_2} [\omega_{ks} a_{ks}^\dagger a_{ks} + \omega_{ks} b_{ks}^\dagger b_{ks}], && \text{(F.3)}\\
\frac{\mathcal{H}_{int}}{\hbar} &= g_1[(a_{ks_1}^\dagger + b_{ks_1}^\dagger)|1\rangle\langle 3| + |3\rangle\langle 1|(a_{ks_1} + b_{ks_1})] \\
&+ g_2[(a_{ks_2}^\dagger + b_{ks_2}^\dagger)|2\rangle\langle 3| + |3\rangle\langle 2|(a_{ks_2} + b_{ks_2})]. && \text{(F.4)}
\end{aligned}$$

Here, $a_{ks}^\dagger$ (a_{ks}) and $b_{ks}^\dagger$ (b_{ks}) are the photon creation (annihilation) operators of the two Raman radiation fields propagating along the $x-$axis. The symbols $s = s_1, s_2$ denotes the polarization (circular and linear) of the Raman fields. The energy of the three Zeeman states are represented by $\hbar\omega_i$ (i = 1,2,3). The frequency ω_{ks} of the fields are linearized centred around some frequency ω_s with a dispersion relation $\omega_{ks} = v_g k_s$ where v_g is the group velocity. The coupling amplitudes of the beams with the 3LS are g_1, g_2, which we take here to be independent of frequency resulting in Markovian

dynamics. The Raman beams are in the coherent state $|E_{s_1}, \omega_{s_1}\rangle, |E_{s_2}, \omega_{s_2}\rangle$ satisfying:

$$\begin{aligned} a_{ks_1}(t_0)|E_{s_1}, \omega_{s_1}\rangle &= \delta(\omega_{ks_1} - \omega_{s_1})E_{s_1}|E_{s_1}, \omega_{s_1}\rangle, && \text{(F.5)} \\ a_{ks_2}(t_0)|E_{s_2}, \omega_{s_2}\rangle &= 0, && \text{(F.6)} \\ b_{ks_1}(t_0)|E_{s_1}, \omega_{s_1}\rangle &= 0, && \text{(F.7)} \\ b_{ks_2}(t_0)|E_{s_2}, \omega_{s_2}\rangle &= \delta(\omega_{ks_2} - \omega_{s_2})E_{s_2}|E_{s_2}, \omega_{s_2}\rangle. && \text{(F.8)} \end{aligned}$$

where we assume that the Raman beams are propagating along the same direction to couple the valance electron in the Λ-type 3LS. Here, E_{s_1} and E_{s_2} are the amplitude of the Raman beams, and ω_{s_1} and ω_{s_2} are their frequencies. We find that $\Omega_{13} = g_1 E_{s_1}/v_g$ and $\Omega_{23} = g_2 E_{s_2}/v_g$.

Sources of dissipation in spin systems. We can further add interactions of the electron with some baths of bosons, e.g., phonons, causing different losses such as dephasing and non-radiative decay.

$$\begin{aligned} \frac{\mathcal{H}_{loss}}{\hbar} &= \sum_k \omega_k [d_{1,k}^\dagger d_{1,k} + d_{2,k}^\dagger d_{2,k} + d_{3,k}^\dagger d_{3,k} + f_{1,k}^\dagger f_{1,k} \\ &+ f_{2,k}^\dagger f_{2,k}], && \text{(F.9)} \\ \frac{\mathcal{V}_{int}}{\hbar} &= (\tilde{\gamma}_1 d_{1,k}^\dagger |1\rangle\langle 3| + \tilde{\gamma}_2 d_{2,k}^\dagger |2\rangle\langle 3| + \tilde{\gamma}_3 d_{3,k}^\dagger |1\rangle\langle 2| + h.c.) \\ &+ \tilde{\lambda}_1 (f_{1,k} + f_{1,k}^\dagger)|3\rangle\langle 3| + \tilde{\lambda}_2 (f_{2,k} + f_{2,k}^\dagger)|2\rangle\langle 2|, && \text{(F.10)} \end{aligned}$$

where $d_{1,k}, d_{2,k}, d_{3,k}$ are the annihilation operators associated with the dissipative bath, and $f_{1,k}, f_{2,k}$ are annihilation operators associated with the dephasing baths coupled to $|1\rangle, |2\rangle$, respectively. The 3LS and bosonic bath fields are considered to be uncoupled and uncorrelated at time $t = t_0$.

Definition of atomic operators. Let us define different transition operators of the 3LS as following: $\sigma^\dagger = |3\rangle\langle 1|, \mu^\dagger = |2\rangle\langle 3|, \nu^\dagger = |1\rangle\langle 2|$. Within such transition operators, the Hamiltonian of the 3LS and interactions are redefined as

$$\begin{aligned} \frac{\mathcal{H}_{3LS}}{\hbar} &= \omega_1 \nu^\dagger \nu + \omega_2 \mu^\dagger \mu + \omega_3 \sigma^\dagger \sigma, && \text{(F.11)} \\ \frac{\mathcal{H}_{int}}{\hbar} &= g_1 [(a_{ks_1}^\dagger + b_{ks_1}^\dagger)\sigma + \sigma^\dagger (a_{ks_1} + b_{ks_1})] \\ &+ g_2 [(a_{ks_2}^\dagger + b_{ks_2}^\dagger)\mu^\dagger + \mu (a_{ks_2} + b_{ks_2})]. && \text{(F.12)} \end{aligned}$$

We shall theoretically derive the Raman driven spectrum using two different ap-

proaches, namely: Heisenberg-Langevin equations and phenomenological master equations based on OBEs. We will compare the experimentally obtained driven power spectrum with the formula derived using OBEs, and extract the information about intrinsic spin coherence rate between the ground Zeeman states.

F.2 Heisenberg-Langevin equations

We send the Raman laser beams on ^{87}Rb atoms at time $t \geq t_0$, and write the Heisenberg equations for the operators of the 3LS and the radiation fields. We formally solve the Heisenberg equations of the field operators, and substitute those solutions in the Heisenberg equations of the 3LS's operators which then have the form of quantum Langevin equations. Finally, we take quantum expectation of these Heisenberg-Langevin equations of operators of the 3LS in the initial state $|\varphi\rangle = |E_{s_1}, \omega_{s_1}\rangle \otimes |E_{s_2}, \omega_{s_2}\rangle$ of the Raman beams. We define following variables:

$$\begin{aligned} S_1(t) &= \langle\sigma(t)\rangle e^{i\omega_{s_1}(t-t_0)}, \quad S_{11}(t) = \langle\sigma^\dagger(t)\sigma(t)\rangle, \\ S_2(t) &= \langle\nu^\dagger(t)\rangle e^{i(\omega_{s_1}-\omega_{s_2})(t-t_0)}, \quad S_{22}(t) = \langle\nu^\dagger(t)\nu(t)\rangle, \\ S_3(t) &= \langle\mu(t)\rangle e^{-i\omega_{s_2}(t-t_0)}, \end{aligned}$$

where $\langle A(t)\rangle \equiv \langle\varphi|A(t)|\varphi\rangle$. The Heisenberg-Langevin equations after the quantum expectation can be written in the form of a differential matrix equation as following [233, 309–311]:

$$\frac{d\boldsymbol{\mathcal{S}}(t)}{dt} = \boldsymbol{M}\boldsymbol{\mathcal{S}}(t) + \boldsymbol{\Omega}, \tag{F.13}$$

where $\boldsymbol{\mathcal{S}} = [S_1, S_2, S_3, S_{11}, S_{22}, S_3^*, S_2^*, S_1^*]^T$, and $\boldsymbol{\Omega} = [0, 0, i\Omega_{23}, 0, 2\gamma_3, -i\Omega_{23}, 0, 0]^T$. We introduce the detuning of the Raman beams from the corresponding transitions as $\Delta_{13} = \omega_{s_1} - \omega_3 + \omega_1$ and $\Delta_{23} = \omega_{s_2} - \omega_3 + \omega_2$. We further write the Raman beam induced decay rates as $\Gamma_i = \pi g_i^2/v_g$ $(i = 1, 2)$, and the rates of different losses as $\gamma_j = \pi\tilde{\gamma}_j^2/v_g$ $(j = 1, 2, 3)$ and $\lambda_i = \pi\tilde{\lambda}_i^2/v_g$ $(i = 1, 2)$. Finally, we present the matrix $\boldsymbol{M}$

governing the Markovian dynamics of electron in the 3LS:

$$\boldsymbol{M} = \begin{pmatrix} i\zeta_1 & -i\Omega_{23} & 0 & i\Omega_{13} & -i\Omega_{13} & 0 & 0 & 0 \\ -i\Omega_{23} & -i\left(\zeta_2^* - \zeta_1^*\right) & i\Omega_{13} & 0 & 0 & 0 & 0 & 0 \\ 0 & i\Omega_{13} & -i\zeta_2^* & -2i\Omega_{23} & -i\Omega_{23} & 0 & 0 & 0 \\ i\Omega_{13} & 0 & -i\Omega_{23} & -2\left(2\left(\Gamma_1+\Gamma_2\right)+\gamma_1+\gamma_2\right) & 0 & i\Omega_{23} & 0 & -i\Omega_{13} \\ -i\Omega_{13} & 0 & 0 & 2\left(2\Gamma_1+\gamma_1-\gamma_3\right) & -2\gamma_3 & 0 & 0 & i\Omega_{13} \\ 0 & 0 & 0 & 2i\Omega_{23} & i\Omega_{23} & i\zeta_2 & -i\Omega_{13} & 0 \\ 0 & 0 & 0 & 0 & 0 & -i\Omega_{13} & i\left(\zeta_2-\zeta_1\right) & i\Omega_{23} \\ 0 & 0 & 0 & -i\Omega_{13} & i\Omega_{13} & 0 & i\Omega_{23} & -i\zeta_1^* \end{pmatrix}$$

where the complex variables are:

$$\begin{aligned} \zeta_1 &= \Delta_{13} + i(2\Gamma_1 + 2\Gamma_2 + \gamma_1 + \gamma_2 + \lambda_1), \\ \zeta_2 &= \Delta_{23} + i(2\Gamma_1 + 2\Gamma_2 + \gamma_1 + \gamma_2 + \gamma_3 + \lambda_1 + \lambda_2). \end{aligned}$$

Since the matrix $\boldsymbol{M}$ and $\boldsymbol{\Omega}$ are independent of time, the steady state of the 3LS would be time independent, and independent of initial conditions as long as it exists. Due to the presence of dissipative terms we can assume the system will reach steady state as time tends to infinity. The steady-state solution of the variables can be obtained from

$$\boldsymbol{\mathcal{S}}(t \to \infty) = \boldsymbol{M}^{-1}\boldsymbol{\Omega}, \tag{F.14}$$

which we shall use to find $S_2(t \to \infty)$ ($\equiv S_2(\infty)$) for our later purpose.

Ground-state coherence. Let us now define the power spectrum for the ground-state spin coherence of ^{87}Rb atoms driven by the Raman beams as

$$\begin{aligned} P(\omega) &= \frac{1}{2\pi}\int_{-\infty}^{\infty} d\tau e^{i\omega\tau}\langle\nu^\dagger(t+\tau)\nu(t)\rangle \\ &= \frac{1}{\pi}\mathrm{Re}\Big[\int_0^{\infty} d\tau e^{i\omega\tau}\langle\nu^\dagger(t+\tau)\nu(t)\rangle\Big]. \end{aligned} \tag{F.15}$$

To evaluate the ground-state coherence, we need to find two-time correlators of the atomic operators. For this, we now introduce a set of two-time correlators:

$$\begin{aligned}
S_{12}(\tau) &= \langle\sigma(t+\tau)\nu(t)\rangle e^{i(\omega_{s_1}\tau+\omega_{s_2}(t-t_0))},\\
S_{22}(\tau) &= \langle\nu^\dagger(t+\tau)\nu(t)\rangle e^{i(\omega_{s_1}-\omega_{s_2})\tau},\\
S_{32}(\tau) &= \langle\mu(t+\tau)\nu(t)\rangle e^{-i(\omega_{s_2}\tau+\omega_{s_1}(t-t_0))},\\
S_{112}(\tau) &= \langle\sigma^\dagger(t+\tau)\sigma(t+\tau)\nu(t)\rangle e^{-i(\omega_{s_1}-\omega_{s_2})(t-t_0)},\\
S_{222}(\tau) &= \langle\nu^\dagger(t+\tau)\nu(t+\tau)\nu(t)\rangle e^{-i(\omega_{s_1}-\omega_{s_2})(t-t_0)},\\
S_{32p}(\tau) &= \langle\mu^\dagger(t+\tau)\nu(t)\rangle e^{i(\omega_{s_2}(\tau+2(t-t_0))-\omega_{s_1}(t-t_0))},\\
S_{22p}(\tau) &= \langle\nu(t+\tau)\nu(t)\rangle e^{-i(\omega_{s_1}-\omega_{s_2})(\tau+2(t-t_0))},\\
S_{12p}(\tau) &= \langle\sigma^\dagger(t+\tau)\nu(t)\rangle e^{-i(\omega_{s_1}(\tau+2(t-t_0))-\omega_{s_2}(t-t_0))},
\end{aligned}$$

which satisfy the following differential matrix equation:

$$\frac{d\tilde{\boldsymbol{\mathcal{S}}}(\tau)}{d\tau} = \boldsymbol{M}\tilde{\boldsymbol{\mathcal{S}}}(\tau) + \tilde{\boldsymbol{\Omega}}, \tag{F.16}$$

We can derive an expression for $P(\omega)$ from our theory:

$$P(\omega) = \frac{1}{2\pi}(I_2(\omega) + I_2^*(\omega)) + |S_2(\infty)|^2\delta(\omega - \omega_{s_1} + \omega_{s_2}), \tag{F.17}$$

where the first part is contribution from incoherent scattering in the nonlinear regime at large Ω_{13} and Ω_{23}, and the second part is due to coherent scattering which is what we mostly observe in the experiment. These sharp peaks appear at spectral frequency $\omega = \omega_{s_1} - \omega_{s_2}$, and the peak heights are weighted by a Lorentzian-like envelope given by $|S_2(\infty)|^2$. We can achieve a simple expression for $|S_2(\infty)|^2$ when $\Omega_{13} = \Omega_{23} = \Omega$, $\Gamma_1 = \Gamma_2 = \Gamma$ and $\Delta_{23} - \Delta_{13} = \Delta_{21}$:

$$\begin{aligned}
&|S_2(\infty)|^2\\
=\ &\frac{\Omega^4(64\Gamma^2\Delta_{21}^2 + (\Delta_{21}^2 - 4\Omega^2)^2}{(\Delta_{21}^2(32\Gamma^2 + \Delta_{21}^2 + 2\Delta_{23}\Delta_{13}) + 2\Delta_{21}^2\Omega^2 + 8\Omega^4)^2}.
\end{aligned}$$

Appendix G

Popular article based on the thesis work

Article title: Human perception of magnetic fields

Some of the inherent capabilities typical to a class of animals may seem strange to humans, but always beyond our imagination to possess it. Case in point: the forecast of an earthquake by some wild animals, birds' vision of the world beyond our definitive color spectrum, or for that matter, the most commonly known yet peculiar one, emission of ultrasonic waves by bats for navigation. However, there is no end to such amazing abilities of animals. Nevertheless, what surprised me the most as a child, for an animalistic trait, was the accuracy with which migratory birds could travel across countries, and often, continents.

During one of my visits to the Chilika Lake in the coastal state of Odisha as a teenager, I saw innumerable birds of different colors and sizes, and I was convinced about their migration from afar. At that time, I heard that these birds migrate from Russia, Siberia, Mongolia, Iraq, Iran, Afghanistan, or even, close home, from the Himalayas, every year during the harsh winter, and move in to the more comfortable coastal areas, like the Chilika. Moreover, right as the winter tends to give away to the mild spring, they move back in flocks to their "own" countries. Later, I learned that these birds could sense and follow the geomagnetic field lines and that was the reason for their accurate landing and taking flights at different locations across the globe.

According to scientists, there is a massive and powerful bar magnet right at the center of the earth, generally referred to as the geomagnet. The strength of the geomagnetic field is quite low on the surface of the Earth ranging between a quarter and a half Gauss. To put that into perspective, the magnetic field produced from a typical

refrigerator door magnet is about hundred Gauss. The geomagnetic field lines emanate from the southernmost tip of the Earth, i.e., the South Pole, and encircle across the globe until they reach and end at the North Pole. Birds possess a particular kind of protein in their eyes, called Cryptochrome, which help them in sensing and following the geomagnetic field lines (see Fig. 1(a)). Migratory birds use this ability to assess the altitude and direction as they move. While as humans, we use google maps for this purpose.

However, it is not just birds that can sense the geomagnetic fields; there are a lot of other animals as well who use this ability to navigate through their journey. Red foxes in North America use the geomagnetic field lines as a rangefinder in order to accurately jump and pounce on their prey, turtles use this sensor to locate their homes in the depth of the seas. Different kinds of dogs, snails, frogs, lobsters, fishes, (especially whales and eels) as well as insects and bacteria have the ability of sensing the geomagnetic field lines.

Now, the obvious question that springs up in our minds is: Can humans also perceive the geomagnetic field lines? Recent studies have shown that some humans actually can sense these field lines in certain situations, although the evidences are not conclusive enough yet, and research is still going on to this end. However, one thing can be said that humans have not been able to navigate through by sensing the geomagnetic field, or at least, yet. In simpler terms, humans cannot "see" the fictitious faint lines of geomagnetic fields.

Nevertheless, with the advancement of science, particularly in physics and medical sciences, over the last few decades, the bio-magnetic fields originating from the brain, heart, liver and some other organs of humans can be traced and measured. There are two processes in which magnetic field can be generated in human body:

A. Organs as brain, heart etc. create an electric current while performing bio-informatics, and in the process, generate an extremely weak magnetic field.

B. Humans, while consuming food and during respiration, allow some magnetic substances to enter and accumulate inside the liver, lungs or muscles, which in turn create very weak magnetic fields.

Let us now try to look at the strength of such bio-magnetic fields. The strength of the field created in A. is about one part in ten millionth of the geomagnetic field, while in that of B., it is about one part in a million. Such feeble magnetic fields are not even felt by birds and animals. However, humans, with the aid and advent of science and technology, can measure such fields. In the Magnetoencephalography (MEG) technique (see Fig. 1(b)), based on the distribution of bio-magnetic fields, internal composition of brain can be imaged as well as examine the activities involved,

while in the Magnetocardiography (MCG) technique, the efficiency of heart can be examined. At present, scientists can measure a magnetic field of almost any strength, as well as trace the field lines accurately. Down below is an explainer in lucid terms.

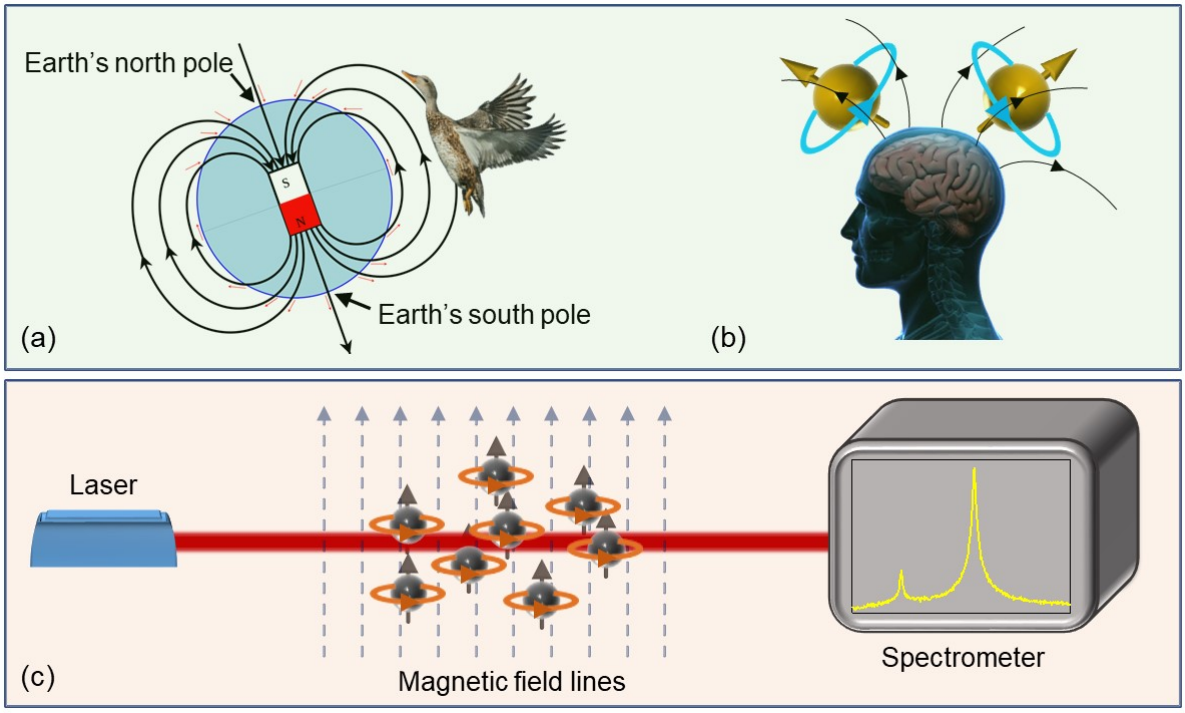

Figure G.1: (a) Birds' perception of geomagnetic field lines. Picture credit: Google. (b) Electron's spin precession in a magnetic field emanate from human brain: basics of MEG (brain) imaging. Picture credit: Human brain has been taken from Google. (c) Simple schematic of the magnetic field measurement setup. Yellow signal (taken in our laboratory) on the spectrometer provides the accurate measurement of magnetic field where the electron's spin is precessing.

Scientists take the help of one of the most fundamental particles of an atom called electron, to measure the magnetic fields. It is a well-known fact that everything around us in this universe is composed of the infinitesimally small atoms. While the size of an atom is just a millionth part of a human hair, it is the ruler of its own kingdom. Nucleus, as the name suggests, lies at the heart of the atom, and as the planets revolve around the sun, electron rotates about their own axis while revolving around the nucleus. The rotation about its own axis is regarded as electron spin, which is an intrinsic property of electrons. Because of the electronic spin, a magnetic dipole is generated in the electron. Due to this magnetic dipole, electrons, when entering the field of any magnetic matter, starts to precess along the direction of the field lines like a spinning top. How fast it precess? That depends on the strength of the magnetic field. If the magnetic field strength is more, it precess in a faster rate and if the magnetic field strength is less,

it precess slowly. Now, all that is left for us is to measure this speed of electron spin precession with precision to establish a correlated measurement of the strength of the magnetic field in which the electron revolves along. That problem was solved by the discovery and fruitful utilization of spectrometers (see Fig. 1(c)). Recent studies have shown that using this technique, direction and field strength as low as one billionth of the geomagnetic field can be measured with high precision. Scientists claim that using this technique, magnetic fields with strength even lower than those of bio-magnetic fields can be determined with precision, opening doors for many fundamental studies in physics and chemistry, which have remained as open questions until now. Furthermore, in earth sciences, a precise measurement of magnetic field enables geophysicists to get the pinpoint locations of the minefield containing minerals and oils.

Thus, it can be said that humans have taken the aid of simulation of measuring electronic spin precession to perceive a magnetic field, which birds and animals do by their own inherent capabilities. While humankind might not have been as "blessed" as the other organisms of the animal kingdom, it sure has utilized one inherent property-curiosity, to its fullest, in order to develop science and technology to such a level as to match, and at times, (like this precise measurement of magnetic field) even better that of the others in the kingdom.

Bibliography

[1] Valerii S. Zapasskii, "Spin-noise spectroscopy: from proof of principle to applications," Adv. Opt. Photon. **5**, 131–168 (2013).

[2] G. G. Kozlov, A. A. Fomin, M. Yu. Petrov, I. I. Ryzhov, and V. S. Zapasskii, "Raman scattering model of the spin noise," Opt. Express **29**, 4770–4782 (2021).

[3] Nikolai A Sinitsyn and Yuriy V Pershin, "The theory of spin noise spectroscopy: a review," Rep. Prog. Phys. **79**, 106501 (2016).

[4] S. A. Crooker, D. G. Rickel, A. V. Balatsky, and D. L. Smith, "Spectroscopy of spontaneous spin noise as a probe of spin dynamics and magnetic resonance," Nature **431**, 49 (2004).

[5] Maheswar Swar, Dibyendu Roy, Dhanalakshmi D, Saptarishi Chaudhuri, Sanjukta Roy, and Hema Ramachandran, "Measurements of spin properties of atomic systems in and out of equilibrium via noise spectroscopy," Opt. Express **26**, 32168–32183 (2018).

[6] Yuval Cohen, Krishna Jadeja, Sindi Sula, Michela Venturelli, Cameron Deans, Luca Marmugi, and Ferruccio Renzoni, "A cold atom radio-frequency magnetometer," Appl. Phys. Lett. **114**, 073505 (2019).

[7] Katja Gosar, Tina Arh, Tadej Mežnaršič, Ivan Kvasič, D. Ponikvar, T. Apih, Rainer Kaltenbaek, Rok Žitko, Erik Zupanič, Samo Beguš, and Peter Jeglič, "Single-shot stern-gerlach magnetic gradiometer with an expanding cloud of cold cesium atoms," Phys. Rev. A **103**, 022611 (2021).

[8] Ryuta Yamamoto, Jun Kobayashi, Kohei Kato, Takuma Kuno, Yuto Sakura, and Yoshiro Takahashi, "Site-resolved imaging of single atoms with a faraday quantum gas microscope," Phys. Rev. A **96**, 033610 (2017).

[9] M A Kristensen, M Gajdacz, P L Pedersen, C Klempt, J F Sherson, J J Arlt, and A J Hilliard, "Sub-atom shot noise faraday imaging of ultracold atom clouds," J. Phys. B **50**, 034004 (2017).

[10] Miroslav Gajdacz, Poul L. Pedersen, Troels Mørch, Andrew J. Hilliard, Jan Arlt, and Jacob F. Sherson, "Non-destructive faraday imaging of dynamically controlled ultracold atoms," Rev. Sci. Instrum. **84**, 083105 (2013).

[11] D. Yang, C. Laflamme, D. V. Vasilyev, M. A. Baranov, and P. Zoller, "Theory of a quantum scanning microscope for cold atoms," Phys. Rev. Lett. **120**, 133601 (2018).

[12] Jakob Meineke, Jean-Philippe Brantut, David Stadler, Torben Müller, Henning Moritz, and Tilman Esslinger, "Interferometric measurement of local spin fluctuations in a quantum gas," Nat. Phys. **8**, 454–458 (2012).

[13] Alessio Recati and Sandro Stringari, "Spin fluctuations, susceptibility, and the dipole oscillation of a nearly ferromagnetic fermi gas," Phys. Rev. Lett. **106**, 080402 (2011).

[14] Ehud Altman, Eugene Demler, and Mikhail D. Lukin, "Probing many-body states of ultracold atoms via noise correlations," Phys. Rev. A **70**, 013603 (2004).

[15] Dibyendu Roy, Luyi Yang, Scott A. Crooker, and Nikolai A. Sinitsyn, "Cross-correlation spin noise spectroscopy of heterogeneous interacting spin systems," Sci. Rep. **5**, 9573 (2015).

[16] Paul Niklas Jepsen, Jesse Amato-Grill, Ivana Dimitrova, Wen Wei Ho, Eugene Demler, and Wolfgang Ketterle, "Spin transport in a tunable heisenberg model realized with ultracold atoms," Nature **588**, 403–407 (2020).

[17] Maheswar Swar, Dibyendu Roy, Subhajit Bhar, Sanjukta Roy, and Saptarishi Chaudhuri, "Detection of spin coherence in cold atoms via faraday rotation fluctuations," Phys. Rev. Research **3**, 043171 (2021).

[18] Subhajit Bhar, Maheswar Swar, Urbashi Satpathi, Supurna Sinha, Rafael Sorkin, Saptarishi Chaudhuri, and Sanjukta Roy, "Measurements and analysis of response function of cold atoms in optical molasses," Optics Continuum **1**, 171–188 (2022).

[19] Taro Ito, Noboru Shimomura, and Tsutomu Yabuzaki, "Transfer of precessing spin polarizations between different kinds of atoms with same g-factor," Journal of the Physical Society of Japan **72**, 1302–1303 (2003).

[20] V. Mugundhan, Maheswar Swar, Subhajit Bhar, and Saptarishi Chaudhuri, "A real-time digital receiver for correlation measurements in atomic systems," IEEE Transactions on Instrumentation and Measurement **70**, 1–8 (2021).

[21] Maheswar Swar, Dibyendu Roy, Dhamodaran Dhanalakshmi, Saptarishi Chaudhuri, Sanjukta Roy, and Hema Ramachandran, Measurements of Temporal Fluctuations of Magnetization in Alkali Vapor and Applications (Emerging Trends in Advanced Spectroscopy, ISBN: 9788770220828, 2019).

[22] Daniel A. Steck, "Rubidium 87 d line data," ().

[23] Daniel A. Steck, "Rubidium 85 d line data," ().

[24] C. Cohen-Tannoudji, J. Dupont-Roc, and G. Grynberg, Atom-Photon Interactions: Basic Processes and Applications, A Wiley-Interscience publication (Wiley, 1998).

[25] J.J. Sakurai and J. Napolitano, Modern Quantum Mechanics (Cambridge University Press, 2020).

[26] D.J. Griffiths and D.F. Schroeter, Introduction to Quantum Mechanics (Cambridge University Press, 2019).

[27] C. Cohen-Tannoudji, B. Diu, B. Dui, F. Laloë, S.R. Hemley, N. Ostrowsky, and D.B. Ostrowsky, Quantum Mechanics, A Wiley interscience publication No. v. 2 (Wiley, 1977).

[28] W. Happer and B. S. Mathur, "Off-resonant light as a probe of optically pumped alkali vapors," Phys. Rev. Lett. **18**, 577–580 (1967).

[29] Scott Jeffrey Seltzer, Developments in alkali-metal atomic magnetometry, Ph.D. thesis, Princeton University (2008).

[30] W. Opechowski, "Magneto-optical effects and paramagnetic resonance," Rev. Mod. Phys. **25**, 264–268 (1953).

[31] P. Bertrand, Electron Paramagnetic Resonance Spectroscopy: Fundamentals (Springer International Publishing, 2020).

[32] J.A. Weil and J.R. Bolton, Electron Paramagnetic Resonance: Elementary Theory and Practical A (Wiley, 2007).

[33] S. Appelt, A. Ben-Amar Baranga, C. J. Erickson, M. V. Romalis, A. R. Young, and W. Happer, "Theory of spin-exchange optical pumping of ^{3}He and ^{129}Xe," Phys. Rev. A **58**, 1412–1439 (1998).

[34] WILLIAM HAPPER, "Optical pumping," Rev. Mod. Phys. **44**, 169–249 (1972).

[35] D. Budker and M. Romalis, "Optical magnetometry," Nat. Phys. **3**, 227 (2007).

[36] W. Happer and H. Tang, "Spin-exchange shift and narrowing of magnetic resonance lines in optically pumped alkali vapors," Phys. Rev. Lett. **31**, 273–276 (1973).

[37] W. Happer and A. C. Tam, "Effect of rapid spin exchange on the magnetic-resonance spectrum of alkali vapors," Phys. Rev. A **16**, 1877–1891 (1977).

[38] I. M. Savukov and M. V. Romalis, "Effects of spin-exchange collisions in a high-density alkali-metal vapor in low magnetic fields," Phys. Rev. A **71**, 023405 (2005).

[39] Or Katz and Ofer Firstenberg, "Synchronization of strongly interacting alkali-metal spins," Phys. Rev. A **98**, 012712 (2018).

[40] Edward M. Purcell and George B. Field, "Influence of Collisions upon Population of Hyperfine States in Hydrogen." **124**, 542 (1956).

[41] H. N. de Freitas, M. Oria, and M. Chevrollier, "Spectroscopy of cesium atoms adsorbing and desorbing at a dielectric surface," Applied Physics B **75**, 703–709 (2002).

[42] G. D. Cates, S. R. Schaefer, and W. Happer, "Relaxation of spins due to field inhomogeneities in gaseous samples at low magnetic fields and low pressures," Phys. Rev. A **37**, 2877–2885 (1988).

[43] G. D. Cates, D. J. White, Ting-Ray Chien, S. R. Schaefer, and W. Happer, "Spin relaxation in gases due to inhomogeneous static and oscillating magnetic fields," Phys. Rev. A **38**, 5092–5106 (1988).

[44] S. D. Stoller, W. Happer, and F. J. Dyson, "Transverse spin relaxation in inhomogeneous magnetic fields," Phys. Rev. A **44**, 7459–7477 (1991).

[45] S. Pustelny, D. F. Jackson Kimball, S. M. Rochester, V. V. Yashchuk, and D. Budker, "Influence of magnetic-field inhomogeneity on nonlinear magneto-optical resonances," Phys. Rev. A **74**, 063406 (2006).

[46] S. A. Wolf, D. D. Awschalom, R. A. Buhrman, J. M. Daughton, S. von Molnár, M. L. Roukes, A. Y. Chtchelkanova, and D. M. Treger, "Spintronics: A spin-based electronics vision for the future," Science **294**, 1488–1495 (2001).

[47] Igor Žutić, Jaroslav Fabian, and S. Das Sarma, "Spintronics: Fundamentals and applications," Rev. Mod. Phys. **76**, 323–410 (2004).

[48] E B Aleksandrov and V S Zapasskii, "Magnetic resonance in the Faraday-rotation noise spectrum," Sov. Phys. JETP **54** (1981).

[49] Tycho Sleator, Erwin L. Hahn, Claude Hilbert, and John Clarke, "Nuclear-spin noise," Phys. Rev. Lett. **55**, 1742 (1985).

[50] Takahisa Mitsui, "Spontaneous noise spectroscopy of an atomic magnetic resonance," Phys. Rev. Lett. **84**, 5292–5295 (2000).

[51] F. Bloch, "Nuclear induction," Phys. Rev. **70**, 460–474 (1946).

[52] R Kubo, "The fluctuation-dissipation theorem," Reports on Progress in Physics **29**, 255 (1966).

[53] R. Balescu, Equilibrium and Non-Equilibrium Statistical Mechanics, A Wiley interscience publication (Wiley, 1975).

[54] L.D. Landau and E.M. Lifshitz, Statistical Physics: Volume 5, v. 5 (Elsevier Science, 2013).

[55] A. Kuzmich, Klaus Mølmer, and E. S. Polzik, "Spin squeezing in an ensemble of atoms illuminated with squeezed light," Phys. Rev. Lett. **79**, 4782–4785 (1997).

[56] J. L. Sørensen, J. Hald, and E. S. Polzik, "Quantum noise of an atomic spin polarization measurement," Phys. Rev. Lett. **80**, 3487–3490 (1998).

[57] J. B. Johnson, "Thermal agitation of electricity in conductors," Phys. Rev. **32**, 97–109 (1928).

[58] H. Nyquist, "Thermal agitation of electric charge in conductors," Phys. Rev. **32**, 110–113 (1928).

[59] Ming Chen Wang and G. E. Uhlenbeck, "On the theory of the brownian motion ii," Rev. Mod. Phys. **17**, 323–342 (1945).

[60] S. Chandrasekhar, "Brownian motion, dynamical friction, and stellar dynamics," Rev. Mod. Phys. **21**, 383–388 (1949).

[61] D R White, R Galleano, A Actis, H Brixy, M De Groot, J Dubbeldam, A L Reesink, F Edler, H Sakurai, R L Shepard, and J C Gallop, "The status of johnson noise thermometry," Metrologia **33**, 325–335 (1996).

[62] DIVYA SHARMA, HEMA RAMACHANDRAN, and N. KUMAR, "Lévy statistical fluctuations from a random amplifying medium," Fluctuation and Noise Letters **06**, L95–L101 (2006).

[63] Anderson S. L. Gomes, Ernesto P. Raposo, André L. Moura, Serge I. Fewo, Pablo I. R. Pincheira, Vladimir Jerez, Lauro J. Q. Maia, and Cid B. de Araújo, "Observation of lévy distribution and replica symmetry breaking in random lasers from a single set of measurements," Sci Rep **6**, 27987 (2016).

[64] D. A. Ivanov and A. G. Abanov, "Phase transitions in full counting statistics for periodic pumping," EPL (Europhysics Letters) **92**, 37008 (2010).

[65] Israel Klich and Leonid Levitov, "Quantum noise as an entanglement meter," Phys. Rev. Lett. **102**, 100502 (2009).

[66] A. H. Myerson, D. J. Szwer, S. C. Webster, D. T. C. Allcock, M. J. Curtis, G. Imreh, J. A. Sherman, D. N. Stacey, A. M. Steane, and D. M. Lucas, "High-fidelity readout of trapped-ion qubits," Phys. Rev. Lett. **100**, 200502 (2008).

[67] D. B. Gutman, Yuval Gefen, and A. D. Mirlin, "Full counting statistics of a luttinger liquid conductor," Phys. Rev. Lett. **105**, 256802 (2010).

[68] Y.V. Nazarov, "Full counting statistics and field theory," Annalen der Physik **16**, 720–735 (2007).

[69] W. M. Itano, J. C. Bergquist, J. J. Bollinger, J. M. Gilligan, D. J. Heinzen, F. L. Moore, M. G. Raizen, and D. J. Wineland, "Quantum projection noise: Population fluctuations in two-level systems," Phys. Rev. A **47**, 3554–3570 (1993).

[70] R.M. White, Quantum Theory of Magnetism: Magnetic Properties of Materials, Springer Series in Solid-State Sciences (Springer Berlin Heidelberg, 2013).

[71] M.M. Glazov, Electron & Nuclear Spin Dynamics in Semiconductor Nanostructures, Series on Semiconductor Scienc (OXFORD University Press, 2018).

[72] Georg M. Müller, Michael Oestreich, Michael Römer, and Jens Hübner, "Semiconductor spin noise spectroscopy: Fundamentals, accomplishments, and challenges," Physica E: Low-dimensional Systems and Nanostructures **43**, 569–587 (2010).

[73] M. M. Glazov and V. S. Zapasskii, "Linear optics, raman scattering, and spin noise spectroscopy," Opt. Express **23**, 11713–11723 (2015).

[74] Smirnov D. S., Mantsevich V. N., and Glazov M. M., "Theory of optically detected spin noise in nanosystems," Phys. Usp **64** (2021).

[75] H. C. Torrey, "Bloch equations with diffusion terms," Phys. Rev. **104**, 563–565 (1956).

[76] M. Oestreich, M. Römer, R. J. Haug, and D. Hägele, "Spin noise spectroscopy in gaas," Phys. Rev. Lett. **95**, 216603 (2005).

[77] Sebastian Starosielec and Daniel Hägele, "Ultrafast spin noise spectroscopy," Applied Physics Letters **93**, 051116 (2008).

[78] Scott A. Crooker, Lili Cheng, and Darryl L. Smith, "Spin noise of conduction electrons in n-type bulk gaas," Phys. Rev. B **79**, 035208 (2009).

[79] Georg M. Müller, Michael Römer, Jens Hübner, and Michael Oestreich, "Efficient data averaging for spin noise spectroscopy in semiconductors," Applied Physics Letters **97**, 192109 (2010).

[80] M. Römer, J. Hübner, and M. Oestreich, "Spatially resolved doping concentration measurement in semiconductors via spin noise spectroscopy," Applied Physics Letters **94**, 112105 (2009).

[81] M. Römer, H. Bernien, G. Müller, D. Schuh, J. Hübner, and M. Oestreich, "Electron-spin relaxation in bulk gaas for doping densities close to the metal-to-insulator transition," Phys. Rev. B **81**, 075216 (2010).

[82] Qiong Huang and Duncan S. Steel, "Optical excitation effects on spin-noise spectroscopy in semiconductors," Phys. Rev. B **83**, 155204 (2011).

[83] Fabian Berski, Hendrik Kuhn, Jan G. Lonnemann, Jens Hübner, and Michael Oestreich, "Ultrahigh bandwidth spin noise spectroscopy: Detection of large g-factor fluctuations in highly-n-doped gaas," Phys. Rev. Lett. **111**, 186602 (2013).

[84] P. S. Pershan, J. P. van der Ziel, and L. D. Malmstrom, "Theoretical discussion of the inverse faraday effect, raman scattering, and related phenomena," Phys. Rev. **143**, 574–583 (1966).

[85] I. I. Ryzhov, G. G. Kozlov, D. S. Smirnov, M. M. Glazov, Y. P. Efimov, S. A. Eliseev, V. A. Lovtcius, V. V. Petrov, K. V. Kavokin, A. V. Kavokin, and V. S. Zapasskii, "Spin noise explores local magnetic fields in a semiconductor," Sci. Rep. **6**, 21062 (2016).

[86] Fabian Berski, Jens Hübner, Michael Oestreich, Arne Ludwig, A. D. Wieck, and Mikhail Glazov, "Interplay of electron and nuclear spin noise in n-type gaas," Phys. Rev. Lett. **115**, 176601 (2015).

[87] Matthias Braun and Jürgen König, "Faraday-rotation fluctuation spectroscopy with static and oscillating magnetic fields," Phys. Rev. B **75**, 085310 (2007).

[88] C. Kehl, G. V. Astakhov, K. V. Kavokin, Yu. G. Kusrayev, W. Ossau, G. Karczewski, T. Wojtowicz, and J. Geurts, "Observation of the magnetic soft mode in (cd,mn)te quantum wells using spin-flip raman scattering," Phys. Rev. B **80**, 241203 (2009).

[89] M. M. Glazov and E. Ya. Sherman, "Theory of spin noise in nanowires," Phys. Rev. Lett. **107**, 156602 (2011).

[90] M. M. Glazov, M. A. Semina, E. Ya. Sherman, and A. V. Kavokin, "Spin noise of exciton polaritons in microcavities," Phys. Rev. B **88**, 041309 (2013).

[91] Yuriy V. Pershin, Valeriy A. Slipko, Dibyendu Roy, and Nikolai A. Sinitsyn, "Two-beam spin noise spectroscopy," Appl. Phys. Lett. **102**, 202405 (2013).

[92] P. Glasenapp, A. Greilich, I. I. Ryzhov, V. S. Zapasskii, D. R. Yakovlev, G. G. Kozlov, and M. Bayer, "Resources of polarimetric sensitivity in spin noise spectroscopy," Phys. Rev. B **88**, 165314 (2013).

[93] Valeriy A. Slipko, Nikolai A. Sinitsyn, and Yuriy V. Pershin, "Hybrid spin noise spectroscopy and the spin hall effect," Phys. Rev. B **88**, 201102 (2013).

[94] Fuxiang Li, Yuriy V. Pershin, Valeriy A. Slipko, and N. A. Sinitsyn, "Nonequilibrium spin noise spectroscopy," Phys. Rev. Lett. **111**, 067201 (2013).

[95] S. V. Poltavtsev, I. I. Ryzhov, M. M. Glazov, G. G. Kozlov, V. S. Zapasskii, A. V. Kavokin, P. G. Lagoudakis, D. S. Smirnov, and E. L. Ivchenko, "Spin noise spectroscopy of a single quantum well microcavity," Phys. Rev. B **89**, 081304 (2014).

[96] Wang-Kong Tse, A. Saxena, D. L. Smith, and N. A. Sinitsyn, "Spin and valley noise in two-dimensional dirac materials," Phys. Rev. Lett. **113**, 046602 (2014).

[97] Brennan C. Pursley, X. Song, and V. Sih, "Resonant and time-resolved spin noise spectroscopy," Applied Physics Letters **107**, 182102 (2015).

[98] A. V. Poshakinskiy and S. A. Tarasenko, "Spatiotemporal spin fluctuations caused by spin-orbit-coupled brownian motion," Phys. Rev. B **92**, 045308 (2015).

[99] M. M. Glazov, "Spin noise of localized electrons: Interplay of hopping and hyperfine interaction," Phys. Rev. B **91**, 195301 (2015).

[100] Luyi Yang, Nikolai A. Sinitsyn, Weibing Chen, Jiangtan Yuan, Jing Zhang, Jun Lou, and Scott A. Crooker, "Long-lived nanosecond spin relaxation and spin coherence of electrons in monolayer mos2 and ws2," Nature Physics **11**, 830–834 (2015).

[101] D. S. Smirnov, "Spin noise of localized electrons interacting with optically cooled nuclei," Phys. Rev. B **91**, 205301 (2015).

[102] S. Cronenberger, D. Scalbert, D. Ferrand, H. Boukari, and J. Cibert, "Atomic-like spin noise in solid-state demonstrated with manganese in cadmium telluride," Nature Communications **6**, 8121 (2015).

[103] William D. Rice, Wenyong Liu, Thomas A. Baker, Nikolai A. Sinitsyn, Victor I. Klimov, and Scott A. Crooker, "Revealing giant internal magnetic fields due to spin fluctuations in magnetically doped colloidal nanocrystals," Nature Nanotechnology **11**, 137–142 (2016).

[104] A. Bechtold, F. Li, K. Müller, T. Simmet, P.-L. Ardelt, J. J. Finley, and N. A. Sinitsyn, "Quantum effects in higher-order correlators of a quantum-dot spin qubit," Phys. Rev. Lett. **117**, 027402 (2016).

[105] Fuxiang Li and N. A. Sinitsyn, "Universality in higher order spin noise spectroscopy," Phys. Rev. Lett. **116**, 026601 (2016).

[106] D. S. Smirnov, B. Reznychenko, A. Auffèves, and L. Lanco, "Measurement back action and spin noise spectroscopy in a charged cavity qed device in the strong coupling regime," Phys. Rev. B **96**, 165308 (2017).

[107] D. S. Smirnov, Ph. Glasenapp, M. Bergen, M. M. Glazov, D. Reuter, A. D. Wieck, M. Bayer, and A. Greilich, "Nonequilibrium spin noise in a quantum dot ensemble," Phys. Rev. B **95**, 241408 (2017).

[108] J. G. Lonnemann, E. P. Rugeramigabo, M. Oestreich, and J. Hübner, "Closing the gap between spatial and spin dynamics of electrons at the metal-to-insulator transition," Phys. Rev. B **96**, 045201 (2017).

[109] A. L. Balk, F. Li, I. Gilbert, J. Unguris, N. A. Sinitsyn, and S. A. Crooker, "Broadband spectroscopy of thermodynamic magnetization fluctuations through a ferromagnetic spin-reorientation transition," Phys. Rev. X **8**, 031078 (2018).

[110] Daniel Hägele and Fabian Schefczik, "Higher-order moments, cumulants, and spectra of continuous quantum noise measurements," Phys. Rev. B **98**, 205143 (2018).

[111] Julia Wiegand, Dmitry S. Smirnov, Jens Hübner, Mikhail M. Glazov, and Michael Oestreich, "Spin and reoccupation noise in a single quantum dot beyond the fluctuation-dissipation theorem," Phys. Rev. B **97**, 081403 (2018).

[112] M. M. Sharipova, A. N. Kamenskii, I. I. Ryzhov, M. Yu. Petrov, G. G. Kozlov, A. Greilich, M. Bayer, and V. S. Zapasskii, "Stimulated spin noise in an activated crystal," Journal of Applied Physics **126**, 143901 (2019).

[113] N. V. Kozyrev, R. R. Akhmadullin, B. R. Namozov, Yu. G. Kusrayev, I. V. Sedova, S. V. Sorokin, and S. V. Ivanov, "Multiple spin-flip raman scattering in cdse/znmnse quantum dots," Phys. Rev. B **99**, 035301 (2019).

[114] Dinh-Hoi Bui, Quoc-Huy Ninh, Huu-Nha Nguyen, and Van-Nham Phan, "Ferromagnetic transition and spin fluctuations in diluted magnetic semiconductors," Phys. Rev. B **99**, 045123 (2019).

[115] S. Cronenberger, C. Abbas, D. Scalbert, and H. Boukari, "Spatiotemporal spin noise spectroscopy," Phys. Rev. Lett. **123**, 017401 (2019).

[116] D. S. Smirnov and K. V. Kavokin, "Optical resonance shift spin-noise spectroscopy," Phys. Rev. B **101**, 235416 (2020).

[117] Dennis Kudlacik, Victor F. Sapega, Dmitri R. Yakovlev, Ina V. Kalitukha, Elena V. Shornikova, Anna V. Rodina, Eugeniius L. Ivchenko, Grigorii S. Dimitriev, Michel Nasilowski, Benoit Dubertret, and Manfred Bayer, "Single and double electron spin-flip raman scattering in cdse colloidal nanoplatelets," Nano Letters **20**, 517–525 (2020).

[118] A. N. Kamenskii, V. O. Kozlov, N. S. Kuznetsov, I. I. Ryzhov, G. G. Kozlov, M. Bayer, A. Greilich, and V. S. Zapasskii, "Invariants in the paramagnetic resonance spectra of impurity crystals," (2021), arXiv:2106.12637 [cond-mat.mes-hall] .

[119] I. A. Merkulov, Al. L. Efros, and M. Rosen, "Electron spin relaxation by nuclei in semiconductor quantum dots," Phys. Rev. B **65**, 205309 (2002).

[120] R. Dahbashi, J. Hübner, F. Berski, J. Wiegand, X. Marie, K. Pierz, H. W. Schumacher, and M. Oestreich, "Measurement of heavy-hole spin dephasing in (inga)as quantum dots," Applied Physics Letters **100**, 031906 (2012).

[121] N. A. Sinitsyn, Yan Li, S. A. Crooker, A. Saxena, and D. L. Smith, "Role of nuclear quadrupole coupling on decoherence and relaxation of central spins in quantum dots," Phys. Rev. Lett. **109**, 166605 (2012).

[122] S. A. Crooker, J. Brandt, C. Sandfort, A. Greilich, D. R. Yakovlev, D. Reuter, A. D. Wieck, and M. Bayer, "Spin noise of electrons and holes in self-assembled quantum dots," Phys. Rev. Lett. **104**, 036601 (2010).

[123] Yan Li, N. Sinitsyn, D. L. Smith, D. Reuter, A. D. Wieck, D. R. Yakovlev, M. Bayer, and S. A. Crooker, "Intrinsic spin fluctuations reveal the dynamical response function of holes coupled to nuclear spin baths in (in,ga)as quantum dots," Phys. Rev. Lett. **108**, 186603 (2012).

[124] Alexandre Faribault and Dirk Schuricht, "Spin decoherence due to a randomly fluctuating spin bath," Phys. Rev. B **88**, 085323 (2013).

[125] Dibyendu Roy, Yan Li, Alex Greilich, Yuriy V. Pershin, Avadh Saxena, and Nikolai A. Sinitsyn, "Spin noise spectroscopy of quantum dot molecules," Phys. Rev. B **88**, 045320 (2013).

[126] Fuxiang Li, Avadh Saxena, Darryl Smith, and Nikolai A Sinitsyn, "Higher-order spin noise statistics," **15**, 113038 (2013).

[127] H. Horn, A. Balocchi, X. Marie, A. Bakin, A. Waag, M. Oestreich, and J. Hübner, "Spin noise spectroscopy of donor-bound electrons in zno," Phys. Rev. B **87**, 045312 (2013).

[128] Luyi Yang, P. Glasenapp, A. Greilich, D. Reuter, A. D. Wieck, D. R. Yakovlev, M. Bayer, and S. A. Crooker, "Two-colour spin noise spectroscopy and fluctuation correlations reveal homogeneous linewidths within quantum-dot ensembles," Nat. Commun. **5**, 4949 (2014).

[129] Johannes Hackmann and Frithjof B. Anders, "Spin noise in the anisotropic central spin model," Phys. Rev. B **89**, 045317 (2014).

[130] Shao-Wen Chen and Ren-Bao Liu, "Faraday rotation echo spectroscopy and detection of quantum fluctuations," Scientific Reports **4**, 4695 (2014).

[131] D. S. Smirnov and M. M. Glazov, "Exciton spin noise in quantum wells," Phys. Rev. B **90**, 085303 (2014).

[132] J. Hackmann, Ph. Glasenapp, A. Greilich, M. Bayer, and F. B. Anders, "Influence of the nuclear electric quadrupolar interaction on the coherence time of hole and electron spins confined in semiconductor quantum dots," Phys. Rev. Lett. **115**, 207401 (2015).

[133] I. I. Ryzhov, M. M. Glazov, A. V. Kavokin, G. G. Kozlov, M. Aßmann, P. Tsotsis, Z. Hatzopoulos, P. G. Savvidis, M. Bayer, and V. S. Zapasskii, "Spin noise of a polariton laser," Phys. Rev. B **93**, 241307 (2016).

[134] M. M. Glazov, "Spin fluctuations of nonequilibrium electrons and excitons in semiconductors," Journal of Experimental and Theoretical Physics **122**, 472–483 (2016).

[135] A. N. Kamenskii, M. Yu. Petrov, G. G. Kozlov, V. S. Zapasskii, S. E. Scholz, C. Sgroi, A. Ludwig, A. D. Wieck, M. Bayer, and A. Greilich, "Detection and amplification of spin noise using scattered laser light in a quantum-dot microcavity," Phys. Rev. B **101**, 041401 (2020).

[136] A. N. Kamenskii, A. Greilich, I. I. Ryzhov, G. G. Kozlov, M. Bayer, and V. S. Zapasskii, "Giant spin-noise gain enables magnetic resonance spectroscopy of impurity crystals," Phys. Rev. Research **2**, 023317 (2020).

[137] I. I. Ryzhov, V. O. Kozlov, N. S. Kuznetsov, I. Yu. Chestnov, A. V. Kavokin, A. Tzimis, Z. Hatzopoulos, P. G. Savvidis, G. G. Kozlov, and V. S. Zapasskii,

"Spin noise signatures of the self-induced larmor precession," Phys. Rev. Res. **2**, 022064 (2020).

[138] N. V. Leppenen, L. Lanco, and D. S. Smirnov, "Quantum zeno effect and quantum nondemolition spin measurement in a quantum dot–micropillar cavity in the strong coupling regime," Phys. Rev. B **103**, 045413 (2021).

[139] Judith Schlagnitweit and Norbert Müller, "The first observation of carbon-13 spin noise spectra," Journal of Magnetic Resonance **224**, 78–81 (2012).

[140] Guillaume Ferrand, Gaspard Huber, Michel Luong, and Hervé Desvaux, "Nuclear spin noise in nmr revisited," The Journal of Chemical Physics **143**, 094201 (2015).

[141] M. A. McCoy and R. R. Ernst, "Nuclear spin noise at room temperature," Chemical Physics Letters **159**, 587–593 (1989).

[142] Maria Theresia Pöschko, Victor V. Rodin, Judith Schlagnitweit, Norbert Müller, and Hervé Desvaux, "Nonlinear detection of secondary isotopic chemical shifts in nmr through spin noise," Nature Communications **8**, 13914 (2017).

[143] Yuan-Yu Jau and Tony Carter, "Vapor-cell-based atomic electrometry for detection frequencies below 1 khz," Phys. Rev. Applied **13**, 054034 (2020).

[144] Hang Li, Jian-Peng Dou, Xiao-Ling Pang, Chao-Ni Zhang, Zeng-Quan Yan, Tian-Huai Yang, Jun Gao, Jia-Ming Li, and Xian-Min Jin, "Multipartite entanglement of billions of motional atoms heralded by single photon," npj Quantum Information **7**, 146 (2021).

[145] Ran Finkelstein, Eilon Poem, Ohad Michel, Ohr Lahad, and Ofer Firstenberg, "Fast, noise-free memory for photon synchronization at room temperature," Science Advances **4**, eaap8598 (2018).

[146] P.A. Bokhan, V.V. Buchanov, N.V. Fateev, M.M. Kalugin, M.A. Kazaryan, A.M. Prokhorov, and D.E. Zakrevskii, Laser Isotope Separation in Atomic Vapor (Wiley, 2006).

[147] Daryl W. Preston, "Doppler-free saturated absorption: Laser spectroscopy," American Journal of Physics **64**, 1432–1436 (1996).

[148] Yahel Horowicz, Or Katz, Oren Raz, and Ofer Firstenberg, "Critical dynamics and phase transition of a strongly interacting warm spin-gas," (2021), arXiv:2104.08622 [quant-ph] .

[149] Junyi Lee, Attaallah Almasi, and Michael Romalis, "Improved limits on spin-mass interactions," Phys. Rev. Lett. **120**, 161801 (2018).

[150] Roy Shaham, Or Katz, and Ofer Firstenberg, "Strong coupling of alkali spins to noble-gas spins with hour-long coherence time," (2021), arXiv:2102.02797 [quant-ph] .

[151] Ryotaro Inoue, Shin-Ichi-Ro Tanaka, Ryo Namiki, Takahiro Sagawa, and Yoshiro Takahashi, "Unconditional quantum-noise suppression via measurement-based quantum feedback," Phys. Rev. Lett. **110**, 163602 (2013).

[152] N. Behbood2013, G. Colangelo, F. Martin Ciurana, M. Napolitano, R. J. Sewell, and M. W. Mitchell, "Feedback cooling of an atomic spin ensemble," Phys. Rev. Lett. **111**, 103601 (2013).

[153] Bogdan Mihaila, Scott A. Crooker, Dwight G. Rickel, Krastan B. Blagoev, Peter B. Littlewood, and Darryl L. Smith, "Quantitative study of spin noise spectroscopy in a classical gas of ^{41}K atoms," Phys. Rev. A **74**, 043819 (2006).

[154] G. E. Katsoprinakis, A. T. Dellis, and I. K. Kominis, "Measurement of transverse spin-relaxation rates in a rubidium vapor by use of spin-noise spectroscopy," Phys. Rev. A **75**, 042502 (2007).

[155] G. E. Katsoprinakis, M. Polis, A. Tavernarakis, A. T. Dellis, and I. K. Kominis, "Quantum random number generator based on spin noise," Phys. Rev. A **77**, 054101 (2008).

[156] I. K. Kominis, "Sub-shot-noise magnetometry with a correlated spin-relaxation dominated alkali-metal vapor," Phys. Rev. Lett. **100**, 073002 (2008).

[157] Šimon Kos, Alexander V. Balatsky, Peter B. Littlewood, and Darryl L. Smith, "Spin noise of itinerant fermions," Phys. Rev. B **81**, 064407 (2010).

[158] H. Horn, G. M. Müller, E. M. Rasel, L. Santos, J. Hübner, and M. Oestreich, "Spin-noise spectroscopy under resonant optical probing conditions: Coherent and nonlinear effects," Phys. Rev. A **84**, 043851 (2011).

[159] V. S. Zapasskii, A. Greilich, S. A. Crooker, Yan Li, G. G. Kozlov, D. R. Yakovlev, D. Reuter, A. D. Wieck, and M. Bayer, "Optical spectroscopy of spin noise," Phys. Rev. Lett. **110**, 176601 (2013).

[160] Fuxiang Li, Jie Ren, and Nikolai A. Sinitsyn, "Quantum zeno effect as a topological phase transition in full counting statistics and spin noise spectroscopy," **105**, 27001 (2014).

[161] A. T. Dellis, M. Loulakis, and I. K. Kominis, "Spin-noise correlations and spin-noise exchange driven by low-field spin-exchange collisions," Phys. Rev. A **90**, 032705 (2014).

[162] P. Glasenapp, N. A. Sinitsyn, Luyi Yang, D. G. Rickel, D. Roy, A. Greilich, M. Bayer, and S. A. Crooker, "Spin noise spectroscopy beyond thermal equilibrium and linear response," Phys. Rev. Lett. **113**, 156601 (2014).

[163] Dibyendu Roy, Rajeev Singh, and Roderich Moessner, "Probing many-body localization by spin noise spectroscopy," Phys. Rev. B **92**, 180205 (2015).

[164] Z. Yue and M. E. Raikh, "Evolution of inhomogeneously broadened spin-noise spectrum with ac drive," Phys. Rev. B **91**, 155301 (2015).

[165] Vito Giovanni Lucivero, Ricardo Jiménez-Martínez, Jia Kong, and Morgan W. Mitchell, "Squeezed-light spin noise spectroscopy," Phys. Rev. A **93**, 053802 (2016).

[166] Fuxiang Li, S. A. Crooker, and N. A. Sinitsyn, "Higher-order spin-noise spectroscopy of atomic spins in fluctuating external fields," Phys. Rev. A **93**, 033814 (2016).

[167] G. G. Kozlov, I. I. Ryzhov, and V. S. Zapasskii, "Light scattering in a medium with fluctuating gyrotropy: Application to spin-noise spectroscopy," Phys. Rev. A **95**, 043810 (2017).

[168] Yong-Min Li, Xu-Yang Wang, Zeng-Liang Bai, Wen-Yuan Liu, Shen-Shen Yang, and Kun-Chi Peng, "Continuous variable quantum key distribution*," Chinese Physics B **26**, 040303 (2017).

[169] V. G. Lucivero, N. D. McDonough, N. Dural, and M. V. Romalis, "Correlation function of spin noise due to atomic diffusion," Phys. Rev. A **96**, 062702 (2017).

[170] M. Yu. Petrov, I. I. Ryzhov, D. S. Smirnov, L. Yu. Belyaev, R. A. Potekhin, M. M. Glazov, V. N. Kulyasov, G. G. Kozlov, E. B. Aleksandrov, and V. S. Zapasskii, "Homogenization of doppler broadening in spin-noise spectroscopy," Phys. Rev. A **97**, 032502 (2018).

[171] K. Mouloudakis, M. Loulakis, and I. K. Kominis, "Quantum trajectories in spin-exchange collisions reveal the nature of spin-noise correlations in multispecies alkali-metal vapors," Phys. Rev. Research **1**, 033017 (2019).

[172] Yuanjiang Tang, Ya Wen, Ling Cai, and Kaifeng Zhao, "Spin-noise spectrum of hot vapor atoms in an anti-relaxation-coated cell," Phys. Rev. A **101**, 013821 (2020).

[173] A. V. Poshakinskiy and S. A. Tarasenko, "Spin noise at electron paramagnetic resonance," Phys. Rev. B **101**, 075403 (2020).

[174] A. A. Fomin, M. Yu. Petrov, G. G. Kozlov, M. M. Glazov, I. I. Ryzhov, M. V. Balabas, and V. S. Zapasskii, "Spin-alignment noise in atomic vapor," Phys. Rev. Research **2**, 012008 (2020).

[175] Guiying Zhang, Ya Wen, Jian Qiu, and Kaifeng Zhao, "Spin-noise spectrum in a pulse-modulated field," Opt. Express **28**, 15925–15933 (2020).

[176] A. A. Fomin, M. Yu. Petrov, I. I. Ryzhov, G. G. Kozlov, V. S. Zapasskii, and M. M. Glazov, "Nonlinear spectroscopy of high-spin fluctuations," Phys. Rev. A **103**, 023104 (2021).

[177] A. A. Fomin, M. Yu. Petrov, G. G. Kozlov, A. K. Vershovskii, M. M. Glazov, and V. S. Zapasskii, "Anomalous light-induced broadening of the spin-noise resonance in cesium vapor," Phys. Rev. A **103**, 042820 (2021).

[178] Ya Wen, Xiangyu Li, Guiying Zhang, and Kaifeng Zhao, "Zero-field spin noise spectrum of an alkali vapor with strong spin-exchange coupling," (2021), arXiv:2106.05540 [quant-ph] .

[179] V. Guarrera, R. Gartman, G. Bevilacqua, and W. Chalupczak, "Spin-noise spectroscopy of a noise-squeezed atomic state," Phys. Rev. Research **3**, L032015 (2021).

[180] A. Theodore Forrester, Richard A. Gudmundsen, and Philip O. Johnson, "Photoelectric mixing of incoherent light," Phys. Rev. **99**, 1691–1700 (1955).

[181] R. HANBURY BROWN and R. Q. TWISS, "Correlation between photons in two coherent beams of light," Nature **177**, 27–29 (1956).

[182] A D Buckingham and P J Stephens, "Magnetic optical activity," Annual Review of Physical Chemistry **17**, 399–432 (1966).

[183] F. Meier and B.P. Zakharchenya, Optical Orientation, ISSN (Elsevier Science, 2012).

[184] F. Bitter, "The optical detection of radiofrequency resonance," Phys. Rev. **76**, 833–835 (1949).

[185] R. Giri, S. Cronenberger, M. Vladimirova, D. Scalbert, K. V. Kavokin, M. M. Glazov, M. Nawrocki, A. Lemaître, and J. Bloch, "Giant photoinduced faraday rotation due to the spin-polarized electron gas in an n-gaas microcavity," Phys. Rev. B **85**, 195313 (2012).

[186] Richard C. Mockler, "Atomic beam frequency standards," (Academic Press, 1961) pp. 1 – 71.

[187] V. S. Zapasskii, A. Greilich, S. A. Crooker, Yan Li, G. G. Kozlov, D. R. Yakovlev, D. Reuter, A. D. Wieck, and M. Bayer, "Optical spectroscopy of spin noise," Phys. Rev. Lett. **110**, 176601 (2013).

[188] M. Arditi and T. R. Carver, "Hyperfine relaxation of optically pumped rb^{87} atoms in buffer gases," Phys. Rev. **136**, A643 (1964).

[189] "Crc handbook of chemistry and physics. 81st edition edited by david r. lide (national institute of standards and technology). crc press: boca raton, fl. 2000. 2556 pp. $129.95. isbn 0-8493-0481-4," Journal of the American Chemical Society **122**, 12614–12614 (2000).

[190] Andrei Nikolaevich Nesmeianov and Robert. Gary, Vapor pressure of the chemical elements (Elsevier, Amsterdam; London; New York, 1963).

[191] Xiaohu Liu, Chang Chen, Tianliang Qu, Kaiyong Yang, and Hui Luo, "Transverse spin relaxation and diffusion-constant measurements of spin-polarized 129xe nuclei in the presence of a magnetic field gradient," Scientific Reports **6**, 24122 (2016).

[192] N. Castagna, G. Bison, G. Di Domenico, A. Hofer, P. Knowles, C. Macchione, H. Saudan, and A. Weis, "A large sample study of spin relaxation and magnetometric sensitivity of paraffin-coated cs vapor cells," Applied Physics B **96**, 763–772 (2009).

[193] Chang Chen, Qiyuan Jiang, Zhiguo Wang, Yi Zhang, Hui Luo, and Kayiong Yang, "A non-interference method for measurement of transverse relaxation time

of the alkali metal magnetometer in nuclear magnetic resonance oscillator," AIP Advances **10**, 065303 (2020), https://doi.org/10.1063/5.0007009 .

[194] Deok-Young Lee, Sangkyung Lee, and Sin Hyuk Yim, "Measurement of a129xe transverse relaxation rate without the influence of rb polarization-induced magnetic gradient," Appl. Opt. **60**, 7290–7296 (2021).

[195] N. Castagna and A. Weis, "Measurement of longitudinal and transverse spin relaxation rates using the ground-state hanle effect," Phys. Rev. A **84**, 053421 (2011).

[196] M. V. Romalis, E. Miron, and G. D. Cates, "Pressure broadening of rb D_1 and D_2 lines by ^{3}he, ^{4}he, n_2, and xe: Line cores and near wings," Phys. Rev. A **56**, 4569 (1997).

[197] A. H. Couture, T. B. Clegg, and B. Driehuys, "Pressure shifts and broadening of the cs d1 and d2 lines by he, n2, and xe at densities used for optical pumping and spin exchange polarization," J. Appl. Phys. **104**, 094912 (2008).

[198] Rujie Li, Yang Li, Liwei Jiang, Wei Quan, Ming Ding, and Jiancheng Fang, "Pressure broadening and shift of k d1 and d2 lines in the presence of 3he and 21ne," Eur. Phys. J. D **70**, 139 (2016).

[199] E. Arimondo, M. Inguscio, and P. Violino, "Experimental determinations of the hyperfine structure in the alkali atoms," Rev. Mod. Phys. **49**, 31–75 (1977).

[200] I. I. Ryzhov, S. V. Poltavtsev, K. V. Kavokin, M. M. Glazov, G. G. Kozlov, M. Vladimirova, D. Scalbert, S. Cronenberger, A. V. Kavokin, A. Lemaître, J. Bloch, and V. S. Zapasskii, "Measurements of nuclear spin dynamics by spin-noise spectroscopy," Applied Physics Letters **106**, 242405 (2015).

[201] S. Bize, Y. Sortais, M. S. Santos, C. Mandache, A. Clairon, and C. Salomon, "High-accuracy measurement of the 87 rb ground-state hyperfine splitting in an atomic fountain," Europhysics Letters (EPL) **45**, 558–564 (1999).

[202] Claude Cohen-Tannoudji and Alfred Kastler, "I optical pumping," in Progress in Optics, Vol. 5 (Elsevier, 1966) pp. 1–81.

[203] Alfred Kastler, "Optical methods of atomic orientation and of magnetic resonance*," Journal of the Optical Society of America **47**, 460–465 (1957).

[204] Or Katz and Ofer Firstenberg, "Transverse optical pumping of spin states," Communications Physics **2**, 58 (2019).

[205] M. Auzinsh, D. Budker, and S. Rochester, Optically Polarized Atoms: Understanding Light-atom Interactions (OUP Oxford, 2010).

[206] W. Happer, Y.Y. Jau, and T. Walker, Optically Pumped Atoms (Wiley, 2010).

[207] I. K. Kominis, T. W. Kornack, J. C. Allred, and M. V. Romalis, "A subfemtotesla multichannel atomic magnetometer," Nature **422**, 596–599 (2003).

[208] J. Kitching, S. Knappe, and E. A. Donley, "Atomic sensors – a review," IEEE Sensors Journal **11**, 1749–1758 (2011).

[209] D. Sheng, S. Li, N. Dural, and M. V. Romalis, "Subfemtotesla scalar atomic magnetometry using multipass cells," Phys. Rev. Lett. **110**, 160802 (2013).

[210] Andrew Horsley, Guan-Xiang Du, and Philipp Treutlein, "Widefield microwave imaging in alkali vapor cells with sub-100 μm resolution," New Journal of Physics **17**, 11 (Nov 2015), cLASSICAL AND QUANTUM MECHANICS, GENERAL PHYSICS.

[211] J. Dupont-Roc, S. Haroche, and C. Cohen-Tannoudji, "Detection of very weak magnetic fields (109gauss) by 87rb zero-field level crossing resonances," Physics Letters A **28**, 638–639 (1969).

[212] I. Novikova, R. L. Walsworth, and Y. Xiao, "Electromagnetically induced transparency-based slow and stored light in warm atoms," Laser & Photonics Reviews **6**, 333–353 (2012).

[213] Klemens Hammerer, Anders S. Sørensen, and Eugene S. Polzik, "Quantum interface between light and atomic ensembles," Rev. Mod. Phys. **82**, 1041–1093 (2010).

[214] Christoffer B. Møller, Rodrigo A. Thomas, Georgios Vasilakis, Emil Zeuthen, Yeghishe Tsaturyan, Mikhail Balabas, Kasper Jensen, Albert Schliesser, Klemens Hammerer, and Eugene S. Polzik, "Quantum back-action-evading measurement of motion in a negative mass reference frame," Nature **547**, 191–195 (2017).

[215] Or Katz, Roy Shaham, Eugene S. Polzik, and Ofer Firstenberg, "Long-lived entanglement generation of nuclear spins using coherent light," Phys. Rev. Lett. **124**, 043602 (2020).

[216] Finkelstein Ran, Poem Eilon, Michel Ohad, Lahad Ohr, and Firstenberg Ofer, "Fast, noise-free memory for photon synchronization at room temperature," Science Advances **4**, eaap8598 (XXXX).

[217] Thad G. Walker and William Happer, "Spin-exchange optical pumping of noble-gas nuclei," Rev. Mod. Phys. **69**, 629–642 (1997).

[218] Timothy Chupp and Scott Swanson, "Medical imaging with laser-polarized noble gases," in Advances In Atomic, Molecular, and Optical Physics, Vol. 45 (Academic Press, 2001) pp. 41–98.

[219] F. Kuchler, E. Babcock, M. Burghoff, T. Chupp, S. Degenkolb, I. Fan, P. Fierlinger, F. Gong, E. Kraegeloh, W. Kilian, S. Knappe-Grüneberg, T. Lins, M. Marino, J. Meinel, B. Niessen, N. Sachdeva, Z. Salhi, A. Schnabel, F. Seifert, J. Singh, S. Stuiber, L. Trahms, and J. Voigt, "A new search for the atomic edm of 129xe at frm-ii," Hyperfine Interactions **237**, 95 (2016).

[220] G. Vasilakis, J. M. Brown, T. W. Kornack, and M. V. Romalis, "Limits on new long range nuclear spin-dependent forces set with a $\mathbf{K}-{}^3\mathrm{He}$ comagnetometer," Phys. Rev. Lett. **103**, 261801 (2009).

[221] M. Smiciklas, J. M. Brown, L. W. Cheuk, S. J. Smullin, and M. V. Romalis, "New test of local lorentz invariance using a $^{21}\mathrm{Ne}-\mathrm{Rb}-\mathbf{K}$ comagnetometer," Phys. Rev. Lett. **107**, 171604 (2011).

[222] Alexander D. Cronin, Jörg Schmiedmayer, and David E. Pritchard, "Optics and interferometry with atoms and molecules," Rev. Mod. Phys. **81**, 1051–1129 (2009).

[223] R. Wynands and Weyers S., "Atomic fountain clocks," Metrologia **42**, S64 (2005).

[224] A. Bertoldi, G. Lamporesi, L. Cacciapuoti, M. de Angelis, M. Fattori, T. Petelski, A. Peters, M. Prevedelli, J. Stuhler, and G. M. Tino, "Atom interferometry gravity-gradiometer for the determination of the newtonian gravitational constant g," Eur. Phys. J. D **40**, 271 (2006).

[225] Th. Hänsch and P. Toschek, "Theory of a three-level gas laser amplifier," Zeitschrift für Physik A Hadrons and nuclei **236**, 213–244 (1970).

[226] B. Lounis and C. Cohen-Tannoudji, "Coherent population trapping and fano profiles," J. Phys. II France **2**, 579–592 (1992).

[227] G. Alzetta, A. Gozzini, L. Moi, and G. Orriols, "An experimental method for the observation of r.f. transitions and laser beat resonances in oriented na vapour," Il Nuovo Cimento B (1971-1996) **36**, 5–20 (1976).

[228] R. M. Whitley and C. R. Stroud, "Double optical resonance," Phys. Rev. A **14**, 1498–1513 (1976).

[229] E. Arimondo and G. Orriols, "Nonabsorbing atomic coherences by coherent two-photon transitions in a three-level optical pumping," Lettere al Nuovo Cimento (1971-1985) **17**, 333–338 (1976).

[230] H. R. Gray, R. M. Whitley, and C. R. Stroud, "Coherent trapping of atomic populations," Optics Letters **3**, 218–220 (1978).

[231] E. Arimondo, "V coherent population trapping in laser spectroscopy," in Progress in Optics, Vol. 35 (Elsevier, 1996) pp. 257–354.

[232] Michael Fleischhauer, Atac Imamoglu, and Jonathan P. Marangos, "Electromagnetically induced transparency: Optics in coherent media," Rev. Mod. Phys. **77**, 633–673 (2005).

[233] M.O. Scully and M.S. Zubairy, Quantum Optics (Cambridge University Press, 1997).

[234] Bayram Tekin, "Stern–gerlach experiment with higher spins," Eur. J. Phys. **37**, 035401 (2016).

[235] A. Ben-Kish and M. V. Romalis, "Dead-zone-free atomic magnetometry with simultaneous excitation of orientation and alignment resonances," Phys. Rev. Lett. **105**, 193601 (2010).

[236] Or Katz, Or Peleg, and Ofer Firstenberg, "Coherent coupling of alkali atoms by random collisions," Phys. Rev. Lett. **115**, 113003 (2015).

[237] Earl Babcock, Ian Nelson, Steve Kadlecek, Bastiaan Driehuys, L. W. Anderson, F. W. Hersman, and Thad G. Walker, "Hybrid spin-exchange optical pumping of ^{3}He," Phys. Rev. Lett. **91**, 123003 (2003).

[238] B. Lancor and T. G. Walker, "Polarization limits in k-rb spin-exchange mixtures," Phys. Rev. A **83**, 065401 (2011).

[239] M. V. Romalis, "Hybrid optical pumping of optically dense alkali-metal vapor without quenching gas," Phys. Rev. Lett. **105**, 243001 (2010).

[240] S. Haroche and C. Cohen-Tannoudji, "Resonant transfer of coherence in nonzero magnetic field between atomic levels of different g factors," Phys. Rev. Lett. **24**, 974–978 (1970).

[241] Haruhiko Ito, Taro Ito, and Tsutomu Yabuzaki, "Accumulative transfer of transverse magnetic moment between spin-locked rb and cs atoms," Journal of the Physical Society of Japan **63**, 1337–1344 (1994).

[242] J Skalla, G Wäckerle, and M Mehring, "Coherence transfer between atomic transitions of different g-factor by modulated optical excitation," Optics Communications **127**, 31 – 36 (1996).

[243] Jeffrey A Wepman and J Randy Hoffman, RF and IF digitization in radio receivers: Theory, concepts, and examples (NTIA Report 96-328, 1996).

[244] O. Jamin, Broadband Direct RF Digitization Receivers, Analog Circuits and Signal Processing (Springer International Publishing, 2013).

[245] Marcelo Alejandro Luda, Martin Drechsler, Christian Tomás Schmiegelow, and Jorge Codnia, "Compact embedded device for lock-in measurements and experiment active control," Review of Scientific Instruments **90**, 023106 (2019).

[246] G. A. Stimpson, M. S. Skilbeck, R. L. Patel, B. L. Green, and G. W. Morley, "An open-source high-frequency lock-in amplifier," Review of Scientific Instruments **90**, 094701 (2019).

[247] Kazuyuki Takeda, "A highly integrated fpga-based nuclear magnetic resonance spectrometer," Review of Scientific Instruments **78**, 033103 (2007).

[248] Ronald Newbold Bracewell and Ronald N Bracewell, The Fourier transform and its applications, Vol. 31999 (McGraw-Hill New York, 1986).

[249] James W. Cooley, Peter A. W. Lewis, and Peter D. Welch, "The fast fourier transform and its applications," IEEE Transactions on Education **12**, 27–34 (1969).

[250] P. Duhamel and M. Vetterli, "Fast fourier transforms: A tutorial review and a state of the art," Signal Processing **19**, 259–299 (1990).

[251] M. E. Tiuri, "Radio astronomy receivers," IEEE Transactions on Military Electronics **8**, 264–272 (1964).

[252] V Mugundhan, Design of digital receivers for low frequency radio astronomy, Ph.D. thesis, Indian Institute of Astrophysics (2018).

[253] Parishwad P Vaidyanathan, "Multirate digital filters, filter banks, polyphase networks, and applications: a tutorial," Proceedings of the IEEE **78**, 56–93 (1990).

[254] RF Emerson, "Biplex pipelined fft," The Deep Space Network Progress Report , 42–34 (1976).

[255] Jack Hickish, Zuhra Abdurashidova, Zaki Ali, Kaushal D Buch, Sandeep C Chaudhari, Hong Chen, Matthew Dexter, Rachel Simone Domagalski, John Ford, Griffin Foster, et al., "A decade of developing radio-astronomy instrumentation using casper open-source technology," Journal of Astronomical Instrumentation **5**, 1641001 (2016).

[256] CASPER Signal Processing Collaboration, "Casper signal processing libraries," https://casper.ssl.berkeley.edu/wiki/Block_Documentation.

[257] Pavel Demin, "Red pitaya notes," http://pavel-demin.github.io/red-pitaya-notes/.

[258] Eugene Hogenauer, "An economical class of digital filters for decimation and interpolation," IEEE transactions on acoustics, speech, and signal processing **29**, 155–162 (1981).

[259] Richard Lyons, "Understanding cascaded integrator-comb filters," Embed Syst Program **18**, 14–27 (2005).

[260] PA Fridman, "Statistically stable estimates of variance in radio-astronomy observations as tools for radio-frequency interference mitigation," The Astronomical Journal **135**, 1810 (2008).

[261] John M Ford and Kaushal D Buch, "Rfi mitigation techniques in radio astronomy," in 2014 IEEE Geoscience and Remote Sensing Symposium (IEEE, 2014) pp. 231–234.

[262] MD Prouty, R Johnson, I Hrvoic, and AK Vershovskiy, "Geophysical applications," Optical Magnetometry , 319 (2013).

[263] G Bison, R Wynands, and A Weis, "A laser-pumped magnetometer for the mapping of human cardiomagnetic fields," Applied Physics B **76**, 325–328 (2003).

[264] Y. Uchikawa and M. Kotani, "Measurement of magnetic field produced from the human body," IEEE Translation Journal on Magnetics in Japan **7**, 600–607 (1992).

[265] K B Davis, M O Mewes, M R Andrews, N J Van Druten, D S Durfee, D M Kurn, and W Ketterle, "Bose-Einstein condensation in a gas of sodium atoms," Physical Review Letters **75**, 3969–3973 (1995).

[266] M H Anderson, J R Ensher, M R Matthews, C E Wieman, and E A Cornell, "Observation of Bose-Einstein condensation in a dilute atomic vapor," Science **269**, 198–201 (1995).

[267] Richard P. Feynman, "Simulating physics with computers," International Journal of Theoretical Physics **21**, 467–488 (1982).

[268] J. Ignacio Cirac and Peter Zoller, "Goals and opportunities in quantum simulation," Nature Physics **8**, 264–266 (2012).

[269] I. M. Georgescu, S. Ashhab, and Franco Nori, "Quantum simulation," Rev. Mod. Phys. **86**, 153–185 (2014).

[270] Johnson, Tomi H, Clark, Stephen R, and Jaksch, Dieter, "What is a quantum simulator?" EPJ Quantum Technol. **1**, 10 (2014).

[271] Immanuel Bloch, Jean Dalibard, and Sylvain Nascimbène, "Quantum simulations with ultracold quantum gases," Nature Physics **8**, 267–276 (2012).

[272] R. Blatt and C. F. Roos, "Quantum simulations with trapped ions," Nature Physics **8**, 277–284 (2012).

[273] Alán Aspuru-Guzik and Philip Walther, "Photonic quantum simulators," Nature Physics **8**, 285–291 (2012).

[274] Maciej Lewenstein, Anna Sanpera, Veronica Ahufinger, Bogdan Damski, Aditi Sen(De), and Ujjwal Sen, "Ultracold atomic gases in optical lattices: mimicking condensed matter physics and beyond," Advances in Physics **56**, 243–379 (2007).

[275] Steven Chu, "The manipulation of neutral particles," Rev. Mod. Phys. **70**, 685–706 (1998).

[276] William D Phillips, "Laser cooling and trapping of neutral atoms," Reviews of Modern Physics **70**, 721–741 (1998).

[277] Claude N Cohen-Tannoudji, "Manipulating atoms with photons," Reviews of Modern Physics **70**, 707–719 (1998).

[278] William D Phillips, John V Prodan, and Harold J Metcalf, "Laser cooling and electromagnetic trapping of neutral atoms," Journal of the Optical Society of America B **2**, 1751 (1985).

[279] P. D. Lett, W. D. Phillips, S. L. Rolston, C. E. Tanner, R. N. Watts, and C. I. Westbrook, "Optical molasses," Journal of the Optical Society of America B **6**, 2084 (2008).

[280] A. M. Steane, M. Chowdhury, and C. J. Foot, "Radiation force in the magneto-optical trap," J. Opt. Soc. Am. B **9**, 2142–2158 (1992).

[281] H J Metcalf and P van der Straten, "Laser Cooling and Trapping," Journal of the Optical Society of America B Graduate Texts in Contemporary Physics, **20**, 887 (2001).

[282] Kazuko Shimizu, "Laser Cooling and Trapping of Neutral Atoms," in Shinku/Journal of the Vacuum Society of Japan, Vol. 38 (Wiley-VCH Verlag GmbH & Co. KGaA, Weinheim, Germany, 1995) pp. 847–853.

[283] V I Balykin and Wonho Jhe, "Atom Optics," in Journal of the Korean Physical Society, Vol. 37 (Springer, 2000) pp. 654–660.

[284] W. R. HINDMARSH, Nature, Oxford master series in physics, Vol. 239 (Oxford University Press, 2005) pp. 351–352.

[285] A.M. Fox, M. Fox, D.P.A.M. Fox, and Oxford University Press, Quantum Optics: An Introduction, Oxford Master Series in Physics (OUP Oxford, 2006).

[286] Paul D Lett, Richard N Watts, Christoph I Westbrook, William D Phillips, Phillip L Gould, and Harold J Metcalf, "Observation of Atoms Laser Cooled below the Doppler Limit," Physical Review Letters **61**, 169–172 (1988).

[287] J. Dalibard and C. Cohen-Tannoudji, "Laser cooling below the doppler limit by polarization gradients: simple theoretical models," J. Opt. Soc. Am. B **6**, 2023–2045 (1989).

[288] T. W. Hodapp, C. Gerz, C. Furtlehner, C. I. Westbrook, W. D. Phillips, and J. Dalibard, "Three-dimensional spatial diffusion in optical molasses," Applied Physics B **60**, 135–143 (1995).

[289] A G Truscott, D Baleva, N R Heckenberg, and H Rubinsztein-Dunlop, "Short-term spatial diffusion in $\sigma^{+\smile}\sigma^{-}$ optical molasses," Optics Communications **145**, 81–85 (1998).

[290] Morgan W. Mitchell and Silvana Palacios Alvarez, "Colloquium: Quantum limits to the energy resolution of magnetic field sensors," Rev. Mod. Phys. **92**, 021001 (2020).

[291] Immanuel Bloch, Jean Dalibard, and Wilhelm Zwerger, "Many-body physics with ultracold gases," Rev. Mod. Phys. **80**, 885–964 (2008).

[292] N. Behbood, F. Martin Ciurana, G. Colangelo, M. Napolitano, Géza Tóth, R. J. Sewell, and M. W. Mitchell, "Generation of macroscopic singlet states in a cold atomic ensemble," Phys. Rev. Lett. **113**, 093601 (2014).

[293] R. Thomas, J. S. Otto, M. Chilcott, A. B. Deb, and N. Kjærgaard, "Reducing number fluctuations in an ultracold atomic sample using faraday rotation and iterative feedback," (2021), arXiv:2102.01773 [cond-mat.quant-gas] .

[294] Y. Liu, E. Gomez, S. E. Maxwell, L. D. Turner, E. Tiesinga, and P. D. Lett, "Number fluctuations and energy dissipation in sodium spinor condensates," Phys. Rev. Lett. **102**, 225301 (2009).

[295] Martijn Jasperse, "Faraday magnetic resonance imaging of bose-einstein condensates," (2017).

[296] Christopher Immer James Simpson, John Lane and Robert Youngquist, "Simple analytic expressions for the magnetic field of a circular current loop." Tech Rep: **1–3** (2001).

[297] Brian Julsgaard, Alexander Kozhekin, and Eugene S. Polzik, "Experimental long-lived entanglement of two macroscopic objects," Nature **413**, 400–403 (2001).

[298] G. Vasilakis, H. Shen, K. Jensen, M. Balabas, D. Salart, B. Chen, and E. S. Polzik, "Generation of a squeezed state of an oscillator by stroboscopic back-action-evading measurement," Nature Physics **11**, 389–392 (2015).

[299] H. Häffner, W. Hänsel, C. F. Roos, J. Benhelm, D. Chek-al kar, M. Chwalla, T. Körber, U. D. Rapol, M. Riebe, P. O. Schmidt, C. Becher, O. Gühne, W. Dür, and R. Blatt, "Scalable multiparticle entanglement of trapped ions," Nature **438**, 643–646 (2005).

[300] P. Neumann, N. Mizuochi, F. Rempp, P. Hemmer, H. Watanabe, S. Yamasaki, V. Jacques, T. Gaebel, F. Jelezko, and J. Wrachtrup, "Multipartite entanglement among single spins in diamond," Science **320**, 1326–1329 (2008).

[301] A. D. O'Connell, M. Hofheinz, M. Ansmann, Radoslaw C. Bialczak, M. Lenander, Erik Lucero, M. Neeley, D. Sank, H. Wang, M. Weides, J. Wenner, John M. Martinis, and A. N. Cleland, "Quantum ground state and single-phonon control of a mechanical resonator," Nature **464**, 697–703 (2010).

[302] T. D. Ladd, F. Jelezko, R. Laflamme, Y. Nakamura, C. Monroe, and J. L. O'Brien, "Quantum computers," Nature **464**, 45–53 (2010).

[303] Luca Pezzè, Augusto Smerzi, Markus K. Oberthaler, Roman Schmied, and Philipp Treutlein, "Quantum metrology with nonclassical states of atomic ensembles," Rev. Mod. Phys. **90**, 035005 (2018).

[304] Armin Ridinger, "Towards quantum degenerate fermi mixtures: Photoassociation of weakly bound ^{6}li - ^{40}k molecules," (2011).

[305] B.E.A. Saleh and M.C. Teich, Fundamentals of Photonics, Wiley series in pure and applied optics (Wiley India, 2007).

[306] E. A. Donley, T. P. Heavner, F. Levi, M. O. Tataw, and S. R. Jefferts, "Double-pass acousto-optic modulator system," Review of Scientific Instruments **76**, 063112 (2005).

[307] T. Bergeman, Gidon Erez, and Harold J. Metcalf, "Magnetostatic trapping fields for neutral atoms," Phys. Rev. A **35**, 1535–1546 (1987).

[308] Alan L. Migdall, John V. Prodan, William D. Phillips, Thomas H. Bergeman, and Harold J. Metcalf, "First observation of magnetically trapped neutral atoms," Phys. Rev. Lett. **54**, 2596–2599 (1985).

[309] Dibyendu Roy, "Critical features of nonlinear optical isolators for improved nonreciprocity," Phys. Rev. A **96**, 033838 (2017).

[310] Pooja Manasi and Dibyendu Roy, "Light propagation through one-dimensional interacting open quantum systems," Phys. Rev. A **98**, 023802 (2018).

[311] Athul Vinu and Dibyendu Roy, "Amplification and cross-kerr nonlinearity in waveguide quantum electrodynamics," Phys. Rev. A **101**, 053812 (2020).